Multinary metal oxide semiconductors – A study of different material systems and their application in thin-film transistors

Dissertation
M.Sc. Shawn Sanctis
Fachbereich Chemie | October 2019

TECHNISCHE UNIVERSITÄT DARMSTADT

Fachbereich Anorganische Chemie
Eduard-Zintl-Institut für Anorganische und Physikalische Chemie

Multinary metal oxide semiconductors - A study of different material systems and their application in thin-film transistors

vom Fachbereich Chemie

der Technischen Universität Darmstadt

zur Erlangung des Grades

Doctor rerum naturalium (Dr. rer. nat.)

Dissertation

von **Shawn Sanctis, M. Sc.**

Erstgutachter : Prof. Dr. rer. nat. Jörg J. Schneider

Zweitgutachter: PD Dr.-Ing. Oktay Yilmazoglu

Darmstadt 2019

Sanctis, Shawn: **Multinary metal oxide semiconductors - A study of different material systems and their application in thin-film transistors**

Multinäre Metalloxidhalbleiter - Eine Untersuchung verschiedener materialsysteme und deren Anwendung in Dünnschichttransistoren

Darmstadt, Technische Universität Darmstadt
Jahr der Veröffentlichung der Dissertation auf TUprints: 2020
Tag der Einreichung: 11.10.2019
Tag der mündlichen Prüfung: 25.11.2019

Erklärung A

Shawn Sanctis

Klappacher Str.3

64285 Darmstadt

Datum 11.10.2019

Erklärung

Ich erkläre hiermit, dass ich meine Dissertation selbstständig und nur mit den angegebenen Hilfsmitteln angefertigt habe.

Shawn Sanctis

Erklärung B

Shawn Sanctis

Klappacher Str.3

64285 Darmstadt

Datum 11.10.2019

Erklärung

Ich erkläre hiermit, noch keinen Promotionsversuch unternommen zu haben.

Shawn Sanctis

Erklärung C

Erklärung zum Eigenanteil an den Veröffentlichungen

Shawn Sanctis Datum 11.10.2019

Klappacher Str.3

64285 Darmstadt

Im Folgenden ist aufgelistet, mit welchem Anteil ich an den Veröffentlichungen beteiligt war.

Publikationsliste

Wissenschaftliche Artikel als Erstautor

1. Mein Anteil an der folgenden Veröffentlichung beträgt 75%
Sanctis, S.; Krausmann, J.; Guhl, C.; Schneider, J. J., Stacked Indium Oxide/Zinc Oxide Heterostructures as Semiconductors in Thin Film Transistor Devices: A Case Study using Atomic Layer Deposition. *Journal of Materials Chemistry C 2018*, 6 (3), 464-472.

2. Mein Anteil an der folgenden Veröffentlichung beträgt 75%
Sanctis, S.; Hoffmann, R. C.; Koslowski, N.; Foro, S.; Bruns, M.; Schneider, J. J., Aqueous Solution Processing of Combustible Precursor Compounds into Amorphous Indium Gallium Zinc Oxide (IGZO) Semiconductors for Thin Film Transistor Applications. *Chemistry–An Asian Journal* 2018, 13 (24), 3912-3919.

3. Mein Anteil an der folgenden Veröffentlichung beträgt 75%
Sanctis, S.; Hoffmann, R. C.; Bruns, M.; Schneider, J. J., Direct Photopatterning of Solution–Processed Amorphous Indium Zinc Oxide and Zinc Tin Oxide Semiconductors—A Chimie Douce Molecular Precursor Approach to Thin Film Electronic Oxides. *Advanced Materials Interfaces* 2018, 5 (15), 1800324.

4. Mein Anteil an der folgenden Veröffentlichung beträgt 75%
Sanctis, S.; Koslowski, N.; Hoffmann, R.; Guhl, C.; Erdem, E.; Weber, S.; Schneider, J. J., Toward an understanding of thin-film transistor performance in solution-processed amorphous zinc tin oxide (ZTO) thin films. *ACS applied materials & interfaces* 2017, 9 (25), 21328-21337.

5. Mein Anteil an der folgenden Veröffentlichung beträgt 75%
Sanctis, S.; Hoffmann, R. C.; Precht, R.; Anwand, W.; Schneider, J. J., Understanding the temperature-dependent evolution of solution processed metal oxide transistor characteristics based on molecular precursor derived amorphous indium zinc oxide. *Journal of Materials Chemistry C* 2016, 4 (46), 10935-10944.

6. Mein Anteil an der folgenden Veröffentlichung beträgt 75%
Sanctis, S.; Hoffmann, R. C.; Eiben, S.; Schneider, J. J., Microwave assisted synthesis and characterisation of a zinc oxide/tobacco mosaic virus hybrid material. An active hybrid semiconductor in a field-effect transistor device. *Beilstein journal of nanotechnology* 2015, 6 (1), 785-791.

7. Mein Anteil an der folgenden Veröffentlichung beträgt 75%
Sanctis, S.; Hoffmann, R. C.; Schneider, J. J., Microwave synthesis and field effect transistor performance of stable colloidal indium-zinc-oxide nanoparticles. *RSC Advances* 2013, 3 (43), 20071-20076.

Wissenschaftliche Artikel aus Kooperationen

1. Mein Anteil an der folgenden Veröffentlichung beträgt 30%
Koslowski, N.; **Sanctis, S.**; Hoffmann, R. C.; Bruns, M.; Schneider, J. J., Synthesis, Dielectric Properties and Application in a Thin Film Transistor Device of Amorphous Aluminum Oxide $Al_X O_Y$ Using a Molecular Based Precursor Route. *Journal of Materials Chemistry C* **2019,** *7* (4), 1048-1056.

2. Mein Anteil an der folgenden Veröffentlichung beträgt 30%
Krausmann, J.; **Sanctis, S.**; Engstler, J.; Luysberg, M.; Bruns, M.; Schneider, J. J., Charge Transport in Low-Temperature Processed Thin-Film Transistors Based on Indium Oxide/Zinc Oxide Heterostructures. *ACS applied materials & interfaces* **2018,** *10* (24), 20661-20671.

3. Mein Anteil an der folgenden Veröffentlichung beträgt 20%
Hoffmann, R. C.; Koslowski, N.; **Sanctis, S.**; Liedke, M. O.; Wagner, A.; Butterling, M.; Schneider, J. J., Metal Oxide Double Layer Capacitors by Electrophoretic Deposition of Metal Oxides. Fabrication, Electrical Characterization and Defect Analysis Using Positron Annihilation Spectroscopy. *Journal of Materials Chemistry C* **2018,** *6* (35), 9501-9509.

4. Mein Anteil an der folgenden Veröffentlichung beträgt 30%
Atanasova, P.; Hoffmann, R. C.; Stitz, N.; **Sanctis, S.;** Burghard, Z.; Bill, J.; Schneider, J. J.; Eiben, S., Engineered Nanostructured Virus/Zno Hybrid Materials with Dedicated Functional Properties. *Bioinspired, Biomimetic and Nanobiomaterials* **2018,** *8* (1), 2-15.

5. Mein Anteil an der folgenden Veröffentlichung beträgt 30%
Hoffmann, R. C.; **Sanctis, S.**; Schneider, J. J., Molecular Precursors for ZnO Nanoparticles: Field-Assisted Synthesis, Electrophoretic Deposition, and Field-Effect Transistor Device Performance. *Inorganic Chemistry* **2017,** *56* (13), 7550-7557.

6. Mein Anteil an der folgenden Veröffentlichung beträgt 75%
Hoffmann, R. C.; **Sanctis, S.**; Erdem, E.; Weber, S.; Schneider, J. J., Zinc Diketonates as Single Source Precursors for Zno Nanoparticles: Microwave-Assisted Synthesis, Electrophoretic Deposition and Field-Effect Transistor Device Properties. *Journal of Materials Chemistry C* **2016,** *4* (30), 7345-7352

7. Mein Anteil an der folgenden Veröffentlichung beträgt 30%
Atanasova, P.; Stitz, N.; **Sanctis, S.**; Maurer, J. H.; Hoffmann, R. C.; Eiben, S.; Jeske, H.; Schneider, J. J.; Bill, J., Genetically Improved Monolayer-Forming Tobacco Mosaic Viruses to Generate Nanostructured Semiconducting Bio/Inorganic Hybrids. *Langmuir* **2015,** *31* (13), 3897-3903.

Shawn Sanctis

Erklärung D

Erklärung zur Begutachtung der Veröffentlichungen

Referent: Prof. Dr. Jörg J. Schneider
Korreferent: PD Dr.-Ing. Oktay Yilmazoglu

Darmstadt, 11.10.2019

Weder Referent (Prof. Dr. Jörg J. Schneider) noch Korreferent (PD Dr.-Ing. Oktay Yilmazoglu) der vorliegenden kumulativen Doktorarbeit waren an der Begutachtung nachstehender Veröffentlichungen beteiligt:

1. **Sanctis, S.**; Krausmann, J.; Guhl, C.; Schneider, J. J., Stacked Indium Oxide/Zinc Oxide Heterostructures as Semiconductors in Thin Film Transistor Devices: A Case Study using Atomic Layer Deposition. *Journal of Materials Chemistry C* **2018**, 6 (3), 464-472.

2. **Sanctis, S.**; Hoffmann, R. C.; Koslowski, N.; Foro, S.; Bruns, M.; Schneider, J. J., Aqueous Solution Processing of Combustible Precursor Compounds into Amorphous Indium Gallium Zinc Oxide (IGZO) Semiconductors for Thin Film Transistor Applications. *Chemistry–An Asian Journal* **2018**, 13 (24), 3912-3919.

3. **Sanctis, S.**; Hoffmann, R. C.; Bruns, M.; Schneider, J.J., Direct Photopatterning of Solution–Processed Amorphous Indium Zinc Oxide and Zinc Tin Oxide Semiconductors—A Chimie Douce Molecular Precursor Approach to Thin Film Electronic Oxides. *Advanced Materials Interfaces* **2018**, 5 (15), 1800324.

4. **Sanctis, S.**; Koslowski, N.; Hoffmann, R.; Guhl, C.; Erdem, E.; Weber, S.; Schneider, J. J., Toward an Understanding of Thin-Film Transistor Performance in Solution-Processed Amorphous Zinc Tin Oxide (ZTO) Thin Films. *ACS Applied Materials & Interfaces* **2017**, 9 (25), 21328-21337.

5. **Sanctis, S.**; Hoffmann, R. C.; Precht, R.; Anwand, W.; Schneider, J. J., Understanding the Temperature-Dependent Evolution of Solution Processed Metal Oxide Transistor Characteristics based on Molecular Precursor Derived Amorphous Indium Zinc Oxide. *Journal of Materials Chemistry C* **2016**, 4 (46), 10935-10944.

6. **Sanctis, S.**; Hoffmann, R. C.; Eiben, S.; Schneider, J. J., Microwave Assisted Synthesis and Characterisation of a Zinc Oxide/Tobacco Mosaic Virus Hybrid Material. An Active Hybrid Semiconductor in a Field-Effect Transistor Device. *Beilstein Journal of Nanotechnology* **2015**, 6 (1), 785-791.

7. **Sanctis, S.**; Hoffmann, R. C.; Schneider, J. J., Microwave Synthesis and Field Effect Transistor Performance of Stable Colloidal Indium-Zinc-Oxide Nanoparticles. *RSC Advances* **2013**, 3 (43), 20071-20076.

_____	_____
Referent	Korreferent
(Prof. Dr. Jörg. J. Schneider)	(PD Dr.-Ing. Oktay Yilmazoglu)

ACKNOWLEDGEMENTS

I express my sincere gratitude towards **Prof. Dr. Jörg J. Schneider** for his mentorship and relentless support during the course of this Ph.D. dissertation. His constant encouragement towards novel scientific ideas and guidance to completion of this work provided me with an immense learning experience on a personal and scientific level.

I deeply thank **Dr. Rudolf Hoffman** for providing me with several molecular metal oxide precursors and his chemistry expertise crucial to the results published within this dissertation. I am indebted to **Dr. Jörg Engstler** for TEM analysis as well as his constant scientific insights into the material analysis and characterizations. I would also like to thank **M.Sc. Jan Krausmann** for the collaborative work based on the fabrication of thin-film transistors via atomic layer deposition as well as **M.Sc. Nico Koslowski** for his constant assistance with the precursors synthesis and chemical analysis. Scientific discussions with **Dr. Ruben Precht** and **M.Sc. Conrad Guhl** regarding XPS investigations and **Tobias Weingärtner** for the AES measurements is gratefully acknowledged. I would also like to express my sincere thanks to the project collaboration partners during the course of the work: **Dr. med. Sabine Eiben** from the Institute of Biomaterials and Biomolecular Systems of the University of Stuttgart for providing the virus nanoparticles. I would like to extend my thanks to the collaborative partners from the Institute of Material Science at the University of Stuttgart: **Dr. Petia Atanasova** for her assistance with photoluminescence measurements, **Prof. Dr. Joachim Bill** and **Dr. Nina Stitz** for fruitful discussions on the mineralization process of metal oxide nanoparticles.

I am grateful to my recent and former coworkers **Dr. Mikhail Pashchanka, Dr. Mathias Nowotny, Dr. Deepu J. Babu, Dr. Peter Krauß, Ute Schmidt, M.Sc. Silvio Heinschke, Dipl. -Ing Ildiko Balog, M.Sc. Jonathan Stott, Dr. Tobias Wombacher, M.Sc. Sherif Okeil,** and **Dr. Tim Herdt** for creating a conducive personal and scientific atmosphere as well as for constant support during the Ph.D.

I express my deepest gratitude towards my family for their unwavering support and ongoing encouragement during the course of this PhD. I hope I have not overlooked anyone but if I have, it is certainly not for the lack of appreciation.

Abstract

Metal oxide semiconductors are emerging class of semiconductors with tremendous potential to replace existing silicon-based semiconductors in a wide variety of next generation electronic applications. Solution processing of metal oxide semiconductor offers a low-cost fabrication of oxide thin film transistors for large area film coatings. Use of traditional metal oxide precursors such metal salts require the addition of several additives to optimize the formation of the desired multinary metal oxide semiconductors.

Within this thesis, the use of well-defined, specifically tailored molecular precursor compounds with desired properties such air-stable complexes with solubility in desired aqueous or organic solvents, microwave synthesis of oxide nanoparticles, reduction of process temperature for the formation of metal oxides as well as direct photo-patterning of the multinary oxides are demonstrated. Firstly, indium zinc oxide nanoparticles were synthesized by a rapid microwave-assisted decomposition employing solutions of molecular air stable In and Zn Schiff-base type oximato precursors with methoxyiminopropionato ligands which led to the stable suspensions of IZO nanoparticles with a consistent particle size of ~ 5nm. The removal of adherent organic and hydroxy moieties by annealing at 450°C thus led to an excellent semiconducting behaviour of the finally resulting high quality IZO TFTs with a mobility of 8.7 cm^2 /V.s, an $I_{on/off}$ ratio of 2.8×10^5 and a threshold voltage V_{th} of +3.3 V. This strategy was also extended towards the synthesis of the a bio-inorganinc ZnO/TMV hybrid semiconductor, where a slightly modified precursor formulation with optimal amount of the base (TEAOH) provides mild basic conditions to ensure an efficient microwave based decomposition of the zinc complex and the in-situ formation of crystalline zinc oxide nanoparticles at a low temperature of 60°C . The ZnO nanoparticles mineralize selectively onto the TMV scaffold with and any structural damage to the TMV. For an optimum number (6 cycles) of ZnO mineralization, a field-effect mobility (μ_{sat}) of 6.7×10^{-4} cm^2/V.s, V_{th} of +4.7 V and an $I_{on/off}$ of 9.0×10^5 without the need for any post-process thermal annealing. Similarly, employemnt of a new Sn(II) oximato precursor in combination with the zinc oximato precursor was employed for the formation of ZTO thin fim semiconductors. XRD analysis shows that the decomposition the tin(II) precursor alone, at temperatures as low as 350°C. The EPR investigations revealed only surface defects and not bulk defect sites with a higher defect concentration observed for the SnO_2 compared to the ZnO. Hence, the precursor chemical composition with higher tin content with a Sn:Zn ratio of

7:3 delivered the optimum performance of the of the ZTO TFTs with a μ_{sat} of 5.18 cm^2/V.s, V_{th} of 7.5 V and a high $I_{on/off}$ of 6 x 10^8 when annealed at a moderate temperature of 350°C. The oximato precursors were also explored for their direct DUV-based photo-patterning of IZO and ZTO semiconductors. This is enabled by accessing the intrinsic ability of the precursor thin film to undergo selective decomposition under UV irradiation and generate site-selective patterning of oxide semiconductors, thereby eliminating the need for the traditional photolithography process. At annealing temperatures of 350°C, high performance TFTs with a μ_{sat} of 7.8 cm^2/V.s, V_{th} of 0.3 and a high $I_{on/off}$ of 3.5 x 10^8 for IZO and 3.6 cm^2/V.s, V_{th} of 2.4 and a high $I_{on/off}$ of 5.3 x 10^7 for ZTO TFTs was achieved. In order to achieve low -temperature solution processing, tailored multimetallic zinc and indium coordination compounds, $[Zn_4O(dmm\text{-}NO)_6]$ and $In_3O_3(dmm\text{-}NO_2)_3$·(toluene) with nitro- and nitroso-functionalized dimethylmalonato ligands were investigated for the combustion synthesis of semiconducting indium zinc oxide (IZO) thin films at low processing temperatures. Devices annealed only at 250°C show an active TFT performance and at 300°C already demonstrate a robust FET performance with a μ_{sat} of 2.1 cm^2/V.s, V_{th} of +11.5 V and an $I_{on/off}$ of 3.3 × 10^7 greater than that of the conventional amorphous hydrogenated silicon and also displays its potential to use integrated with plastic compatible temperatures ≤ 300°C, towards flexible electronics.

Another approach based on water-soluble, well-defined urea nitrate coordination compounds of indium(III), gallium(III) and zinc(II) for the formation of amorphous IGZO thin films was succefully demonstrated. DSC analysis confirms the exothermic decomposition of all three precursors arising from the urea-nitrate (fuel-oxidiser) combination. Interestingly, IGZO TFTs processed even at 200°C show active TFT perfortmance and TFTs annealed at 300°C and 350°C exhibit a good device performance with charge-carrier mobilities μ_{sat} of 1.7 cm^2/V·s and 3.1 cm^2/V·s, respectively as well as current on-off ratios of >10^7 in both cases. Such precursors are highly suitable for use in aqueous (non-toxic) solution processing of IGZO semiconductors.

Lastly, an ALD based In_2O_3/ZnO heterostructure design delivering high performance TFTs was successfully demonstrated using trimethyl indium and diethyl zinc as molecular precursors. Generation of an optimised In_2O_3/ZnO heterostructure based on sequential deposition of the individual oxides, processed at a reasonably low temperature regime (250–300°C) deliver high performance TFTs by the likely formation of 2D electron gas transport at the heterostructure interface. Devices based on such a fabrication process demonstrated an average saturation field-effect mobility μ_{sat} of 6.5 cm^2/V.s and a high current on/off ratio of 4.6 x 10^7 and a low

subthreshold swing (SS) of 0.7 V/dec. respectively, at a reasonable processing temperature of 300°C with potential applications in the field of large-area oxide electronics.

Kurzfassung

Metalloxidhalbleiter stellen eine Klasse von Halbleitern mit einem enormen Potenzial dar konventionelle Halbleiter auf Siliziumbasis in einer Vielzahl von elektronischen Anwendungen der nächsten Generation zu ersetzen. Die Prozessierung aus Lösung von Metalloxidhalbleitern bietet eine kostengünstige Herstellung von Oxid-Dünnfilmtransistoren für großflächige Beschichtungen. Die Verwendung herkömmlicher Metalloxidvorläufer (z.B. Metallsalze) erfordert die Zugabe mehrerer Additive, um die Bildung der gewünschten multinären Metalloxidhalbleiter zu erreichen. Im Rahmen dieser Arbeit wird die Verwendung von definierten, maßgeschneiderten molekularen Vorläuferverbindungen demonstriert. Diese stellen luftstabile Komplexe dar, welche in wässrigen oder organischen Lösungsmitteln löslich sind. Zudem wird die Erzeugung von Oxidnanopartikeln aus solchen Vorläufern mittels Mikrowellensynthese berichtet. Desweiteren werden auch direkte Fotostrukturierungen der multinären Oxide untersucht. Es wurden Indiumzinkoxid (IZO) Nanopartikel durch eine mikrowellenunterstützte Zersetzung unter Verwendung von Lösungen molekularer luftstabiler Oximato-Vorläufer vom In- und Zn-Schiff-Base-Typ mit Methoxyiminopropionato-Liganden synthetisiert, die zu stabilen Suspensionen von IZO-Nanopartikeln mit einer konstanten Partikelgröße von ~ 5 nm führten. Die Entfernung anhaftender organischer und Hydroxy-Einheiten durch thermische Behandlung bei 450°C führte zu einem hervorragenden Halbleiterverhalten der resultierenden hochqualitativen IZO-TFTs mit einer Mobilität von 8,7 cm^2/V.s, einem Strom-Ein/Aus -Verhältnis von $2{,}8\times10^5$ und einer Schwellspannung V_{th} von+3,3 V. Diese Strategie wurde auch auf die Synthese eines bio-anorganischen ZnO/TMV-Hybridhalbleiters ausgedehnt, bei dem eine modifizierte Vorläuferformulierung mit optimaler Menge der Base (TEAOH) milde Grundbedingungen bietet, um eine effiziente Synthese, welche eine mikrowellenbasierte Zersetzung des Zinkkomplexes und in-situ-Bildung von kristallinen Zinkoxid-Nanopartikeln bei einer niedrigen Temperatur von 60°C gewährleistet, zu realisieren. Die ZnO-Nanopartikel mineralisieren selektiv auf dem TMV-Gerüst. Für eine optimale Anzahl (6 Zyklen) von ZnO-Mineralisierungen wurde eine Feldeffektmobilität (μsat) von $6{,}7 \times 10^{-4}$ cm^2 / V.s, eine V_{th} von +4,7 V und ein $I_{on/off}$ von $9{,}0 \times 10^5$ ohne erforderliche thermische Nachbehandlung erzielt. In ähnlicher Weise wurde die Verwendung eines neuen Sn (II) -Oximato-Vorläufers in Kombination mit dem Zinkoximato-Vorläufer zur Bildung von ZTO-Dünnschichthalbleitern verwendet. Die XRD-Analyse zeigt, dass die Zersetzung des Zinn

(II) -Vorläufers bei Temperaturen von nur 350°C erfolgt. EPR-Untersuchungen ergaben Oberflächendefekte und keine Bulk-Defektstellen mit einer höheren Defektkonzentration für SnO_2 im Vergleich zu ZnO. Die chemische Zusammensetzung der Vorstufe mit höherem Zinngehalt und einem Sn: Zn-Verhältnis von 7: 3 lieferte bei moderaten Prozesstemperaturen von 350 °C Transistorkennwerte von μ_{sat} 5,18 cm^2/V.s, einem V_{th} von 7,5 V und einem hohen $I_{on/off}$ von 6 x 10^8. Die Oximato-Vorläufer wurden auch auf ihre Fähigkeit zur direkten DUV-basierten Fotostrukturierung von IZO- und ZTO-Halbleitern untersucht. Bei Kalzinierungstemperaturen von 350°C wurden TFT-Bauteile mit einem μ_{sat} von 7,8 cm^2/V.s, einem V_{th} von 0,3 V und einem hohen $I_{on/off}$ von 3,5 x 10^8 für IZO als Halbleiter erreicht. Für ZTO-TFTs wurden Werte von 3,6 cm^2/V.s, einem V_{th} von 2,4 V und einem hohen $I_{on/off}$ von 5,3 x 10^7 erzielt. Für die Realisierung einer Tieftemperatur-Lösungsprozessierung wurden maßgeschneiderte multimetallische Zink- und Indium-Koordinationsverbindungen der Zusammensetzung [Zn_4O (dmm-NO)$_6$] und In_2O_3(dmm-NO_2)$_3$·(Toluol) mit Nitro- und Nitroso-funktionalisierten Dimethylmalonato-Liganden untersucht. Bei 250°C prozessierte Bauelemente weisen bereits eine aktive TFT-Leistung auf, bei 300 °C prozessierte eine TFT-Leistung μ_{sat} von 2,1 cm^2/V.s, einem V_{th} von +11,5 V und einem $I_{on/off}$ von 3,3 × 10^7.

Ein weiterer Ansatz, der auf wasserlöslichen, definierten Harnstoffnitrat-Koordinationsverbindungen von Indium (III), Gallium (III) und Zink (II) zur Bildung amorpher IGZO-Dünnfilme basiert, wurde ebenfalls erfolgreich demonstriert. Die DSC-Analyse bestätigt die exotherme Zersetzung aller drei Vorläufer. Interessanterweise zeigen IGZO-TFTs, die bei 200 °C hergestellt wurden, bereits TFT-typisches Verhalten. Bei 300 °C und 350 °C prozessierte TFTs zeigen eine Leistung mit Ladungsträgermobilitäten μ_{sat} von 1,7 cm^2/V·s bzw. 3,1 cm^2/V·s sowie Strom Ein-Aus-Verhältnisse von > 10^7. Solche Vorläufer eignen sich somit hervorragend für die Herstellung von IGZO-Halbleitern in wässriger Lösung.

Schließlich wurde ein auf dem ALD Verfahren basierende In_2O_3/ ZnO-Heterostrukturdesign, unter Verwendung von Trimethylindium und Diethylzink als molekulare Vorläufer, demonstriert. Die Erzeugung einer optimierten In_2O_3/ZnO-Heterostruktur auf der Grundlage der sequentiellen Abscheidung der einzelnen Oxide, die in einem niedrigen Temperaturbereich (250–300 °C) durchgeführt wird, liefert funktionelle TFT-Bauteile. Bauelemente, die auf einem solchen Herstellungsprozess basieren, zeigen, bei einer moderaten Prozesstemperatur von 300°C, eine durchschnittliche Sättigungsfeldeffektmobilität μsat von 6,5 cm^2/V.s und ein hohes

Strom-Ein / Aus-Verhältnis von $4{,}6 \times 10^7$ und einem niedrigen Sub-threshold Swing (SS) von 0,7 V / Dekade.

List of Abbreviations

AFM	atomic force microscopy
Al	aluminum
Al_2O_3	aluminum oxide
AM-LCD	active-matrix liquid crystal display
AM-OLED	active-matrix organic light emitting diode
Au	gold
C	carbon
Ci	capacitance per unit area
CBM	conduction band minimum
Cl	chlorine
DI	de-ionized
DLS	dynamic light scattering
DNA	deoxyribonucleic acid
DOS	density-of-states
E_g	energy of the band gap
FET	field-effect transistor
FPD	flat panel display
Ga_2O_3	gallium oxide
GIXRD	grazing incident X-ray diffraction
H_2O	water
HCl	hydrochloric acid
HfO_2	hafnium oxide
HNO_3	nitric acid
In	indium
In_2O_3	indium oxide
IGZO	indium gallium zinc oxide
ITO	indium tin oxide
IZO	indium zinc oxide
$I_{on/off}$	current ratio between the on-state and off-state of the device
I_{DS}	current across the drain and source electrodes

I_{GS}	current across the gate and source electrodes
LTPS	low temperature polysilicon
MIM	metal-insulator-metal
MIS	metal-insulator-semiconductor
MOSFET	metal oxide semiconductor field-effect transistor
N	nitrogen
O	oxygen
PAS	positron annihilation spectroscopy
PI	polyimide
PTFE	polytetrafluoroethylene
PVP	polyvinyl pyrrolidone
RFID	radio-frequency identification
RNA	ribonucleic acid
Rms	root mean square
rpm	revolutions per minute
SEM	scanning electron microscopy
Si	silicon
SiO_2	silicon dioxide
Sn	tin
SnO_2	tin dioxide
SS	sub-threshold swing
TGA	thermogravimetric analysis
TEAOH	tetraethylammonium hydroxide
TFT	thin-film transistor
TEM	transmission electron microscopy
TMV	tobacco mosaic virus
UHV	ultra-high vacuum
UPS	ultraviolet photoelectron spectroscopy
UV-Vis	ultraviolet-visible
VBM	valence band maximum
V_{DS}	voltage across the source and drain electrodes
V_{GS}	voltage across the gate and source electrodes

V_{th}	threshold voltage
V_o	oxygen vacancy
XPS	X-ray photoelectron spectroscopy
XRD	X-ray diffraction
Y_2O_3	yttrium oxide
Zn	zinc
ZnO	zinc oxide
ZTO	zinc tin oxide
μ	mobility
μ_{fe}	field-effect mobility
μ_{lin}	linear field-effect mobility
μ_{sat}	saturation field-effect mobility

Table of contents

1 Introduction

The introductory chapter of the present dissertation consists of the evolutionary importance, concepts and technological advances in usage of metal oxide thin-films as semiconductors. Additionally, a brief overview of the different metal oxide semiconductors, working principle of thin-film transistors and application of metal oxides in thin-film transistors are presented. The following chapters primarily present the solution processing methods of semiconducting multinary metal oxide thin-films comprising of zinc oxide, indium oxide, tin(IV) oxide and gallium oxide. The chemical, material and electrical properties of different metal oxide systems such as indium zinc oxide (IZO), zinc tin oxide (ZTO) and indium gallium zinc oxide (IGZO) derived from various molecular precursor compounds is presented. In addition, synthesis and processing methods based on microwave synthesis of colloidal metal oxide nanoparticles for the fabrication of semiconductor metal oxide films as well as a metal oxide/virus nanoparticle-based hybrid material, combustion processing of metal oxide thin-films in aqueous and non-aqueous systems and direct photopatterning of such metal oxide thin films is presented. The next section discusses the atomic layer deposition (ALD) process and its optimization for the generation of multi-layered heterostructure semiconductor films comprised indium oxide and zinc oxide and their influence thin-film transistor properties. This is followed by organisation of the cumulative dissertation consisting of published results based on the above mentioned multinary metal oxide systems.

1.1 Emerging importance of metal oxide thin film transistors

For several decades, amorphous hydrogenated silicon (a-Si:H) has been employed as a well-established semiconductor material in flat panel display backplane thin-film transistors (TFT).[1,2] However, with an ever-increasing demand for improved performance in terms of the semiconductor mobility and display resolution, the need in innovation of new materials to enable an improved performance has become a mandatory requirement to meet the demands of emerging display technologies.[3, 4] The flat panel display (FPD) market was evaluated at $ 100 billion in 2013 with compounded annual growth rate (CAGR) of 11%.[5-8] Furthermore, leading back-plane display technology such as active-matrix organic light emitting diode (AM-OLED) and active-matrix liquid crystal display (AM-LCD) are projected as significant beneficiaries of high performance display semiconductors, which are able to improve upon the mobilities of a-Si:H. Low temperature polysilicon (LTPS) semiconductors offer mobilities 100

times faster than a-Si:H and are used in early AM-OLED backplanes.[7] However, the intrinsic polycrystalline nature of LTPS inhibits a uniform performance over large areas due to the potential barriers induced between the individual grain boundaries, preventing uniform charge carrier transport over large active display areas. Additionally, its polycrystalline nature hinders the formation of a smooth semiconductor/dielectric interface leading to a non-uniform electric field across the traditional dielectric silicon dioxide (SiO_2).[9, 10] Moreover the cost arising from integration of LTPS within existing a-Si:H fabrication facilities are rather high due to differences in its deposition techniques and activation via laser annealing across the large substrate areas, which inturn increases the overall production costs.[11] As a result LTPS based technologies are largely restricted to smaller display sizes, unable to scale-up to large area display backplanes. [8]

a)

	Metal oxide	a-Si:H	LTPS
Mobility $cm^2/V.s$	~10-30	~1	~50-100
Microstructure	amorphous	amorphous	polycrystalline
V_{th} uniformity	$\sim 10^9$	$<10^6$	$<10^7$
Current On-Off ratio	poor	good	mediocre
Fabrication complexity	low	low	high
Semiconductor	n-type	n-type	n and p-type

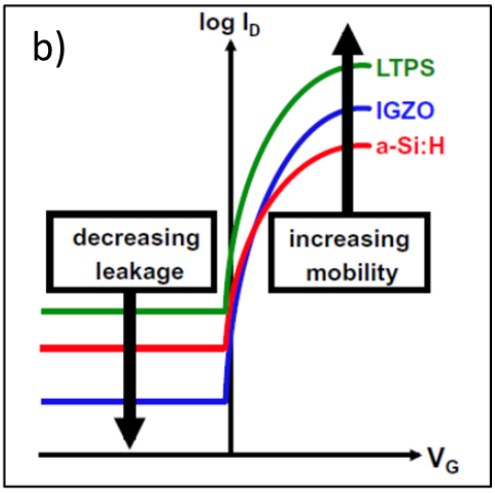

Figure 1 a) Comparative tabulated electronic properties of metal oxides, amorphous hydrogenated silicon and low temperature polysilicon with respect to their material and electronic properties. b) Model representation of a TFT performance graph representing for the same. (* n-type and p-type is achieved via phosphorous and boron doping respectively.)

Hence, in order to further realize the full potential of LCD and OLED based display panels, semiconductors that are better in terms of material conformity and performances metrics greater than a-Si:H such as high mobilities, lower TFT off-state drain current, faster switching speeds (high refresh rate) and lower power consumption, have been much sought after. Although, LTPS possess much higher semiconductor mobilities, amorphous oxide semiconductors (AOS) offer a unique trade-off in terms of TFT performance and scalability for advanced display technology. This is where next-gen display technologies needing ultra-high resolution (UHD) displays with higher TFT switching speeds cannot be met by exisiting a-Si:H

materials, which is readily enabled by the use of AOS materials.[11]

Material transparency is one of the key considerations to be taken into account as far as display semiconductors are concerned. Post-transition metal oxides such as indium oxide (In_2O_3), zinc oxide (ZnO), tin(IV) oxide (SnO_2) serve as wide-bandgap metal oxides (E_g~ 3- 3.5eV), suitable for applications as transparent oxide semiconductors. [12, 13]

A novel material design concept was proposed by Hosono and co-workers in the late 90s, which gained a wide acceptance within the scientific community in 2006.[14] The novel material composition mainly comprises of post-transition metal oxides such as indium oxide, gallium oxide as well as zinc oxide which is often considered as a post-transition metal oxide. The resultant material generates an amorphous indium gallium zinc oxide (IGZO) material which delivers a high performance transparent semiconductor with the general material performance exceeding that of the conventional a-Si:H technology. Its amorphous nature, with increased TFT mobilities, low operation voltages and lower off-state currents is one of the crucial reasons for tremendous research and investment to aid their integration into flat panel displays (FPD).[15]

1.2 Thin-film transistors

A thin film transistor is a three-electrode device which operates under a electric-field and are categorically considered as a field-effect transistors (FET). The TFT device architecture mainly comprises of a conducting “gate” electrode, gate insulator/dielectric, active semiconductor channel and conducting “source” and “drain” electrodes. The same components can be shuffled around to generate different geometries where the position of the gate and the source/drain electrode can be either at the top or bottom depending on the need of the actual large area circuit. The functionality of device operation occurs when a current flow through the semiconductor layer between the source and drain electrodes which is controlled by the generated electric-field induced between the gate and drain electrodes. In order to ensure that the generated current does not flow between the gate and drain electrode, a highly insulating dielectric layer is incorporated between the semiconductor and the gate electrodes. In order to minimize the amount leakage current and reduce the amount of voltage required to operate the TFT, the gate insulator/dielectric with a high dielectric constant is applied. As the flow of charges upon application of voltage can be modulated by the generation of the electric -field at the dielectric-semiconductor interface, these devices qualify as “Field-effect” transistors. It should be noted that TFTs are not to be confused with MOSFETs (Metal Oxide Semiconductor

Field-Effect transistors) based on the established silicon semiconductors commonly used in integrated microchips. The major differences between a TFT and MOSFET are as follows. Firstly, the manufacturing of MOSFETS utilises single-crystal silicon which typically require elevated growth temperatures (> 1000°C). In contrast TFT materials can be easily deposited at relatively low fabrication temperatures, which enables the formation of all the TFT components on glass as well as plastic substrates. Secondly, the flow of charge carriers in TFTs is based on the accumulation of charges within the semiconductor layer while that of a MOSFET is regulated by the formation of an inversion layer at the dielectric/semiconductor interface. Hence, for TFTs there exists a dedicated n-type semiconductor layer whereas MOSFETs utilize p-type silicon substrates to generate n-type MOSFETs. Additionally, n-type and p-type dedicated silicon semiconductors are realized by elemental doping of phosphorous (n-type) and boron (p-type). The addition of pentavalent phosphorous contributes free electrons, greatly increasing the electron conductivity of the intrinsic Si semiconductor. The addition of trivalent impurities such as boron to an intrinsic semiconductor creates deficiencies of valence electrons, called "holes".[16, 17] With regards to the different functional layers required to fabricate a transistor, TFTs are similar to the existing MOSFET layers consisting of same basic functional layers such as the electrodes (source, drain and gate), the dielectric/insulating layer and the active semiconductor layer. Based on the requirements of the larger circuit design and feasibility of fabrication, TFTs exist in four different basic device geometries as shown in **Figure 2**.

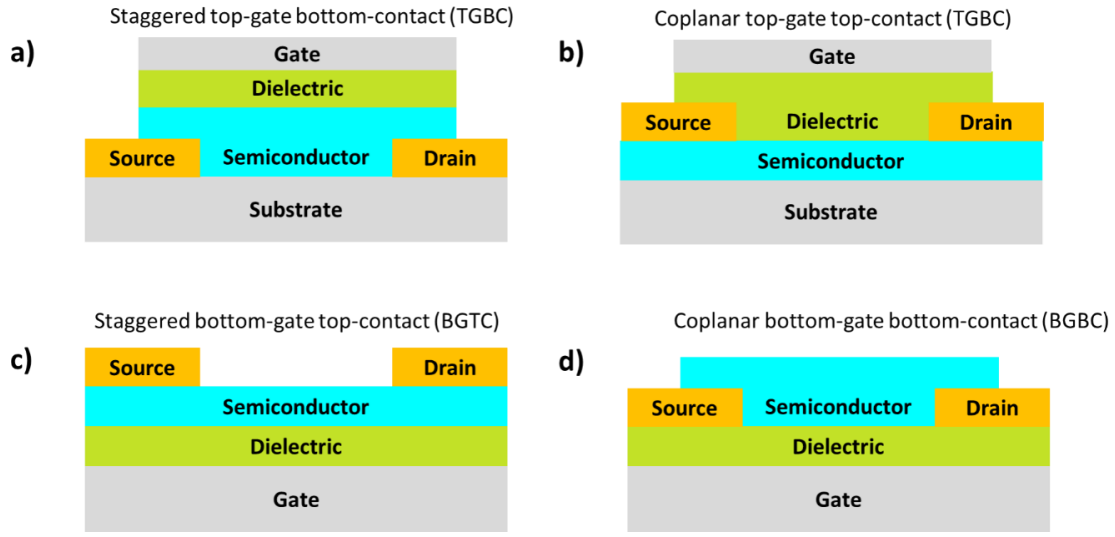

Figure 2 Common TFT device architectures: (a) staggered, top-gate bottom-contact (TGBC) (b) coplanar, top-gate top-contact (TGBC) (c) staggered, bottom-gate top-contact (BGTC) and, (d) coplanar, bottom-gate bottom-contact (BGBC).

Within each of the device configurations, the source and drain electrodes are in contact with the semiconductor and the gate electrode is separated from the semiconductor layer by the dielectric layer. Depending on the position of the gate as well as the source-drain electrodes as well as the structured deposition of the electrodes and semiconductor layer, the different device geometries such as Staggered top-gate bottom-contact, coplanar top-gate bottom- contact, staggered bottom-gate top-contact and coplanar bottom-gate bottom-contact are achieved.The critical dimensions of the source and drain electrodes such as the channel length (L) and the channel width (W) define the active area of the semiconductor which is involved in the transport of charges through the semiconductor.

The flow of charge carriers under an applied voltage can be best understood by the change in the alignment of the energy bands of the metal, insulator and the semiconductor also known as the metal-insulator-semiconductor (MIS) energy diagram representing the three individual layers **Figure 3**.

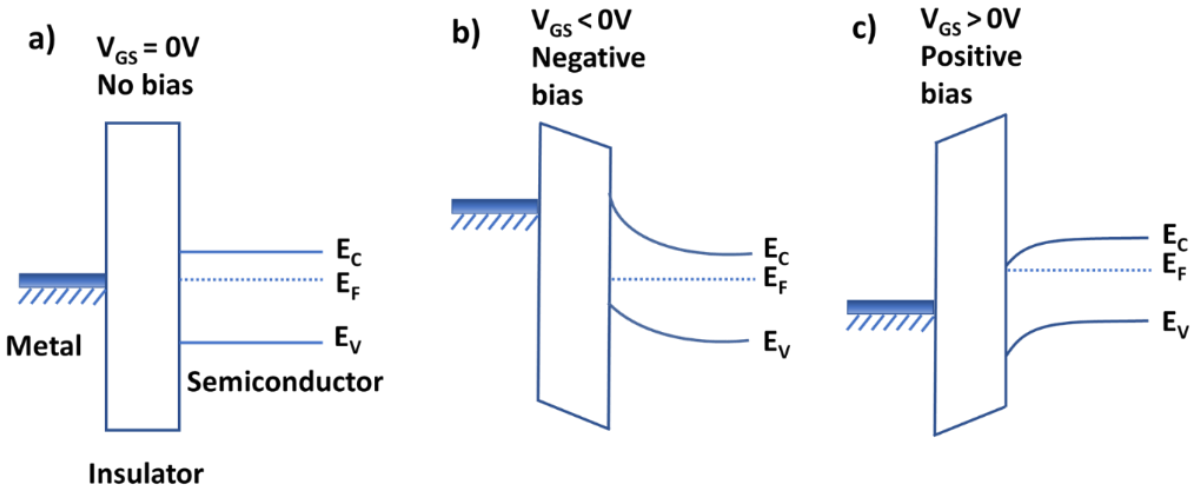

Figure 3 Energy band diagram representing a metal-insulator-semiconductor MIS capacitor for a unipolar n-type semiconductor at three different gate voltage (V_{GS}) bias conditions (a) no bias (b) negative bias and (c) positive bias. E_C, E_V and E_F typically describe the energy level (E) associated the with the conduction band (C), valence band (V) and the fermi-level (F) of the semiconductor which change accordingly under different applied V_{GS} conditions.

Under ideal conditions, when a zero voltage is applied to the gate terminal (V_{GS} = 0V), the transistor is in a typically off-state, since there is nominal accumulation of charges at the semiconductor-dielectric interface, where implies that the accumulated charge carriers are not sufficient to produce a measurable current. When a negative gate voltage is applied (V_{GS} < 0V), the mobile charge carriers (electrons) are repelled from the semiconductor and generate a

depletion region near the semiconductor-dielectric interface which extends within the bulk region of the semiconductor. Herein, the depletion region mainly comprises localized charge carriers. As a result, the energy band of the semiconductor bends upwards upon the application of the negative gate voltage. In such a case as well, sufficient charge carriers are not formed at the interface, regardless of the existing electromagnetic field generated between the source-drain electrodes. When a positive gate bias ($V_G > 0V$) is applied at the gate, the majority carriers, i.e. electrons here, are accumulated at the semiconductor-dielectric interface.

The semiconductor energy bands bend downward in response to the applied positive voltage at the gate which shifts the metal fermi level accordingly. The phenomenon is often referred to as band-bending. The extent of this bending depends on the magnitude of the applied positive gate voltage. The higher the positive gate voltage magnitude, the higher is the concentration of carriers accumulated at the interface. This accumulation layer of the free majority carriers is also referred to as the TFT active channel layer or the conducting channel layer. This switches the TFT is in an on-state when the lateral field applied between the source and drain contacts allows for an appreciable current I_{DS} to flow through the TFT gate induced conducting channel. The flow of current though the semiconductor channel depends mainly on the concentration of charge carriers generated for given applied bias voltage as well as well as the insulating material used, which is usually assessed with regards to its dielectric constant ε_r. The dielectric constant of a material can be extracted from the MIS structure. The typical capacitance can be determined by performing characteristic capacitance-voltage (CV) measurements for a device in its on-state or accumulation state, by employing the equation below.

$$\varepsilon_r = \frac{C_G \, d_{ins}}{\varepsilon_0 \, (L \times W)} \qquad \text{Equation 1.1}$$

Herein, ε_0 is the permittivity of the dielectric in free space, C_G is the obtained capacitance of the dielectric with the device, L and W are the channel length and channel width of the transistor which defines the active channel area and can otherwise serve as the area of the gate electrode in the MIS structure. The sensitivity of the induced charge carriers (Q) within the channel can be calculated from the capacitance (C_G) of the MIS structure area of the transistor by the following equation.

$$Q = C_G \, (V_{GS} - V_{th}) \qquad \text{Equation 1.2}$$

Herein, the threshold voltage (V_{th}) is defined as the voltage where the transistor begins to transition from the depletion regime (off-state) towards the accumulation regime (on-state), which ideally takes place at 0 V, assuming ideal material and fabrication requirements are met without the generation of undesirable defects during the processes.

The increase in charge carrier concentration exhibits a clear dependency on the applied gate voltage as observed in Eq. 1.2, thereby increasing the current extracted out of the transistor device. Additionally, the field generated between the source-drain electrodes upon the application of V_{DS} in conjunction with the V_{GS} also play a crucial role in controlling the resultant current-voltage (IV) characteristics of the device. The role of V_{GS} as well as the V_{DS} in influencing the IV- characteristics of the transistor can be discussed based on the current characteristics with changing the above mentioned V_{GS} and V_{DS} accordingly.

In order to gain a deeper understanding of the current-voltage characteristics with respect to the operation of a thin film transistor, it is important to understand the importance the of the key performance parameters which are obtained via the IV characteristics. The successful operation of a TFT is assessed by evaluating the key parameter metrics such as its field-effect mobility (μ_{FE}), current on-off ratio ($I_{on/off}$) and its threshold voltage (V_{th}) which are extracted from the transfer characteristics and output characteristics obtained during the electrical measurement of the transistor. A typical example of the transfer characteristics as well as the output characteristics are shown below in **Figure 4**.

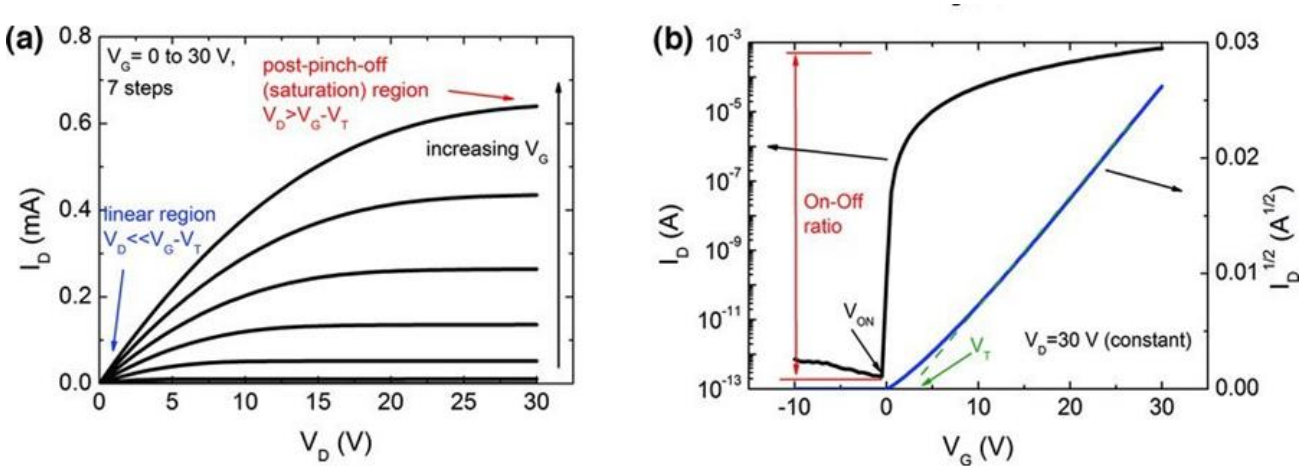

Figure 4 Electrical characterization of a typical TFT (a) output curves (I_D against V_D) in linear scales and (b) transfer curve (I_D against V_G) in a logarithmic y-scale. Adapted with permission[2] Copyright 2012, WILEY-VCH Verlag GmbH & Co. KGaA.

For a dedicated n-type semiconductor, when a given gate voltage V_{GS} is applied, the capacitively

induced charge carriers are generated at the semiconductor- dielectric interface, which are measured across the source and drain terminals. In principle, this phenomenon governs the behaviour of the transistor and is essential to understand the change measured current of a TFT for an applied V_{GS}.

The field-effect mobility (μ_{FE}) of a semiconductor material is characterised by the number of charge carriers that can be transported through the active material. The transport of such charge carriers is typically governed by the number of charge carriers intrinsically available within the semiconductor material as well as the other mechanisms such as scattering of charge carriers due to lattice vibrations, point defects, ionised impurity defects and grain boundary defects. For thin-film transistors, the mobility of the charge carriers is calculated depending on the applied voltage across the Source-Drain (V_{DS}) electrodes as well as the voltage applied between the gate-source electrodes (V_{GS}), which determines whether the field-effect mobility is extracted in the linear regime or the saturation regime, which are appropriately called as linear field-effect mobility or saturation field-effect mobility. When the mobility of the device is calculated at very low applied V_{DS}, where $V_{DS} \sim 0 << V_{GS.}$ The extracted mobility in this case is defined as linear field-effect mobility (μ_{lin}) by equation 1.3

At low V_{DS} ($V_{DS} \sim 0 \ll V_{GS}$), defined as linear field-effect mobility (μ_{lin}):

$$I_{DS} = \frac{W}{L}\, \mu_{lin}.\, C_i \left[(V_{GS} - V_{th}).V_{DS} - \frac{V_{DS}^2}{2}\right] \qquad \text{Equation 1.3}$$

At high V_{DS} ($V_{DS} \gg V_{GS} - V_{th}$), defined as saturation mobility (μ_{sat}):

$$I_{DS} = \frac{W}{L}\, \mu_{sat}.\, C_i\, (V_{GS} - V_{th})^2 \qquad \text{Equation 1.4}$$

where W denotes the channel width, L the channel length, Ci as the capacitance per unit area of the dielectric layer, V_{DS} as the drain to source voltage, and V_{GS} as the gate to source voltage. Threshold voltage (V_{th}) is the gate voltage, at which significant current flow initiates (conducting channel or accumulation layer) between source and drain via the channel formed at the semiconductor/insulator interface. The value is usually extracted from the $I_{DS}^{1/2}$ vs. V_{GS} characteristics, as shown in **Figure 4b**. The plot of $I_{DS}^{1/2}$ vs V_{GS} intersects the x-axis (V_{GS}) at the value of V_{th}.

Subthreshold swing (SS) is the inverse of the maximum slope of the transfer characteristics:

This represents how rapidly IDS increases by one decade under an increasing applied V_{GS}, and is given by the following Equation 1.5

$$SS = \left(\frac{d \log I_{DS}}{d V_{GS}}\right)^{-1} \qquad \text{Equation 1.5}$$

Small values of SS (generally, 0.1~0.5 V/decade) reflect low power consumption for the microelectronic devices. The output characteristics represents the TFT operation, where I_{DS} is plotted against V_{DS} for various V_{GS}, are shown in **Figure 4a**. As V_{DS} increases under constant V_{GS}, I_{DS} increase linearly and then saturates to a value called "hard saturation". Both characteristics are representative of TFT behaviour and reflect the relative performance of the TFT.

1.3 Metal oxide semiconductors

Research based on metal oxide semiconductors can be dated back to early 1960s, which demonstrated the potential of ZnO , In_2O_3 and SnO_2 as functional semiconductors in TFTs.[18, 19] Although present demonstration of the capabilities of oxide semiconductor TFTs have achieved an enhanced degree of progress, the first reported oxide transistor was realized by Klasens and Koelmans in 1964, by employing tin dioxide (SnO_2) as an active semiconductor layer with a staggered bottom-gate geometry on commercial glass as a substrate.[20]

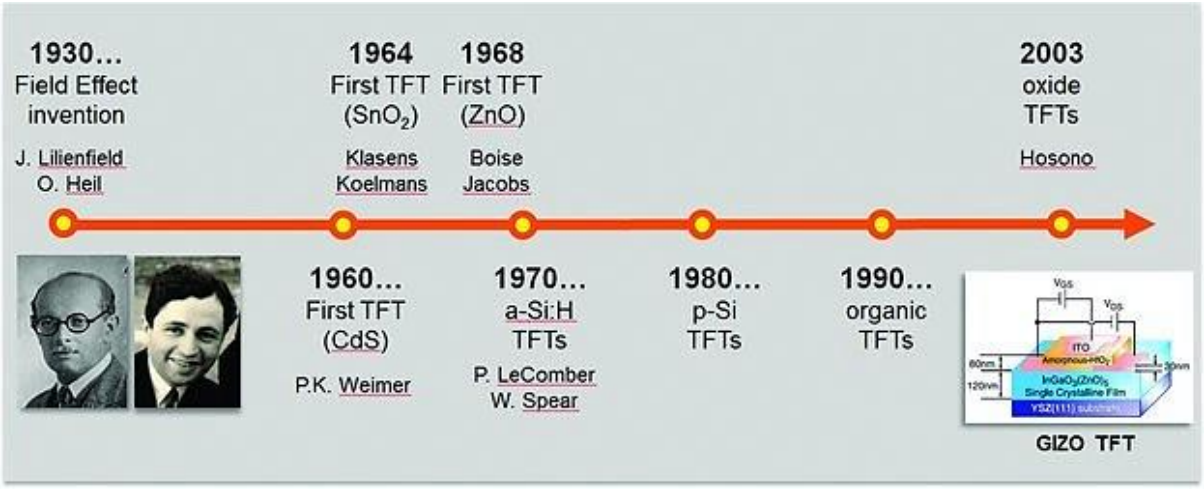

Figure 5 A visual timeline of significant achievements related to developments in field of transistor materials and technology. Reproduced with permission.[2] Copyright 2012, WILEY -VCH Verlag GmbH & Co. KGaA.

The reported SnO_2 transistors demonstrated marginal electrical activity of the transistor performance matrices. Nevertheless, it laid the foundation and primary proof-of-concept and

encouraged research efforts towards the application of semiconducting metal-oxide in TFTs. Thereafter, the very first zinc oxide based TFT was reported by Boesen and Jacobs in 1968 but had similar performance issues to turn-off the TFT. The electrical switching ability is much needed for the primary function of the transistor to operate as a switch which can be switched "on" or "off" merely by application of voltage across the device.[21] These potential oxides laid the basis of practical TFTs, which have since then, seen an incremental progress leading up to device performances in the recent decades. In the last decade, significant progress in the use of such individual oxides as active semiconductor channel materials has been achieved by optimization of the material deposition conditions as well as its physical dimensions. Masuda and co-workers demonstrated active ZnO TFT performance operating in depletion mode, using a pulsed laser deposition method to deposit ZnO at 450°C with effective device mobilities (μ_{eff}) of 1 $cm^2/V.s$ [22] Hoffman and co-workers demonstrated an active ZnO TFT deposited via ion beam sputtering which exhibited a fairly high μ_{eff} of 2.5 $cm^2/V.s$ and an $I_{on/off}$ of ~ 10^7. Improvement in TFT mobility was attributed to enhanced crystallinity of the ZnO which was annealed at 800°C in oxygen.[23] However, extremely high annealing temperatures were an impediment to transfer this research in practical applications. Later, Carcia and co-workers developed a radio-frequency (RF) sputtering process with active control of the oxygen partial pressure during the room temperature ZnO deposition, which had a $\mu > 2$ $cm^2/V.s$ and an $I_{on/off} > 10^6$ which demonstrated the importance of an oxygen environment during the ZnO deposition.[24] This process was intensively optimised and implemented by the Fortunato group where precise control of the oxygen partial pressure and well as optimization of a suitable device geometry (staggered top-gate bottom contact) which displayed high μ ~ 50 $cm^2/V.s$.[25] This research further cemented the importance of the deposition atmosphere and partial pressure to achieve high performance ZnO TFT with significant advantages in the field of transparent electronics. Similarly, the use of In_2O_3 and SnO_2 as active semiconductor channels has also been pursued in parallel.

SnO_2 has been investigated as a semiconductor channel for TFTs by various research groups. Among the early leading research, Presley and co-workers demonstrated SnO_2 TFTs , wherein the SnO_2 channel layer (20nm) was deposited via RF sputtering.[26] The deposited films annealed at 600°C exhibited a μ_{fe} of 2 $cm^2/V.s$ and $I_{on/off}$ of 10^5. However, the requirement for high temperature annealing as well as the harsh etching SnO_2 from a commercialization perspective, makes it a less suitable candidate to be employed in the fabrication of thin-film active semiconductors.[27, 28]

In_2O_3 is known for being a highly conducting transparent oxide with a high intrinsic charge carrier concentration ($> 10^{19}$ cm^{-3}) and established as electrode material in oxide electronics.[29] However, successful reduction in the charge carriers and bringing charge carrier concentration into the semiconducting region ($< 10^{18}$ cm^{-3}) had remained an impeding factor for use as an active semiconductor. Lavareda and co-workers fabricated a In_2O_3 TFT where the material was deposited using plasma enhanced CVD, where the importance of controlling the oxygen partial pressure was key to achieve a performance with a μ_{fe} of 0.02 $cm^2/V.s$ and a reasonable $I_{on/off}$ of 10^4.[30] In order to further control the charge carrier concentration, Vygranenko and co-worker used an ion-beam evaporation technique for the In_2O_3 deposition in order to have a better control in manipulating the charge carrier concentration of the deposited thin film.[31] The InO_x TFTs based on this technique displayed a high device performance with a μ_{fe} of 3.3 $cm^2/V.s$ and an $I_{on/off}$ of 10^6. It was suggested that the precise control of the oxygen ion beam flux enabled the desired semiconducting performance. The influence of film thickness ranging between 5 to 20 nm of the deposited InO_x at 100°C was investigated by Dhananjay et al. and demonstrated that thicker films exhibited a higher device mobility of ~ 34 $cm^2/V.s$ for the measured TFTs.[32] Thicker films exhibited a grain growth via Oswald ripening, thereby reducing the particle grain boundaries and subsequently reducing the detrimental potential barriers arising from typically smaller particle grains.

Although significant progress in the deposition and fabrication of the previously mentioned individual oxides has been achieved, the incapability of homogeneous deposition of these metal oxides over large surface areas resulted in reduced scientific interest. This is largely due to the polycrystalline nature and poor ability to achieve conformal, homogeneous thin film coatings which consequently lead to inconsistent and poor performance of the fabricated TFTs.[33] This led to the invention of amorphous multinary metal oxide semiconductors, commercially know as IGZO or GIZO, which are made using a mixture of indium, gallium and zinc oxide sources. Details regarding the fundamentals of the such amorphous oxide semiconductors are eloborated in the next section.

1.4 Multinary amorphous metal oxide semiconductors

In early 1996, Hosono and Nomura reported the quaternary amorphous oxide semiconductor (AOS) and widely accepted by the scientific community in 2004, consisting a combination of indium oxide, zinc oxide and gallium oxide which is currently recognized as indium gallium

zinc oxide (IGZO).[34 35] Although this concept was first demonstrated in other multinary systems such as hydrogen doped (H^+) cadmium germanium oxide (Cd_2GeO_4), silver antimony oxide ($AgSbO_3$) and cadmium lead oxide (Cd_2PbO_4) with mobilities of up to 12 $cm^2/V.s$, concerns regarding their toxicity and necessity of H^+ doping made IGZO a well suited option for producing transparent AOS.[36-39] Thereafter, immense progress in implementation of AOS materials as transparent TFT for flexible and large area electronics have begun to widely replace silicon as the semiconductor of choice for advanced transparent electronics. Additionally, the electroactive properties of amorphous IGZO exhibit a greater extent of electrical stability in comparison with its amorphous silicon counterpart.[41] Furthermore, with regards to material functionality, such multinary oxide semiconductors have paved the way for diverse applications such as inverters, ring-oscillators, storage memory and sensors.[42-50]

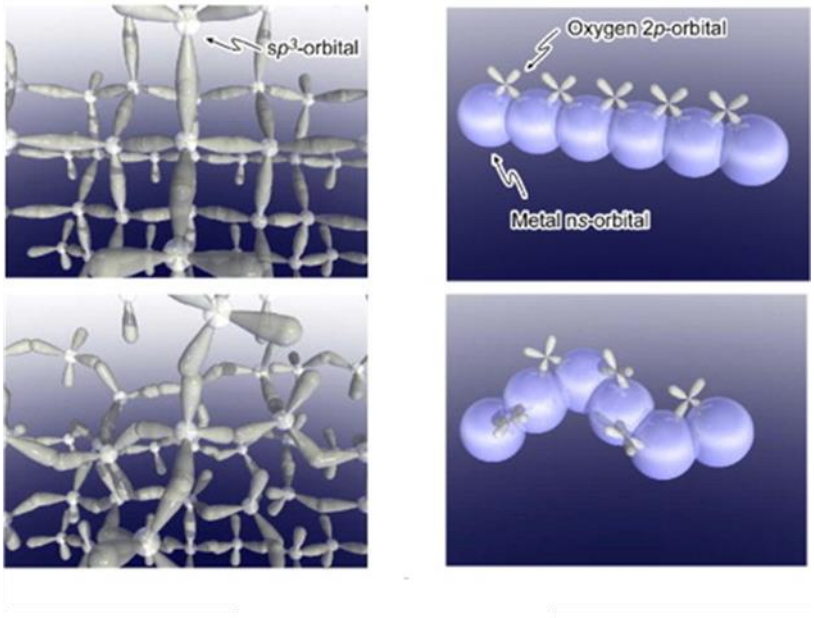

Figure 6 Covalent semiconductors have carrier transport paths composed of strongly directive sp^3 orbitals, so structural randomness greatly degrades the magnitude of bond overlap and in turn degrades its carrier mobility. Amorphous oxide semiconductors composed of post-transition-metal cations. Spheres denote metal s orbitals. The orbital contribution of oxygen 2p orbitals is small. Direct overlap between neighboring metal s orbitals is rather large and is not significantly affected even in an amorphous structure. Adapted with permission.[40] Copyright 2006, Elsevier.

A schematic representation of the conduction mechanism of covalent and ionic semiconductors are shown in **Figure 6**. The choice of cations for generating AOS materials consists of post-transition metals with an electronic configuration $(n\text{-}1)\ d^{10}\ ns^0$ where $(n \geq 4)$. The primary reason

for such material choice is because the lowest unoccupied states in the conduction band minimum (CBM) largely consists of spatial orbital spread of the spherical metal ns^0 orbitals with relatively small electron effective mass and a high electron mobility despite having disorder in its amorphous material state.

This significant advantage of the ionic oxide semiconductors over the covalent silicon-based semiconductors is due to its insensitivity to the bond angle distortion in the overlap between the vacant orbitals of the neighbouring atoms, whereas in covalent semiconductors the bond angle distortions create high concentration of deep localized trap states, which extensively degrade the effective mobility of the charge carriers. Moreover, the dominant electron pathway in ionic materials is via conduction band minimum (CBM) which differs from the valence band maximum (VBM) which serves as a hole transport pathway in p-type semiconductors. The extent of overlap between the vacant s-orbitals of the neighbouring or adjacent cation is extremely large in comparison with the contributions arising from the VBM which is relatively small. This has effectively been demonstrated in individual oxides such as ZnO, In_2O_3 and SnO_2 which were earlier demonstrated as effective metal oxide conductors.[51-54]

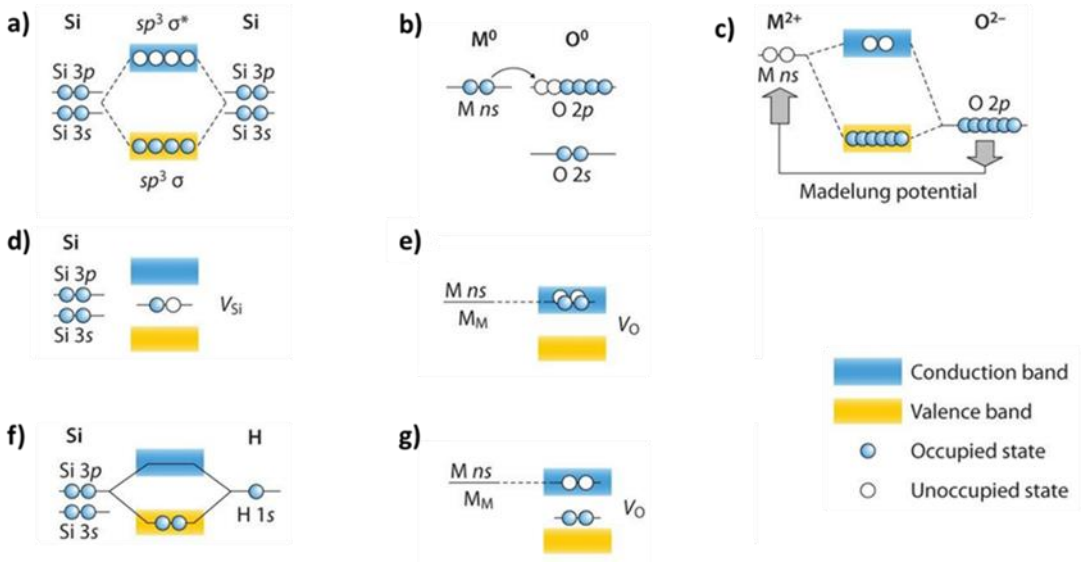

Figure 7 Schematic electronic structures of silicon and ionic oxide semiconductors. (a–c) Bandgap formation mechanisms in (a) covalent and (b,c) ionic semiconductors. (d–g) Electronic structures of defects in (d,f) silicon and (e,g) metal oxides. Solid and hollow circles are used to represent the occupied and unoccupied states, respectively. Adapted with permission.[40] Copyright 2006, Elsevier.

As shown in **Figure 7**, in Si the band gap (Eg) is defined as the gap between the VBM and CBM. The conduction band minimum (CBM) and valence band maximum (VBM) are made of anti-

bonding (sp^3 σ*) and bonding (sp^3 σ) states of Si sp^3 hybridized orbitals, and its band gap is formed by the energy splitting of the σ*–σ levels (**Figure 7a**). The former is known to be the bonding sp^3-hybridized σ-orbitals and the latter is known to be the anti-bonding sp^3-hybridized σ∗-orbitals. If a Si vacancy (V_{Si}) is formed, a dangling bond (unpaired electron) state with one unpaired electron is generated within the bandgap (**Figure 7d**) which can act as a trap state for electrons and holes detrimental to the charge transport in n or p-type Si devices. These dangling bonds or trap states are often passivated by hydrogen treatment which eliminates the trap states within the bandgap **(Figure 7f**). The band diagram of an AOS is displayed in **Figure 7b**.

The transfer of electrons from the metal to the oxygen leads to a reorganization of the band structure whereby the energetic level of the metallic cation is increased and that of the oxygen anion is reduced as per the Madelung potential (**Figure 7c**). The Madelung potential is the difference between the negative electrostatic potential at the metal cation site and the positive potential at the oxygen anion site. The band-like transport of the charge carriers in non-transition metal oxides occurs within the modified band structure in which the VBM is formed by the completely filled O 2p-orbitals while the CBM is formed by the vacant metallic s-orbitals with a large spatial spread (**Figure 7e**). If an O vacancy (V_O) is now created, states in or near the CBM states appear which can act as shallow donors, but not as trap centres for electrons (**Figure 7g**). These states are not stable and relax to fully occupied states near the VBM that can no longer act as electron trap centres. For AOS materials. the Madelung potential plays a crucial role in the increased bandgap and a reduced concentration of electron trap states within the band gap.

Some of the major advantages that such a class AOS materials over existing a-silicon as an active material are listed below:

- **High electron mobility**: AOS TFTs exhibit effective device mobilities > 10 cm^2/V.s and can be further increased ≥ 50 cm^2/V.s by modifying the chemical composition of the materials used and deposition conditions.
- **Compatibility with high-k dielectrics**: A large variety of high-k dielectrics can be used to fabricate AOS TFTs including Al_2O_3, Y_2O_3 and HfO_2 among several other materials.[55-57] The amorphous characteristics and ionic nature such dielectrics leads to an improved bonding situation and fewer defects at the semiconductor/dielectric interface.
- **Low voltage operation**: The amorphous nature and the band-like charge transport of the AOS produce a reduced concentration of defects within the band gap in comparison

with traditional silicon based covalent semiconductors. This enables the operation of the TFTs at voltages of ≤ 5V and sub-threshold slope of 0.1 V/decade.[58, 59]

- **Processing temperature:** The deposition and thermal processing temperatures to produce stable AOS thin films can be achieved at temperatures ranging from room temperature up to ≤350°C, depending of the deposition technique used. This makes them suitable for fabrication of TFTs on plastic substrates, making them an attractive choice of materials in the field of flexible plastic as well as paper-based electronics.[35 60, 61]
- **Device fabrication and reduced off-state current:** Silicon-based transistors need the formation of a p-n junction wherein the source-drain electrodes are used to suppress the TFT operation while switching between the p or n type region**.** Since AOS materials are dedicated n-type semiconductors, a simple source-drain electrode deposition enables the lowering of the off-current and raising the on-current which in turn generates a high $I_{on/off}$ highly desirable of next generation display technology with high refresh rates.
- **Material deposition homogeneity:** AOS materials can be deposited over large area substrates with excellent uniformity with a typical surface roughness between 0.3 -0.5 nm. This makes them less susceptible to material porosity and reduced electronic performance arising of grain boundaries of polycrystalline materials.[62, 63]

Due to the attractive chemical, material and electronic properties mentioned above the commercial validation and industrial manufacturing IGZO based LCD displays has begun since 2012.[6, 64] In addition to its electronic superiority, it also helps makes portable devices thinner, lighter and smaller in comparison with silicon-based displays based on the choice of substrate and smaller required batteries.[65]

2 Solution processing of amorphous oxide semiconductor TFTs

Material deposition of metal oxide are broadly classified in vacuum-based deposition techniques and deposition via solution-based coatings. Vacuum-based deposition techniques include RF sputtering, pulsed laser deposition and atomic layer deposition.[66-69] These deposition techniques enable of generation of high quality films which are highly desired for optoelectronic applications. However, such techniques suffer from low throughput due to the low material deposition rates as well as expensive vacuum-based setups with rather small deposition chambers which hinder their application in large area deposition of the metal oxides. Solution process techniques are cost-effective alternative methods which possess the ability to generate metal oxide thin films via a variety of deposition techniques. In terms of its economic viability, solution processing of oxide semiconductors reduces the overall manufacturing cost by 64%.[70] Some of the most widely used techniques are spin coating, bar coating, spray coating, inkjet printing and chemical bath deposition and are schematically summarized in **Figure 8**.[71-79]

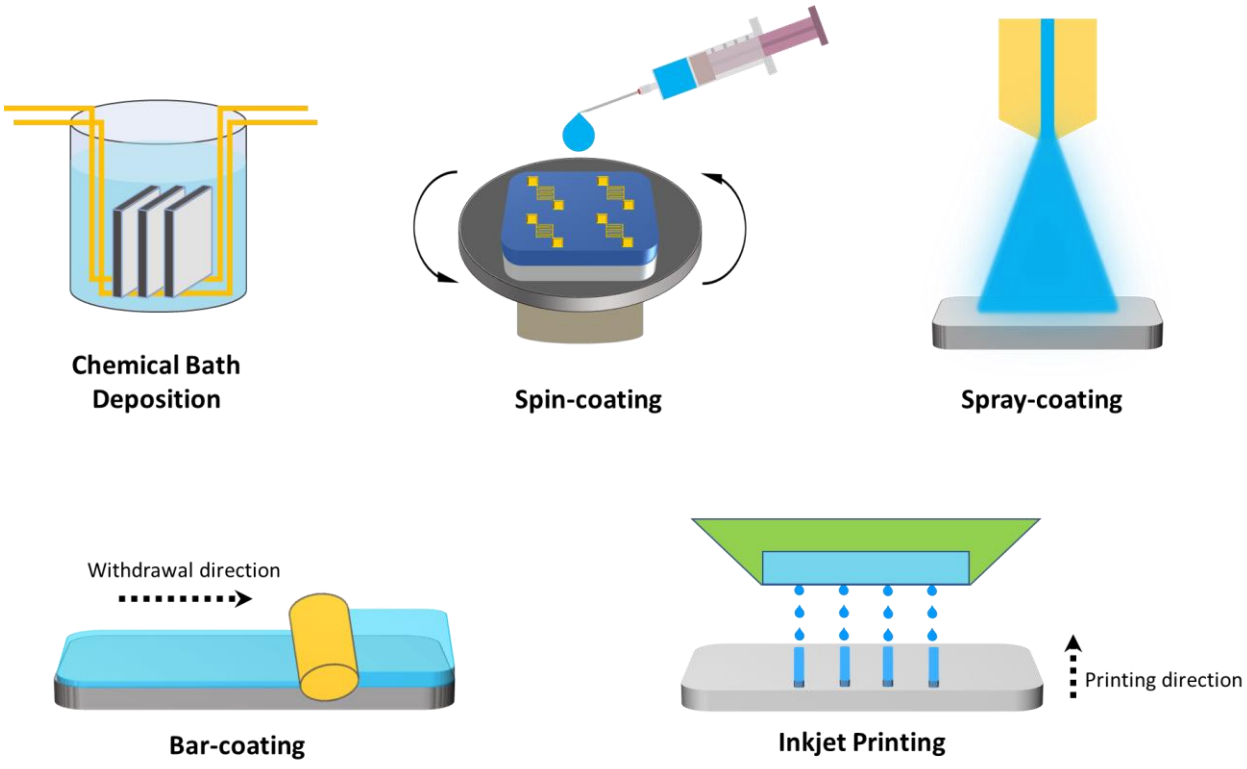

Figure 8 Schematic representation of the different methods used for the deposition of metal oxide precursor films. Precursor liquids solutions in all the above deposition methods are indicated in blue.

Coating of the precursor formulations is a crucial step in the fabrication of thin film metal oxides. Post the selection of desired precursors, it is imperative to develop the desired coating solution

which is compatible with the coating process as well as the substrate of choice. The typical strategy for the optimization of coating solutions consists of optimum solubility of the precursors in a specific solvent. Addition of other cosolvents and stabilizers as additives are often pursued to obtain stable precursor coating solutions. Formulations of a coating solution primarily consist of two main approaches, namely, the sol-gel precursor formulations or direct use of precursors dissolved in a solvent and colloidal suspensions consisting of nanoparticles of the metal oxides.

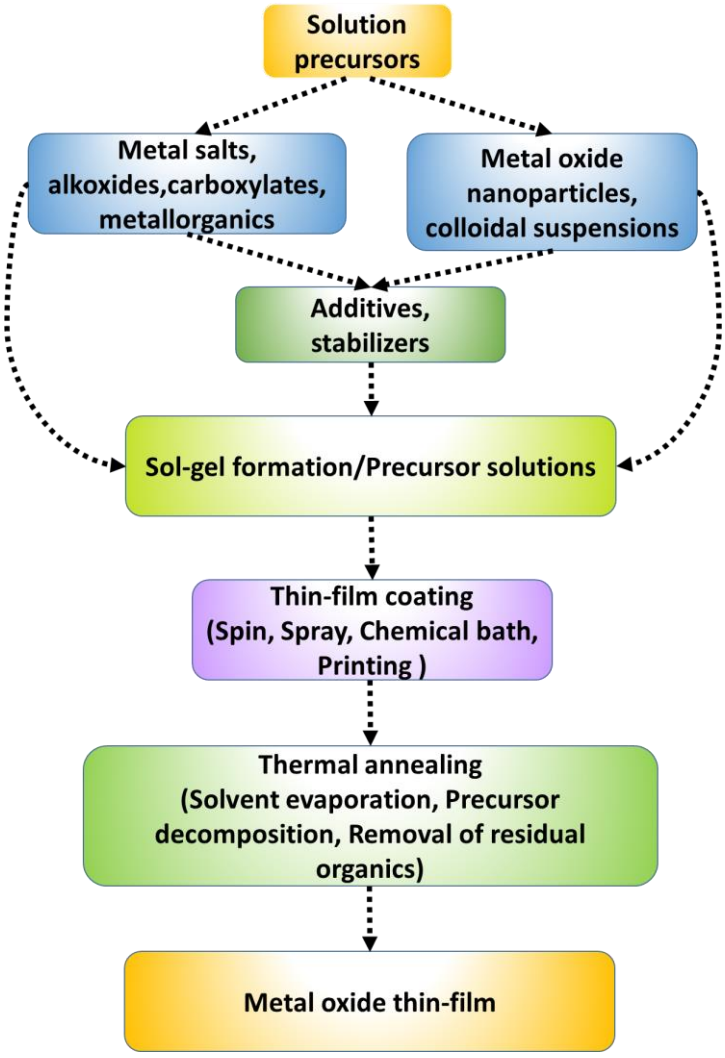

Figure 9 Schematic representation of the general steps involved in the solution processing of metal oxide thin films. Adapted with permission.[80] Copyright 2011, Royal society of Chemistry

As described in the **Figure 9**, solution processing allows for the use of a wide variety of precursors, additive formulations and thin-film coating methods for the formation of uniform precursor thing films which upon annealing get converted into the desired metal oxide thin-films. An overview of the importance and influence of the precursors used in the formation of

the desired semiconductor film and well as the synthesis of colloidal oxide nanoparticles are discussed in the following sub-sections of this chapter.

2.1 Precursor influence on material and electronic properties of metal oxide TFTs

The solution processing of precursor-based metal oxide thin film coatings is largely based on sol-gel chemistry using the previously described metal salts such as metal nitrates, metal acetates and metal chlorides. The application of sol-gel chemistry allows the for the conversion of a precursor/solvent system to undergo a transformation into a sol or a colloidal suspension, which further gets converted into a network structure of the sol, forming a gel.[81] Intensive investigations on the application of the sol-gel method via metal salts has been applied to metal oxides with a variety of electronic applications such as ZnO, In_2O_3, SnO_2, Ga_2O_3, AlO_X, HfO_X and Ta_2O_5.[82-86]

Metal precursors such as alkoxides, acetates, nitrates and chlorides are the most popular choices for the fabrication of metal oxide thin film coatings due to their ease of commercial availability. A metal alkoxide precursor molecule $M(OR)_n$ is generally formed between a metal cation (M^+) and an alkoxide (RO^-) which is the conjugate base of an alcohol (ROH). For a given metal alkoxide, it is known that a lower electronegativity (χ) of the metal ion causes it to be more electrophilic and exhibits a reduced tolerance towards nucleophilic reactions such as hydrolysis. Although oxide thin-films produced from alkoxides posses the least residual contamination and low processing temperatures, the precursor coatings need to be carried out under inert atmospheres to avoid hydrolysis and eventual sedimentation of the metal hydroxide species. This make them less cost-efficient for thin-film fabrication. These metal alkoxides can be stabilized for ambient atmosphere coating, by the addition of a chelating agent such as acetylacetone depending on the binding strength of the chelate ligand in the presence of the existing alkoxide ligand and the cation involved.[87, 88] However, the presence of the chelating agent in the precursor solution can sometimes lead to the corrosion of the underlying material and lead to inconsistent electronic performance, when the semiconductor film is integrated into the pre-exisiting functional device layers and substrates.[89]

Metal acetates belong to a class of carboxylate precursors are formed when the metal salt consists of a carboxylic acid group which can be represented as $M\text{-}(RCOO)_n$ where R stands for the organic moiety attached to the carboxylate group. The negative charge located on the carboxylate anion is delocalized between the two oxygen atoms in the existing structure which provides stability to the ion. The anion can bind to the metal cation as a monodentate or

polydentate ligand resulting different structures. The most traditionally used carboxylate salt consists of the acetate (CH_3COO^-) anion. The increase in length of the alkyl chain changes their solubility in turn, wherein shorter alkyl chains afford a greater degree of solubility in common polar solvents for coatings like water and 2- methoxyethanol. The gradual increase in the alkyl chain length of the carboxylate group of the precursor, such as the 2-ethylhexanoate group are better soluble in non-polar solvents. The increased solubility the zinc acetate precursor $Zn(CH_3COO)_2 \cdot 2H_2O$ is typically associated with it being the zinc precursor of choice to manufacture ZnO thin films from a solution route. On the other hand, indium acetate $In(CH_3COO)_3$ has a poor solubility in comparison with other indium salts which largely restricts its use as a precursor material. Precursor solubility in sufficiently high concentrations are necessary to ensure that the resultant metal oxide film is dense enough. Under low precursor concentrations, the final metal oxide thin film generally consists of pores or cracks within the microstructure of the film due solvent evaporation as well as decomposition of the ligand moieties of the corresponding precursor.[90] Repeated iterations of the coating process helps fill the voids or cracks generated from single coating procedures, which increases the density of the final ceramic thin-film.[90]

For cations such as indium and gallium, metal nitrates and metal chlorides are the most commonly used precursors for the generation of multinary thin film semiconductors comprising of indium, zinc, gallium and tin oxides. Metal chlorides decompose only at higher temperatures, due to the strong ionic bonds between the metal and the chloride anions. Additionally, residual Cl^- anions with the final metal oxide diminish the possibility of obtain high quality films.[91] Metal nitrates on the other hand, serve as viable alternative to the chloride precursor system due the requirements of lower decomposition temperatures arising from a much weaker ionic bond between the metal and the nitrate anion. Additionally, thermal decomposition of metal nitrate precursors do not contain residual nitrogen content from the nitrate anion, when the precursor films are heated to higher temperatures (> 350 °C).[92]

Based on this sol-gel route, in 2007 Chang *et al.* demonstrated spin coated IZO based TFTs with a high mobility of 16 $cm^2/V.s$ using metal chloride salts and commonly used 2-Methoxyethanol (2-ME) as a solvent. However, this was achieved at an extremely high processing temperature of 600 °C.[93, 94] Later, in 2008 Bae *et al.* demonstrated high performance spin coated IZO based TFTs with a mobility 7.1 $cm^2/V.s$ using metal acetates dissolved in 2-ME, with the addition of ethanolamine and acetylacetone as stabilizers and processed at 500 °C.[84] It should be noted in general that metal acetates have poor solubility and also do not form stable sols in alcohols

which leads to the precipitation in the absence of a stabilizing agent. In 2012, Kim *et al.* compared the performance of spin coated IZO TFTs, primarily based on two precursor combinations to clarify the role of the precursor used and their resultant ceramic quality as well as electronic performance.[95] The first precursor mixture contained a combination of indium nitrate and zinc acetate. The second precursor consisted of indium nitrate and zinc nitrate while maintaining identical synthesis, processing conditions and an annealing temperature of 300 °C in both cases. The resultant IZO films from the nitrate precursors only, showed a much high TFT mobility (μ_{FET}) of 1.92cm^2/V.s in comparison to the IZO films from the nitrate/acetate precursor mixture with a poor (μ_{FET}) of 0.55cm^2/V.s . For the given annealing temperature, the IZO films prepared by using the zinc acetate precursors contained a larger number of organic residues resulting in the increased formation of trap sites, poor charge carrier concentration and higher film resistivity. In contrast, much lower residual precursor contamination was observed in the nitrate based IZO films. These results demostrate the importance of a clean decomposition of the precurosr within which the volatile nitrate precursors show the highest mass loss at lower temperatures, with increased thermal budget needed for acetate and chloride precursors as shown below in **Figure 10**.

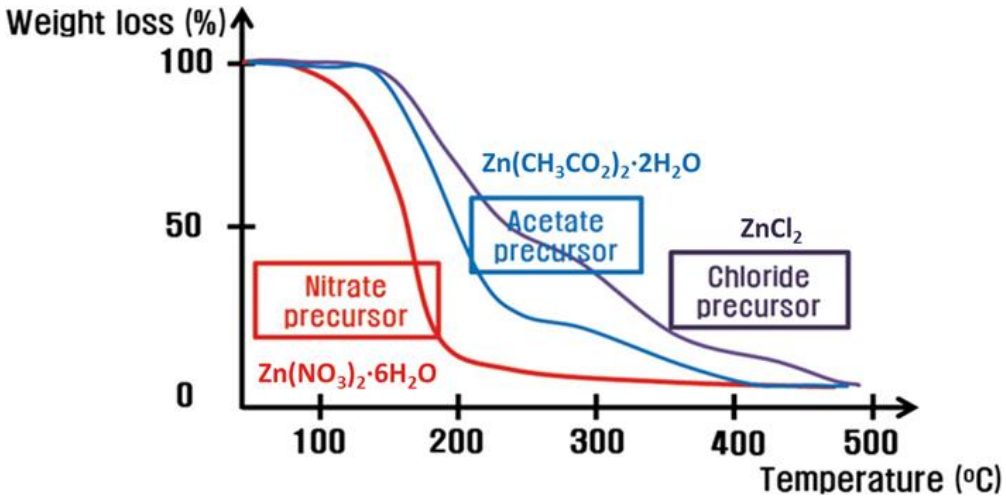

Figure 10 Thermogravimetric analysis comparing the weight loss with increasing temperature of three commonly used zinc precursors: zinc nitrate (red), zinc acetate (blue) and zinc chloride (purple). Adapted with permission under creative commons.[99] Copyright 2013, Taylor & Francis.

These findings provides a direct correlation to the choice of precursors used during the synthesis of metal oxide films via a solution process. The thermogravimetric analysis of the zinc precursors as well as copper precursors provides a good argument for the use of metal nitrate salts in

comparison with metal acetates and metal chlorides.[96 97] Recently, further evidence of the choice of precursors was systematically investigated by Kim *et al.* where IZO based TFTs were fabricated the formation of thin films using the conventional nitrate, acetate and chloride salts which were annealed at 500 °C.[98] Therein, the IZO films based on nitrate salts showed the highest μ_{FET} of 15.36 $cm^2/V.s$ and an $I_{on/off}$ of $\sim 10^7$, while TFTs fabricated from the acetates and chlorides exhibited a μ_{FET} of 10.73$cm^2/V.s$ and 5.61$cm^2/V.s$ and an $I_{on/off}$ of $\sim 10^7$ and 10^6 respectively. This concept was later extended to IGZO based TFTs with such volatile nitrate based precursor salts.

The tuning of the material composition can be easily achieved by mixing the metal precursors in the desired ratio to deliver optimum material performance. This is rather difficult in the routinely such sputter-based techniques with use a ceramic target of the AOS with a predefined composition which do not allow the fine tuning of the device performance based on the other materials used in fabricating the complete TFT architecture. To this end, solution processing techniques provide a unique opportunity to fabricate oxide thin-films over large area substrates. As observed from the overview of various precursors mentioned above, it is evident that choice of precursor, plays a significant role in obtaining high quality metal oxide thin-films. However, the nature of the precursor ligand, need for additional stabilizers and additives as well as high processing temperatures still pose certain limitations in terms of their practical applications on a large scale.[98]

Molecular precursor complexes are a class of precursors, which offer a defined decomposition mechanism which gives an improved clarity into the formation of the desired metal oxide thin-film. This offers the possibility of tailoring the precursor with desired properties to aid the solution processing on thin-film metal oxide semiconductors. Such properties would primarily include air-stable complexes with solubility in desired aqueous or organic solvents, clean precursor decomposition with volatile by-products, reduction of process temperature for the formation of metal oxides as well as direct photo-patterning of precursors.

Use of such precursors play a vital role in coping with the demands to make solution processing a viable process for mass manufacturing These defined molecular precursor compounds used for the fabrication of thin-film AOS has been of critical to this work and are mentioned below.

- Oximato complexes of Zn, In and Sn(II)
- Functionalized malonato complexes of Zn and In
- Urea-nitrate complexes of In, Ga and Zn

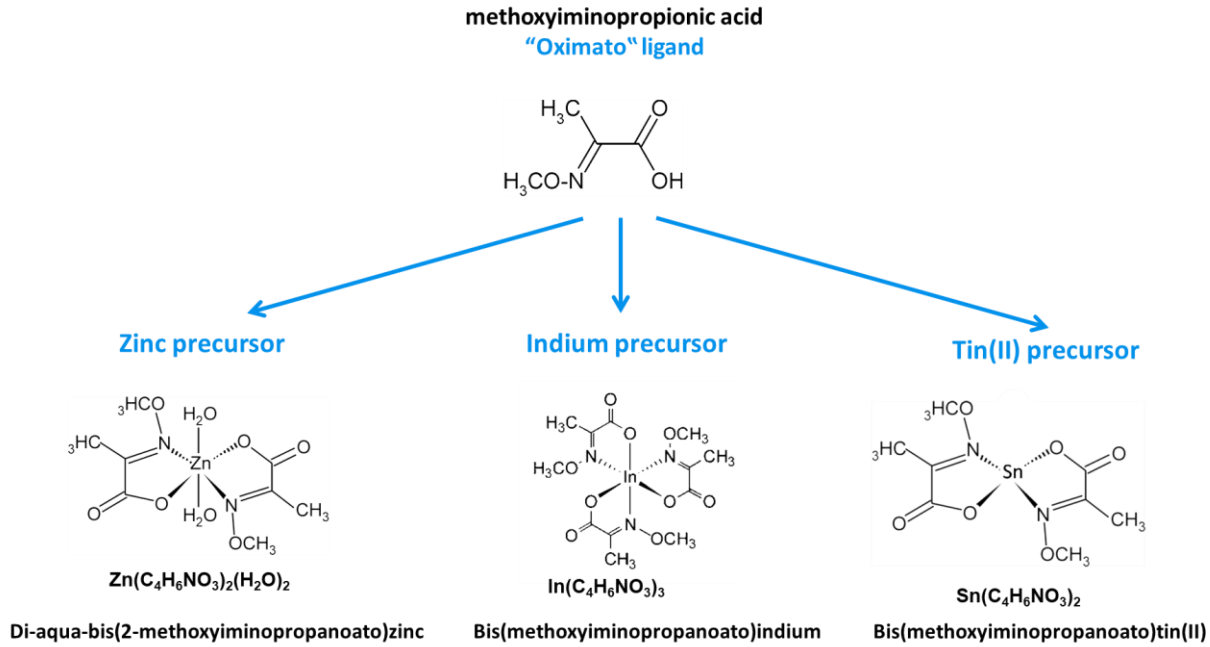

Figure 11 Schematic representation of the molecular structure of the zinc, indium and tin (II) oximato complexes derived from methoxyiminopropionic acid ligand.

Each class of the above-mentioned precursors possess a distinct advantage with respect to traditional solution processing precursors. The "oximato" precursors are synthesized using the methoxyiminopropionic ligands. The schematic chemical structure of these precursors are shown in **Figure 11**. Synthesis and application of the zinc oximato complex as a suitable alternative for the formation of printed nanoscale ZnO transistors with at μ_{sat} of 1.02 x 10^{-3} cm^2/V.s achieved under mild thermal conditions (150°C) has been previously reported by our group.[100, 101] In order to further increase the performance of the fabricated TFTs, oximato complexes of In and Zn for the formation of amorphous IZO with a μ_{sat} of 7.5 cm^2/V.s, optimized via semiconductor layer engineering have also been reported previously.[90] These results establish the efficacy of such defined precursor complexes in generating high quality semiconductor films for TFT applications via the molecular precursor route.

As a part of this thesis, the application of these oximato precursors were further extended to the formation of high performance, indium-free zinc-tin-oxide (ZTO) TFTs by successful synthesis of the Sn(II) oximato complex, microwave synthesis and TFT application of monodispersed colloidal IZO nanoparticles, microwave synthesis of ZnO nanoparticles for biomineralization of a biological virus template and well a novel approach towards direct photo-patterning of high performance IZO and ZTO TFTs.

3 Low-temperature solution processing routes towards oxide TFTs

To realize flexible devices, low-temperature processing is essential because the thermal budget of bendable substrates is well below processing temperatures ≤ 350°C. However, due to its inherent oxide-formation mechanism, the solution process requires relatively high annealing temperature (>450°C). Specifically, the need for high temperatures comes from the necessity to remove organic ligands in the precursor molecules. Organic residue generated by organic solvents and precursors acts as an obstacle to decomposition and complete conversion to the desired metal oxide during fabrication. Several novel precursor formulation strategies such the use of alkoxides, combustion synthesis as well aqueous precursor processing are discussed in the following sub-sections.

3.1 Alkoxide precursor processing route

An approach of precursor optimization via the metal alkoxide route has been demonstrated by the Sirringhaus group to improve TFT performance by lowering the residual impurities. This in turn helps to reduce the required processing temperature and simultaneously improve the performance at a given temperature.[102] The "sol-gel on chip" approach employs the formation of IGZO precursor solutions of molecular precursors of indium, gallium and zinc such as the indium oxo cluster $[In_5O(OPr^i)_4(OPr^i)_4(OPr^i)_5]$, zinc-*bis*-methoxyethoxide $[Zn(OC_2H_4OCH_3)_2]$ and the gallium -*tris*-isopropoxide $[Ga(OPr^i)_3]$ which were dissolved in anhydrous alcohol as a solvent and spin-coated under an inert gas atmosphere . The spin coated films were then hydrolysed and annealed in a high -moisture environment (50% relative humidity) "wet annealing", where the precursors readily undergo decomposition and improved formation of the desired multinary metal oxide. The IZO TFTs fabricated via this approach demonstrated high performance at 230°C with a μ_{lin} of ~7 $cm^2/V.s$ and an $I_{on/off}$ of 10^8. However annealing the films in ambient air "dry annealing" led to poorly performing devices with a μ_{lin} of ~ 0.7 $cm^2/V.s$ and good TFT performance could be obtained only at temperatures ≥350°C with a μ_{lin} of 15 $cm^2/V.s$ at 450°C. Thin film formation using such highly reactive precursors is certainly beneficial in producing contamination-free metal oxide films with notable TFT performance. Although these precursors cannot be used for ambient atmospehere processing due to precursor hydrolysis amd delicate handling during the precursor thin film formation, it certainly paves the way for novel developments of easily decomposed precursors under mild temperature

conditions as well as formation of volatile organic by-products generated during the precusor decomposition reduced annealing temperatures.

3.2 Combustion processing route

The process of high quality ambient processing from a solution phase was further improved by by using acetylacetone and ammonia or urea as a basic agent.[103] The effective use of the urea and acetylacetone as "fuel" and the nitrate from the salts as an "oxidizer" enables a highly exothermic reaction at molecular level ($T_{reaction}$=700°C) of the precursor mixtures verified via differential thermal analysis (DTA) measurements, although the annealing temperature was only between 200-250°C. A schematic representation of the difference in energy required by processing conventional precursors as well as combustion precursors is shown in **Figure 12**. By-products of the precursor decomposition largely consists of volatile gaseous by-products such as H_2O, CO_2 and N_2. On the other hand, fabrication of thicker films (70nm) lead to a greater degree of porosity due to the increased evolution of gases during the combustion process which escape during the metal oxide film formation.

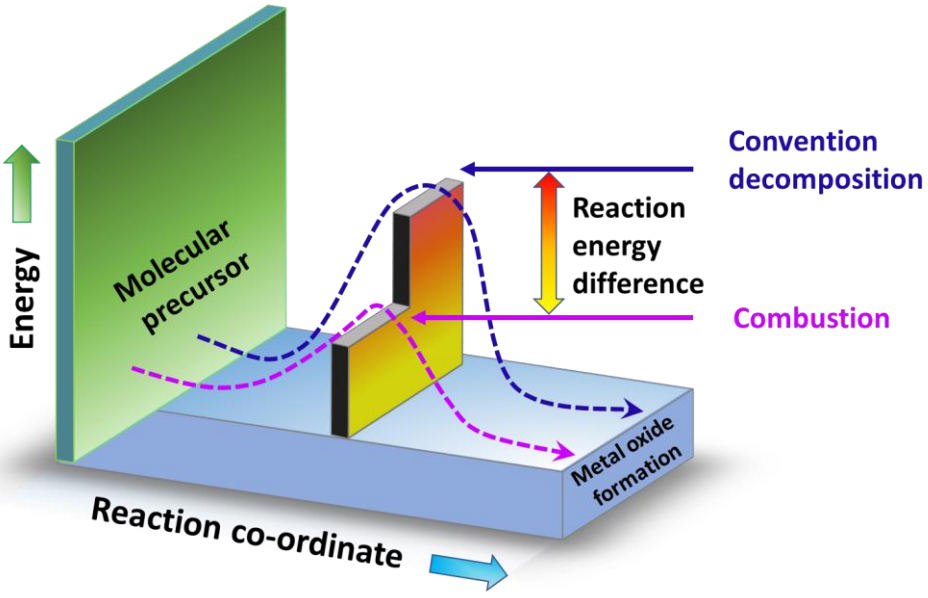

Figure 12 Schematic representation of the reaction energy needed for the conversion of the the metal oxide precursor via the use of conventional precursors in comparison with combustion precursors.

However, these hurdles have been later overcome by implementing a spray coating technique for the oxide film deposition, wherein the precursor mixtures were directly sprayed onto a pre-heated substrate with the same annealing temperatures as performed previously for the spin

coated films.[103] Spray coating enables the faster decomposition of the micro- droplets produced by the spray nozzle, due to a faster heat transfer across the individual droplets and voids generated can be filled with the next droplets which come in contact with the film generated on the pre-heated substrate. This void filling mechanism was much effectively in comparison to spin-coated films or bulk decomposition of films via combustion synthesis, where multiple iterations of spin- coating and calcination of the precursor films were necessary to obtain a highly dense film.[104-106] The density of the films verified by positron annihilation spectroscopy (PAS) to study the degree of the porosity obtained for IGZO (1:1:1, In:Ga:Zn) films.[61] This spectroscopic technique is highly sensitive and is capable of porosity /void detection down to the nanoscale or even an atomic scale, with a void detection capability as small as 0.3 nm existing within the bulk of an inorganic or polymeric film.[107, 108] Within metal oxide thin films, the positrons which are implanted interact with electrons, results in the formation of positronium (Ps) particles, which facilitate the detection of porosity across the thickness of the whole film. A schematic working principle of the path travelled by the positrons and its interaction with defects such as the voids and trap states within the film are shown in **Figure 13.**

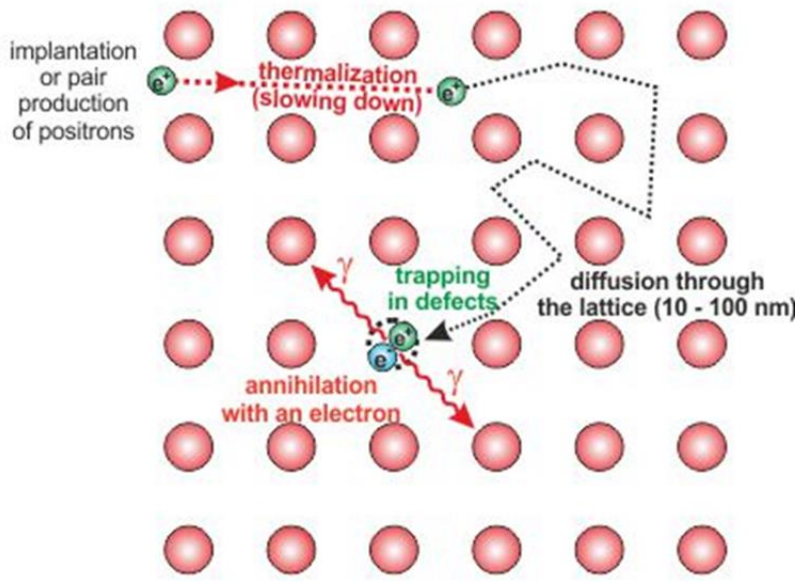

Figure 13 Schematic representation of the working principle of the positron annihillation spectroscopy (PAS) showing the path travelled by the positrons and the annihillation upon interation with an electron at potential defect sites.[109]

The critical S -parameter is defined as the ratio of counts in the central part of the detected annihilation peak to the total number of counts in the whole peak, for a given implanted annihilation line (> keV). This in-turn gives the fraction of positrons annihilating with electrons of low momentum (valence electrons) and is therefore a measure of the positron annihilation in any open volume within the thin film which is under investigation. A typical mapped graph of the S-parameter versus the ion implantation energy proceeds via a curve with a minimum. More importantly, the observed differences the S- parameter minima for different processing conditions gives a clear indication of the porosity within the film, wherein lower S-parameter minima indicates a lower pore volume concentration within the film. For the IGZO films processed via spray coating, the S- parameter far lower than that of the spin coated films was observed, wherein the spray coated films had a mean pore size((Φ) of ~ 0.4-0.6 nm, while the spin coated films had a (Φ) of ~ 1-2 nm. Such an efficient route to low-temperature solution processing under ambient environments has led to the development of additional "fuels" such as sugars like glucose, sucrose and sorbitol to further increasing the localized exothermic environment and achieve and improved TFT performance at similar low-temperatures.[110]

During the course of my work, the previously mentioned In and Zn precursors consisting of nitro-functionalized groups have been investigated for the potential towards low temperature processing of amorphous IZO semiconductor via the combustion route. The functionalized malonato complexes are the second type of molecular precursors investigated within the thesis. The Zn and In malonato complexes such as the dimethyl 2-hydroxyiminomalonato zinc, $[Zn_4O(dmm\text{-}NO)_6]$ and the dimethyl 2-nitromalonato indium $[In_3O_3(dmm\text{-}NO_2)_3]$toluene were employed as combustible molecular precursors wherein the nitro groups facilitate the combustion processing. Th exothermic decomposition pathway helps to significantly reduce the processing temperature in order to realize active IZO semiconductor performance with temperatures as low as 250°C up to 350°C sufficient to deliver an active high-performance semiconductor when implemented into transistor devices. The IZO material exhibits high performance with a μ_{sat} of 6 $cm^2/V.s$ and in $I_{on/off}$ ratio of 10^7 at a processing temperature of 350°C. Further details of the precursor decomposition, material and electrical characterizations can be found in Section 6.5

3.3 Aqueous precursor processing route

Aqueous solution processing has been a well sought after, solution processing route for metal oxide semiconductors. The main motivation relies on the key advantages of using water as a hydrocarbon-free, and environmentally benign solvent which may present a huge advantage as far as applications for large area electronics are concerned.

In this realm, a class of precursors based on zinc ammine and hydroxy nitrate compounds have been well studied with the formation of resultant complexes such as zinc ammine hydroxide ($Zn(OH)_2(NH_3)_x$), zinc ammine hydroxy nitrates ($Zn_5(OH)_8(NO_3)_2.2NH_3$) and zinc hydroxy nitrate hydrates ($Zn_5(OH)_8(NO_3).2H_2O$ and other similar compounds in the same class of precursors. [111-113]

In 2008, the Meyers group demonstrated the utility of synthesizing an aqueous ammine-hydroxo zinc complex $[Zn(OH)_x(NH_3)_y^{(2-x)+}]$ by careful control of the added ammonia concentration. The *in-situ* formation of the resultant complex enabled a very low decomposition of the precursor and crystallization of the resultant ZnO <150°C .[111] Although the synthesis of such ammine hydroxide nitrate has been studied earlier, its application towards the fabrication of semiconducting ZnO thin films was demonstrated for the first time. The TFTs processed at 150°C and 300°C exhibited a performance of μ_{FET} =0.4 $cm^2/V.s$ and 4.3 $cm^2/V.s$, with $I_{on/off}$ ratio of ~ 10^6 and >10^6 in the respective cases. The hydroxy nitrate compounds typically decompose via formation of ZnO with an additional intermediate species ($Zn_3(OH)_4(NO_3)_2$) at 80–120°C and fully decompose to ZnO at 120–170°C. This approach was further refined by Anthopoulos and co-workers in 2013, by controlling the annealing atmosphere (N_2/O_2) and reducing precursor impurity and decomposition via UV irradiation (wavelength = 253.7 nm ,97% and 184.9 nm ,3%) of the precursor films. The TFTs fabricated via this approach demonstrated a high TFT mobility of 10 $cm^2/V.s$ when the final films were annealed at 180°C.[114] Although these approaches have been to display high TFT performance, they suffer from improvement in performance due to the inherent formation of grain boundaries in such polycrystalline ZnO films. The important advantages of using an aqueous route was further studied in depth by Bae and co-workers, where a significant change in the TFT performance was observed of IZO films fabricated using water and 2-methoxyethanol (2-ME) as model solvents but using the same nitrate salts of indium and zinc in both cases, keeping all other synthesis and processing conditions identical. The indium nitrate/water system was studied in-depth, where the formation of “aqua” ions coordinated to the In^{3+} cation was identified. The

reason for the formation ability of the aqua complex was attributed to the high dielectric constant of pure water (>80) and can also behave as a σ-donor molecule that acts as nucleophilic ligand.[115] The *in-situ* formation of the hexa-aqua coordinated $[In(OH_2)_6]^{3+}$ ion was identified by a unique peak arising at 485 cm^{-1} in the Raman spectra , which corresponds to the totally symmetric In-O stretching vibrations for the given expected structure. A second peak at 720 cm^{-1} was assigned to the free nitrate anions which did not have any impact on the formation of the complex. This was also further confirmed via TGA analysis of the indium oxide precursor solution prepared via the aqueous route and the 2-methoxyethanol route. The formation of such an aqua ligand containing precursor enables the low-temperature decomposition and the eventual formation of the oxide.

In_2O_3 TFTs based on the aqueous solutions demonstrated a mobility of 2.62 cm^2/V.s which were further improved via annealing under vacuum conditions. A detailed investigation concerning the ability of various metal salts such as chlorides, acetates, nitrates and fluorides to form the hexa-aqua ligand, followed by the studies of the decomposition pathway of these complexes was performed by Yang Yang and coworkers.[116] Once again, it was systematically proven that the complexes formed from the nitrates proved to be the best route for fabrication of the indium oxide semiconductor-based TFT. Residual anions from the precursor usually remain with the bulk of the film, when annealed at low temperatures. Although the fluoride-based precursors have a rather sluggish decomposition which was completed only at higher temperatures (>400°C), their TFT performance was much better than the films derived from the acetate precursor, which completely decomposes at temperatures slightly above 300°C. This was explained on the basis that the fluorine molecule has a similar ionic radius as that of oxygen and can readily occupy the oxygen deficient site within the In_2O_3 lattice.[117] In comparison with the other precursors, the volatile nitrate anion readily dissociates and vaporizes as nitric acid at a much lower temperature in comparison with acetate, fluoride and chloride anions resulting in the formation of pure oxide without any anion impurities, which if present in the film can act as scattering centres for the charge carriers, thereby reducing the performance of the fabricated device. This approach was extended to the fabrication of low temperature dielectrics using aluminium nitrate as the starting precursor for the formation of the hexa-aqua aluminium complex. The TFTs constructed through this approach, using In_2O_3 as the semiconductor and AlO_x as a the dielectric layer exhibited a high TFT performance of μ_{FET} of 36.31cm^2/V.s and an $I_{on/off} > 10^7$.

Within the aqueous route, controlled manipulation of the pH of the solution has also demonstrated a potential to optimise the performance of the TFT based on the formation of defects generated within the final ceramic oxide, resulting from the change in the pH of the starting precursor solution. Under aqueous condition the pH of the solution determines the degree of hydrolysis of the metal cation. At a low pH (acidic conditions), the metal cation is much more strongly bound to the anion and undergoes a series of complex decomposition steps, leading to higher decomposition temperatures needed to ensure complete formation of the oxide.[118, 119] In contrast, the earlier mentioned ammine complexes which have a high pH (basic conditions) need a far lower annealing temperature and form a much denser oxide, because the basic environment of the precursor solution facilitates easier dehydroxylation, followed by dehydration of the metal cation resulting in a more complete formation of the metal oxide.

Moon and co-workers performed a systematic study for zinc oxide based TFTs, where they employed zinc hydroxide particles in an aqueous medium which were made acidic by the addition of acetic acid and also made basic by the addition of aqueous ammonia to form two stable types of precursor solutions which were employed in the fabrication of spin coated ZnO TFTs. At low pH, strong electrostatic attractions exist between the metal cation and the counter anion [acetate, (CH_3COO)] and hinders the formation of the hydroxo ligand, which is easily formed in the basic solution [ammonia, (NH_3)].

As a result, the higher thermal energy is needed to for the removal of the acetate ligand. The material characterization of the derived ZnO also showed stark differences when annealed at the same temperature (350°C). XPS analysis of the ZnO derived from acetate showed a higher concentration of metal hydroxide (M-OH) as well oxygen vacancy defects, implying a poor formation of the metal-oxygen-metal (M-O-M) framework. On the other hand, the ZnO derived from ammonia showed a significant reduction in the concentration of the hydroxide as well as oxygen vacancy related species, with a high concentration of M-O-M species.

Additionally, XRD investigations revealed that ZnO derived from acetate have an amorphous nature even when annealed upto 450°C , while the ZnO derived from ammonia showed a crystalline wurtzite structure with a high degrees of orientation along the c-axis (0 0 2) even when annealed at 350°C. This was clearly reflected in the TFT performance (350°C) where ZnO films from the addition of NH_3 exhibited a μ_{FET} of 7.65cm^2/V.s, V_{th} of 0.7 and an $I_{on/off}$ of $\sim 10^7$ while the (CH_3COO) derived ZnO films showed no active TFT performance.

These results clearly show that the basic nature of the precursor solution is highly favourable in the formation of high quality metal oxide TFTs.

Urea-nitrate complexes of Zn, In and Ga are the third type of precursors investigated within the duration of this thesis. A schematic representation of the mentioned precursors is shown in **Figure 14**. These novel precursors were synthesized and employed for the formation of an amorphous indium-gallium-zinc oxide (IGZO) semiconductor and finally evaluated for its TFT performance. These well-defined precursor compounds undergo an exothermic decomposition via "fuel- oxidizer" combustion system wherein the urea acts as the "fuel" and the nitrate anion serves as an oxidizing agent. Additionally, these precursors are highly soluble and stable

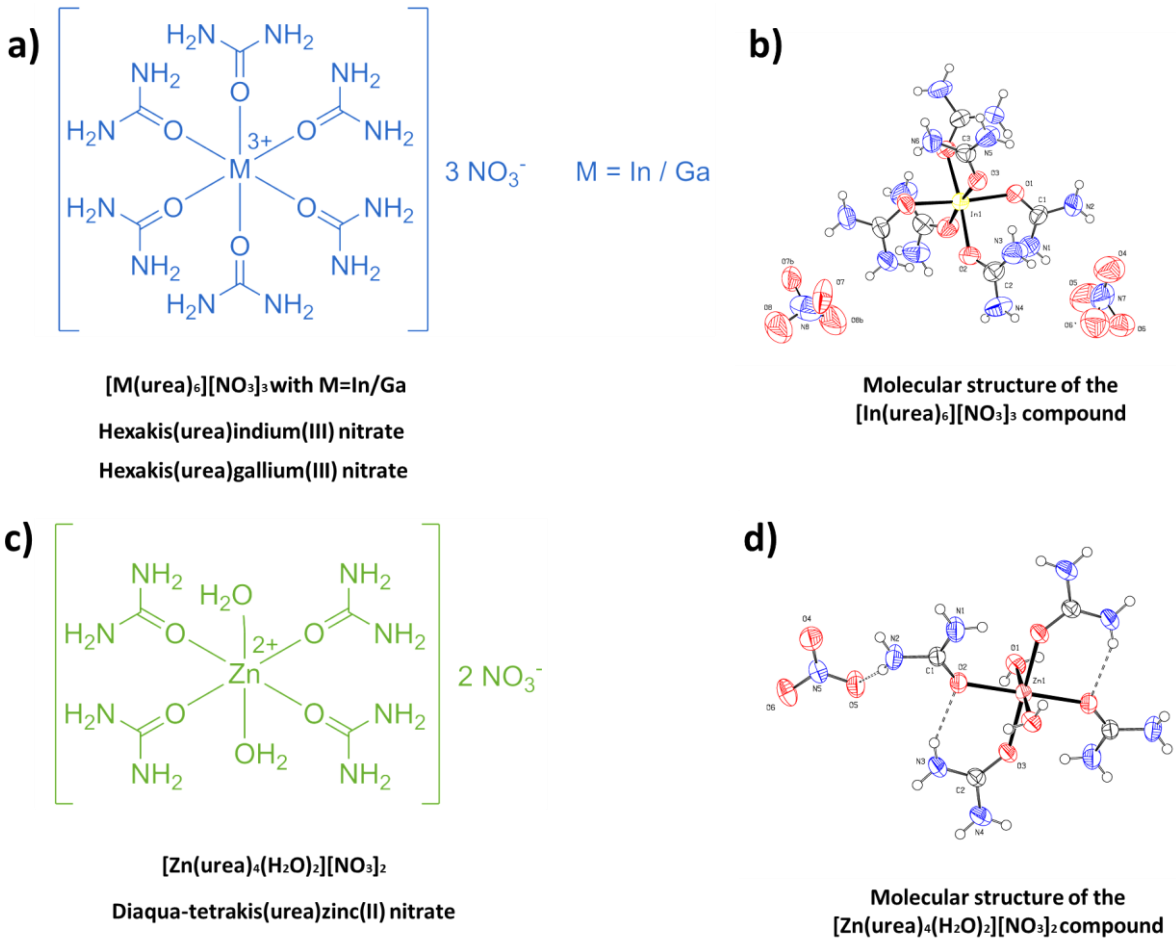

Figure 14 Schematic representation of the urea-nitrate co-ordination compounds a) indium and gallium and c) zinc and corresponding molecular structure obtained by single crystal X-ray crystallography of the b) indium and d) zinc compounds.

in water, thereby preventing the need for addition of any further stabilizing agents to obtain a suitable precursor solution for solution processing applications. Further details of the precursor

synthesis, crystal structure, decomposition as well as the material and electrical characterization can be found in Section 6.6

3.4 Microwave synthesis of colloidal nanoparticles.

The ability of inorganic nanomaterials to exhibit unique physical and chemical properties in the nanoscale regime is a significant factor in boosting advanced research including improved synthesis methods for the generation of inorganic nanoparticles.[120, 121] Bulk quantities of nanoscale materials have been widely synthesized using gas-phase techniques which are economical in a general sense.[122-124] However, the necessity of controlling the size, shape and other morphological aspects have yielded promising results from a solution/liquid phase synthesis route.[125-130] Several liquid phase synthesis methods such as aqueous coprecipitation,[81, 115] non-aqueous sol-gel methods,[131-135] hydrothermal,[136, 137] solvothermal,[136] sonochemical,[138, 139] template-assisted synthesis [140] as well as biomimetic approaches[141-145] offer a greater degree of control with regards to fine tuning of the morphological properties of the inorganic nanomaterials.

Since the early works of LaMer, it is well established that during the formation of colloidal nanoparticles, it is essential to have a separation between the nucleation stage as well as the growth stage to ensure a uniform size distribution of the nanoparticles.[146, 147] A schematic representation of the nucleation and possible modes of growth regime based on the type of particle growth is shown in **Figure 15**. Single step nucleation induces particle growth via Ostwald ripening leading to uniform particle size, whereas additional nucleation sites lead to coalescence, which are followed by subsequent growth of nanoparticle clusters.[134, 148] Inconsistencies in the formation of nanoparticles and multiple particles growth events can be significantly increased due to variation in the thermal gradients among the various components of the reaction medium. This leads to non-uniform particles size which consequently results in a broad size distribution of the synthesized nanoparticles.

In comparison with conventional heating methods, microwave irradiation based dielectric heating provides a homogeneous heating with enhanced heating rates, which facilitate optimum conditions for nanoparticle synthesis with a narrow size distribution. Microwaves are electromagnetic radiations which have a frequency between 0.3 upto 300 GHz which translate to wavelengths of 1mm to 1m. All domestic microwave appliances such as commercial microwaves operate at a dedicated frequency of 2.45 GHz (wavelength =12.25 cm) to avoid

any interference with other applications such as telecommunications and radar technology which operate in the GHz frequency range as well. Microwave synthesis is largely dependent on the effective heating of the materials involved in synthesis by dielectric heating of the solvents or the precursors involved. The dielectric heating can be defined as the ability of the materials (material precursors, additives and the solvent) to absorb the microwave energy and convert it into heat.[149, 150]

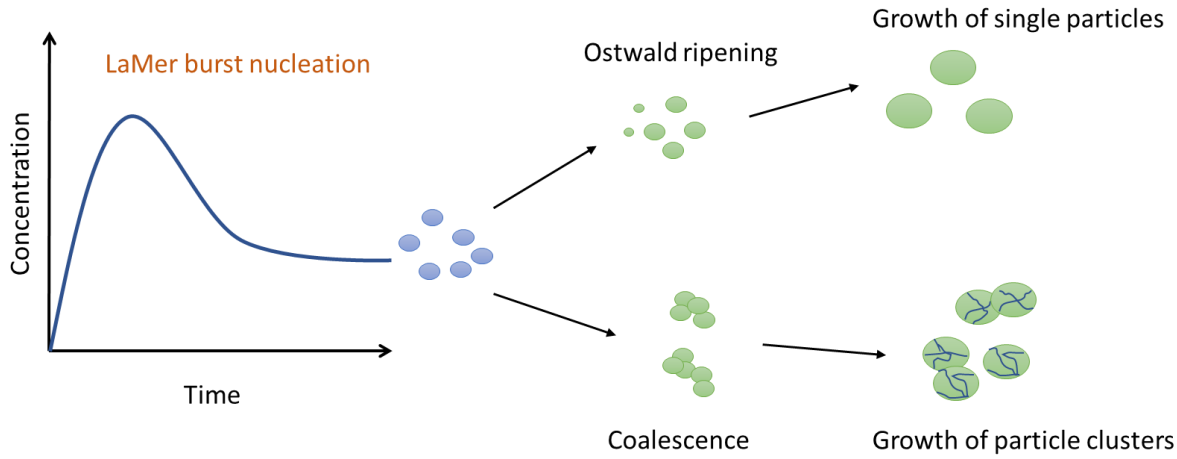

Figure 15 Schematic representation of the LaMer nanoparticle growth model showing the nucleation and subsequent Ostwald ripening or coalescence growth stages of nanoparticles resulting in single particle growth or growth of particle clusters in solution.

The dielectric heating properties of a material primarily depends on two factors. The first factor is the dielectric constant (ε') which is the ability of the material to be polarized when an electric field is applied to the material. The second factor is the dielectric loss (ε") which describes the effective ability of the material to convert the electromagnetic radiation into heat. The ratio of these two factors can be used to define a third factor knows as the dielectric loss tangent tanδ, where tanδ= ε'/ ε". This factor provides an accurate measure of the ability of a material to convert the applied electromagnetic energy into heat for a given temperature and applied frequency.[151]

Liquid phase microwave synthesis possesses several advantages over conventional heating. Microwave heating allows for homogeneous heating of all components within the liquid medium based on their individual tanδ. This enables higher heating rates for the chemical reactions with no physical contact between the reaction mixtures/solvents and the heating source. Additionally, it enables a higher degree of control of the reaction with higher

reproducibility and product yields. Moreover, the selective dielectric heating of the reaction solutions enables the suppression of possible side reactions. [153, 154]

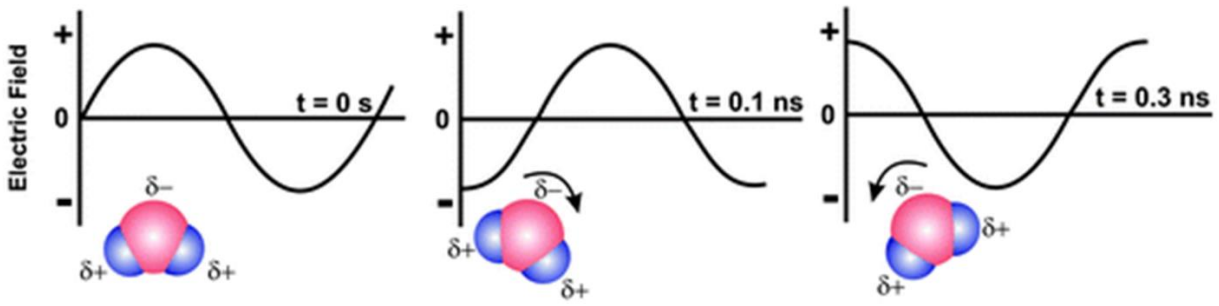

Figure 16 Schematic representation of the dipole polarization mechanism displaying the rapid oscillation of the dipolar molecule at different times (ns=nanosecond) under constant switching of the electric field generated during microwave irradiation. Adapted with permission.[152] Copyright 2010, Royal Society of Chemistry.

Application of nanoscaled ZnO in the production of thin-film semiconductor TFTs via solution processing often requires the need for polymeric stabilizing agents to obtain a homogeneous colloidal suspension. In such cases, the need for a high thermal budget for precursor decomposition towards formation of ZnO nanoparticles are eliminated and a thermal annealing at 150°C to evaporate the solvent appears sufficient to form ZnO thin-film .[155, 156] However, the incomplete removal of the polymeric agent severely deteriorates the performance of the fabricated TFTs with optimized μ_{FET} still $< 10^{-2}$ $cm^2/V.s$. Ludwigs et al. demonstrated the use of metallorganic Zn precursors for the fabrication of ZnO TFTs, wherein the residual organics were completely removed under vacuum. Although the organic fragments were carefully removed from the ZnO film, the resultant TFT performance did not exceed a μ_{FET} of 10^{-4} $cm^2/V.s$.[157] Commercial suspensions of core-shell ZnO nanoparticles with a 1nm organic shell dispersed in methyl-tert-butyl ether exhibit an impressive TFT performance with a μ_{FET} of 0.8×10^{-2} $cm^2/V.s$ when annealed at only 100°C .[158] However, the volatile nature of the solvent used restricts its applications for large area coating as inkjet printing processes. These results facilitate the need for in-situ generation of stable nanoparticles in a desired solvent suitable for coating as well as printing applications of such colloidal nanoparticle suspensions.

Synthesis of uniform colloidal ZnO nanoparticles using the previously mentioned oximato precursors have been previously reported by our group.[159] The facile decomposition of the precursor leads to the formation of stable nanoparticles clusters with a core shell structure. The ZnO nanoparticle core consists of an organic shell of 1nm, which consists of residual fragments

of the ligand species which enable is stability over several months and do not undergo any visible sedimentation. The size of the ZnO nanoparticles can be increased (30- 140nm) by increasing the precursor concentration as well the increasing carbon chain length of the alkoxy groups (RO) of the alkoxyethanol ($RO-C_2H_4OH$) solvents used for the microwave synthesis, ranging from methoxyethanol to butoxyethanol. The TFTs prepared from spin-coating the homogeneous nanoparticle suspensions and annealed at 325°C exhibit a TFT μ_{sat} of 0.045cm^2/V.s and $I_{on/off}$ of 4.5 x 10^5. These results were one of the highest reported values for ZnO nanoparticles generated *in-situ* and directly processed without the need for and modification or addition in the nanoparticle suspension.

Using the same strategy, highly monodispersed colloidal IZO nanoparticles (5nm) were synthesized and resultant stable colloidal suspensions were investigated for their thin film performance.[160] The colloidal suspensions synthesized in ethoxyethanol were stable over several months and did not undergo any flocculation or sedimentation as monitored by dynamic light scattering (DLS) techniques due to the presence of the adsorbed species of the dissociated ligands of the oximato precursor. Additionally, no separate phases of individual In_2O_3 or ZnO nanocrystallites were observed and the particles exhibit an amorphous nature as investigated by XRD and TEM investigations. The TFTs performance of the IZO suspensions formed via spin-coating and subsequent thermal annealing at 450°C exhibit a high TFT performance with a μ_{sat} of 8.7 cm^2/V.s, V_{th} of 3.3V and an $I_{on/off}$ of 2.5 x 10^5. The complete details of this study can be found in Section 6.1 which includes the microwave synthesis parameters as well as material, optical and electronic characterization of the IZO nanoparticles as well as the IZO thin-films fabricated by employing the nanoparticle suspension.

4 Site-selective deposition of solution processed oxide semiconductors

Solution processed metal oxides and their potential towards large-area fabrication has generated tremendous interests in the field of next generation display technology via roll-to-roll fabrication by various coating methods such as inkjet printing, screen printing, flexographic printing, gravure printing among other techniques.[72, 74, 161-165] Additionally, solution processing of such materials avoids the need for sophisticated coating and processing equipment in comparison with gas-phase methods such chemical vapour deposition, sputter deposition, pulsed laser deposition etc.[66, 166-169] which often require vacuum conditions and the need to be processed in a cleanroom environment which makes the process by far more complicated.

Low temperature solution processing of metal oxide for the fabrication electronic devices has achieved significant progress in the last years. However, the scope of industrial integration of such functional electronic films has been limited due to the extensive photolithography needed to structure these oxide layer into a multilayer device architecture to enable the manufacturing of flexible plastic electronics.[161, 170] Photolithography enables the ability to scale up to the process with site-selective deposition of the oxides across the large-area target substrates.[171] However, the need to use sacrificial polymer resists and their processing, accompanied by the usage of strong acidic chemical etchants during the development of the oxide films often leads to electrical and morphological deterioration of the deposited oxide layer.[63, 172-174] Several strategies for micro-patterning of inorganic oxide exist to date which rely on chemical modification of the target substrates such as generating hydrophobic and hydrophilic patterns on the substrate for selective wetting of the oxide precursors, gravure printing, polydimethylsiloxane (PDMS) stamping and direct writing via selective laser ablation of precursor films.[175-179] Such strategies have exhibited encouraging results in terms of the TFTs fabricated via such patterning processes.

4.1 Direct photo-patterning of metal oxide semiconductors

In recent years, considerable progress has been achieved with site selective deposition of solution precursors via various deposition methods. However, there are still several fabrication hurdles in terms of consistency in film thickness and pattern resolution over large areas which are essential to realize high performance TFTs for large scale fabrication. An attractive alternative to surpass such existential drawbacks involves the use of photosensitive precursors which allow for the direct patterning of inorganic oxide precursor films upon exposure to

ultraviolet light whose wavelength matches that of the intrinsic precursor absorption wavelength.[1, 170] In general, the available chromophores (i.e. the part of the molecule responsible for its colour) are restricted to the ligand-to-metal charge transfer bands and the π-π* or n-π* transitions in double bonds within the ligand framework.

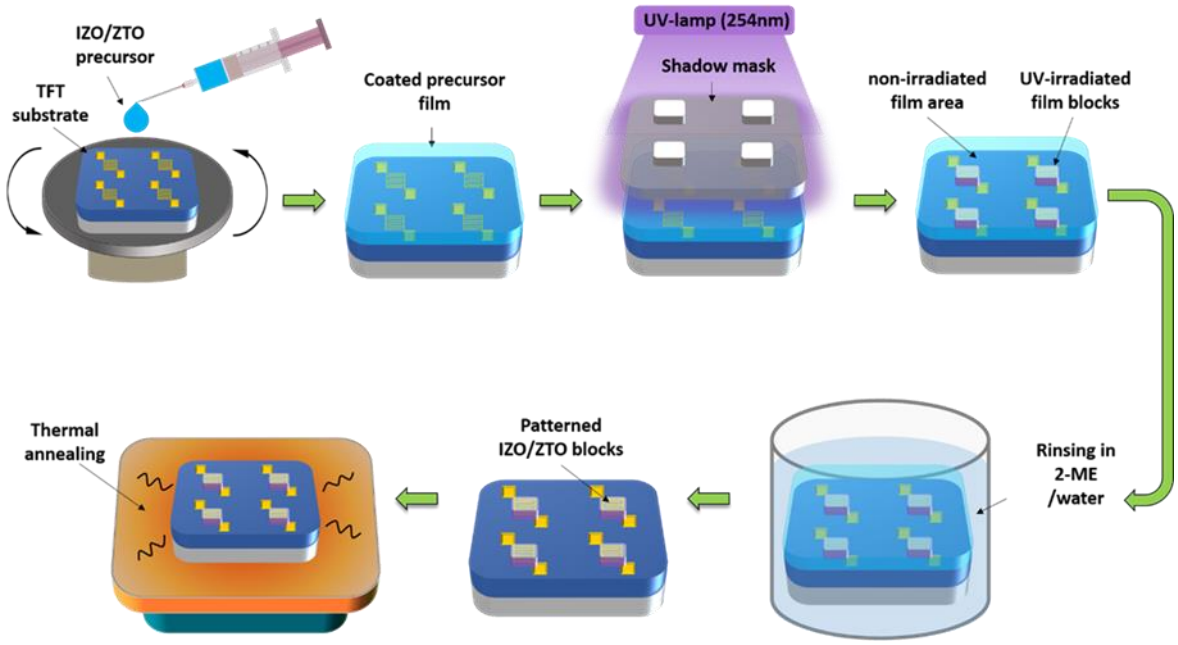

Figure 17 Schematic representation of the steps employed within this work for the direct UV photo-processing of semiconducting IZO/ZTO thin films from the oximato precursor solutions fabricated on a TFT substrate.

In order for the precursors to be suitable for photopatterning, they need to essentially function as a negative photoresist, wherein the sections of the film exposed to DUV irradiation via a shadow mask, partially decompose into a polymerised network which adheres to the target substrate. The unexposed regions can be easily removed via common organic solvents in which the parent precursor is soluble, but not the intermediate product formed after DUV irradiation. A schematic representation of the steps involved in s typical DUV photo-patterning approach using oximato precursors during this work is shown in **Figure 17**.

To this end, successful approaches for direct photopatterning have been demonstrated using metal diacrylate, metal acetylacetonates or by addition of photosensitive acetylacetone and benzoylacetone to the existing precursor solutions.[170, 172, 180-182] However, the use of photosensitive additives or the use of bulky organic photosensitive ligands often need additional high annealing temperatures (>400°C) to remove the residual impurities arising from the

incomplete decomposition of the precursor at lower temperatures. Although, deep ultra-violet radiation (DUV) with peak emission wavelength of 254 nm (90%) has been utilized for precursor decomposition, research pertaining to the patterning of precursors is rather scarce.[161, 183, 184] This is primarily due to the fact that peak emissions at ~ 254nm irradiation corresponds to a emitted energy of ~471 kJ/mol which is effective in decomposing majority of the organic bonds within the precursor, such as the C-C bond, C-O bond and the C-H bond with bond dissociation energies of 348kJ/mol, 352kJ/mol and 413kJ/mol respectively.[161, 185, 186] However, upon partial decomposition of the precursors, the intermediate product do not adhere well to the substrate and is completely washed away during the rinsing step for the development of the pattern. In other cases, the precursor film strongly adheres to the substrate directly upon spin coating and development of the pattern relies on different etching rates of the DUV exposed and non-exposed areas, which to some degree creates limitations in the generation of the multifunctional layered architecture of TFTs.[187]

In the case of diacrylate based precursors, it was reported that the zinc precursor undergoes an α-cleavage mechanism, wherein the DUV irradiation attacks C=C bonds and enables cross-linking via C-C bond formation.[188-190] The resultant DUV exposed film remained insoluble in iso-propanol which was used to rinse away the parent precursor film. Photo-patternable precursors generated by the addition of photosensitive chelate ligand such as benzoylacetone, the DUV irradiation enabled the π-π* transition, decomposing the chelate rings of the benzoylacetone and resulting in the cross-linking polymerization process. As a result, the DUV exposed films were insoluble in 2-methoxyethanol or ethanol, which was used to wash away the non-irradiated areas of the films and develop the desired pattern. However, there always exists a trade-off between the ability of bulky photosensitive ligands for patterning and the resultant TFT performance achieved from such precursors. The primary cause for this is the incomplete decomposition of the precursors post-patterning at moderate temperatures (350°C) and residual impurities from the ligand which require high temperature annealing for complete removal. Also, the nature of oxygen-related defects is significantly altered, resulting in the poor performance of the devices. For example, photopatterned ZnO TFTs from the zinc diacrylate precursor , annealed at 450°C exhibited an average μ_{FET} of 0.2cm^2/V.s, V_{th} of 14.9 V and an $I_{on/off}$ of 1.2 x 10^5, while ZTO TFTs fabricated via the addition of benzoylacetone exhibited a μ_{sat} of 0.03cm^2/V.s, V_{th}= 3.94 V and an $I_{on/off}$ of 6.85 x 10^5 when annealed at 350°C.[180, 181]

In contrast to the current approaches, tailored precursors with Schiff-base methoxyiminopropionic acid “oximato” ligands used in this work represent an ideal alternative

as an additive-free approach for facile photo-patterning of the desired inorganic metal oxides. These metal complexes possess an intrinsic broad absorption in the DUV range between 200-300nm with an absorption maximum at ~ 250nm, which is ideal for DUV patterning with a prominent irradiation at a wavelength of 254nm. Upon patterning with DUV light, through a shadow, the cleavage of the N-O bond within the ligand framework occurs while the carboxy fragments of the precursor remain intact. The DUV irradiated portion of the precursor does not dissolve in the parent solvent (2-Methoxyethanol), ethanol or water which were used to easily rinse and wash away the non-irradiated precursor. This enables a very convenient approach for the facile photopatterning of amorphous semiconducting IZO and ZTO thin-films. The patterned thin-films show active TFT performance when annealed at 250°C. An optimized performance is achieved when annealed at 350°C and exhibit high TFT performance with a μ_{sat} of 7.8 cm^2/V.s, V_{th} of 0.3 V and an $I_{on/off}$ of 3.5 x 10^8 for the IZO TFTs and a μ_{sat} of 3.6 cm^2/V.s, V_{th} of 2.4 V and an $I_{on/off}$ of 6.4 x 10^7 for the ZTO TFTs Such an approach can certainly be extended towards the photopatterning of other metal-oxide with a variety of functional mechanical, electronic and magnetic properties. The complete photo-patterning process, material and electrical characterization performed in this work can be found in Section 6.3

4.2 Biomineralization on a biological template

The growth of significant interest to mimic naturally occurring organic-inorganic or bio-inorganic hybrids due to their ability for self-assembly paves the way of unique material synthesis strategies in contrast to conventional approaches.[191] Biological templates for self-assembly or site-selective deposition onto such biological templates proteins, viruses, bacteriophages as well as deoxyribonucleic acid (DNA) have demonstrated the potential to pattern inorganic nanoparticles and generate hybrid nanostructures with unique functional properties.[192-204] The scope of such hybrid materials extends beyond the fundamentals which govern the synthesis and binding of the organic and the inorganic phases , where such functional hybrid materials have been used as active materials in applications such as semiconductors, batteries, catalysts, medical imaging materials, sensors and memory devices.[204-213] Virus templates or scaffolds are one of the emerging materials for the fabrication of materials in the field of bionanoelectronics.[214] Among such materials, the is one of the oldest and biologically well-studied material which has shown its ability to form functional and electronically active materials when combined with inorganic nanoparticles.[215] The TMV consists of well-defined rod or tubular structure with a length of 300nm, with an outer an inner diameter of 18nm and 4nm

respectively with an internal ribonucleic acid (RNA) structure an outer coat protein shell containing ~ 2130 identical coat protein units. [216, 217]. The most commonly studied wild-type (wt.) variant, cystiene, histidine mutants and the E50Q (RNA absent) mutant as shown in **Figure 18a,b**.

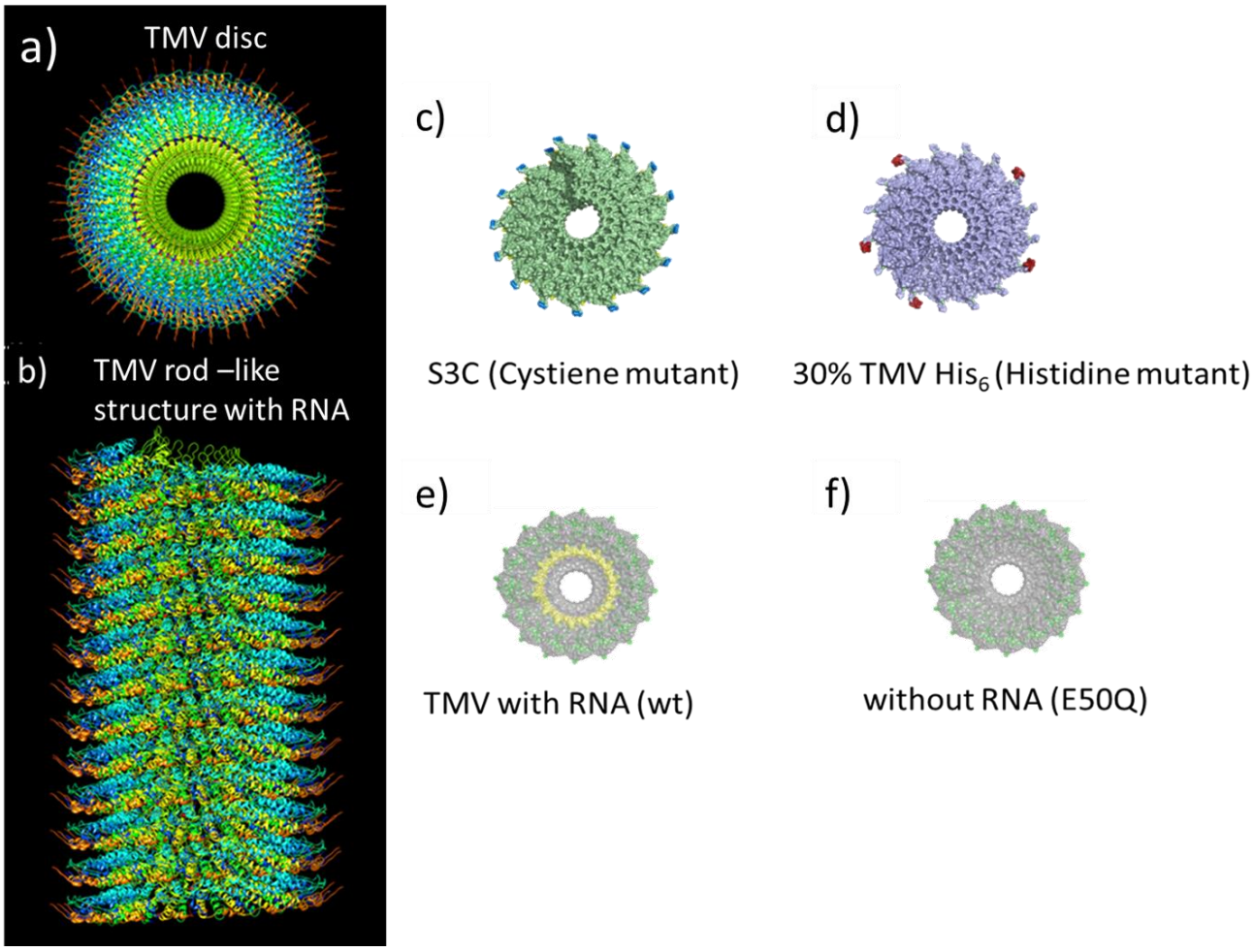

Figure 18 Molecular model of the a) horizontal cross section and b) vertical section the rod-like wild-type (wt) TMV. Adapted with permission.[218] Copyright 2013, AIP publishing. Molecular model of the genetically modified TMV coat protein including the c) cysteine, d) histidine e) wt-TMV and f) E50Q mutant. The cysteine and histidine mutants have the coat protein modification, while the E50Q mutant consists of self-assembled coat protein discs without the RNA. (Courtesy Dr. Sabine Eiben, University of Stuttgart)

The advancing research in the area of virology and material science has shown that the TMV's robust ability to remain stable under a broad pH range (pH 3-10) facilitates the binding of metallic as well metal oxide particles in reducing and oxidising environments. [219-227] Additionally, genetically modification of the TMV particles with amino acids and peptides can

be implemented to specifically target the binding of a specific metal ion for the formation of various bio-inorganic nanostructures.[228-236] The TMV as a biological template also has a remarkable thermal stability of up to 70°C, which aids in to formation and growth of different metals or metal oxides via sol-gel reaction.

Given the unique role of the TMV coat proteins and the potential to manipulate the surface charges, the TMV particles can themselves be self-assembled and structured by a variety of methods ranging from 1D to 3D nanostructures. The pre-existing high aspect ratio of the TMV can be further enhanced by increasing their head-to-tail linkage of multiple TMV nanorods resulting in the formation of nanowires. Such bio-nanowires can be production under acidic environments (pH<4), which arises from reduced interfacial repulsion of the charges on the TMV and favours a head-to-tail assembly as a result of minimised repulsive surface charges.[237, 238] Such long range ordering of the TMV particles can only be maintained under the desired pH conditions , which otherwise leads to disassembly of the head-to-tail arrangements due the dominance of the repulsive negative surface charges at higher pH conditions. However, permanent structuring of these long TMV nanowires can be easily achieved by polymerization with biocompatible polymers such as polyaniline.[239] Genetic modification of the TMV surface via the generation of the cysteine mutant TMV-1Cys facilitates the vertical assembly of the TMV virus onto gold surfaces via the gold-thiol groups present in the cysteine groups.[240-242] The structured TMV scaffold with subsequent deposition of nickel (Ni) nanoparticles as well as vanadium oxide (V_2O_5) have show promising potential as electrode materials in battery applications due the high surface area 3D scaffold provided by the TMV in contrast with planar deposition of the metal/metal oxides for the fabrication of electrode materials in batteries. The ability of the TMV to form various complex heirarchial nanostructures utilising their unique ability of surface functionalization and genetic modifications of the coat protein allows for improved generation of high surface area bio-templates to fabricate a variety of functional nanostructured coating and can be diversified to other relevant materials in the future.

Although the versatility of the TMV to act as a high aspect ratio bio template at a nanoscale has been well explored, the electronic and mechanical properties arising from the synergistic combination of the biological TMV in combination with metals as well as metal oxides as gained renewed interest to understand the role of the coat proteins and the RNA in the electroactive response within the hybrid bio inorganic material. TMV also possess interesting electronic properties due to the negatively charge surface of the coat protein. For a hybrid material consisting of platinum nanoparticle coated TMV, the current-voltage measurements (I-V

characteristics) of the material showed a hysteresis in the conductivity measurements with a distinct difference between its forward and reverse direction voltage sweep.[209] Such behaviour essentially corresponds to that of a memory device called as a memristor, although the observed characteristics were not suitable for analysis as per standard memristor physics but certainly laid the grounds for further investigations of the observed phenomenon.

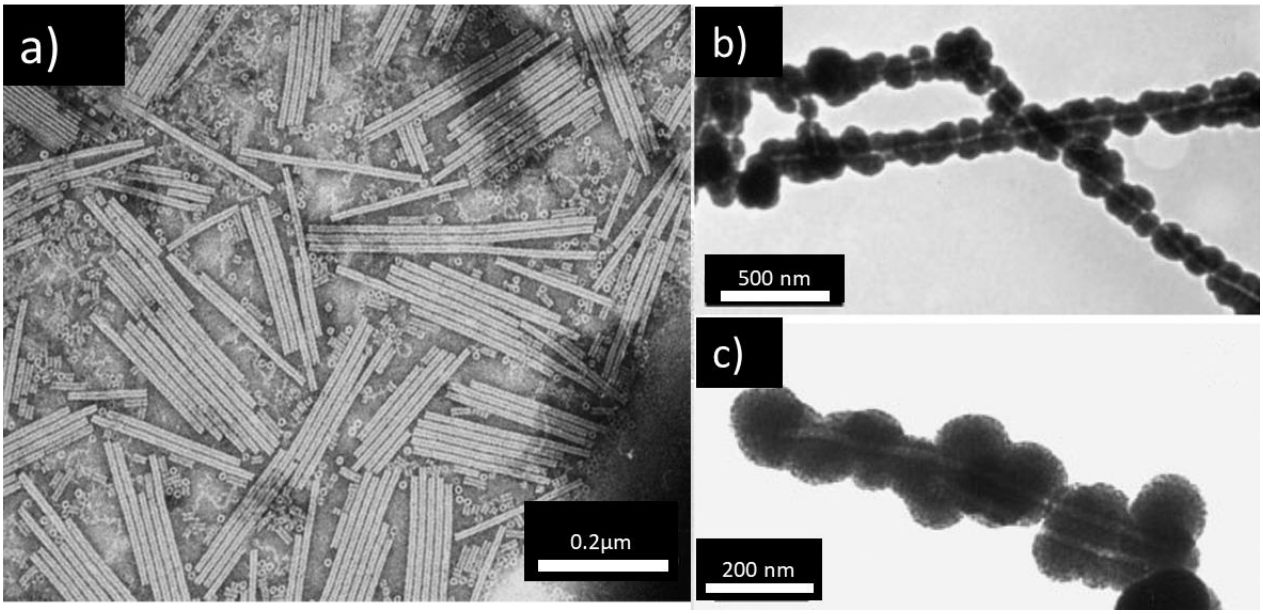

Figure 19 a) HR-TEM images of wt TMV nanoparticles. Adapted with permission.[218] Copyright 2013 AIP publications. Pt(II) pretreated TMVs metallized with b) nickel and c) cobalt by electroless deposition. Adapted with permission. [243] Copyright 2004, WILEY-VCH Verlag GmbH & Co. KGaA.

The preparation of the hybrid material within the device was performed by spin coating a solution of polyvinyl alcohol (PVA) consisting of platinum nanoparticle coated TMV, with aluminium electrodes which served as electrical contacts for the electrical characterisations. Along with the I-V characteristics, data retention characteristics were also measured via a semiconductor parameter analyser (SPA) which clearly indicated the material could be switched between an On-state and an Off-state based on the application of a positive voltage pulse of (2.5V) turn on the memristor or in other words “write” the data and on the other hand, application of a negative voltage pulse (-1.5V) to switch off the device or “erase” the data. The memory storage effect was attributed to the injected charges being trapped within the nanoparticles at the Pt nanoparticle interface and the insulating TMV coat protein which served as an insulating barrier due to which charge retention was possible. Upon application of sufficient voltage, the effective potential barrier could be overcome, leading to charge transport

through the guanine nucleobase within the TMV-RNA which acts charge-donor groups. It was concluded that the effective charge transport through the RNA in the On-state of the device was due to the Fowler-Nordheim tunnelling effect and not primarily due to thermionic charge injection which initially facilitates the storage of charges at the trap-sites present at the nanoparticle/coat-protein interface. These results proved that the a TMV-platinum nanoparticle hybrid material could serve as an electronically active rewritable random-access memory device which takes advantage of the electronic storage properties arising out of such a bio-inorganic hybrid material.

Research carried out during the course of this work investigated the electronic effects of the TMV in combination with ZnO as a hybrid semiconductor. ZnO is an attractive material with semiconducting properties such as a wide band-gap, high electron mobility and its economically viability.[244, 245] Although ZnO can be deposited via vacuum-based techniques at near room temperatures, the effect irradiation and gaseous environments and temperatures generated during the process cannot ensure that the TMV is biologically active. Hence, solution-based processes preformed at near room temperature (60-70°C) serve as an ideal platform to synthesize a TMV/ZnO hybrid material, at which the biological activity of the TMV can be ensured to remain intact and can be investigated. However, as-synthesized zinc oxide by itself, deposited solution-based processes does not exhibit viable electronic properties due a large concentration of zinc and oxygen related defects present within the material. Hence, the material usually needs to be annealed up to very high temperatures (>RT upto 500°C) in order to render the material as a semiconductor.[71, 246-248]

Earlier investigations reported prior to this work with our collaborative research with the Institute for Material Science and the Institute for Biomaterials and Biological systems at the University of Stuttgart, had successfully demonstrated that non-aqueous mineralization of ZnO on wt-TMV immobilized on the pre-structed FET device, displayed active transistor behaviour in its as prepared state.[249] However, no activity was observed for ZnO which was mineralized directly onto the FET substrate. As discussed earlier, ZnO derived from a solution process contains a large number of atomic defects which need to be passivated via high temperature annealing. Another advantage of this process is that the ZnO preferentially nucleated and forms nanoparticles onto the TMV which serves a structure directing and site-selective bio-template for the deposition of ZnO, essentially forming polycrystalline ZnO nanowires. Similar results have previously been demonstrated for the selective mineralization of metal clusters onto wt-TMV effective binding of the metal ions on the TMV. This synthesis was facilitated by the coat

proteins which contain amino acids such as serine, threonine which contain hydroxyl (-OH) functional groups as well as the carboxyl (-COOH) group present on the terminus of the coat protein which effectively act as ligands for the metal ion binding, under controlled pH conditions via electroless deposition [243]. Investigations by other research groups, based on viruses and enzymes via scanning tunnelling microscopy show that charge transport indeed occurs through the macromolecular structure of such biologically active materials via the tunnelling effect similar to that reported for the TMV/platinum nanoparticle based memory devices.[250, 251] However, the hybrid bio-inorganic semiconductor material generated by direct mineralization of the ZnO onto the TMV has not yet been implemented within the field effect transistor.

The use of ZnO nanoparticles derived via solution process still need an adequate thermal annealing post-deposition[155, 158], which clearly emphasizes the active role of the TMV in the bio-inorganic hybrid semiconductor fabricated under mild chemical conditions. In order to synthesize the TMV/ZnO hybrid semiconductor, TMV particles were immobilized on the FET substrate by first coating the substrate with aqueous zinc acetate to provide divalent Zn^{2+} cations and removed after 10 minutes via a stream of argon. This improves the adhering of the negatively charged TMV on the substrate. The pre-fabricated FET substrate comprised of interdigital gold electrodes structured on a highly n-doped Si substrate with thermally grown SiO_2 dielectric layer (SiO_2 = 90nm). The mineralization solution consisted of zinc acetate dihydrate $Zn(OOCCH_3)_2{\cdot}2H_2O$ [10mM], polyvinylpyrrolidone (PVP) [10mM] and tetraethylammonium hydroxide (TEAOH) [25mM] and was carried out at 60°C for 1.5 hours per mineralization cycle. The TEAOH acts as a basic agent to facilitate the olation and oxolation steps in the formation of ZnO while PVP is primarily used to control the nucleation rate and rapid increase in particle size of the ZnO nanoparticle as a result of the Ostwald ripening phenomenon.[119] The repeated mineralization cycles can be performed to achieve the desired thickness coating of the ZnO onto the TMV template. The electrical characterization of the TMV/ZnO hybrid material by measuring the transfer and output characteristics of the TMV/ZnO hybrid after 15 mineralization cycles of the ZnO onto the TMV exhibited a effective charge carrier mobility of 1.15 x 10^{-2} $cm^2/V.s$, V_{th} of 2.1V and an $I_{on/off}$ ratio of 5.8 x 10^4. Reference ZnO generated from ZnO alone with identical mineralization cycles did not show any active transistor performance and the device was in the Off-state in the entire range of the gate- voltage (V_{gs}) sweep range (-5 V to 30 V).

Within the duration of this work, an alternative procedure for the generation of the TMV/ZnO hybrid material was developed via microwave synthesis of the ZnO nanoparticles using a molecular precursor route. Complete details of this research can be found in Section 6.4. The procedure employed the use of diaqua-bis[2-(methoxyimino)propanato]zinc(II) or zinc "oximato" as a molecular precursor which has been previously reported by our group.[77, 101, 159] The motivation behind this approach was to investigate the effect of a new mineralization approach with a well-defined precursor which under goes a clear decomposition with volatile by-products enabling the production of high quality of ZnO. The mineralization solution was prepared similar to the recipe defined earlier with the only change being the choice of precursor used. The zinc oximato precursor is known to produce stable nanoparticles under microwave irradiation.[159] Adaptation of this procedure in a methanolic solution with the addition of PVP and TEAOH helped the generation of stable ZnO nanoparticles under mild microwave conditions, with an applied power of 50 Watts (dynamic mode) , with an average applied power of just 15 Watts for one mineralization cycle which is completed in 30 minutes. The formation of the ZnO nanoparticles was confirmed via UV-Vis, dynamic light scattering (DLS) technique as well as TEM measurements which confirm an average particle size of 5 nm. For the mineralization of the TMV with ZnO, the FET substrate consisting of the immobilised TMV was completely immersed in 10 ml of the mineralization solution and the microwave reaction was carried out at mild reaction temperature of 60°C. Microwave decomposition with zinc acetate salt usually requires higher temperature (250°C) via microwave synthesis for the formation stable colloidal ZnO particles.[252] Such high temperatures were deemed unsuitable for the mineralization of the TMV and were not investigated further. The zinc oximato precursor decomposition in the presence of the basic agent TEAOH was investigated via ^{13}C NMR spectroscopy and distinct chemical shifts were observed for the release of acetonitrile (δ = 117.30 ppm) with other trace signals from the residual free ligand which can be expected for such a base catalysed reaction. The decomposition mechanism was in accordance with second-order type Beckmann rearrangement reaction.[253] Successful mineralization of the ZnO onto the TMV immobilized on the TFT substrate was verified via AFM as shown in the **Figure 20 a,b**. A schematic representation of the TMV/ZnO FET is shown in **Figure 20c**. The number of ZnO mineralization cycles of also had a clear influence of the TMV/ZnO hybrid, where different FET performance metrics were observed when the mineralization cycles were increased from 3 to 12. The influence of the ZnO layer thickness and uniformity is known to have a critical influence on the FET performance and needs careful optimization.[23, 254] All prepared TMV/ZnO FETs via

the microwave route showed active semiconductor behaviour without the need for any high temperature annealing, owing to the presence of the electroactive TMV template.

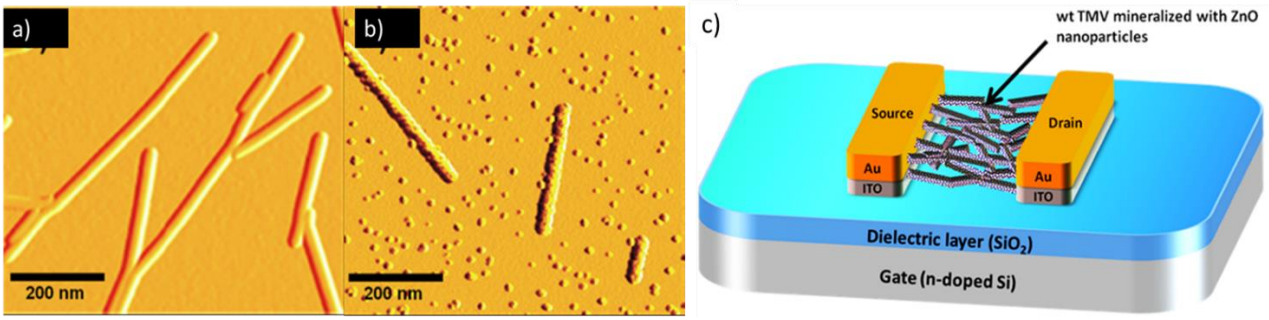

Figure 20 AFM micrographs of a) the bare wt. TMV template immobilized on a Si/SiO_2 substrate as well as b) the wt TMV template after 1 cycle of ZnO mineralization performed in this work. c) Schematic representation of the TMV/ZnO hybrid semiconductor employed in a TFT device. Adapted with permission under creative commons.[218] Copyright Beilstein Institut.

Lower number of deposition cycles (3 cycles) exhibited very weak transfer characteristics with significantly reduced $I_{on/off}$ of 10.2×10^2, accompanied by higher threshold voltages V_{th}= 17.7 V and low mobility value μ_{sat} of 8.0×10^{-6} $cm^2/V.s$. Increasing the deposition cycles (15 cycles) deteriorated the overall transistor performance with high ON and Off currents with poor $I_{on/off}$ = 1.0×10^2 and displayed a conductive nature with an increased mobility μ_{sat} of 1.6×10^{-3} $cm^2/V.s$. Optimization of the number of mineralization cycles with respect to reasonable trade-offs for the μ_{sat}, V_{th} and $I_{on/off}$ was achieved with 6 mineralization cycles which exhibited a mobility μ_{sat} of 6.7×10^{-4} cm^2/Vs, V_{th} of +4.7 V and an $I_{on/off}$ of 9.0×10^5. A higher $I_{on/off}$ ratio with respect to previously reported values was potentially attributed to a higher degree of oriented ZnO nanoparticles resulting from the use of the molecular precursor employed in the work. Thus, a new microwave synthesis route for the mineralization of ZnO on to the TMV template to create a bio-inorganic hybrid active semiconductor is developed. This new process enabled to obtain improved FET performance in some respects as well as reduce the time needed per mineralization cycle from 1.5 hrs to 30 mins. The improved synthesis route via the molecular precursor route can certainly be extended to a clear and controlled deposition of metal oxides in combination with functional biological templates with unique electrical and physical properties.

5 Atomic layer deposition (ALD) of oxide semiconductors

Atomic layer deposition (ALD) is a well-known conventional material deposition technique to obtain well-defined thin films across a variety of target substrates.[255, 256] The unique property of the ALD relies on its ability of self-limited surface reactions, where a defined dosage/pulse of the precursor in combination with an inert carrier gas is released into the reaction chamber, followed by subsequent release of the oxidising agent, in the case of metal oxides.

The reaction is basically divided in to two “half-reactions” in order to complete one deposition cycle of the desired material. The first “half-reaction” consists of one precursor pulse which is released into the reaction chamber and held for a sufficient period of time (seconds), where the precursor is deposited on the target substrate by partially reaction with the surface groups present on the substrate or via chemisorption.[257] This process ensures that the precursor adheres well to the substrate. In the case of the silicon, silicon-dioxide or polymeric substrates, the surface hydroxyl groups react with the precursor, wherein the precursor undergoes partial decomposition.[258] This is followed by the release of the oxidizing agent, which in most cases is water. The water pulse is also held for a few seconds to ensure complete precursor decomposition, followed by purging the reaction chamber with a stream of inert gas which facilitates the beginning of the next deposition cycle. The precursor reaction steps using trimethyl indium and diethyl zinc are in the presence of water as a oxidising agent are given by the following equations. The chemical equations for such a type of deposition is formulated for ZnO in equation 5.1 with aterisks denoting active surface species and double vertical lines denotthe surface itself:

$$||-OH* \xrightarrow[-C_2H_6]{Zn(C_2H_5)_2} ||-O-Zn-C_2H_5 \xrightarrow[-C_2H_6]{H_2O} ||-O-Zn-OH* \qquad \text{Equation 5.1}$$

Due to the different stoichiometry of In_2O_3 films, deposition may be denoted split into two half reactions 5.2 and 5.3 with the overall stoichiometry as shown in equation 5.4

$$In-OH* \xrightarrow[-CH_4]{In(CH_3)_3} In-O-In(CH_3)_2* \qquad \text{Equation 5.2}$$

$$In-CH_3* \xrightarrow[-CH_4]{H_2O} In-OH* \qquad \text{Equation 5.3}$$

$$2In(CH_3)_2 + 3H_2O \rightarrow In_2O_3 + 3CH_4 \qquad \text{Equation 5.4}$$

Stronger oxidising agent such as ozone (O_3) or hydrogen peroxide (H_2O_2) are occasionally used in order to decompose precursors which do not undergo complete reactions with H_2O. [259-261]. The reliability of the precursor deposition also depends on the deposition temperature within which successful deposition of the precursor is carried out. This desired temperature range varies for different precursors depending on the anion or ligand of the corresponding metal and is often known as the "ALD temperature window" which typically ranges from 100°C to 300°C for most of the precursors employed.[262] With a large variety of precursors developed for the conformal coating of large scale deposition of metals, metal oxides and metal nitrides and the increasing need for miniaturization and complex structures in the field of microelectronics, ALD has presented itself as a front runner for the fabrication and conformal deposition of next generation nanostructures in the field of microelectronics.

5.1 Heterostructure stacks of indium oxide/zinc oxide semiconductor TFTs

In the past decades, investigations and application of ALD-based films has largely been devoted to the development of metal layers and dielectric layers comprising mainly of metal oxides and metal nitride layers.[260, 263, 264] However, with the rise of flexible electronics based on plastic substrates, ALD technology has seen an increasing rise in the development of active semiconductor layers for TFT applications , apart from metal contacts and inorganic dielectric layers. Initial investigations of semiconducting layers were largely focussed on the deposition of zinc oxide using diethyl zinc (DEZ) and H_2O, owing to their easy availability and facile deposition conditions.[265-280] A comprehensive review concerning the precursors used, reaction kinectics , film growth rates and the quality of the result ZnO has been summarised by Tynell and coworkers.[281] Fabrication of ZnO TFTs using ALD have shown impressive performance and reliability due to the precise control over the reaction kinetics as well as film thickness, both of which are highly relevant to produce high performance TFTs. However, typical ZnO TFTs based on conventional SiO_2 dielectrics for ALD report TFT mobility values between 0.1 and 10 $cm^2/V.s$ based on based on the type of reactor used, deposition temperature, flow of gases, type of oxidizing agent used among others. Such parameters are also know to influence the TFT performance, although the starting precursor in all cases remains the same.[275, 277, 278] Tsai *et al.* reported ZnO TFTs with a mobility of 20 $cm^2/V.s$ which is among the highest reported values for ALD-based ZnO TFTs.[282] Although such reported values are obtained by the use of high-k dielectric materials Al_2O_3 and HfO_2 which are well known to deliver higher TFT performance,

due lower leakage currents in comparison with the standard SiO_2 dielectric. TFTs based solely on ZnO often suffer from device instability in terms of voltage bias stress and degradation over time resulting commonly from oxygen vacancy related defects. In order to improve device performance, cations such as Hf and Al have been used to produce doped ZnO TFTs such as AlZnO (AZO) and ZnHfO with enhanced stability. [283-285] In recent times, high performance multinary amorphous InGaZnO (IGZO) TFTs with mobilities of 3.5 $cm^2/V.s$ have also been fabricated via a sophisticated "Spatial ALD" which used co-injection of sophisticated indium and gallium precursors in combination with diethyl zinc which demonstrates the potential of fabrication amorphous oxide semiconductors via ALD.[68, 285] A similar strategy without co-injection was shown by using a single premixed precursor formulation (In:Ga:Zn, 1:1:3) using sophisticated precursors to fabricate IGZO TFT with impressive mobilities of 6.1 to 14.8 cm2/V.s for deposition temperatures between 130°C to 170°C.[69] However, more recently, multilayer architecture for generation of heterostructure semiconductors has facilitated the fabrication of high performance TFTs, wherein controlled thickness of dielectric oxides help to control the passivation of defects as well as the growth direction of the ZnO layer.[283, 286, 287] Interesting, fabrication of multilayer heterostructures based on individual binary semiconductor/semiconductor structures towards the generation of high performance TFTs are rather scarce while only investigations based on pulsed laser deposition of ZnO/SnO_2 heterostructures have been reported.[288]

The studies carried out during this thesis conducted the investigations on generating high performance heterostructure semiconductors with highly tuneable properties with precision deposition of the metal oxide via ALD. Complete details of the ALD parameters, influence of the heterostructure design as well as the material and elctronic characterization can be found in Section 6.7. Using trimethyl indium and diethyl zinc as starting precursors with water as an oxidising agent, successful fabrication of high performance TFTs using stacks in indium oxide/zinc oxide (In_2O_3/ZnO) were demonstrated. A schematic representation of the ALD supercycles and the corresponding generation of a In_2O_3/ZnO heterostructure stack is shown in **Figure 21**. The overall film consisted of alternating layers of ultrathin well-defined In_2O_3 and ZnO. The final film of the multi-layered heterostructure stacks annealed at 300°C, consisted of a ultrathin (9 nm) thick film consisting of four alternating layer of In_2O and ZnO. The deposition of the heterstructure stacks results in a highly crystalline material in which the lattice planes of the crystalline material were visible in the HR-TEM investigations as shown in **Figure 22**.

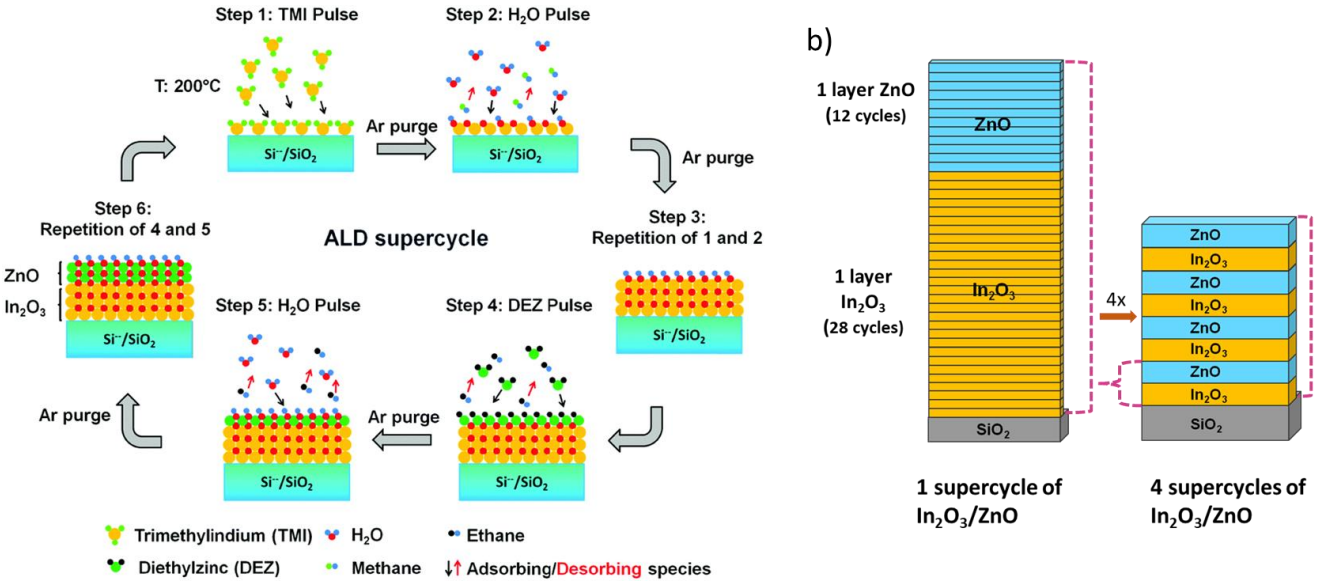

Figure 21 a) Schematic representation of a single supercycle performed for the deposition of the In_2O_3/ZnO heterostructure stack from the precursors TMI and DEZ. Steps (1) and (2) depict the indium precursor (TMI) deposition and partial reaction, followed by removal of volatile by-products with an Ar purge and final conversion to the indium oxide with a H_2O pulse. Steps (4) and (5) depict the deposition of the zinc precursor (DEZ) on the indium oxide layer, with analogous reaction steps as for the indium precursor TMI. Steps (3) and (6) indicate multiple iterations of the individual precursor cycles to achieve the desired deposition thicknesses. b) Schematic representation of building a heterostructure stack of In_2O_3/ZnO on a Si/SiO_2 substrate

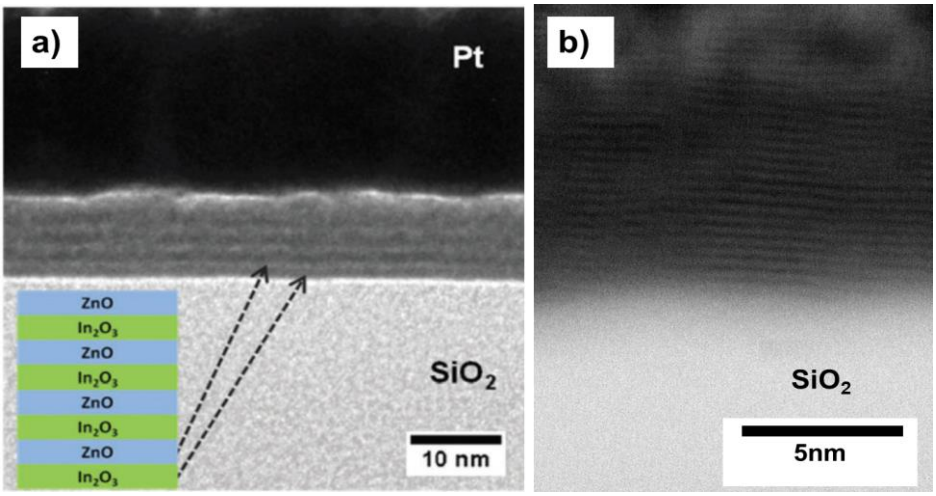

Figure 22 Cross-sectional TEM micrographs obtained via FIB sample prepara-tion of a) four stacks of the heterostucture, b) high-resolution zoom-in image of the In_2O_3/ZnO heterostructure stacks which display the visible lattice planes of the crystalline heterostructure material.

Apart from the optimization of the individual layer thickness of each of the individual metal oxide, it was found the number of such stacks played an important role. Higher number of stacks

(6 stacks) increased the conductivity of the overall film, thereby increasing the off-current and reducing the $I_{on/off}$ ratio as well as TFT mobility which are undesired. On the other hand very few number of stacks (3 stacks) resulted in much higher threshold voltages and relatively poor mobility values. The nature for such behaviour investigated via angle-resolved XPS wherein the oxygen O1s core spectra revealed that the initial layer in contact with the dielectric interface contained fewer hydroxyl (-OH) groups (6.8 at.%) and defect sites while containing a higher percentage (93.2 at.%) of well- coordinated oxygen arising from the lattice oxygen from the metal-oxygen-metal (M-O-M) bonds. This ration of defects proportionally gets inverted where the upper-most layers of the film consisted of higher amounts of hydroxyl species (15.5 at%) and a slightly reduced amount (84.5 at.%) of the M-O-M species. Higher amounts of hydroxyl groups and oxygen vacancy defects within thicker films are known to increase the charge carrier concentration of the film which in turn increases its conductivity and adversely affect the TFT performance in terms of the TFT mobility, threshold voltage and $I_{on/off}$. Similar observations were by the Fortunato group, for sputter based IZO TFTs, where device degradation occurs beyond a certain optimal film thickness.[289] Additionally, for an increasing film thickness, an increase in off-current and a negative shift in the Vth has been attributed to deep-donor like states arising from oxygen vacancy related defects, thereby increasing the overall trap density.[290-292] Moreover, we observed that the order of the sequential deposition also play a crucial role in improving the TFT performance. Multiple stacks generated by first depositing the ZnO layer followed by the In_2O_3 layer (ZnO/In_2O_3, 4 stacks) within the heterostructure architecture delivered relatively inferior performance average field-effect mobility ($\mu_{sat.}$) of 1.07 cm^2/ V.s, V_{th} of 10 V, $I_{on/off}$ ratio of 5.2×10^6 and a sub-threshold swing (SS) of 1.85 V/dec in comparison with the deposition of In_2O_3 first (In_2O_3/ZnO, 4 stacks) which had a comparatively high device performance with an average field-effect mobility ($\mu_{sat.}$) of 6.5 cm^2 /V.s, V_{th} of 8.9 V, $I_{on/off}$ ratio of 5×10^7 and a substantially reduced SS of 0.7 V/dec. The reason for such enhancement in the TFT performance was due the highly conductive nature of the In_2O_3 when employed in a TFT device whereas ZnO TFTs yielded a semiconducting behaviour with rather poor performance as expected. Additionally, literature based on the metal oxide TFTs deposited either via sputtering or solution processing of semiconducting layers with a higher charge carrier concentration at the dielectric interface, followed by subsequent deposition of layers with reduced charge carrier concentration has shown substantial improvement in the overall transistor performance.[293, 294] Moreover, our finding were well supported by the AFM result, wherein a individual layer of In_2O_3 films had a slightly higher surface roughness (R_{RMS} ~ 0.34

nm) in comparison with the ZnO films (R_{RMS} ~ 0.22 nm). The optimised heterostructure had an intermediate surface roughness ((R_{RMS} ~ 0.28 nm), which proved that the overall chemical composition of the multi-layered films played a dominant role in tuning the TFT performance, where a smoother surface topology of the films did not contribute towards improved device performance. Interestingly, recent literature also attributes the high performance and reliability of such TFTs on the 2D-electron gas (2DEG) at the heterointerface (**Figure 23**), consisting of a high electron concentration which becomes the dominant pathway of charge transport, with reduced resistance at the heterointerface.[291, 295, 296]. Within a fabricated heterostructure, the electrons reduce their energy by migrating out of the different semiconductor layers due the potential difference between the two semiconductors and accumulate at the heterointerface, where they form a 2D electron gas (2DEG) in close proximity to the heterointerface.[297] Additionally, the locally confined charge carriers at the interface do not get significantly affected from the trap states in the bulk stack which minimizes the ionized impurity scattering from the bulk material and promotes a higher charge carrier mobility higher than that of the individual semiconductors when employed in a FET device.[298, 299]

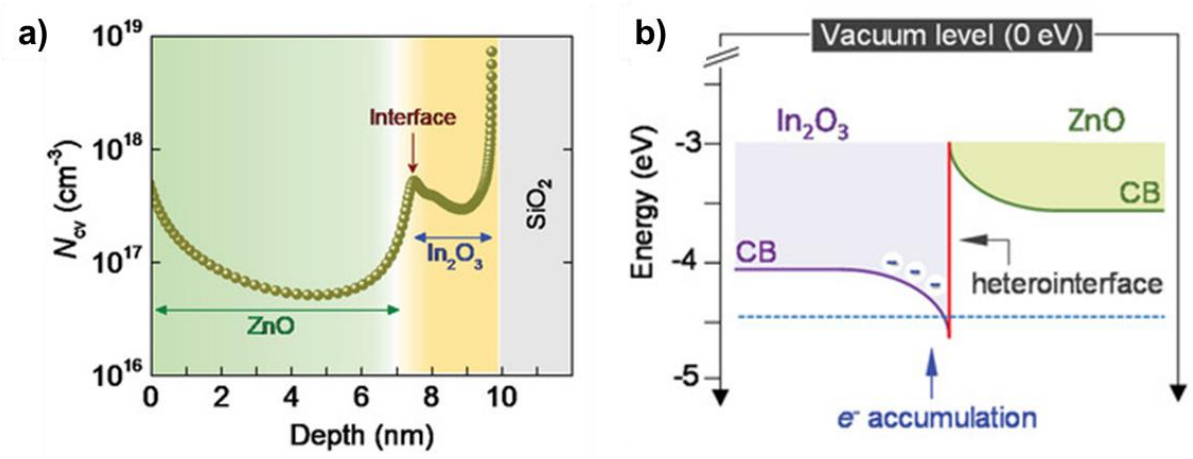

Figure 23 Distribution of charge carrier density (NCV) measured from the C–V data as a function of heterojunction depth where an increase charge carrier concentration is observed. d) Energy band diagram and accumulation of charge carriers (electrons) of the In_2O_3/ZnO heterointerface. Adapted with permission.[296] Copyright 2019, WILEY-VCH Verlag GmbH & Co. KGaA.

Research based on application of transparent heterostructure metal oxide semiconductors posses a broad scope in terms of factors influencing the chemical and electronic properties in the area of next generation electronic technologies such high performance FinFETs (resembling

the vertical fin of a fish) and memory devices which have evolved into 3D architectures.[300, 301] ALD presents itself as the most suitable candidate for the deposition of ultrathin function films with precise conformal coating for such technologies with promising capabilities of roll-to-roll mass manufacturing.[302, 303]

6 Organisation of the cumulative part of this dissertation

The following chapters of this thesis are arranged into three categories. The first category consists of the publications associated with the processing and application of the different metal-oxide semiconductors (colloidal IZO nanoparticles, ZnO/TMV hybrid, ZTO and photo-patterning of IZO & ZTO) fabricated using the metal oximato complexes synthesized using the Schiff-base methoxyiminopropionato ligand.

The second category consists of publications related to the low-temperature combustion processing of IZO TFTs fabricated using the nitro and nitroso functionalized malonato ligands of In and Zn as well the combusting processing of IGZO TFTs employing the urea-nitrate co-ordination compounds of In, Ga and Zn.

The third category consists of In_2O_3/ZnO semiconductor heterostructure TFTs fabricated using diethyl zinc and trimethyl indium precursors via atomic layer deposition (ALD).

6.1 Microwave synthesis and field effect transistor performance of stable colloidal indium zinc oxide nanoparticles.

Indium zinc oxide nanoparticles were prepared by microwave-assisted decomposition employing solutions of molecular air stable In and Zn precursors of Schiff base type.The controlled decomposition of mixtures of stable molecular precursors by heating with microwave radiation is a straightforward technique for obtaining stable suspensions of IZO nanoparticles. The stability against flocculation or sedimentation is mainly due to the organic residues from the precursor molecules residing on the surface of the nanoparticles and stabilizing them to a notable extent. This formation mechanism is well known and avoids the addition of other stabilizing agents. These ready to use dispersions with shelf-lives of several months were obtained at comparably low temperature of 140°C by heating mixtures of indium and zinc complexes with Schiff base oximato ligands in 2-ethoxyethanol. IZO particles prepared therefrom with an In : Zn ratio of 60 : 40 display an average diameter of about 5 nm and appeared amorphous in nature. No phase separation of the colloidal suspensions was observed, in contrast to the decomposition of solid mixtures of the same precursors, which lead to an amorphous IZO matrix with crystalline bixbyite In_2O_3 nanoparticles . The ceramization process starts with the particle formation already during the initial microwave heating. To achieve a good semiconducting behaviour, though, final processing at higher temperatures was required, which finally removes additional surface hydroxylation as well as adherent traces of organic residues which comprise of ligand fragments. Even after annealing the IZO remained completely amorphous, which is an essential feature for its superior electronic performance. Thin films of the colloidal particles with a uniform surface coverage and low roughness could be obtained by spin-coating on silicon-dioxide substrates. X-ray photoelectron spectroscopy showed that oxide formation had occurred after the microwave reaction, but could be improved further by annealing the films at elevated temperatures. The removal of adherent organic and hydroxy moieties at 450 °C thus led to an excellent semiconducting behaviour of the finally resulting IZO films. Obtained thin film transistors exhibited a n-type enhancement mode performance, with a mobility of 8.7 cm^2/V.s, an $I_{on/off}$ ratio of 2.8×10^5 and a threshold voltage V_{th} of +3.3 V.

RSC Advances

RSC Publishing

PAPER

View Article Online
View Journal | View Issue

Cite this: *RSC Adv.*, 2013, **3**, 20071

Microwave synthesis and field effect transistor performance of stable colloidal indium-zinc-oxide nanoparticles†

Shawn Sanctis, Rudolf C. Hoffmann and Jörg J. Schneider*

Received 7th August 2013
Accepted 20th August 2013

DOI: 10.1039/c3ra44222e

www.rsc.org/advances

Indium zinc oxide nanoparticles were prepared by microwave-assisted decomposition employing solutions of molecular air stable In and Zn precursors of Schiff base type. Stable colloidal ready to use dispersions with shelf-lives of several months were obtained at comparably low temperature of 140 °C by heating mixtures of indium and zinc complexes with Schiff base oximato ligands in 2-ethoxyethanol. IZO particles prepared therefrom with an In : Zn ratio of 60 : 40 display an average diameter of about 5 nm and appeared amorphous in nature. Thin films of the colloidal particles with a uniform surface coverage and low roughness could be obtained by spin-coating on silicon dioxide substrates. X-ray photoelectron spectroscopy showed that oxide formation had occurred after the microwave reaction, but could be improved further by annealing the films at elevated temperatures. The removal of adherent organic and hydroxy moieties at 450 °C thus led to an excellent semiconducting behaviour of the finally resulting IZO films. Obtained thin film transistors exhibited a n-type enhancement mode performance, with a mobility of 8.7 $cm^2 V^{-1} s^{-1}$, an $I_{on/off}$ ratio of 2.8×10^5 and a threshold voltage V_{th} of +3.3 V.

Introduction

The commercial success of advanced response–time displays has sparked interest in amorphous metal oxide semiconductors, as the more conventionally hydrogenated amorphous silicon (a-Si:H) is not able to keep up with the required semiconducting performance.[1–3] Thereby indium zinc oxide (IZO) and indium gallium zinc oxide (IGZO) are among the most widely investigated multinary metal oxide systems due to their high transparency (>90%), excellent current switching capacity and ease of large scale fabrication.[4] The deposition of such oxidic materials is usually performed using conventional vapour-phase techniques like radio-frequency sputtering[5] as well as pulsed laser deposition.[6]

The employment of solution deposition[7] offers a cost-effective alternative to these established techniques and might thus allow a more expanded and unprecedented employment of these class of materials.[8–12] Currently the widespread use of such coating procedures, though, are limited by the choice and applicability of available deposition solutions. Especially the use of air-sensitive molecular precursors such as alkoxides might require immediate utilization and could be cumbersome in a large-scale process.[12] The inclusion of an intermediate step with the formation of nanoscale oxide particles in the solvent prior to the deposition on the substrate is an interesting extension of the solution deposition technique.[13–16]

We have previously reported the synthesis of stable dispersions of zinc oxide nanoparticles by the microwave-assisted decomposition of a zinc oximato complex ("oximato" refers always to the methoxy-iminopropionato ligand framework herein) as single source precursor to ZnO.[17] This route might also be suitable for the synthesis of multinary or multicomponent metal oxide particles which are meanwhile the most intensively studied class of materials giving access to high performance inorganic semiconductor materials. Therefore one could start with solutions of mixtures of the corresponding oximato complexes. Although large structural differences exist between oximato complexes of various metals (ranging from simple mononuclear compounds to multinuclear hydroxo or oxo-bridged cage structures) the start of the ceramisation is always determined by the decay of the common oximato ligand. Thus the decomposition temperatures of various metal oximato complexes are in a very narrow range making them an ideal family in which a defined composition in a final binary or ternary ceramic can be fine tuned.[18–22] Rapid heating, which is available in a microwave set-up for chemical synthesis, could thus avoid the formation of mixtures of binary metal oxides and rather yield the desired multinary compound.[16,23] In the present study this was achieved for IZO, which could be finally processed as an active semiconducting layer in a field effect transistor (FET) device displaying with excellent electronic

Department of Chemistry, Eduard-Zintl-Institute, Inorganic Chemistry, Technische Universität Darmstadt, Petersenstr. 18, 64287 Darmstadt, Germany. E-mail: joerg.schneider@ac.chemie.tu-darmstadt.de

† Electronic supplementary information (ESI) available: UV/Vis of IZO suspensions, TEM and GI-XRD of In_2O_3, AFM of IZO films, monitoring of conditions in microwave during reaction. See DOI: 10.1039/c3ra44222e

characteristics compared to the current state of the art for solution processed FETs.

Experimental details

The molecular precursors tris[2-(methoxyimino)-propanoato]-indium(III) and diaqua-bis[2-(methoxyimino)-propanato]zinc(II) were synthesized as previously reported.[19,20] Stock solutions (0.5 weight% in 2-ethoxyethanol) of the indium and zinc precursor were prepared and subsequently mixed in proportions of 5.00 g : 2.40 g corresponding to a molar ratio of In : Zn = 60 : 40. Microwave reactions were performed in a Discover (CEM Corporation) microwave reactor with the glassware supplied by the manufacturer. Therefore the reaction solution (~7 ml), was filtered with a hydrophobic syringe filter, (PTFE membrane, Millipore, 0.2 μm) directly into 35 ml tubes. Reactions were carried out by heating with continuous power 300 W for 4 minutes to 140 °C and immediate cooling to room temperature using compressed air, afterwards (Fig. S1 and S2†). The IZO suspensions obtained in this way were then used for further characterization and the FET device fabrication.

Quartz slides (20 × 20 mm^2) as well as the prefabricated FET substrates were sequentially cleaned in an ultra-sonic bath with acetone, water and iso-propanol, respectively; for ten minutes each. Substrates for FET devices (15 × 15 mm^2) consisted of n-doped silicon with a 90 nm layer of SiO_2, on which gold electrodes were attached with an intermediate adhesive layer of indium tin oxide. The electrodes possessed an inter-digital structure with a channel width W of 10 mm and a channel length of L of 20 μm.[18,19]

Transmission Electron Microscopy (TEM) was performed using Tecnai F20 G2 F20 (FEI) working at 200 kV, using samples on SiO or lacey carbon coated copper grid. Dynamic light scattering (DLS) measurements of the IZO suspensions were performed using a Zetasizer Nano (Malvern). Photoluminescence measurements were carried out using Fluorolog-3 (Horiba), excitation wavelength 250 nm. X-ray Photoelectron Spectroscopy (XPS) analysis was performed with ESCALab 250 (Thermo VG Scientific) using monochromated Al Kα radiation. UV/Vis Spectroscopy were performed using Lambda 900 (Perkin Elmer). Ellipsometry measurements were carried out using a Nanofilm_ep3 (Accurion) with the modelling software provided by the manufacturer. Atomic force microscopy was performed (AFM) with a CP-II (Bruker-Veeco) using silicon cantilevers. Grazing incidence XRD (GI-XRD) investigations were performed with a Seifert PTS 3003 diffractometer using a Cu anode and an X-ray mirror on the primary side with a graphite monochromator used to separate the Cu K-alpha line on the secondary side which was separated by 40 mA and 40 kV. FET characteristics were measured under darkness, using an HP 4155A Semiconductor Parameter Analyzer (Agilent) in a glove box. Charge carrier mobility in the saturation regime μ_{SAT} as well as the threshold voltage V_{th} were derived from a linear fitting of the square root of the source drain current (I_{DS}) as a function of gate source voltage (V_{GS}). Further details of the parameter extractions for the fabricated FET were published earlier.[17,18]

Results and discussion

The experimental conditions for the formation of the IZO nanoparticles were adjusted and optimised in several steps. The solvent of choice should offer sufficient solubility for both molecular precursors and enable a rapid conversion into ceramic particles. For further processing with spin-coating and inkjet-printing a too low or too high boiling point would be disadvantageous as well as unfavourable wetting properties on common substrates. A first indication is therefore the magnitude of the dielectric loss tangent (tan δ) as a means to determine the ability of the solvent to convert microwave energy into heat at a particular microwave frequency.[24] Thus, methoxyethanol (tan δ = 0.282) only lead to an incomplete decomposition of the precursors, which could be monitored by UV/Vis spectroscopy (Fig. S3a†). On the other hand benzyl alcohol (tan δ = 0.667), which was suggested by Niederberger *et al.*[15,16] for the synthesis of a variety of oxide particles, did not lead to stable suspensions but caused undesired precipitation of solids. The usage of ethoxyethanol (tan δ = 0.301) finally lead to complete conversion to the ceramic (Fig. S3b†) as well as stable suspensions. In accordance with the known decomposition temperatures of the precursors in air, which was available from earlier work[18–20] the reaction was carried out at 140 °C. Reaction times were fixed at 4 minutes max. Shorter intervals lead to incomplete decompositions of the molecular precursors. On the

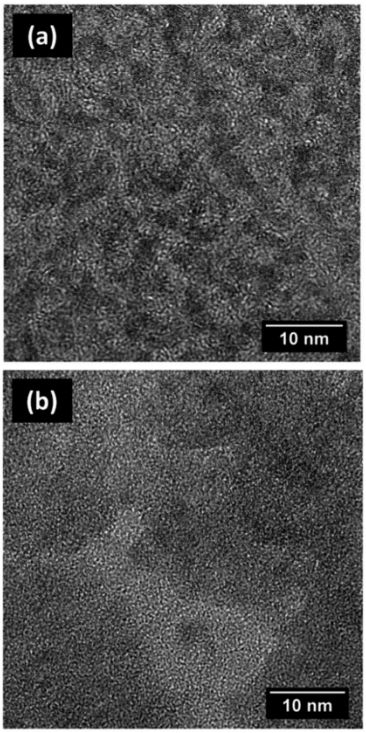

Fig. 1 HRTEM images of IZO samples annealed at (a) 200 °C or (b) 450 °C.

other hand, longer microwave irradiation times (>5 minutes) lead to the formation of agglomerates of larger particles or even precipitation.

The decomposition of mixtures of the indium oximato and zinc oximato complexes (as well as indium oximate alone) by heating in the microwave yielded suspensions, which were clear to the naked eye. These suspensions were stable for several months whereby no visible alteration occurred. DLS measurements (Fig. S4†) indicated a particle size of ~5 nm with a monomodal distribution of the particle size. Further investigations of the particles were carried out by means of TEM (Fig. 1). For the complete evaporation of the solvent and other volatile residues the samples were heated to 200 °C or 450 °C, respectively. In both cases individual particles were hardly discernible. The IZO was mainly amorphous and larger crystalline regions could not be identified. These findings were supported by GI-XRD measurements (Fig. 2), which showed that the IZO was still amorphous even after annealing at 450 °C.

For comparison indium oxide particles were prepared and annealed in the same way. In this case, however, bixbyite nanocrystals were found (Fig. S5†). These findings can be compared with investigations on the formation of IZO thin films from the same indium and zinc oximates by spin-coating of the precursor solutions and direct annealing of the substrates at elevated temperatures (250 or 450 °C).[19] Hereby an amorphous IZO matrix was formed, which contained inclusions of crystalline bixbyite. Presumably, the microwave-assisted reaction in solution allowed a very homogenous distribution of the two precursors. Thus, a phase separation during the conversion and particle formation is mainly avoided.

PL measurements (Fig. 3.) were carried out in order to provide an insight into the defect related states of the synthesized IZO nanoparticles. A strong first peak is located at ~397 nm and second less intense shoulders is located at ~295 nm, ~570 nm and 760 nm respectively. Similar signals at ~295 nm and ~397 nm were observed for pulsed-laser deposited indium oxide thin films and are commonly attributed to singly ionised oxygen-vacancy related defects.[25] The weaker contributions at higher wavelength were also found in colloidal In_2O_3 nanocrystals with a diameter of 4 nm, whereby shifts in the position of these peaks might arise due to quantum confinement.[26–28] Again these findings can be compared with the before-mentioned investigations on the formation of IZO and In_2O_3 thin films from indium and zinc oximates by direct annealing on substrates at elevated temperatures (250 or 450 °C). These revealed identical peaks for In_2O_3 and IZO films derived from the same molecular precursors.[19] Thus, the observed PL peaks do not indicate a clear association with IZO and rather display signals referring to nanocrystalline In_2O_3. This might indicate at the presence of some In_2O_3 within the particles, whereby TEM and XRD hint at a continuous distribution rather than a specific location within the microstructure of the ceramic particles.

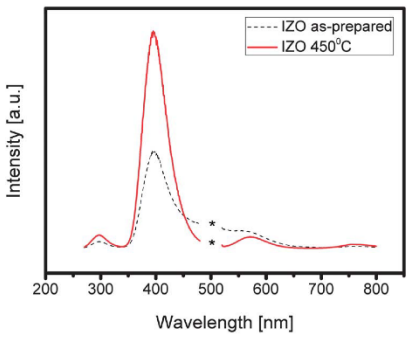

Fig. 3 PL spectra of IZO thin films on quartz after annealing at 200 °C and 450 °C (* — second harmonic omitted).

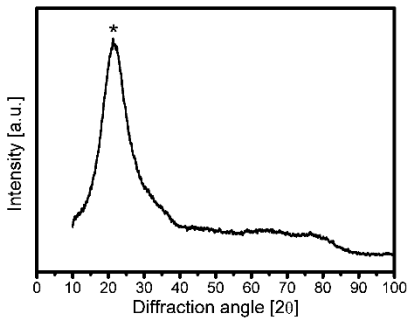

Fig. 2 GI-XRD diffractogram of IZO films formed on quartz after annealing at 450 °C (* = quartz substrate).

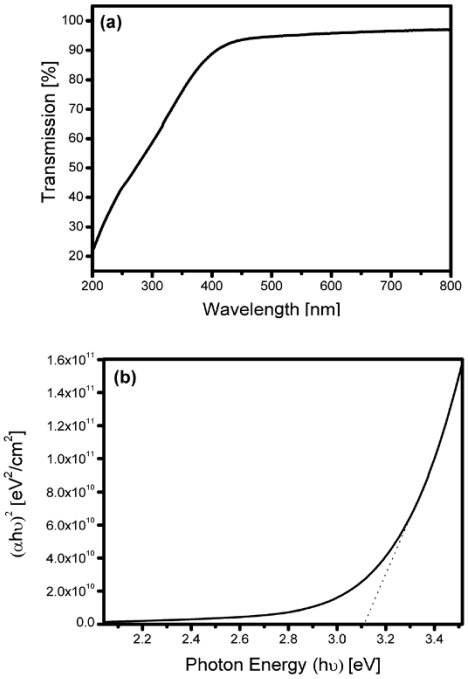

Fig. 4 (a) UV/Vis spectrum of IZO film on quartz after annealing at 450 °C and (b) corresponding Tauc plot.

UV/Vis spectroscopy of the IZO films annealed at 450 °C (Fig. 4) show films with high transparency (>85%) in the visible region. The bandgap energy (E_g) for the IZO film was estimated from the optical transmission spectra of the film annealed at 450 °C, using Tauc's relation $\alpha h\nu = A(h\nu - E_g)^{1/2}$ and assuming a direct band-gap. The estimated bandgap of the IZO film indicates a value of ~3.1 eV which is in good agreement with results obtained by other groups, for solution-processed IZO films.[10,11] The annealed IZO film did not show the onset of a sharp absorption edge, but exhibited a weak broad shoulder at between 275 nm and 300 nm, which is similar to findings by Banger *et al.*[12,17]

Further characterization of the IZO particles was carried out by XPS analysis of particles which were deposited on silicon substrates (Fig. 5). Thereby the as-deposited material was compared with particles after annealing at 450 °C. As expected the In 3d and Zn 2p signals (Fig. 5a and b) did not exhibit specific information and are in agreement with earlier findings for precursor-derived IZO.[12,17] The O 1s spectra clearly showed the presence of several contributions and were analysed in detail. The curve-fitting procedure yielded the best results when four contributions for the as-prepared IZO film (Fig. 5c) and three for the annealed IZO film (Fig. 5d) were used. The peaks located at ~529.9 eV can be attributed to the oxygen in the oxide lattice, whereas the peak at ~531.4 eV is typically associated to surface hydroxy groups.[12,29] Recently, contributions from O^{2-} ions present in the oxygen deficient regions of the amorphous IZO film were discussed separately.[30,31] Further signals at ~532.4 eV and a minor contribution located ~533.4 eV could be assigned to the presence of surface adsorbates such as organic residues (*e.g.* in the form of carboxy groups) from the precursor or decomposition or solvent molecules.[32,33] The presence of the peak at ~529.9 eV in the as-prepared samples indicated that the metal-oxide was already formed in the microwave process. After the annealing step this signal had the largest intensity while the contributions from the other components such as the hydroxylation were clearly diminished. This change in the O 1s part of the XPS spectrum indicated a complete conversion to a nanostructured oxide ceramic.[10] The extent of the formation of the M–O–M framework might be critical with respect to the performance as a semiconductor.

Field-effect transistors were fabricated by spin-coating of suspensions of IZO particles on FET substrates to obtain a homogeneous thin film. These films were then annealed by directly placing the substrates on pre-heated hot-plate at 450 °C. This procedure was repeated several times in order to obtain a dense homogeneous coverage of the semiconductor channel area.[34] The thickness of the IZO films as measured by ellipsometry was between 9 and 15 nm. AFM micrographs of the annealed IZO ceramic film (Fig. S6†) displayed a smooth and homogeneous coverage of the substrate surface displaying an RMS roughness of 1.1 nm. The films thus appeared uniform and no agglomerates, cracks or voids were detected.

The transfer and the output characteristics of the FET are shown in Fig. 6. The performance parameters were determined as charge carrier mobility μ 8.7 $cm^2\ V^{-1}\ s^{-1}$, threshold voltage V_{th} +3.3 V and $I_{on/off}$ ratio 2.8 × 10^5. These characteristics are comparable to the performance of FETs with solution processed

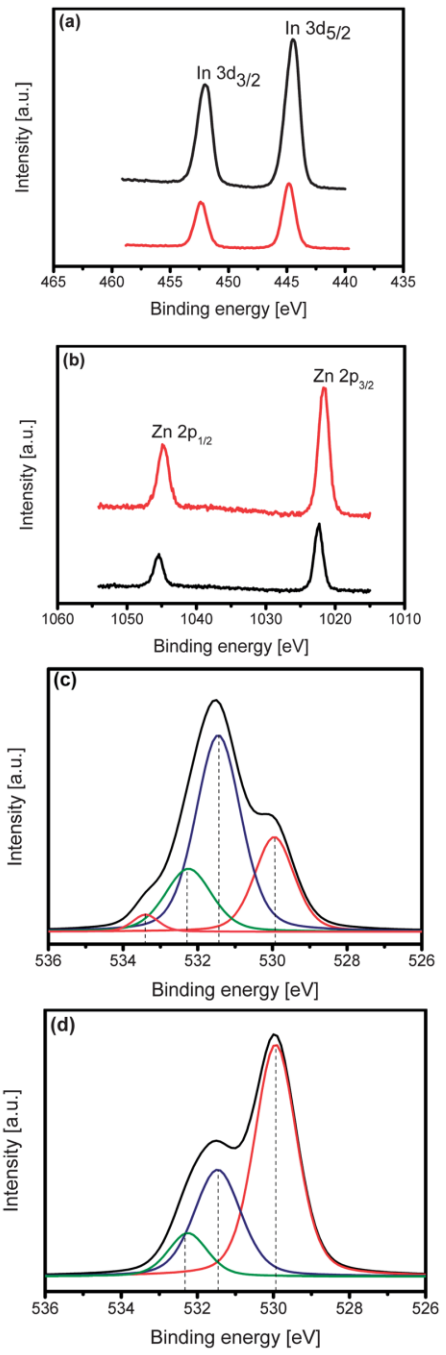

Fig. 5 XPS spectra of (a) In 3d and (b) Zn 2p region of as-prepared (black) and annealed, 450 °C (red) films, as well as O 1s regions of (c) as-prepared and (d) annealed, 450 °C films.

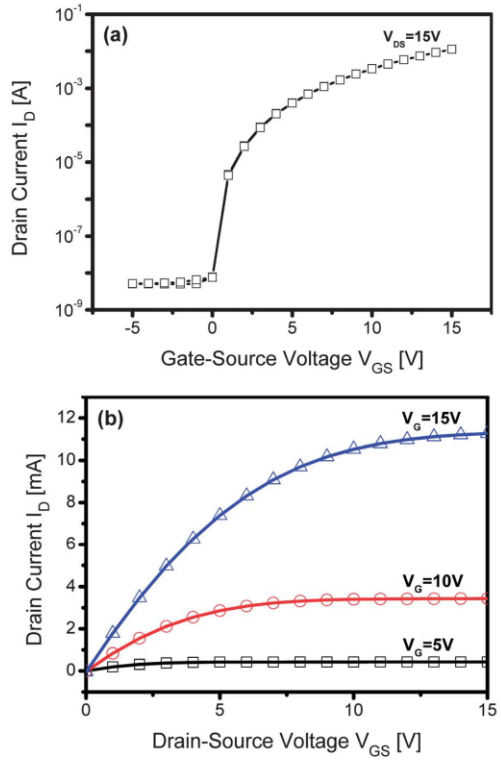

Fig. 6 Performance of a FET produced by deposition of IZO nanoparticles and annealing at 450 °C. (a) Transfer curve for constant source drain voltage at 15 V. (b) Output characteristics obtained from variation of the drain–source voltage from 0–15 V for gate–source voltages from 0–15 V in 5 V steps.

IZO layers, which were processed at similar or higher temperatures.[12,19,29,35] Thus Lee *et al.* obtained FETs with μ 7.4 $cm^2 V^{-1} s^{-1}$ and V_{th} of −26 V at 400 °C or 16.1 $cm^2 V^{-1} s^{-1}$ and V_{th} of −32 V at 600 °C.[35] Jeong *et al.* reported μ 1.54 $cm^2 V^{-1} s^{-1}$ and V_{th} of −6.28 V or 1.1 $cm^2 V^{-1} s^{-1}$ and V_{th} of +25.3 V; both processed at 400 °C, but with different In : Zn ratios.[29] In these cases the extremely negative[29,35] or positive[35] threshold voltages V_{th} diminish the potential use as dedicated n-type enhancement mode FETs. In this respect the results presented in the present work offer an advantageous procedure and an important step forward. In a recent study Banger *et al.* reported charge carrier mobilities of 7–12 $cm^2 V^{-1} s^{-1}$ and V_{th} ~0 V in a sophisticated wet-annealing process at 230–275 °C.[12] Kim *et al.* reported FET devices with μ 0.91 $cm^2 V^{-1} s^{-1}$ at 250 °C or 9.78 $cm^2 V^{-1} s^{-1}$ at 400 °C.[36] An even better performance might be achievable, though, as IZO films produced by sputtering can exhibit charge carriers mobilities higher than 20 $cm^2 V^{-1} s^{-1}$.[37–39]

Conclusions

The controlled decomposition of mixtures of stable molecular precursors by heating with microwave radiation is a straightforward technique for obtaining stable suspensions of IZO nanoparticles. The stability against flocculation or sedimentation is mainly due to the organic residues from the precursor molecules residing on the surface of the nanoparticles and stabilizing them to a notable extent. This formation mechanism is well known and nicely avoids the addition of other stabilizing agents.[16,17] The resulting shelf-life of the obtained colloidal suspensions might be attractive for use in coating and printing applications. Moreover, the rapid increase of the temperature during the microwave heating ensures the simultaneous decomposition of the two precursors and yields nanoparticles with uniform composition and a monomodal sized distribution. Crucial for the homogeneous decomposition process is the identical type and coordination mode of the ligand environment at the metal centers In and Zn in the Schiff base type molecular complexes. No phase separation of the colloidal suspensions was observed, in contrast to the decomposition of solid mixtures of the same precursors, which lead to an amorphous IZO matrix with crystalline bixbiyte inclusions.[19] The ceramization process starts with the particle formation already during the initial microwave heating. To achieve a good semiconducting behaviour, though, final processing at higher temperatures was required, which finally removes additional surface hydroxylation as well as strongly adherent traces of organic residues. Even after annealing the IZO remained completely amorphous, which is an essential feature for its superior electronic performance reported herein.

Acknowledgements

This work has been supported within the DFG SPP 1596, and the Cooperative Research Lab Alliance between Merck KGaA, Darmstadt, and Technische Universität Darmstadt (Merck Lab). We thank Dr M. Kaloumenos (FET), Dr A. Issanin (XPS), Dr J. Engstler (TEM) and Dr J. Brötz (GI-XRD) at Technische Universität Darmstadt as well as Dr P. Atanasova (PL), Universität Stuttgart, for measurements. TEM studies at ERC, Jülich, Germany, are supported through the ERC-TUD1 contract collaboration.

References

1 H. Hosono, *J. Non-Cryst. Solids*, 2006, **352**, 851.
2 E. Fortunato, P. Barquinha and R. Martins, *Adv. Mater.*, 2012, **24**, 2945.
3 J. K. Jeong, *Semicond. Sci. Technol.*, 2011, **26**, 034008.
4 T. Kamiya, K. Nomura and H. Hosono, *Sci. Technol. Adv. Mater.*, 2010, **11**, 044305.
5 E. Fortunato, A. Pimentel, A. Goncalves, A. Marques and R. Martins, *Thin Solid Films*, 2006, **502**, 104.
6 A. Suresh, P. Wellenius, A. Dhawan and J. Muth, *Appl. Phys. Lett.*, 2007, **90**, 123512.
7 R. M. Pasquarelli, D. S. Ginley and R. O'Hayre, *Chem. Soc. Rev.*, 2011, **40**, 5406.
8 D. H. Lee, S. Y. Han, G. S. Herman and C. H. Chang, *J. Mater. Chem.*, 2009, **19**, 3135.

9 M. G. Kim, H. S. Kim, Y. G. Ha, J. Q. He, M. G. Kanatzidis, A. Facchetti and T. J. Marks, *J. Am. Chem. Soc.*, 2010, **132**, 10352.
10 S. Jeong, J. Y. Lee, S. S. Lee, S. W. Oh, H. H. Lee, Y. H. Seo, B. H. Ryu and Y. Choi, *J. Mater. Chem.*, 2011, **21**, 17066.
11 C. G. Choi, S.-J. Seo and B.-S. Bae, *Electrochem. Solid State Lett.*, 2008, **11**, H7.
12 K. Banger, Y. Yamashita, K. Mori, R. Peterson, T. Leedham, J. Rickard and H. Sirringhaus, *Nat. Mater.*, 2010, **10**, 45.
13 M. Niederberger and N. Pinna, *Metal oxide nanoparticles in organic solvents: synthesis, formation, assembly and application*, Springer, 2009.
14 M. Baghbanzadeh, L. Carbone, P. D. Cozzoli and C. O. Kappe, *Angew. Chem., Int. Ed.*, 2011, **50**, 11312.
15 I. Bilecka and M. Niederberger, *Nanoscale*, 2010, **2**, 1358.
16 I. Bilecka and M. Niederberger, *Electrochim. Acta*, 2010, **55**, 7717.
17 J. J. Schneider, R. C. Hoffmann, J. Engstler, A. Klyszcz, E. Erdem, P. Jakes, R.-A. Eichel, L. Pitta-Bauermann and J. Bill, *Chem. Mater.*, 2010, **22**, 2203.
18 J. J. Schneider, R. C. Hoffmann, J. Engstler, O. Soffke, W. Jaegermann, A. Issanin and A. Klyszcz, *Adv. Mater.*, 2008, **20**, 3383.
19 R. C. Hoffmann, M. Kaloumenos, S. Heinschke, E. Erdem, P. Jakes, R.-A. Eichel and J. J. Schneider, *J. Mater. Chem. C*, 2013, **1**, 2577.
20 R. C. Hoffmann, S. Dilfer and J. J. Schneider, *Phys. Status Solidi A*, 2011, **208**, 2920.
21 J. J. Schneider, R. C. Hoffmann, J. Engstler, S. Dilfer, A. Klyszcz, E. Erdem, P. Jakes and R. A. Eichel, *J. Mater. Chem.*, 2009, **19**, 1449.
22 J. J. Schneider, R. C. Hoffmann, A. Issanin and S. Dilfer, *Mater. Sci. Eng., B*, 2011, **176**, 965.
23 L. Luo, L. Hafliger, D. Xie and M. Niederberger, *J. Sol-Gel Sci. Technol.*, 2013, **65**, 28.
24 C. Gabriel, S. Gabriel, E. H. Grant, E. H. Grant, B. S. J. Halstead and D. M. P. Mingos, *Chem. Soc. Rev.*, 1998, **27**, 213.
25 D. Beena, K. J. Lethy, R. Vinodkumar, A. P. Detty, V. P. Mahadevan Pillai and V. Ganesan, *J. Alloys Compd.*, 2010, **489**, 215.
26 W. S. Seo, H. H. Jo, K. Lee and J. T. Park, *Adv. Mater.*, 2003, **15**, 795.
27 I. Hamberg and C. G. Granqvist, *J. Appl. Phys.*, 1986, **60**, R123.
28 H. Zhou, W. Cai and L. Zhang, *Appl. Phys. Lett.*, 1999, **75**, 495.
29 S. Jeong, Y. G. Ha, J. Moon, A. Facchetti and T. J. Marks, *Adv. Mater.*, 2010, **22**, 1346.
30 S. Major, S. Kumar, M. Bhatnagar and K. L. Chopra, *Appl. Phys. Lett.*, 1986, **49**, 394.
31 M. Bowker and R. J. Madix, *Surf. Sci.*, 1982, **116**, 549.
32 S. Bubel, N. Mechau, H. Hahn and R. Schmechel, *J. Appl. Phys.*, 2010, **108**, 124502.
33 T. V. Richter, F. Stelzl, J. Schulz-Gericke, B. Kerscher, U. Wurfel, M. Niggemann and S. Ludwigs, *J. Mater. Chem.*, 2010, **20**, 874.
34 D. E. Walker, M. Major, M. B. Yazdi, A. Klyszcz, M. Haeming, K. Bonrad, C. Melzer, W. Donner and H. von Seggern, *ACS Appl. Mater. Interfaces*, 2012, **4**, 6834.
35 D. H. Lee, Y. J. Chang, G. S. Herman and C. H. Chang, *Adv. Mater.*, 2007, **19**, 843.
36 M. G. Kim, M. G. Kanatzidis, A. Facchetti and T. J. Marks, *Nat. Mater.*, 2011, **10**, 382.
37 E. Fortunato, P. Barquinha, G. Gonçalves, L. Pereira and R. Martins, *Solid-State Electron.*, 2008, **52**, 443.
38 S. H. Lee, B. Bierig and D. C. Paine, *Thin Solid Films*, 2012, **520**, 3764.
39 H. Xu, L. Lan, M. Xu, J. Zou, L. Wang, D. Wang and J. Peng, *Appl. Phys. Lett.*, 2011, **99**, 253501.

6.2 Toward an Understanding of Thin-Film Transistor Performance in Solution-Processed Amorphous Zinc Tin Oxide (ZTO) Thin Films

Zinc tin oxide (ZTO), among others, has emerged as a promising candidate for indium-free amorphous oxide semiconductors, enabling competitive device performance in comparison with its indium-based counterparts. Although a wide variety of zinc salts (acetates, nitrates, and chlorides) have been investigated as possible precursors for zinc in ZTO, analogous alternatives to the starting tin precursor have largely been restricted to tin(II) chlorid. Hence, the requirement of a higher thermal decomposition temperature as well as an increased degree of porosity, due to the evolution of acidic byproducts like HCl vapors during the calcinations of the precursor thin films as well as residual Cl^- ion traces present within the final ceramic cannot be avoided and impede the TFT performance. In this publication, we report on the use of a new tin (II) precursor complex, which along with the previously established zinc precursor, both containing methoxyiminopropionic acid-based ligands, allows the formation of a functional ZTO semiconductor with good performance upon incorporation in TFT devices. Combining the zinc and tin (II) precursors allows a homogeneous start of the thermal decay in a narrow window between 125 and 150 °C due to the very similar thermal decomposition behavior as verified by TGA analysis. Additionally, XRD analysis shows that the decomposition the tin(II) precursor alone, at temperatures as low as 350°C already exhibit a crystalline while the typical tin(II) chloride only crystallizes at much higher temperatures ≥ 450°C establishing the potential of the tailored precursors. XPS analysis comfirms the absense of SnO formation in the ZTO material and the tin oxide in the amorphous matrix is in the SnO_2 chaemical state. Additionally, no significant residual hydrocarbon contamination in the final ZTO ceramic. Uniform distribution of the Zn, Sn(IV) and O species across the surface as well as depth was confirmed via Auger electron spectroscopy. Further comparative defect analysis via EPR analysis of the ZnO and the SnO_2 derived from these precursors was performed. According to the core–shell model, the EPR defect states with resonance at $g_{iso} = 2.0040$ for SnO_2 and $g_{iso} = 2.0032$ for the ZTO, attributed to surface defect spin states. Such defects with with a g-factor of 2 indiucated that the majority of the contributions are from the surface defects and not bulk defect sites, with a higher defect concentration observed for the SnO_2 compared to the ZnO. Hence, the precursor chemical composition of a Sn:Zn ratio of 7:3 delivered the optimum performance of the of the ZTO TFTs with a μ_{sat} of 5.18 $cm^2/V.s$, V_{th} of 7.5 and a high $I_{on/off}$ of 6 x 10^8 when annealed at 350°C

ACS APPLIED MATERIALS & INTERFACES

Research Article

www.acsami.org

Toward an Understanding of Thin-Film Transistor Performance in Solution-Processed Amorphous Zinc Tin Oxide (ZTO) Thin Films

Shawn Sanctis,[†] Nico Koslowski,[†] Rudolf Hoffmann,[†] Conrad Guhl,[‡] Emre Erdem,[§] Stefan Weber,[§] and Jörg J. Schneider*[,†]

[†]Fachbereich Chemie, Eduard-Zintl-Institut, Fachgebiet Anorganische Chemie, Technische Universität Darmstadt, Alarich-Weiss-Straße 12, 64287 Darmstadt, Germany

[‡]Fachgebiet Surface Science, Technische Universität Darmstadt, Jovanka-Bontschits-Straße 2, 64287 Darmstadt, Germany

[§]Institute of Physical Chemistry, Universität Freiburg, Albert Straße 21, 79104 Freiburg, Germany

Supporting Information

ABSTRACT: Amorphous zinc tin oxide (ZTO) thin films are accessible by a molecular precursor approach using mononuclear zinc(II) and tin(II) compounds with methoxyiminopropionic acid ligands. Solution processing of two precursor solutions containing a mixture of zinc and tin(II)−methoxyiminopropinato complexes results in the formation of smooth homogeneous thin films, which upon calcination are converted into the desired semiconducting amorphous ZTO thin films. ZTO films integrated within a field-effect transistor (FET) device exhibit an active semiconducting behavior in the temperature range between 250 and 400 °C, giving an increased performance, with mobility values between μ = 0.03 and 5.5 cm^2/V s, with on/off ratios increasing from 10^5 to 10^8 when going from 250 to 400 °C. Herein, our main emphasis, however, was on an improved understanding of the material transformation pathway from weak to high performance of the semiconductor in a solution-processed FET as a function of the processing temperature. We have correlated this with the chemical composition and defects states within the microstructure of the obtained ZTO thin film via photoelectron spectroscopy (X-ray photoelectron spectroscopy, ultraviolet photoelectron spectroscopy), Auger electron spectroscopy, electron paramagnetic resonance spectroscopy, atomic force microscopy, and photoluminescence investigations. The critical factor observed for the improved performance within this ZTO material could be attributed to a higher tin concentration, wherein the contributions of point defects arising from the tin oxide within the final amorphous ZTO material play the dominant role in governing the transistor performance.

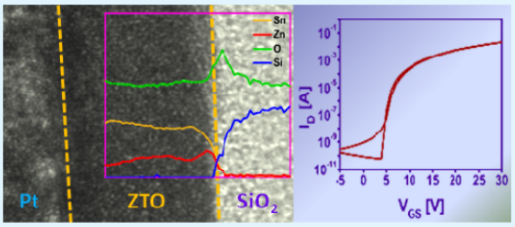

KEYWORDS: *solution process, metal oxide, zinc tin oxide, thin-film transistors, EPR, field-effect transistor, semiconductor*

1. INTRODUCTION

Transparent amorphous metal oxide-based thin-film transistors (TFTs) have received significant attention since their inception by Hosono et al.[1,2] Although oxides, namely, indium zinc oxide (IZO) and indium gallium zinc oxide, have been the preferred compositional choice of the semiconductor, indium-free alternatives have also received significant attention due the estimated scarcity of naturally available indium resources.[3,4] Zinc tin oxide (ZTO), among others, has emerged as a promising candidate for indium-free semiconductors, enabling competitive device performance in comparison with its indium-based counterparts.[5−7]

In a more general manner, solution processing of such amorphous oxide semiconductors paves the pathway for future lower-cost applications, still exhibiting performances greater than those of conventional silicon in terms of their crucial performance parameters, such as charge-carrier mobility and current on−off ratio.[8−11] Although a wide variety of zinc salts (acetates, nitrates, and chlorides) have been investigated as possible precursors for zinc in ZTO, with regard to the effect on the final field-effect transistor (FET) performance, analogous alternatives to the starting tin precursor have largely been restricted to tin(II) chloride.[4,12] Although FETs based on the aforementioned precursor have shown good applicability, they seem to suffer from the requirement of a higher thermal decomposition temperature as well as an increased degree of porosity, due to the evolution of acidic byproducts like HCl vapors during the calcinations of the precursor thin films as well as residual Cl^- ion traces present within the final ceramic.[13−16] Such undesired effects can have a significant impact on the overall performance of the final device. Recent strategies via a redox chloride elimination reaction have been successfully demonstrated, which enabled high device performance based on solution-processed amorphous ZTO-based devices.[17]

Received: May 3, 2017
Accepted: June 2, 2017
Published: June 2, 2017

DOI: 10.1021/acsami.7b06203
ACS Appl. Mater. Interfaces 2017, 9, 21328−21337

In recent works, we have demonstrated the use of molecular precursors, especially coordination compounds containing specifically tailored ligands, that are prone to controlled decomposition and release of products of this process. The use of these compounds also enables application of a precursor−solvent system, which allows solution processing of the resulting metal oxide thin films, without the use of any additives or stabilizers, which could have an ambiguous impact on the formation of the resulting films.[18−20] Herein, we report on the use of a new tin (II) precursor complex, which along with the previously established zinc precursor, both containing methoxyiminopropionic acid-based ligands, allows the formation of a functional ZTO semiconductor with decent-to-very good performance in FET devices.[21] The functional properties of the obtained FETs have been optimized with respect to temperature and their resulting performance could be correlated with the degree of oxidation and formation of defects within the final functional ZTO thin film-based FETs.

2. EXPERIMENTAL SECTION

2.1. Precursor Synthesis. Bis(methoxyiminopropanoato)tin(II) (**1**): The reaction was carried out under inert gas conditions and with dried solvents. Anhydrous tin(II) chloride (1.89 g; 10 mmol) was dissolved in tetrahydrofuran (THF, 100 mL) at room temperature. Thereafter, ammonium 2-(methoxyimino)propionate (2.70 g, 20 mmol), which was obtained from the reaction of methoxyiminopropionic acid and ammonium hydrogen carbonate,[22] was added to this solution. Subsequently, the suspension was heated to 65 °C and stirred for 18 h. The reaction mixture was filtered, and the solvent, removed under vacuum. Evaporation of the solvent yielded a pale white solid product, which was dissolved in dichloromethane (35 mL), filtered, and precipitated again with methyl *tert*-butylether (210 mL). The air-stable final product (2.49 g, 71.05 % of the theoretical yield) crystallized in the form of thin fibrous needles after heating in THF to 60 °C followed by cooling in a refrigerator to 4 °C. Ceramic yield (CY) and elemental analysis (CHN): found CY 42.3 %, C 26.90 %, H 3.96 %, N 9.78 %. Calcd for $Sn(C_4H_6O_3N)_2$: CY 42.9 %, C 27.38 %, H 3.44 %, N 7.98 %. ^{1}H NMR (500 MHz, chloroform-d_1, 25 °C): δ = 4.02 (−OCH_3); 2.00 (−N=C−CH_3) ppm. $^{13}C\{^1H\}$ NMR (500 MHz, chloroform-d_1, 25 °C): δ = 168.46 (−COO); 152.35 (−N=C−); 62.70 (−O−CH_3); 11.48 (−N=C−CH_3) ppm. Electron ionization mass spectrometry *m*/*z* 31 (36%), 40 (54%), 41 (99%), 44 (100%), 72 (39%), 117 (17%) 151 (15%), 190 (8%), 236 (20%), 253 (M^+).

Bis(methoxyiminopropanoato)zinc(II) (**2**): Solid diaqua-bis-(methoxyiminopropanoato)zinc(II)[23] was heated at 75 °C under vacuum (10^{-3} Torr) for 3 h to obtain **2**. No color change was observed.

2.2. FET Characterization. FET substrates were obtained from Fraunhofer IMPS, Dresden. The substrates (15 × 15 mm^2) consist of highly n-doped silicon with a 90 nm silicon oxide dielectric layer. The source−drain electrodes, with channel length L = 20 μm and channel width W = 10 mm (W/L = 500), were fabricated with a 40 nm gold interdigital structure and a 10 nm intermediate adhesion layer of indium tin oxide. Quartz substrates (15 × 15 mm^2) were used for the deposition of the precursor films, which were carefully scratched off; the obtained powders were used for X-ray diffraction (XRD) investigations. All substrates were sequentially cleaned with acetone, water, and 2-propanol for 10 min, respectively. The cleaned substrates were exposed for 2 min to oxygen plasma prior to spin coating to improve adhesion of the spin-coating solutions.

For the preparation of the spin-coating solutions, stock solutions of tin(II) and the zinc precursor were prepared by dissolving 1 wt % of the respective precursors in 2-propanol. After complete dissolution, a clear solution was obtained in both cases. The solutions were then filtered through a 0.22 μm PTFE syringe filter and mixed in the desired Sn/Zn ratio for spin coating the ZTO thin films. Optimized precursor ratios of Sn/Zn were achieved by fabricating devices with different ratios. A relatively lower Sn concentration resulted in poor device performance, whereas an extremely high Sn concentration led to a conductive behavior (Figure S7). On the basis of the obtained results, an optimized Sn/Zn molar ratio of 7:3 was used for all ZTO films produced, which was directly used for spin-coating and fabrication of thin films. The spin coating was carried out under ambient conditions. Thin films were produced with a spinning speed of 2500 rpm for 20 s. The final semiconducting tin oxide thin films were obtained from these spin-coated solutions by thermal treatment on a hot plate at different temperatures for 2 h.

2.3. Material Characterization. Transmission electron microscopy (TEM) was carried out using Tecnai F20 (FEI), with an operating voltage of 200 kV. Samples for the TEM investigations were prepared by depositing diluted precursor solutions onto SiO_2-coated gold grids and annealing at desired temperatures. Atomic force microscopy (AFM) measurements were carried out with CP-II (Bruker-Veeco), with silicon cantilevers. Thermogravimetric analysis (TGA) measurements were performed using a TG209F1-Iris (Netzsch) thermal analyzer, employing aluminum crucibles. XRD was performed on a Rigaku Miniflex 600@40 kV 15 mA diffractometer using Cu Kα_1 radiation (λ = 1.541 Å). XPS measurements were carried out in an integrated ultra-high-vacuum system with a base pressure of 1 × 10^{-9} mbar, equipped with a PHI 5000 VersaProbe photoelectron spectrometer. XPS measurements were performed using a monochromatized Al Kα X-ray source. The hemispherical photoelectron analyzer was operated with a constant analyzer energy of 10 eV (pass energy) to obtain the core spectra with an energy resolution of about 0.6 eV. The spectrometer was calibrated to the Fermi edge and core level lines of sputtered copper foils. Valence band measurements were made using ultraviolet photoelectron spectroscopy (UPS), employing an excitation energy of He I (21.2 eV) and a negative bias of 6 V. The work function (WF) was determined by the secondary electron cutoff. The obtained spectra were fitted with Voigt functions and a Shirley background. X-band (9.86 GHz) electron paramagnetic resonance (EPR) measurements were performed with a Bruker EMX spectrometer using a rectangular TE102 (X-band) resonator. The magnetic field was determined using an NMR gaussmeter (ER 035M; Bruker); for magnetic-field calibration, polycrystalline DPPH with g = 2.0036 was used. Photoluminescence (PL) measurements were performed on Si substrates with an excitation wavelength of 250 nm. Auger spectroscopy: PHI 680 (Physical Electronics) scanning Auger nanoprobe operated at an acceleration voltage of 20 keV and a current of 10 nA. Sputtering was carried out under UHV (5 × 10^{-9} Torr), with an argon ion gun operated at 250 eV and 500 nA.

3. RESULTS AND DISCUSSION

Precursor **1**, $Sn(C_4H_6O_3N)_2$, could be synthesized by the metathesis reaction using tin(II) chloride and ammonium methoxyimino propionate in THF (Scheme 1). The reaction has to proceed at an elevated temperature to ensure complete conversion of the educts into the desired product. At room temperature only, mixtures of **1** and ammonium salts were formed, which could not be further purified. In **1**, the oximato ligand acts a chelating ligand with bidendate N,O coordination toward Sn(II), as reported for polynuclear Sn(IV) complexes with cyano-substituted oximates.[24] Coordination of Sn(II) to the carboxylate groups with solely an O,O coordination of the Schiff base ligand, resembling the bonding in tin(II) acetate, would lead to a different coordination environment with inconsistent spectroscopic data.[25] The thermal decomposition of **1** in oxygen as well as in argon was studied (Figure S1a). The residual mass of 42.31 % corresponds to the quantitative formation of tin(IV) oxide SnO_2 in oxygen, with an expected CY of 42.98%. The decomposition pathway of **1** under argon, however, leads to a different decomposition behavior, resulting in metallic tin and tin(IV)oxide as final products, probably via

DOI: 10.1021/acsami.7b06203
ACS Appl. Mater. Interfaces 2017, 9, 21328−21337

Scheme 1. Reaction Scheme for the Synthesis and Thermal Decomposition of 1 to Sn(IV)O_2 in Air

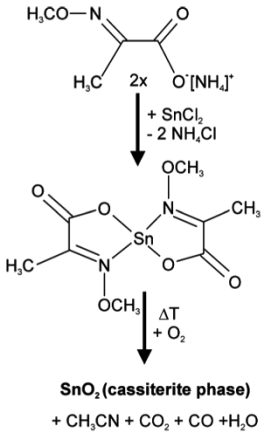

the formation of subvalent Sn(II)O as an intermediate. However, no evidence (see detailed XPS study below) for the formation of metallic tin during decomposition of **1** under oxygen was found, as, for example, reported during the thermal decomposition of tin(II)alkoxides.[26] This qualifies **1** as a clean and versatile new precursor for tin(IV) oxide. The thermal decay under oxygen (Scheme 1) proceeds in a single step at about 125 °C. The gaseous products, as analyzed by means of on-line mass spectrometry, are in agreement with a decomposition process according to a second-order Beckmann reaction (Figure S1b).[23] Thus, acetonitrile (m/z^+ 41) could be observed apart from more unspecific products such as water (m/z^+ 18), carbon dioxide (m/z^+ 44), and carbon monoxide (m/z^+ 28).

The combination of a solution of **1** with the established zinc(II) oximato complex diaqua-bis-(methoxyiminopropanoato)zinc(II),[23] which was successfully used so far for the formation of semiconducting ZnO and amorphous IZO, was found to be disadvantageous in the formation of ZTO using **1** as the molecular tin precursor. This is due to a subsequent hydrolytic cleavage of **1** by the coordinated aquo ligand of the diaqua-bis-(methoxyiminopropanoato)zinc(II) precursor. However, employment of the water-free bis(methoxyiminopropanoato)zinc-(II) compound (**2**) was found to help overcome this problem. Precursor **2** [$Zn(C_4H_6O_3N)_2$] could be obtained from **1** by heating under vacuum[23] (Figure S2 and S3). Combining **1** and **2** allows a homogeneous start of the thermal decay in a narrow window between 125 and 150 °C due to the very similar thermal decomposition behavior (Figure 1). However, a somewhat more sluggish mass loss upon further heating to a higher temperature until the theoretical CY for the zinc precursor **2** compared to that for the tin counterpart **1** is observed.

The products of thermal transformation of **1** as well as of mixtures of **1** and **2** into the oxidic phases were investigated by means of high-resolution TEM (HRTEM) (Figure 2). Therefore, precursor solutions of **1** for SnO_2 and **1** and **2** (ratio 7:3) for ZTO were directly calcined on a TEM grid. In addition, a cross-section of a ZTO film of ∼6 nm, prepared from the precursor solutions on a SiO_2/Si substrate and

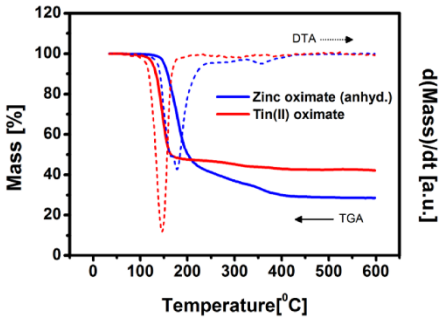

Figure 1. Thermogravimetric mass loss (solid) and differential thermal analysis (dotted) of zinc and tin(II) precursors **1** and **2** under oxygen.

encapsulated with a protective platinum layer, was manufactured using a focused ion beam (FIB). The precursor solutions of **1** and **2** afforded the desired amorphous ZTO phase after calcination, whereas the tin(II) precursor solution containing **1** after deposition and final calcination forms nanocrystalline tin oxide particles.

Moreover film formation at the interface of the SiO_2 layer of the silicon substrate is very smooth and shows no void formation at the dielectric SiO_x interface. XRD analysis of these calcined thin films between 350 and 400 °C, confirmed that tin(IV) oxide, SnO_2 in its tetragonal cassiterite phase (JCPDS No. 77-0450), was obtained. The broadening of the diffraction peaks in the powder diffractogram corroborates the finding of nanoparticulate SnO_2 obtained from the TEM results (Figure S4). Peak broadening could be observed at lower processing temperatures only, potentially indicative of its amorphous nature in those temperature regimes. No other contributions were found in the X-ray diffractograms. Auger electron spectroscopy contributing a surface as well as depth profile was performed for a ZTO thin film annealed at 350 °C to shed light on the distribution of the compositional elements within the final ZTO thin film obtained after spin coating the precursor solution of **1** and **2**, followed by final calcination. A homogeneous distribution of the individual components of Zn, Sn, and O was obtained, confirming the desired chemical composition across the thin film (Figure 3). AFM studies of the SnO_2 and ZTO thin films revealed a homogeneous film surface and substrate coverage, with RMS values well below 1 nm for both (Figure 4). ZTO showed a relatively smoother surface at 350 °C with respect to its 250 °C counterpart, with a reduction in the surface texture, which is often observed for such amorphous ZTO-based thin films as a result of film densification occurring due to more complete metal oxide formation at higher temperatures.[15]

The very similar decomposition behavior of the molecular precursors **1** and **2** inhibits the formation of any phase segregation and thus the avoidance of individual crystalline components of either zinc(II) oxide or tin(IV) oxide in the ternary ZTO film. This fact is highly conducive to the formation of the final amorphous phase within the temperature regime for thin-film processing because individual nanocrystalline zinc or tin(IV) oxide formation within the ZTO amorphous oxide matrix would deteriorate its TFT performance, as has been shown for other multinary oxides.[19,27]

A series of FET devices with a bottom-gate/bottom-contact setup were manufactured on prefabricated substrates (support/

DOI: 10.1021/acsami.7b06203
ACS Appl. Mater. Interfaces 2017, 9, 21328−21337

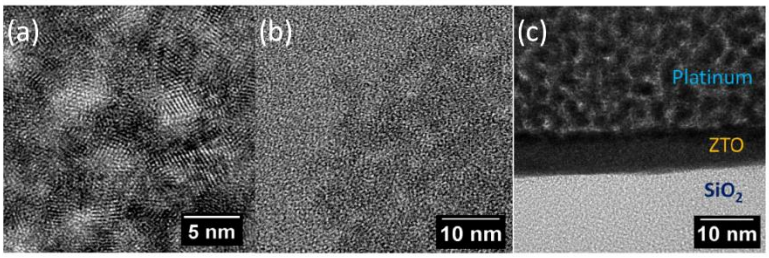

Figure 2. HRTEM images of (a) nanocrystalline SnO_2 and (b) amorphous ZTO, and (c) cross-sectional TEM (FIB) of a ZTO thin film on a Si/SiO_2 substrate. All films were finally calcined at 350 °C.

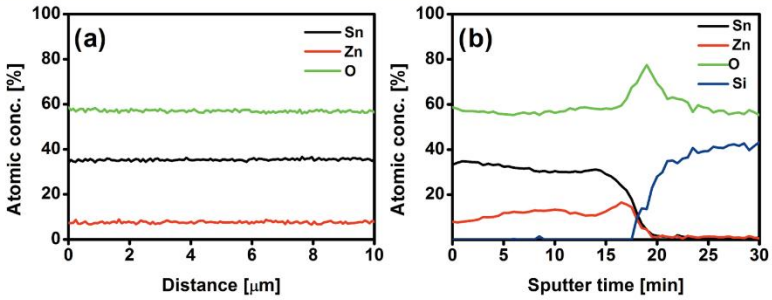

Figure 3. Auger electron spectra of (a) the surface line profile and (b) the depth profile of a ZTO thin film on a silicon substrate annealed at 350 °C.

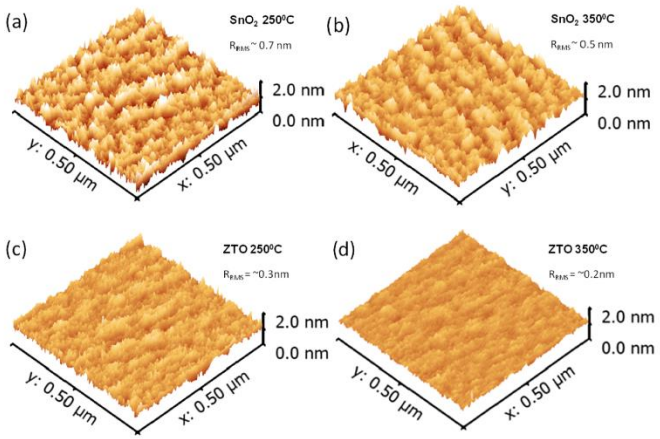

Figure 4. AFM micrographs and root-mean-square roughness (R_{RMS}) for the SnO_2 films annealed at (a) 250 °C and (b) 350 °C and ZTO films annealed at (c) 250 °C and (d) 350 °C, respectively.

gate highly n-doped silicon, dielectric silicon dioxide with interdigital gold electrodes). The ZTO films were obtained by spin coating and annealing on a hot plate at temperatures from 250 to 400 °C in air. A Sn/Zn ratio of 7:3 in the ZTO films was employed for evaluation of the FET performance.

The transfer and output characteristics of an FET device annealed at an optimum temperature of 350 °C as well as the saturation mobility (μ_{sat}), threshold voltage (V_{th}), and current on−off ratio have been determined (Figure 5 and Table 1). Active semiconductor performance was observed at all investigated temperatures (Figure S5).

Devices annealed at 300 °C and higher demonstrate a good FET performance, with charge-carrier mobilities greater than those of conventional amorphous hydrogenated silicon, which is typically ≤ 1 cm^2/V s.[1] Additionally, a systematic decrease in the threshold voltage is observed with an increase in the annealing temperature. A reduction in V_{th} generally arises from the suppression of electron traps at the interface while transitioning from low to high annealing temperatures, thereby increasing the degree of metal oxide formation. This generates the need for higher voltage sweeps to turn on the device at lower temperatures, which is in accordance with previous

DOI: 10.1021/acsami.7b06203
ACS Appl. Mater. Interfaces 2017, 9, 21328−21337

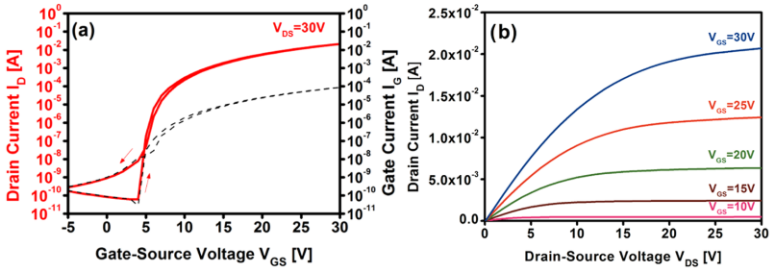

Figure 5. TFT performance characterization of the ZTO films annealed at 350 °C. (a) Transfer characteristics and (b) output characteristics of TFT devices annealed at 350 °C.

Table 1. TFT Performance Parameters for ZTO-Based Devices Annealed at Incremental Temperatures between 250 and 400 °C

temperature (°C)	mobility μ_{sat} ($cm^2/V\ s$)	threshold voltage V_{th} (V)	current on/off ratio $I_{on/off}$
250	0.03	26.3	3.4×10^5
275	0.18	23.5	1.0×10^7
300	1.3	19.6	1.1×10^8
350	5.18	7.5	6.0×10^8
400	5.5	5.5	5.1×10^8

reports.[28] The dependence of the annealing temperatures and corresponding FET performance was studied to establish a suitable temperature regime below the glass-transition temperature (~450 °C) of commercially employed display-glass substrates.

Observation of active FETs at low temperatures between 250 and 300 °C, showing modest transfer characteristics, presents a future window of opportunity to obtain improved performance using further additional postprocessing treatments by calcinations under different atmospheres or using different irradiation techniques. However, within the scope of the current work, high-performance FETs were obtained at a reasonable temperature of 350 °C. These devices exhibit a beneficial reduction in the degree of hysteresis as well as a strong current saturation (Figure 5 and Table 1). Trends based on other key performance parameters of the ZTO-based FET have also been displayed (Figure S6 and Table 2). To obtain a deeper insight into the chemical surface environment of active ZTO thin films, XPS analysis was undertaken for the thin films annealed at different temperatures ranging between 250 and 400 °C. This should allow us to study the stepwise evolution of mixed metal oxide formation starting already from the as-deposited precursor thin film (Figure 6). Core spectra for the Sn components Sn $3d_{3/2}$ at 494.7 eV and $3d_{5/2}$ at 486.3 eV for the 350 °C films hint that Sn exists mostly in the Sn^{4+} state within the ZTO material. However an in-depth study based on Auger spectroscopy and XPS would be required to confirm the same.[29−32] In addition the O1s spectrum helps understand the nature of the different oxide species within the final material and enables an improved qualitative estimation of the electronic situation of the metal oxide.[33,34] The O1s spectra were deconvoluted with two components, arising at about 530 and 532 eV, reflecting contributions from oxidic oxygen as well as OH surface hydroxylation. Although the latter is commonly observed on most metal oxide surfaces, its prominence in comparison with the former can best be attributed either to an incomplete decomposition of the precursor or an incomplete dehydroxylation during the formation of the final ceramic.[33,35]

Table 2. Binding Energy Trends of the Extrapolated WF and the Corresponding Valence Band Edge Maxima for the ZTO Films at Various Annealing Temperatures

annealing temperature (°C)	WF (eV)	valence band maxima (VBM) edge (eV)
250	4.0	3.7
275	4.0	3.6
300	4.0	3.55
350	4.1	3.5
400	4.1	3.45

Additional considerations toward contributions from native point defects arising from oxygen vacancies or interstitial cationic defect sites via peak fitting did not lead to any noteworthy qualitative trends in the investigations.[34,36]

A gradual reduction in a contribution from the M−OH peak and a corresponding increase in the M−O peak were found when employing annealing temperatures between 250 and 300 °C (Figure S7). A comparatively larger change in the ratio from both contributions is observed at 350 and 400 °C (Figure 6d). Interestingly, the nature of the O1s spectra of ZTO is prominently different from those of the IZO thin films previously reported, employing the same ligand environment in the precursors used.[19] For the IZO material, within a similar temperature range, the dominant M−O metal oxide peak is observed, with a prominent M−OH peak shoulder. However, for the ZTO, this contribution, which is related to the hydroxide moiety, is rather minimal and could be observed only upon comparing the contributions from the individual oxide and hydroxide components within the final ZTO ceramic, on the basis of curve fitting of the individual components. A plausible reason for this distinct observation could be the more sluggish and thus only gradual mass loss in TGA after the initial major decomposition step has occurred for the indium precursor, which is less significant than the decomposition process observed for the herein employed tin(II) precursor. This modulation of the comparative changes in the intensity of the two major contributions serves as good insight into the evolution process of the electronic performance of metal oxide semiconductors.[19,34,37] The combined effect of determining oxygen species related to hydroxide moieties as well as the presence of both cationic and oxygen vacancies contributes toward actively changing the WF of the metal oxide semiconductor.[36]

DOI: 10.1021/acsami.7b06203
ACS Appl. Mater. Interfaces 2017, 9, 21328−21337

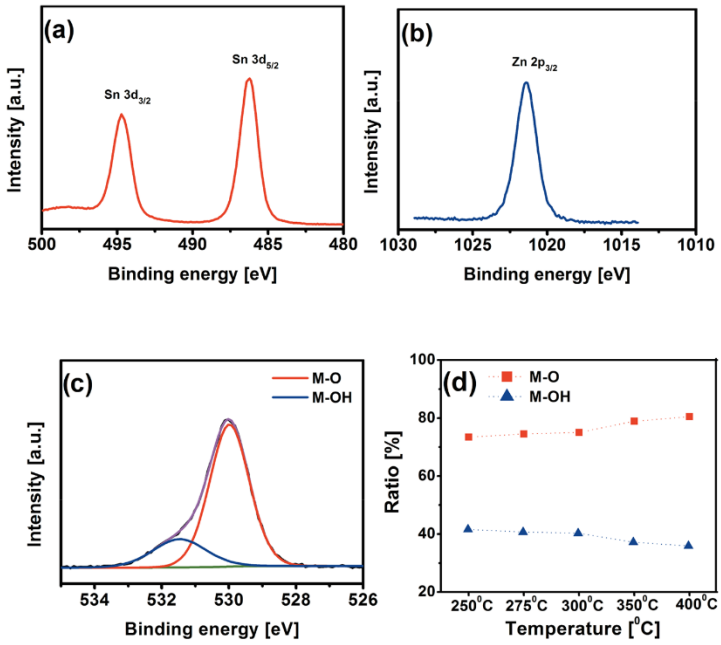

Figure 6. XPS spectra of (a) Sn 3d, (b) Zn 2p, and (c) deconvoluted O1s spectra of the deposited ZTO films annealed at 350 °C; (d) ratio of the M−O to M−OH of the ZTO thin film based on the employed calcination temperatures between 250 and 400 °C.

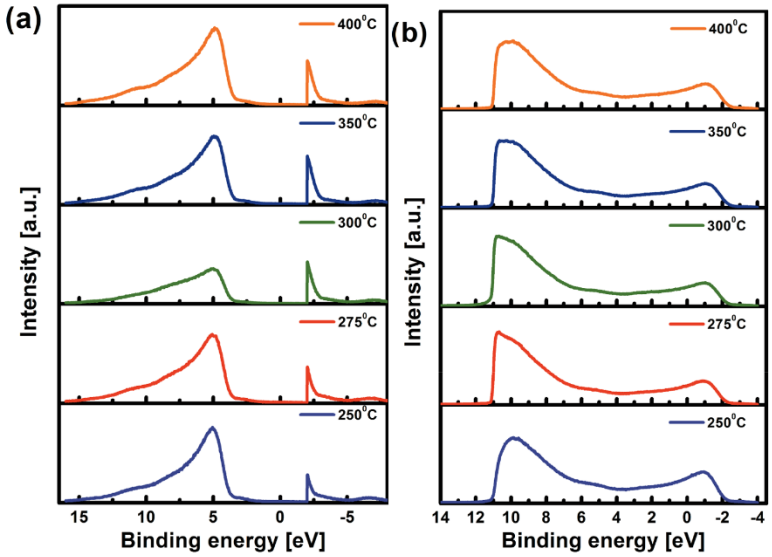

Figure 7. UPS spectra of ZTO thin films annealed at different temperatures. (a) WF and (b) VBM edge trends of ZTO films annealed at 250, 275, 300, 350, and 400 °C.

UPS investigations were performed on the samples also studied via XPS to obtain insight into the evolution of the VBM and the WF of the ZTO films processed in the aforementioned temperature regime (Figure 7). On the basis of the UPS measurements, samples annealed up to 300 °C exhibited a WF of ~4 eV, with a slight increase in the WF for samples annealed at 350 and 400 °C. This is in good accordance with the values reported for multinary amorphous semiconducting oxides.[38,39] The VBM edge decreases gradually with an increase in the annealing temperature, with VBM values ranging from 3.7 to

DOI: 10.1021/acsami.7b06203
ACS Appl. Mater. Interfaces 2017, 9, 21328−21337

3.45 eV for samples processed at 250−400 °C, which is a good indication of successful conversion of the precursors into ZTO, which is well reflected in device performances obtained under annealing at the different temperatures studied. The VBM feature is conventionally attributed to the completely occupied 2p orbital of oxygen from the metal oxide. When analyzed together with the corresponding XPS spectra, a larger magnitude of the M−O contribution with incremental annealing temperatures has been reported to lower the VBM, resulting in a gradual decrease to lower binding energies.[1,39,40]

An increase in point defects, such as oxygen vacancies, was proposed as the most likely cause of this effect, as this would lead to an increased intrinsic charge carrier concentration, provided no additional effects should be considered.[38] This can also be correlated with the observed TFT performance, as an increased "on" current (I_{on}) and a slight reduction in the "off" current (I_{off}) was observed for TFTs processed at 350 and 400 °C, which exhibit a slightly higher WF of ∼4.1 eV for both and a VBM of 3.5 and 3.45 eV, respectively. Employment of a third metal oxide or annealing performed under a dedicated oxygen-rich environment have led to improved device performance by countering the formation of undesired oxygen vacancy-related defects.[41−44]

The EPR spectra for nanocrystalline SnO_2 and ZTO powders annealed at 250 and 350 °C, respectively, give some insight into the defect situation in both materials (Figure 8). At first, the

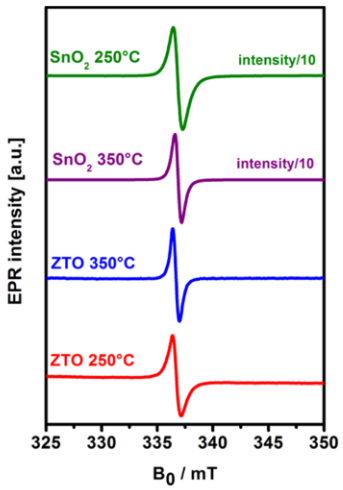

Figure 8. Room temperature X-band EPR spectra at a 325−350 mT field range for SnO_2 and ZTO, both annealed at 250 and 350 °C, respectively.

pure nanocrystalline SnO_2 powders revealed a 10 times higher intensity of the observed EPR signal than that of the amorphous ZTO powders. The EPR spectra for all samples prepared under different processing temperatures reveal an isotropic *g*-factor of 2.0040 for SnO_2 and 2.0032 for the ZTO samples. Slight changes in the *g*-factor of the nanocrystalline SnO_2 in comparison to that of the ZTO-based material might reflect differences in the spin−orbit coupling mechanism, whereas paramagnetically active electron spins arising from defects not only show interactions between different magnetic nuclei[45] (e.g., Sn and Zn) but also display a chemically different local environment. These affect the spin−orbit interactions.[46] Therefore, in the case of pure SnO_2 and mixing of Sn and Zn as in ZTO, a different environment for the defects, in particular on the surface of the materials, is established. The origin of the EPR signal can be assigned to the oxygen vacancy situation on the surface of the two materials. Thus, a different localization of oxygen vacancies changes the *g*-factor as well. This has already been shown previously for ZnO nanoparticles using a core−shell model, with active spin states in the bulk and on the surface of nanocrystalline ZnO particles.[23,47,48] Recently, as a proven structural model, this core−shell model for ZnO nanoparticles was developed to offer a reasonable explanation for the size effects in ZnO nanoparticles and to show that a surface shell with different types and numbers of defect sites surrounds an inner core with additional oxygen defect sites.[23,47−49] The model is also important for estimating the width of the space-charge depletion layer. According to the core−shell model, the EPR defect states with resonance at g_{iso} = 2.0040 for SnO_2 and g_{iso} = 2.0032 for the ZTO sample can be attributed to surface defect spin states. On the other hand, EPR results revealed the importance of the annealing temperature for obtaining contamination-free ZTO samples. The large sweep EPR signal (Figure S9) shows that the ZTO sample annealed at a lower temperature has a broad Gaussian line envelope, which is typical for purely carbon-related organic residuals.[50] This observation is in agreement with the lower FET performance of this particular sample, which shows this carbonaceous contamination, compared to that of the ones calcined at higher temperatures. In contrast, a similar observation of residual carbonaceous species, however, is almost negligible for nanocrystalline SnO_2 in comparison with amorphous ZTO at a lower processing temperature of 250 °C. This indicates that the contribution from the residual carbon arises most obviously from an incomplete calcination of the Zn(II) oximato precursor. This assumption is in accord with the observation from the TGA studies of the Zn(II) precursor compared with the Sn(II) precursor. The paramagnetic nature of such defect-induced carbon centers has been assigned mainly to dangling σ-bonds with an unpaired σ spin density.[51] Both samples at 350 °C exhibit a sharper and isotropic EPR line compared to that of the sample processed at 250 °C, indicating SnO_2 and ZTO materials with more uniformly distributed defect centers at higher temperatures.[52] Moreover, it was also observed that SnO_2 at 250 °C had a higher defect concentration, which was reduced at 350 °C due to thermal passivation of these defects.[53] This would indicate that defect centers, namely, oxygen vacancies of the SnO_2 sample at 350 °C, are localized in a more symmetric environment. Unlike our previous work on the In_2O_3/ZnO system,[54] herein only defects with a *g*-factor of 2 were observed, indicating only contributions from the surface defects and no bulk defect sites. Additionally, on the basis of our earlier EPR investigations, defects based mainly on nanoscaled ZnO were not observed in the current ZTO material system.[23] This is indicative of oxygen defects arising from the highly defective SnO_2 within the ZTO material, whereby their EPR intensity is, however, suppressed to some extent upon incorporation of a suitable amount of ZnO compared to the occurrence of the oxygen defects in the pure SnO_2 nanomaterial.

In addition to EPR spectroscopy, PL studies were performed on nanocrystalline SnO_2 and amorphous ZTO thin films calcined at 250 and 350 °C to obtain further insight into the

DOI: 10.1021/acsami.7b06203
ACS Appl. Mater. Interfaces 2017, 9, 21328−21337

contribution of optically active defects (Figure S10). The SnO_2 films calcined at the aforementioned temperatures displayed two contributions located in the UV (~340 nm) and visible (~640 nm) regions. The peak originating in the UV region of the material processed at 250 °C has been associated with quantum confinement of nanoscaled SnO_2 particles (~2−5 nm) and is absent in bulk SnO_2.[55] This observation is in good agreement with PL investigations on nanoscaled SnO_2 wires studied at a similar excitation wavelength (244 nm).[56] The contribution in the visible region can be attributed to a radiative recombination of electrons trapped at oxygen vacancy-related states of nanoscale SnO_2.[57] Interestingly, for the ZTO samples similar PL active defect contributions were observed beginning only at a processing temperature of 350 °C but not lower. This observation is in line with fact that the EPR spectra for ZTO at 250 °C show the presence of organic residues in the film, which are eliminated at a higher temperature of 350 °C. A plausible explanation for this comes from the altered decomposition process (slightly higher temperature and heating protocol, see TGA study) needed for the zinc(II) oximato precursor compared to the Sn(II) oximato precursor to undergo complete decomposition.

4. CONCLUSIONS

A new Sn(II) precursor for SnO_2 and ZTO was synthesized employing a methoxyiminopropionic acid-based ligand. In combination with the chemically analogous Zn precursor, a successful strategy to generate semiconducting ternary ZTO films and thereby functional FET devices based on amorphous ZTO thin films at reasonable temperatures between 250 and 400 °C was demonstrated. At an optimized annealing temperature of 350 °C, a high device mobility (μ_{sat}) of 5.1 cm^2/V s and a current on/off of 10^8 were obtained. The material performance derived from the employed ZTO precursor solution calcined at different temperatures was investigated with respect to its microstructure and native point defects within the final amorphous ZTO. In the present study, a clear dependency of the FET performance could be established, which is correlated with the degree of oxidation for the ZTO thin films, as determined by XPS and the dominant oxygen vacancy defect contribution, as studied by EPR and PL. These observations elucidate the prominent contributions from the defect-induced SnO_2, which play a crucial role in tuning the performance of FETs based on indium-free, semiconducting ZTO thin films. In conclusion, these investigations could provide improved insight into the semiconductor performance, on the basis of the resulting defects generated from individual precursors employed for solution processing of such multinary amorphous oxide semiconductors.

■ ASSOCIATED CONTENT

Supporting Information

The Supporting Information is available free of charge on the ACS Publications website at DOI: 10.1021/acsami.7b06203.

Precursor studies based on TGA and IR spectroscopy, XRD of the derived SnO_2, ZTO transistor performance between 250 and 400 °C and the corresponding XPS spectra, PL spectra of SnO_2 and ZTO thin films (PDF)

■ AUTHOR INFORMATION

Corresponding Author

*E-mail: joerg.schneider@ac.chemie.tu-darmstadt.de.

ORCID

Jörg J. Schneider: 0000-0002-8153-9491

Author Contributions

The manuscript was written through contributions of all authors. All authors have given approval to the final version of the manuscript.

Funding

S.S. and J.J.S. acknowledge financial support through the DFG SPP 1569 program.

Notes

The authors declare no competing financial interest.

■ ACKNOWLEDGMENTS

TEM investigations were performed at ERC Jülich under contract ERC-TUD1. We acknowledge Dr. J. Engstler (TUDa) for performing TEM investigations, Silvio Heinschke (TUDa) for XRD analysis, and Dr. P. Atanasova (University of Stuttgart) for PL measurements. Auger measurements were carried out at Karlsruhe Nano Micro Facility (KNMF proposal number 2016-015-010549). The assistance of Tobias Weingärtner is gratefully acknowledged.

■ REFERENCES

(1) Kamiya, T.; Hosono, H. Material Characteristics and Applications of Transparent Amorphous Oxide Semiconductors. *NPG Asia Mater* **2010**, *2*, 15−22.

(2) Nomura, K.; Ohta, H.; Takagi, A.; Kamiya, T.; Hirano, M.; Hosono, H. Room-Temperature Fabrication of Transparent Flexible Thin-Film Transistors Using Amorphous Oxide Semiconductors. *Nature* **2004**, *432*, 488−492.

(3) Yabuta, H.; Sano, M.; Abe, K.; Aiba, T.; Den, T.; Kumomi, H.; Nomura, K.; Kamiya, T.; Hosono, H. High-Mobility Thin-Film Transistor with Amorphous $InGaZnO_4$ Channel Fabricated by Room Temperature Rf-Magnetron Sputtering. *Appl. Phys. Lett.* **2006**, *89*, No. 112123.

(4) Chang, Y.-J.; Lee, D.-H.; Herman, G.; Chang, C.-H. High-Performance, Spin-Coated Zinc Tin Oxide Thin-Film Transistors. *Electrochem. Solid-State Lett.* **2007**, *10*, H135−H138.

(5) Chiang, H. Q.; Wager, J. F.; Hoffman, R. L.; Jeong, J.; Keszler, D. A. High Mobility Transparent Thin-Film Transistors with Amorphous Zinc Tin Oxide Channel Layer. *Appl. Phys. Lett.* **2005**, *86*, No. 013503.

(6) Liu, L.-C.; Chen, J.-S.; Jeng, J.-S. Role of Oxygen Vacancies on the Bias Illumination Stress Stability of Solution-Processed Zinc Tin Oxide Thin Film Transistors. *Appl. Phys. Lett.* **2014**, *105*, No. 023509.

(7) Tsai, S.-P.; Chang, C.-H.; Hsu, C.-J.; Hu, C.-C.; Tsai, Y.-T.; Chou, C.-H.; Lin, H.-H.; Wu, C.-C. High-Performance Solution-Processed ZnSnO TFTs with Tunable Threshold Voltages. *ECS J. Solid State Sci. Technol.* **2015**, *4*, P176−P180.

(8) Pasquarelli, R. M.; Ginley, D. S.; O'Hayre, R. Solution Processing of Transparent Conductors: From Flask to Film. *Chem. Soc. Rev.* **2011**, *40*, 5406−5441.

(9) Jeong, S.; Jeong, Y.; Moon, J. Solution-Processed Zinc Tin Oxide Semiconductor for Thin-Film Transistors. *J. Phys. Chem. C* **2008**, *112*, 11082−11085.

(10) Lee, C.-G.; Dodabalapur, A. Solution-Processed Zinc−Tin Oxide Thin-Film Transistors with Low Interfacial Trap Density and Improved Performance. *Appl. Phys. Lett.* **2010**, *96*, No. 243501.

(11) Seo, S.-J.; Choi, C. G.; Hwang, Y. H.; Bae, B.-S. High Performance Solution-Processed Amorphous Zinc Tin Oxide Thin Film Transistor. *J. Phys. D: Appl. Phys.* **2008**, *42*, No. 035106.

(12) Chandra, R. D.; Rao, M.; Zhang, K.; Prabhakar, R. R.; Shi, C.; Zhang, J.; Mhaisalkar, S. G.; Mathews, N. Tuning Electrical Properties in Amorphous Zinc Tin Oxide Thin Films for Solution Processed Electronics. *ACS Appl. Mater. Interfaces* **2014**, *6*, 773−777.

(13) Lee, D.-H.; Chang, Y.-J.; Stickle, W.; Chang, C.-H. Functional Porous Tin Oxide Thin Films Fabricated by Inkjet Printing Process. *Electrochem. Solid-State Lett.* **2007**, *10*, K51−K54.
(14) Zhao, Y.; Dong, G.; Duan, L.; Qiao, J.; Zhang, D.; Wang, L.; Qiu, Y. Impacts of Sn Precursors on Solution-Processed Amorphous Zinc−Tin Oxide Films and Their Transistors. *RSC Adv.* **2012**, *2*, 5307−5313.
(15) Kim, Y. J.; Yang, B. S.; Oh, S.; Han, S. J.; Lee, H. W.; Heo, J.; Jeong, J. K.; Kim, H. J. Photobias Instability of High Performance Solution Processed Amorphous Zinc Tin Oxide Transistors. *ACS Appl. Mater. Interfaces* **2013**, *5*, 3255−3261.
(16) Sykora, B.; Wang, D.; Seggern, H. v. Multiple Ink-Jet Printed Zinc Tin Oxide Layers with Improved Tft Performance. *Appl. Phys. Lett.* **2016**, *109*, No. 033501.
(17) Liu, A.; Guo, Z.; Liu, G.; Zhu, C.; Zhu, H.; Shin, B.; Fortunato, E.; Martins, R.; Shan, F. Redox Chloride Elimination Reaction: Facile Solution Route for Indium-Free, Low-Voltage, and High-Performance Transistors. *Adv. Electron. Mater.* **2017**, *3*, No. 1600513.
(18) Sanctis, S.; Hoffmann, R. C.; Precht, R.; Anwand, W.; Schneider, J. J. Understanding the Temperature-Dependent Evolution of Solution Processed Metal Oxide Transistor Characteristics Based on Molecular Precursor Derived Amorphous Indium Zinc Oxide. *J. Mater. Chem. C* **2016**, *4*, 10935−10944.
(19) Hoffmann, R. C.; Kaloumenos, M.; Heinschke, S.; Erdem, E.; Jakes, P.; Eichel, R.-A.; Schneider, J. J. Molecular Precursor Derived and Solution Processed Indium−Zinc Oxide as a Semiconductor in a Field-Effect Transistor Device. Towards an Improved Understanding of Semiconductor Film Composition. *J. Mater. Chem. C* **2013**, *1*, 2577−2584.
(20) Adl, A. H.; Kar, P.; Farsinezhad, S.; Sharma, H.; Shankar, K. Effect of Sol Stabilizer on the Structure and Electronic Properties of Solution-Processed ZnO Thin Films. *RSC Adv.* **2015**, *5*, 87007−87018.
(21) Schneider, J. J.; Hoffmann, R. C.; Engstler, J.; Soffke, O.; Jaegermann, W.; Issanin, A.; Klyszcz, A. A Printed and Flexible Field-Effect Transistor Device with Nanoscale Zinc Oxide as Active Semiconductor Material. *Adv. Mater.* **2008**, *20*, 3383−3387.
(22) Schneider, J. J.; Hoffmann, R. C.; Issanin, A.; Dilfer, S. Zirconia and Hafnia Films from Single Source Molecular Precursor Compounds: Synthesis, Characterization and Insulating Properties of Potential High K-Dielectrics. *Mater. Sci. Eng., B* **2011**, *176*, 965−971.
(23) Schneider, J. J.; Hoffmann, R. C.; Engstler, J.; Dilfer, S.; Klyszcz, A.; Erdem, E.; Jakes, P.; Eichel, R. A. Zinc Oxide Derived from Single Source Precursor Chemistry under Chimie Douce Conditions: Formation Pathway, Defect Chemistry and Possible Applications in Thin Film Printing. *J. Mater. Chem.* **2009**, *19*, 1449−1457.
(24) Gerasimchuk, N.; Maher, T.; Durham, P.; Domasevitch, K. V.; Wilking, J.; Mokhir, A. Tin(IV) Cyanoximates: Synthesis, Characterization, and Cytotoxicity. *Inorg. Chem.* **2007**, *46*, 7268−7284.
(25) Stafeeva, V. S.; Mitiaev, A. S.; Abakumov, A. M.; Tsirlin, A. A.; Makarevich, A. M.; Antipov, E. V. Crystal Structure and Chemical Bonding in Tin(II) Acetate. *Polyhedron* **2007**, *26*, 5365−5369.
(26) Molloy, K. C. Precursors for the Formation of Tin(IV) Oxide and Related Materials. *J. Chem. Res.* **2008**, *2008*, 549−554.
(27) Fortunato, E.; Pimentel, A.; Gonçalves, A.; Marques, A.; Martins, R. High Mobility Amorphous/Nanocrystalline Indium Zinc Oxide Deposited at Room Temperature. *Thin Solid Films* **2006**, *502*, 104−107.
(28) Chen, H.; Rim, Y. S.; Jiang, C.; Yang, Y. Low-Impurity High-Performance Solution-Processed Metal Oxide Semiconductors Via a Facile Redox Reaction. *Chem. Mater.* **2015**, *27*, 4713−4718.
(29) Gaggiotti, G.; Galdikas, A.; Kačiulis, S.; Mattogno, G.; Šetkus, A. Surface Chemistry of Tin Oxide Based Gas Sensors. *J. Appl. Phys.* **1994**, *76*, 4467−4471.
(30) Liu, L.; An, M.; Yang, P.; Zhang, J. Superior Cycle Performance and High Reversible Capacity of SnO_2/Graphene Composite as an Anode Material for Lithium-Ion Batteries. *Sci. Rep.* **2015**, *5*, No. 9055.
(31) Wang, J.-J.; Lv, A.-F.; Wang, Y.-Q.; Cui, B.; Yan, H.-J.; Hu, J.-S.; Hu, W.-P.; Guo, Y.-G.; Wan, L.-J. Integrated Prototype Nanodevices Via SnO_2 Nanoparticles Decorated SnSe Nanosheets. *Sci. Rep.* **2013**, *3*, No. 2613.
(32) Kövér, L.; Kovács, Z.; Sanjinés, R.; Moretti, G.; Cserny, L.; Margaritondo, G.; Pálinkás, J.; Adachi, H. Electronic Structure of Tin Oxides: High-Resolution Study of XPS and Auger Spectra. *Surf. Interface Anal.* **1995**, *23*, 461−466.
(33) Abedi, N.; Heimel, G. Correlating Core-Level Shifts and Structure of Zinc-Oxide Surfaces. *Phys. Status Solidi B* **2015**, *252*, 755−764.
(34) Banger, K. K.; Yamashita, Y.; Mori, K.; Peterson, R. L.; Leedham, T.; Rickard, J.; Sirringhaus, H. Low-Temperature, High-Performance Solution-Processed Metal Oxide Thin-Film Transistors Formed by a 'Sol−Gel on Chip' Process. *Nat. Mater.* **2011**, *10*, 45−50.
(35) Kelly, L. L.; Racke, D. A.; Schulz, P.; Li, H.; Winget, P.; Kim, H.; Ndione, P.; Sigdel, A. K.; Bredas, J. L.; Berry, J. J.; Graham, S.; Monti, O. L. A. Spectroscopy and Control of near-Surface Defects in Conductive Thin Film ZnO. *J. Phys.: Condens. Matter* **2016**, *28*, No. 094007.
(36) Li, H.; Schirra, L. K.; Shim, J.; Cheun, H.; Kippelen, B.; Monti, O. L. A.; Bredas, J. L. Zinc Oxide as a Model Transparent Conducting Oxide: A Theoretical and Experimental Study of the Impact of Hydroxylation, Vacancies, Interstitials, and Extrinsic Doping on the Electronic Properties of the Polar ZnO (0002) Surface. *Chem. Mater.* **2012**, *24*, 3044−3055.
(37) Sanctis, S.; Hoffmann, R. C.; Schneider, J. J. Microwave Synthesis and Field Effect Transistor Performance of Stable Colloidal Indium-Zinc-Oxide Nanoparticles. *RSC Adv.* **2013**, *3*, 20071−20076.
(38) Kang, D.; Lim, H.; Kim, C.; Song, I.; Park, J.; Park, Y.; Chung, J. Amorphous Gallium Indium Zinc Oxide Thin Film Transistors: Sensitive to Oxygen Molecules. *Appl. Phys. Lett.* **2007**, *90*, No. 192101.
(39) Nomura, K.; Kamiya, T.; Yanagi, H.; Ikenaga, E.; Yang, K.; Kobayashi, K.; Hirano, M.; Hosono, H. Subgap States in Transparent Amorphous Oxide Semiconductor, In−Ga−Zn−O, Observed by Bulk Sensitive X-Ray Photoelectron Spectroscopy. *Appl. Phys. Lett.* **2008**, *92*, No. 202117.
(40) Socratous, J.; Banger, K. K.; Vaynzof, Y.; Sadhanala, A.; Brown, A. D.; Sepe, A.; Steiner, U.; Sirringhaus, H. Electronic Structure of Low-Temperature Solution-Processed Amorphous Metal Oxide Semiconductors for Thin-Film Transistor Applications. *Adv. Funct. Mater.* **2015**, *25*, 1873−1885.
(41) Hennek, J. W.; Smith, J.; Yan, A. M.; Kim, M. G.; Zhao, W.; Dravid, V. P.; Facchetti, A.; Marks, T. J. Oxygen "Getter" Effects on Microstructure and Carrier Transport in Low Temperature Combustion-Processed a-Inxzno (X = Ga, Sc, Y, La) Transistors. *J. Am. Chem. Soc.* **2013**, *135*, 10729−10741.
(42) Jeong, S.; Ha, Y.-G.; Moon, J.; Facchetti, A.; Marks, T. J. Role of Gallium Doping in Dramatically Lowering Amorphous-Oxide Processing Temperatures for Solution-Derived Indium Zinc Oxide Thin-Film Transistors. *Adv. Mater.* **2010**, *22*, 1346−1350.
(43) Park, S. Y.; Song, J. H.; Lee, C. K.; Son, B. G.; Lee, C. K.; Kim, H. J.; Choi, R.; Choi, Y. J.; Kim, U. K.; Hwang, C. S.; Kim, H. J.; Jeong, J. K. Improvement in Photo-Bias Stability of High-Mobility Indium Zinc Oxide Thin-Film Transistors by Oxygen High-Pressure Annealing. *IEEE Electron Device Lett.* **2013**, *34*, 894−896.
(44) Rim, Y. S.; Jeong, W. H.; Kim, D. L.; Lim, H. S.; Kim, K. M.; Kim, H. J. Simultaneous Modification of Pyrolysis and Densification for Low-Temperature Solution-Processed Flexible Oxide Thin-Film Transistors. *J. Mater. Chem.* **2012**, *22*, 12491−12497.
(45) Weil, J. A.; Bolton, J. R. *Electron Paramagnetic Resonance Elementary Theory and Practical Applications*, 2nd ed.; John Wiley: New Jersey, 2007.
(46) Pacchioni, G.; Freund, H. Electron Transfer at Oxide Surfaces. The MgO Paradigm: From Defects to Ultrathin Films. *Chem. Rev.* **2013**, *113*, 4035−4072.
(47) Kaftelen, H.; Ocakoglu, K.; Thomann, R.; Tu, S.; Weber, S.; Erdem, E. EPR and Photoluminescence Spectroscopy Studies on the Defect Structure of ZnO Nanocrystals. *Phys. Rev. B* **2012**, *86*, No. 014113.

DOI: 10.1021/acsami.7b06203
ACS Appl. Mater. Interfaces 2017, 9, 21328−21337

(48) Parashar, S. K. S.; Murty, B. S.; Repp, S.; Weber, S.; Erdem, E. Investigation of Intrinsic Defects in Core-Shell Structured ZnO Nanocrystals. *J. Appl. Phys.* **2012**, *111*, No. 113712.
(49) Erdem, E. Microwave Power, Temperature, Atmospheric and Light Dependence of Intrinsic Defects in ZnO Nanoparticles: A Study of Electron Paramagnetic Resonance (EPR) Spectroscopy. *J. Alloys Compd.* **2014**, *605*, 34−44.
(50) Tampieri, F.; Silvestrini, S.; Ricco, R.; Maggini, M.; Barbon, A. A Comparative Electron Paramagnetic Resonance Study of Expanded Graphites and Graphene. *J. Mater. Chem. C* **2014**, *2*, 8105−8112.
(51) Boukhvalov, D. W.; Osipov, V. Y.; Shames, A. I.; Takai, K.; Hayashi, T.; Enoki, T. Charge Transfer and Weak Bonding between Molecular Oxygen and Graphene Zigzag Edges at Low Temperatures. *Carbon* **2016**, *107*, 800−810.
(52) Repp, S.; Weber, S.; Erdem, E. Defect Evolution of Nonstoichiometric ZnO Quantum Dots. *J. Phys. Chem. C* **2016**, *120*, 25124−25130.
(53) Kamble, V. B.; Bhat, S. V.; Umarji, A. M. Investigating Thermal Stability of Structural Defects and Its Effect on D0 Ferromagnetism in Undoped SnO_2. *J. Appl. Phys.* **2013**, *113*, No. 244307.
(54) Hoffmann, R. C.; Kaloumenos, M.; Heinschke, S.; Erdem, E.; Jakes, P.; Eichel, R.-A.; Schneider, J. J. Molecular Precursor Derived and Solution Processed Indium-Zinc Oxide as a Semiconductor in a Field-Effect Transistor Device. Towards an Improved Understanding of Semiconductor Film Composition. *J. Mater. Chem. C* **2013**, *1*, 2577−2584.
(55) Lee, E. J. H.; Ribeiro, C.; Giraldi, T. R.; Longo, E.; Leite, E. R.; Varela, J. A. Photoluminescence in Quantum-Confined SnO_2 Nanocrystals: Evidence of Free Exciton Decay. *Appl. Phys. Lett.* **2004**, *84*, 1745−1747.
(56) Mazeina, L.; Picard, Y. N.; Caldwell, J. D.; Glaser, E. R.; Prokes, S. M. Growth and Photoluminescence Properties of Vertically Aligned SnO_2 Nanowires. *J. Cryst. Growth* **2009**, *311*, 3158−3162.
(57) Shewale, P. S.; Ung Sim, K.; Kim, Y.-b.; Kim, J. H.; Moholkar, A. V.; Uplane, M. D. Structural and Photoluminescence Characterization of SnO_2: F Thin Films Deposited by Advanced Spray Pyrolysis Technique at Low Substrate Temperature. *J. Lumin.* **2013**, *139*, 113−118.

DOI: 10.1021/acsami.7b06203
ACS Appl. Mater. Interfaces 2017, 9, 21328−21337

6.3 Direct photopatterning of solution processed amorphous indium zinc oxide and zinc tin oxide semiconductors- A chimie douce molecular precursor approach to thin film electronic oxides.

Structuring of the semiconducting layers is essential, in order to combine them with other materials according to the requirements of the final TFT architecture which is conventionally realized via photolithography to obtain thin films with feasible dimensions. Photolithographic patterning enables flexible scalability of film dimensions, but is a complex multistep procedure, which must be adjusted to the environment of the fabricated device. Specifically, IZO and more importantly ZTO thin films are difficult to etch after post-processing, due to their high chemical resistance to commonly used etchants. The additional use of a sacrificial polymer resist films and harsh etchants during the fabrication steps can lead to functional deterioration of the final oxide layer, as far as solution-processed oxides are concerned. This, in-turn, reduces overall turnaround time and costs in terms of roll-to-roll manufacturing large-area electronics. Within this publication, we demonstrate for the first time the use of UV-photopatternable, air, visible light and solution-stable molecular precursors of indium, zinc, and tin based on the established methoxyiminopropionato ligands. The characteristic UV absorption of these precursors allows for the direct UV-based photo-patterning and generation of IZO and indium-free ZTO semiconductors, followed by a moderate thermal annealing (350°C). The precursors do not require the addition of any photo-sensitive polymeric additives or precursors which can only be completely removed at temperature ≥ 500°C. IR investigations reveal that once the precursor films have been exposed to UV irradiation, signals assignable to stretching and deformation modes of the C-H bond of the methoxy group are significantly diminished indicating significant precursor decomposition and no generation of any new functional groups (e.g., nitriles or amides) as by-products from precursor decomposition could be detected. Additionally, N-O cleavage of the Schiff base coordination of the oximato ligands toward the metal center occurrs readily under mild UV-exposure (peak λ = 254 nm, 90%,8 watts), whereas the carboxy unit initially bound to the metal stays still intact under UV irradiation. This enables them to adhere to the substrate while the unexposed precursor films can be readily washed away in the parent solvent (2-Methoxyethanol), leaving behing the desired patterns of the oxide semiconductor. The IZO thin film devices obtained at 250 °C even show charge-carrier mobilities (μ_{sat}) and current on–off ratios ($I_{on/off}$) comparable to amorphous silicon. These can be boosted further, however still under fairly low thermal conditioning of T ≤ 350 °C, to values of 7.8 $cm^2/V.s$, V_{th}

of 0.3 and a high $I_{on/off}$ of 3.5 x 10^8 for IZO and 3.6 $cm^2/V.s$, V_{th} of 2.4 and a high $I_{on/off}$ of 5.3 x 10^7 for ZTO TFTs.

FULL PAPER

Metal Oxide Semiconductors

ADVANCED MATERIALS INTERFACES
www.advmatinterfaces.de

Direct Photopatterning of Solution–Processed Amorphous Indium Zinc Oxide and Zinc Tin Oxide Semiconductors—A Chimie Douce Molecular Precursor Approach to Thin Film Electronic Oxides

*Shawn Sanctis, Rudolf C. Hoffmann, Michael Bruns, and Jörg J. Schneider**

Direct photopatterning of indium zinc oxide (IZO) and zinc tin oxide (ZTO) semiconductors is realized using Schiff-base complexes of indium, zinc, and tin(II) with methoxyiminopropionato ligands as precursors. These precursor complexes are stable under visible light, but they interestingly decompose in the UV region, thereby facilitating a site-selective photopatterning and its subsequent conversion to the desired amorphous oxides. Thin film transistors (TFTs) with photopatterned IZO and ZTO layers exhibit high performance after post-annealing at relatively low temperatures between 250 and 350 °C, with charge-carrier mobilities (μ_{sat}) of 7.8 and 3.6 $cm^2 (V s)^{-1}$ for IZO and ZTO, respectively. The mechanism of the photodecomposition of the precursor films is studied by attenuated total reflectance–Infrared spectroscopy. Apart from the electrical characterization, the resultant UV-patterned oxide thin films are characterized by transmission electron microscopy micrographs of focussed ion beam (FIB)-prepared cross sections, atomic force microscopy, as well as Auger depth profiles. X-ray photoelectron spectroscopy investigations elucidate the influence of surface hydroxylation on the TFT performance. The straightforward approach of facile precursor UV-photopatterning demonstrates its potential feasibility as a low-cost method toward integration of such solution–processed oxide films into large-area electronics.

1. Introduction

Transparent amorphous oxide semiconductors (TAOS), namely indium zinc oxide (IZO) and zinc tin oxide (ZTO), have been recognized as candidates for high-performance semiconductors in next-generation display applications. In order to obtain operating devices, however, apart from the mere film deposition, further essential steps have to be mastered for integration in electronic components. Structuring of the semiconducting layers is essential, in order to combine them with other materials according to the requirements of the final device.[1] Structuring of semiconductor thin films has been realized via photolithography to obtain thin films with feasible dimensions. Photolithographic patterning enables flexible scalability of film dimensions, but is a complex multistep procedure, which must be adjusted to the environment of the fabricated device.[2] Specifically, IZO and more importantly ZTO thin films are difficult to etch after post-processing, due to their high chemical resistance to commonly used etchants.[3] The additional use of a sacrificial polymer resist films and harsh etchants during the fabrication steps can lead to functional deterioration of the final oxide layer, as far as solution-processed oxides are concerned.[4] This, in-turn, reduces overall turnaround time and costs in terms of roll-to-roll manufacturing large-area electronics.[5] On the other hand, the inherent advantages of solution processing to provide alternatives for the generation of patterned structures for this type of processing have been recognized. Especially, site-selective deposition of functional oxides onto desired substrates via printing of metal oxide precursors has been successfully demonstrated.[6] However, current challenges to overcome are concerned with consistent film thickness and reproducibility of desired patterns. In general, a trade-off is usually made between material conformity, deposition reproducibility, and thin film performance.[7] Further structuring approaches rely on manipulating the surface chemistry of the substrate, e.g., using hydrophobic versus hydrophilic patterns, gravure printing, stamping, laser–based direct writing, all of which have demonstrated remarkable results as far as device performance is concerned.[8] Strategies involving the use of direct photopatternable precursors, though, are especially attractive with respect to processing speed and turnover, operational effort, and uniformity of the structured semiconducting films over large areas.

S. Sanctis, Dr. R. C. Hoffmann, Prof. J. J. Schneider
Fachbereich Chemie
Eduard-Zintl-Institut für Anorganische and Physikalische Chemie
Technische Universität Darmstadt
Alarich-Weiss-Straße 12, 64287 Darmstadt, Germany
E-mail: joerg.schneider@ac.chemie.tu-darmstadt.de
Dr. M. Bruns
Institute for Applied Materials – Energy Storage Systems (IAM-ESS)
Karlsruhe Institute of Technology (KIT)
Hermann-von-Helmholtz-Platz 1
D-76344 Eggenstein-Leopoldshafen, Germany
The ORCID identification number(s) for the author(s) of this article can be found under https://doi.org/10.1002/admi.201800324.

DOI: 10.1002/admi.201800324

The procedure of using UV-photopatternable precursors typically involves three steps. In the first step, a film of the precursor(s) is deposited, e.g., by spin coating. Conversion to a solid material is then achieved by irradiation with UV-light through a shadow mask with the desired pattern. In this step, typically UV-photochemistry should be able to convert the precursor toward an active oxide film material. Finally, redundant precursor material from unexposed areas is washed away by rinsing with a suitable solvent, leaving only the patterned features on the substrate. Furthermore, thermal conditioning steps might still be required to transfer the UV-processed film into a fully active electronic semiconductor. Up to date, UV-processing of suitable precursors, however, still needs additional easy-to-perform thermal processing steps, to drive the precursor conversion into the semiconducting metal oxide material to achieve the desired elemental stoichiometry. This processing route, on the other hand, poses challenges as well as possibilities concerning the photoreactivity on the employed precursor materials. The precursors must best be amenable for a full photoconversion reaction into the functional oxide material. In other words, many precursors for transparent conductive oxides possess an $(n-1)d^{10}(n)s^{0}$ configuration of the metal ions, i.e., available chromophores are restricted to ligand-to-metal charge transfer bands and π–π^* or n–π^* transitions in double bonds within the ligand framework. To this end, effective approaches for direct photopatterning have been demonstrated with metal acetylacetonates or simply by addition of acetylacetone and benzoacetone as photosensitive admixtures.[9,10] These admixtures which are added to the solution of the actual metal oxide precursor material help to initiate the initial UV-energy transfer to the molecular precursors, facilitating a smooth decomposition of the otherwise not readily decomposable metal oxide precursor. Similar approaches using acrylate–based ZnO precursor have shown a useful strategy toward direct photopatterning.[4,11] The overall thin film transistor (TFT) performance can be improved further by subsequent processing steps. Typically, thermal post-annealing at elevated temperatures sometimes even higher than 400 °C is required. Nevertheless, attractive device performance parameters of such UV-processed and then thermally conditioned IZO and ZTO films have been reported recently.[9] Therein, the use of a modified gel film precursor is introduced which is subjected to UV-photoprocessing and further thermal conditioning after which the obtained film shows very good TFT performance parameters. Surely enough, further photoactive precursor approaches, which are able to operate under chimie douce conditions and allow a clean decomposition at relatively low temperatures to generate photopatterned indium-based and indium-free amorphous oxides, are highly desirable.

Herein, we demonstrate for the first time the use of UV-photopatternable, air-, visible light-, and solution-stable molecular precursors of indium, zinc, and tin. They can be used to generate amorphous IZO and ZTO semiconductor thin films employing a combined photopatterning and a reasonable thermal conditioning procedure. The precursor approach used herein allows to photopattern the obtained IZO and ZTO thin films and finally process them into semiconducting oxide semiconductors. This is realized by the fact that the precursors follow a clean and chemically closely related decomposition chemistry in the solid state. The IZO thin film devices obtained at 250 °C even show charge-carrier mobilities (μ_{sat}) and current on–off ratios ($I_{on/off}$) comparable to amorphous silicon. These can be boosted further, however still under fairly low thermal conditioning of $T \leq 350$ °C, to values of 7.8 for IZO and 3.6 cm^2 $(V\ s)^{-1}$ for ZTO.

2. Results and Discussions

Metal complexes of indium, zinc, and tin with methoxyimino-propionato ligands (metal oximates) were employed as precursors for the synthesis of IZO and ZTO films (**Figure 1**).

These precursors are accessible in high yields and are stable under air and visible light. They decompose thermally by Beckmann-type rearrangements under modest conditions (≈200 °C) which lead to very clean degradation followed by smooth thin film formation of the desired metal oxides. The ligands degrade under formation of gaseous molecules which leave the converted film under modest conditions (CO_2, CO, CH_3CN, H_2O). Importantly, these products do not contaminate the resulting oxide in any way. Recently, we have described the synthesis and the thermal processing of these molecular precursor compounds into IZO and ZTO.[12] This unique ability of these precursors with respect to soft chemistry qualifies them in an ideal way for a subsequent smooth conversion into IZO and ZTO thin films under a thermal conditioning process eventually necessary after an initial UV-patterning of the precursors which is studied herein for the first time.

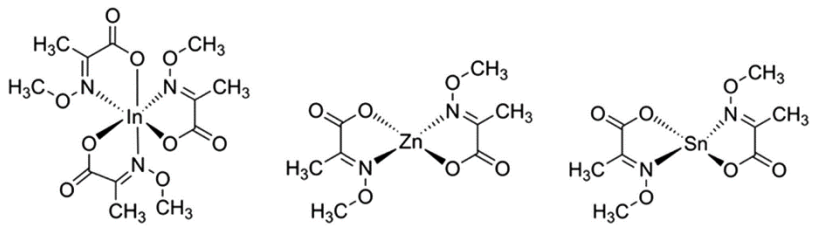

Figure 1. Schematic representation of the molecular structure of the indium(III), zinc(II), and tin(II) oximato precursor compounds containing methoxy-iminopropionato ligands.

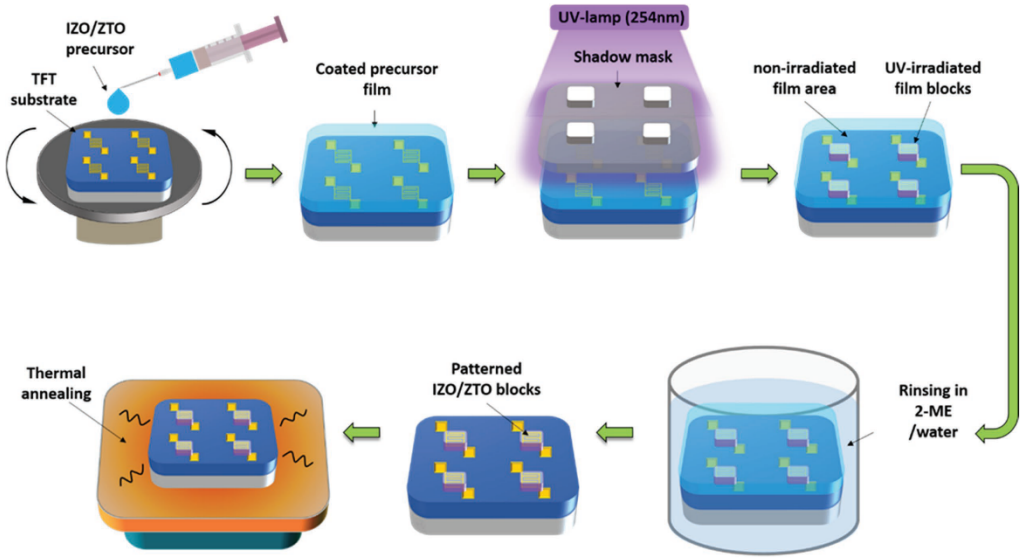

Scheme 1. Schematic representation of the steps employed in the direct UV photoprocessing of semiconducting IZO/ZTO thin films on a TFT substrate.

For the photochemical conversion, first, solutions containing appropriate mixtures of the precursor compounds are deposited by spin coating and are partially converted to the multinary amorphous oxide phases, i.e., IZO or ZTO on the substrate by subjecting the films to UV irradiation (peak $\lambda = 254$ nm, 90%). The absorption maxima of all three, white to light yellowish compounds are thus in the appropriate spectral range for a UV-photopatterning process (Figure S1, Supporting Information). The substrates did not show any warming during UV irradiation indicating that the observed conversion is purely photochemical at that stage. Second, after UV irradiation, washing with 2-methoxyethanol and water was used to remove unreacted precursor (i.e., material covered by shadow mask in the patterning process). Finally, while patterning was already achieved at this stage, further additional annealing at temperatures between 250 and 350 °C is required to obtain the desirable semiconducting behavior. A summary of the complete experimental procedure is illustrated in **Scheme 1** and Figure S2 (Supporting Information).

The conversion of a molecular precursor thin film obtained from the zinc(II) oximato and tin(II) oximato compounds after photopatterning was analyzed by means of IR spectroscopy (attenuated total reflectance (ATR) mode) (**Figure 2**). First, peaks arising from the IR-active vibrations within the thin film of the as-deposited precursor mixture can be assigned to O—H bonds (≈3197 cm^{-1}), C—H bonds from the methoxy groups (≈2947 cm^{-1}), C=N bonds (≈1637 cm^{-1}), symmetric and asymmetric vibrations from the C=O bond (≈1583 cm^{-1}), deformation vibrations of the C—H bonds from the methyl groups and more intense vibrational peaks from the overlapping of the N—O and C—O bonds (≈1054 cm^{-1}).[13] The OH signal might be due to the generation of surface hydroxyl groups introduced during the spin coating process which is completely performed under ambient conditions. No additional signals due to any interaction of the precursor molecules are observed.

Once the precursor films have been exposed to UV irradiation, signals assignable to stretching and deformation modes of the C—H bond of the methoxy group are significantly diminished indicating significant precursor decomposition. Interestingly, investigations of photolytic decomposition of metal oximates are scarce, but photochemical reactions of the pure uncoordinated oxime ligands are known.[14] Reported reaction pathways include syn–anti isomerization, photo-Beckmann rearrangement, nitrile formation, as well as ketone formation.[15] From the IR spectra

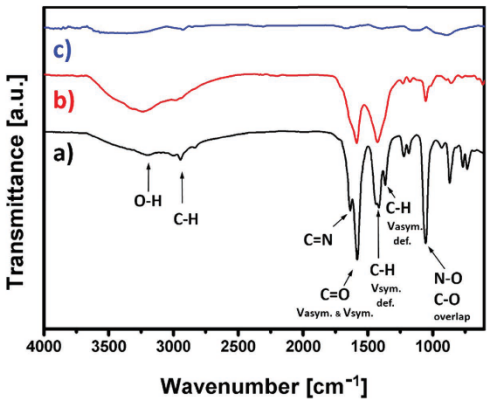

Figure 2. FT-IR spectra of a ZTO thin film obtained from the Zn(II) and Sn (II) oximato precursors at various stages of the photopatterning process, namely, after a) as-prepared thin film after initial spin coating, b) thin film after UV exposure for 10 min, and c) thin film obtained after final thermal annealing at 350 °C for 120 min.

obtained, no generation of any new functional groups (e.g., nitriles or amides) as by-products from precursor decomposition can be detected, whatsoever. However, it can thus be assumed that N–O cleavage of the Schiff base coordination of the oximato ligands toward the metal center occurred, whereas the carboxy unit initially bound to the metal stays still intact under UV irradiation. Therefore, it can be speculated that a decay of the ligand backbone of the oximates might be initiated via cleavage of the metal-bound N–O moiety. After a final thermal conditioning step, the IR spectrum of the resulting ZTO film free of any residual signals assignable to any remaining ligand moieties is obtained (Figure 2c). IZO films also undergo identical photodecomposition pathways as the ZTO films, with no observable differences in their IR spectra. The observed systematic decay of the photoactive component of the ligand is also well reflected in the UV–vis spectrum of the of the IZO and ZTO thin films, displaying an increase in film transparency in the UV region after the patterning step. The films subjected to thermal annealing after the patterning step show an increase in absorption in the UV region, indicative of the formation of the final amorphous oxide, typical of wide band-gap amorphous oxide semiconductors (Figure S3, Supporting Information). Both the IZO and ZTO films show a high optical transparency (>90%) over the full visible-wavelength region.[16]

In order to get an insight in the microstructure of the film, focussed ion beam (FIB)–based cross-sectional transmission electron microscopy (TEM) analysis was performed for the thin films fabricated via photopatterning and subsequent thermal annealing at 350 °C (**Figure 3**a,b). Both films, IZO and ZTO, exhibit a uniform, homogeneous, and amorphous thin film morphology displaying a thickness of ≈10 and ≈6 nm, respectively (Figure 3c,d). Auger electron spectroscopy (AES) depth profile spectra were obtained for the IZO and ZTO films and reveal that the chemical composition of the individual chemical element species involved (In, Zn, Sn, and O) is highly uniform across the depth of the films, indicating the robustness of the formation process.

It is known that controlled exposure to water during the pattern development process employed in UV processing might lead to compositional material leaching as well as crystallization of deposited thin films. However, in certain cases, this has proven to be highly beneficial toward the semiconducting character of the films and indeed enhances the TFT performance of multinary oxides.[17] However, no distinct losses of the chemical elements were detected via AES for samples which were washed with water. Hereby the film adhered well to the substrate even after subjecting them to a brief ultrasonication in water. Additionally, no significant residual carbon contamination from incomplete precursor decomposition was detected within the film, which is known to deteriorate TFT performance severely.[11b] Only trace carbon signals were found on the surface arising from adsorbed environmental species like CO_2.[18] Furthermore, such treated IZO and ZTO films still exhibit a low surface roughness, i.e., R_{RMS} ≈0.23 nm for IZO and R_{RMS} ≈0.25 nm for ZTO after all processing steps, i.e., UV treatment, washing, and further annealing at 350 °C (**Figure 4**).

In order to investigate and detect systematic changes in surface composition of the patterned IZO and ZTO films, X-ray

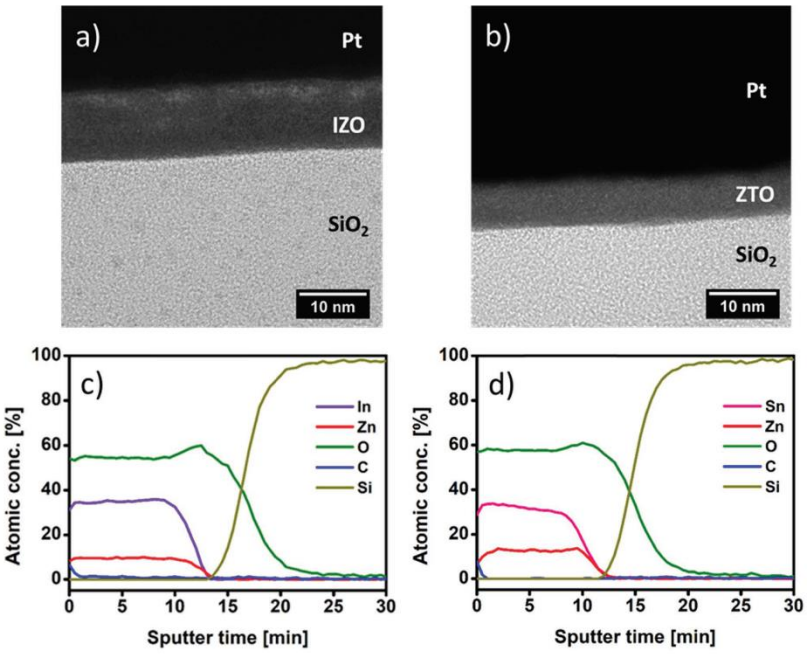

Figure 3. Cross-sectional TEM micrographs obtained by FIB sample preparation of a) IZO and b) ZTO thin films and Auger depth profiles of c) IZO and d) ZTO thin films. All samples were characterized after UV patterning followed by thermal annealing at 350 °C.

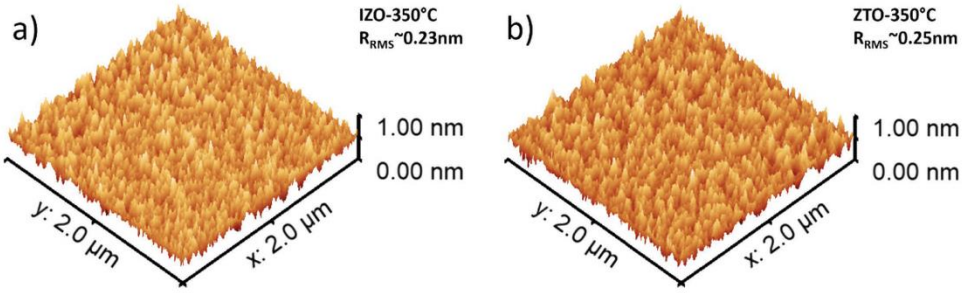

Figure 4. AFM micrographs and root mean square roughness (R_{RMS}) for the photopatterned a) IZO and b) ZTO thin films annealed at 350 °C.

photoelectron spectroscopy (XPS) was performed for films annealed at temperatures between 250 and 350 °C (**Figure 5**; Figure S4, Supporting Information). The core O 1s spectra are deconvoluted into two peaks at ≈530 and ≈532 eV. The former is attributed to coordinated metal–oxygen bonds (M–O), and the latter originates from weak metal–hydroxide bonds (M–OH) as well as hydroxyl species adsorbed on the surface of the films. In both cases, films annealed at 250 °C have a higher concentration of M–OH bonds in comparison with its counterparts annealed at 300 and 350 °C. Significant reduction in the M–OH, and the subsequent increase in M-O at higher temperatures (≥300 °C), is observed in both cases. This is in agreement with previous reports, wherein conversion from the metal hydroxide to the corresponding oxide generally occurred at temperatures >250 °C for larger cations, which was attributed to higher formation energies of the metal oxides.[19]

In order to assess the semiconductor efficiency of such photopatterned IZO and ZTO thin films, TFTs with a bottom-gate/bottom-contact setup were manufactured by spin-coating the precursor solutions onto prefabricated substrates which consist of a substrate/gate highly n-doped Si with a 90 nm SiO_2 dielectric layer on top (Scheme 1; Figure S6, Supporting Information).[12a-c] A carefully selected source–drain electrode geometry with a channel width (W) to length (L) ratio (W/L = 500) was employed to avoid any overestimation of field-effect mobility for the measured TFTs. Critical electrode dimensions with extremely small W/L ratio quite often lead to an overestimation of the effective TFT mobility by a factor of over two decades and must be carefully considered.[20] The source–drain electrodes possess an interdigital structure consisting of gold electrodes with an adhesion layer of indium tin oxide (ITO, 10 nm). Precursor ratios for obtaining an IZO

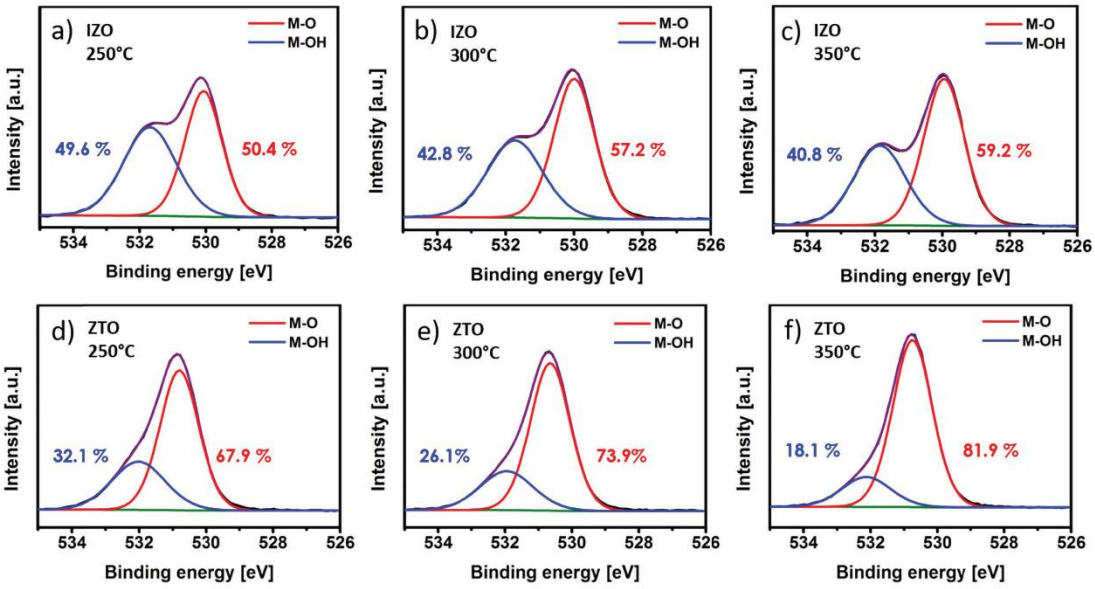

Figure 5. XPS spectra of the O 1s region showing atomic % ratio of coordinated metal–oxygen bonds (M–O) and metal–hydroxide species (M–OH) of the UV-patterned films for a–c) IZO and d–f) ZTO each annealed at 250, 300, and 350 °C, respectively.

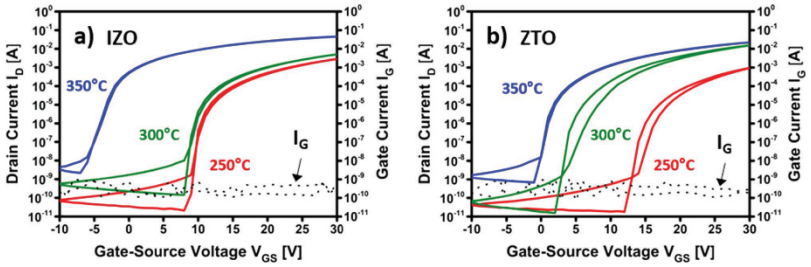

Figure 6. Individual transfer characteristics for the photopatterned IZO- and ZTO-based TFT after final thermal conditioning at different temperatures. Transfer curves of the patterned thin films for a) IZO TFTs and b) ZTO TFTs annealed for 2 h at 250, 300, and 350 °C, respectively. Gate leakage current (I_G) of the patterned devices in both IZO and ZTO material systems is indicated by dotted lines.

composition (In:Zn, 6:4) and a ZTO composition (Sn:Zn, 7:3) were used.[12b,21] The spin-coated and subsequently UV-photopatterned films were finally thermally annealed on a hot plate at temperatures ranging from 250 to 350 °C (±5 °C) in ambient air for 2 h. No additional further post-processing of the so-fabricated devices was employed. It should be mentioned here that sole UV-irradiation of the precursor films does not lead to any electronic behavior whatsoever. We attribute this to the low power input (8 W max.) of the UV-irradiation device used, which needs to add an additional thermal conditioning step.

The crucial transfer and output characteristics of the patterned IZO and ZTO TFTs at the aforementioned temperatures along with the saturation charge-carrier mobility (μ_{sat}), threshold voltage (V_{th}), and current on–off ratio ($I_{on/off}$) have been determined (**Figure 6**; Figure S5 (Supporting Information); **Table 1**). Active semiconductor performance was observed at all investigated temperatures. Devices annealed at 250 °C and higher demonstrate a good field-effect transistor (FET) performance operating in an enhancement mode, with charge-carrier mobilities ≥1 cm^2 $(V\ s)^{-1}$ (typical for amorphous hydrogenated silicon, a-Si-H) in all temperature regimes with the exception of ZTO annealed at 250 °C. Additionally, a systematic decrease in the threshold voltage is observed parallel to an increase in the annealing temperature. A consistent reduction in V_{th} generally arises from the passivation of deep donor electron traps from oxygen vacancy–related point defects dominant at the interface, facilitated by increased formation of M−O bonds within the thin film. This in turn enables the turn-on of the TFTs at lower voltages during systematic transitions from low to high annealing temperature regimes.[20a,22] Moreover, no significant gate leakage current (I_G), with a well suppressed, low leakage current (I_G) was observed in both the IZO- and ZTO-based TFTs, confirming the successful semiconductor patterning as well as a clean removal of the precursor films from undesired areas on the substrate. Recent work which used photopatternable solution with benzoylacetone as a photosensitive chelate ligand with the careful addition of acetylacetone and nitric acid to reduce the thermal budget enables the formation of In_2O_3 and indium gallium zinc oxide (IGZO) TFTs with TFT mobility of 2.24 and 1.15 cm^2 $(V\ s)^{-1}$ and $I_{on/off}$ of 3.1×10^7 and 1×10^8, at 250 °C, respectively.[23] This photosensitive additive–based photopatterning process was further refined by intricate formation of ammonium nitrate via ammonium hydroxide and metal nitrates, which demonstrated an improved performance of IGZO TFTs with a mobility of 16 cm^2 $(V\ s)^{-1}$ and an $I_{on/off}$ of 10^8.[24] However, an additive-free straightforward approach via well-defined metal oxide precursors has been uniquely demonstrated so far, using zinc methacrylate as a precursor to fabricate photopatterned ZnO. The photopatterned ZnO devices demonstrated a TFT mobility of 0.323 cm^2 $(V\ s)^{-1}$ and an $I_{on/off}$ of 1.2×10^5, annealed at 450 °C. A higher thermal budget was needed in this case owing to a higher annealing temperature to ensure suitable decomposition of the bulky methacrylate ligand, which provides scope for improved design for metal oxide precursor for a facile photopatterning approach.[11b] Although photopatterning approaches using indium-based precursors have been demonstrated so far, indium-free alternative such as ZTO to generate photopatterned amorphous oxide TFTs has not yet been reported to the best of our knowledge. Such a direct photoactive precursor-solvent system would be ideal to advance the progress in this direction to enable photopatterning of various functional metal oxides. The observed changes in the comparative increase in the coordinated metal oxide bonds than the hydroxide species (M−O versus M−OH) is well substantiated and consistent with our XPS investigations for both the patterned IZO and ZTO systems investigated here. The dependence of the annealing temperatures and corresponding FET performance was aimed to establish a suitable temperature regime below the glass transition temperature (≈450 °C) of commercially employed display-glass substrates.[25]

Table 1. Overview of performance parameters for photopatterned IZO and ZTO and thermally conditioned TFT devices (250–350 °C).

Annealing temp. [°C]	Mobility, μ_{sat} [cm^2 $(V\ s)^{-1}$]	Threshold voltage, V_{th} [V]	Current on–off ratio, $I_{on/off}$
IZO-250	1.1	11.4	2.1×10^8
IZO-300	3.4	9	1.6×10^8
IZO-350	7.8	0.3	3.5×10^8
ZTO-250	0.7	13.2	4.7×10^7
ZTO-300	2.5	7.5	6.4×10^7
ZTO-350	3.6	2.4	5.3×10^7

3. Conclusion

Indium(III), zinc(II), and tin(II) complexes with methoxyimino-propionic ligands were employed to establish a facile, solution-based route toward the generation of UV-photopatterned IZO and indium-free ZTO semiconductor thin films. The procedure allows direct UV-photopatterning of all precursor films which were directly patterned by spin coating on an FET device substrate using a shadow mask technique. Unreacted precursor material remains soluble and can be removed completely by solvent washing. The edge resolution of the obtained patterns is limited only by the photomask employed in the process. For both molecular precursor systems, a full conversion to the multinary amorphous oxide semiconductors by UV-irradiation followed by a modest thermal annealing was achieved. The obtained thin film materials do not show any sign of residual ligand contamination which corroborates the efficacy of the process. The finally processed thin films (350 °C), when employed in a TFT device, exhibit a high charge-carrier mobility (μ_{sat}) of 7.8 and 3.6 cm^2 $(V\ s)^{-1}$ for the photopatterned IZO and ZTO TFTs and a good current on–off ratio ($I_{on/off}$) of 3.5×10^8 and 5.3×10^7 with successful suppression of the detrimental gate leakage current ($I_G \approx 10^{-9}$ A). Improved TFT performance parameters of the both semiconducting IZO and ZTO layers in the current work were correlated to the improved change in the local oxygen environment with enhanced formation of the metal—oxygen bond and a subsequent decrease in hydroxyl species due to a clean decomposition of the precursor ligand, post the patterning process and relatively low annealing temperatures (≤350 °C).

Such a unique class of molecular precursor with intrinsic photopatterning ability and reasonably high performance of the corresponding amorphous oxide semiconductor (AOS) appears to be an attractive starting point for practical integration with high potential for roll-to-roll manufacturing in the field of large-area electronics. In view of the accessibility of other metal oximato complexes (Zr, Hf),[26] even high κ-oxide dielectric thin film seems accessible with this unique photopatterning approach in the future.

4. Experimental Section

Precursor Synthesis: Precursor synthesis of the indium, zinc, and tin(II) precursors with Schiff-base methoxyiminopropionic acid "oximato" ligands, namely tris[2-(methoxyimino)-propanoato]indium(III), bis[2-(methoxyimino)propanoato]zinc and bis[2-(methoxyimino)-propanoato]tin(II) was reported.[12b,e,21]

Precursor Photopatterning: FET substrates were obtained from Fraunhofer IMPS, Dresden. The substrates (15 × 15 mm^2) consist of a highly n-doped silicon with a 90 nm silicon-oxide dielectric layer. The source–drain electrodes, with a deliberately large channel length L = 20 µm and a channel width W = 10 mm (W/L = 500), were fabricated with 40 nm of gold (interdigital structure) with a 10 nm intermediate adhesion layer of ITO. All substrates were sequentially cleaned, with acetone, water, and 2-propanol for 10 min, respectively. The cleaned substrates were exposed for 10 min to UV treatment (Nanobio analytics, UVC-1014, 8 W (peak λ = 254 nm, 90%; 186 nm, 10%) prior to spin coating, to improve the adhesion of the wet precursor films.

For the preparation of the spin-coating solutions, stock solutions of the indium, zinc, and tin precursors were fabricated by dissolving 3 wt% of the respective precursors each in 2-methoxyethanol. After complete dissolution, a clear transparent solution was obtained in both cases with a pale yellow color of the ZTO solution owing to the slightly broader absorption region of the Sn(II) precursor. The solutions were then filtered through a 0.22 µm polytetrafluoroethylene (PTFE) syringe filter and mixed in the desired In:Zn (6:4) and Sn:Zn (7:3) ratios for spin coating of IZO and ZTO thin films. The spin coating was carried out under ambient conditions with a spinning speed of 2500 rpm for 20 s. The substrates with precursor films were then placed into a substrate holder with an in-house shadow mask consisting of the desired exposed areas and then subjected to UV patterning in the abovementioned UV chamber for 10 min. After the selective UV-induced partial precursor decomposition/polymerization, the unexposed precursor film areas were readily removed by rinsing the substrates in 2-methoxyethanol and water sequentially. The patterned films were finally subjected to thermal annealing in ambient atmosphere at desired temperatures for 10 min. Repeated iterations of the aforementioned procedure were carried out until desired film thickness was achieved. Finally, the films were annealed for 2 h at the desired temperature to generate the functional semiconducting oxide thin films.

Material and Device Characterization: TEM was carried out using Tecnai F20 (FEI), with an operating voltage of 200 kV. Atomic force microscopy (AFM) measurements were carried out with MFP-3D (Asylum Research), with ultrasharp silicon cantilevers. UV–vis measurements were carried out using quartz cuvettes and on clean quartz substrates for the precursor solutions and thin films, respectively (Thermo Scientific-Evolution 600). XPS measurements were performed using a K-Alpha XPS instrument (Thermo Fisher Scientific, East Grinstead, UK) monochromated Al Kα X-ray source (30–400 µm spot size). All spectra were referenced to that of hydrocarbon C 1s peak at 285.0 eV. Auger spectroscopy measurement was performed on a PHI 680 (Physical Electronics) scanning Auger nanoprobe, operated at an acceleration voltage of 20 keV and a current of 10 nA. Sputtering was carried out under ultra-high vacuum (5×10^{-9} Torr) with an argon ion gun operated at 250 eV and 500 nA.

TFT characteristics were determined at V_{ds} = 30 V with an HP 4155A Semiconductor Parameter Analyzer (Agilent) in a glove box under exclusion of air and moisture in the dark. Eight devices were measured for each experimental condition. Charge-carrier mobility (μ_{sat}) and threshold voltage (V_{th}) were derived from a linear fitting of the square root of the source–drain current ($\sqrt{I_{ds}}$) as a function of gate–source voltage V_{gs}.

Supporting Information

Supporting Information is available from the Wiley Online Library or from the author.

Acknowledgements

S.S. and J.J.S. acknowledge financial support through the DFG SPP 1569 program. TEM investigations were performed at ERC Jülich under contract ERC-TUD1. Auger measurements were carried out at Karlsruhe Nano Micro Facility (KNMF proposal number 2016-016-014489) at Karlsruhe Institute of Technology (KIT). The authors thank Tobias Weingärtner (KIT) for carrying out AES measurements and Dr. Jörg Engstler (TUDa) for TEM measurements at ERC-Jülich.

Conflict of Interest

The authors declare no conflict of interest.

Keywords

indium zinc oxide, molecular precursors, photopatterning, thin film transistor, zinc tin oxide

Received: February 27, 2018
Revised: May 13, 2018
Published online: June 27, 2018

[1] a) T. Kamiya, H. Hosono, *NPG Asia Mater.* **2010**, *2*, 15; b) C. Glynn, C. O'Dwyer, *Adv. Mater. Interfaces* **2017**, *4*, 1600610; c) R. M. Pasquarelli, D. S. Ginley, R. O'Hayre, *Chem. Soc. Rev.* **2011**, *40*, 5406; d) K. Si Joon, Y. Seokhyun, K. Hyun Jae, *Jpn. J. Appl. Phys.* **2014**, *53*, 02BA02; e) X. Yu, T. J. Marks, A. Facchetti, *Nat. Mater.* **2016**, *15*, 383.

[2] J. Kim, M.-G. Kim, J. Kim, S. Jo, J. Kang, J.-W. Jo, W. Lee, C. Hwang, J. Moon, L. Yang, Y.-H. Kim, Y.-Y. Noh, J. Yun Jaung, Y.-H. Kim, S. Kyu Park, *Sci. Rep.* **2015**, *5*, 14520.

[3] a) T. L. Breen, P. M. Fryer, R. W. Nunes, M. E. Rothwell, *Langmuir* **2002**, *18*, 194; b) K. Chul Ho, R. You Seung, K. Hyun Jae, *J. Phys. D: Appl. Phys.* **2014**, *47*, 385104.

[4] H. Han, J. Bissell, F. Yaghmaie, C. E. Davis, *Langmuir* **2010**, *26*, 515.

[5] a) Y. S. Rim, S.-H. Bae, H. Chen, N. De Marco, Y. Yang, *Adv. Mater.* **2016**, *28*, 4415; b) J. Perelaer, P. J. Smith, D. Mager, D. Soltman, S. K. Volkman, V. Subramanian, J. G. Korvink, U. S. Schubert, *J. Mater. Chem.* **2010**, *20*, 8446.

[6] a) K. Fukuda, T. Someya, *Adv. Mater.* **2017**, 29; b) P. F. Moonen, I. Yakimets, J. Huskens, *Adv. Mater.* **2012**, *24*, 5526; c) W.-J. Lee, W.-T. Park, S. Park, S. Sung, Y.-Y. Noh, M.-H. Yoon, *Adv. Mater.* **2015**, *27*, 5043.

[7] C.-H. Choi, L.-Y. Lin, C.-C. Cheng, C.-H. Chang, *ECS J. Solid State Sci. Technol.* **2015**, *4*, P3044.

[8] a) C. Gu, J.-S. Lee, *RSC Adv.* **2016**, *6*, 43147; b) Y. Choi, G. H. Kim, W. H. Jeong, H. J. Kim, B. D. Chin, J.-W. Yu, *Thin Solid Films* **2010**, *518*, 6249; c) S. Sung, S. Park, S. Cha, W.-J. Lee, C.-H. Kim, M.-H. Yoon, *RSC Adv.* **2015**, *5*, 38125; d) H.-C. Lin, F. Stehlin, O. Soppera, H.-W. Zan, C.-H. Li, F. Wieder, A. Ponche, D. Berling, B.-H. Yeh, K.-H. Wang, *Sci. Rep.* **2015**, *5*, 10490.

[9] H. S. Lim, Y. S. Rim, H. J. Kim, *Sci. Rep.* **2014**, *4*, 4544.

[10] H. J. Kim, Y.-G. Kim, S. P. Park, D. Kim, N.-E. Kim, J. S. Choi, H. J. Kim, *SID Int. Symp. Dig. Tech. Pap.* **2017**, *48*, 180.

[11] a) C.-C. Yeh, S. Colis, P. Fioux, H.-W. Zan, D. Berling, O. Soppera, *Adv. Mater. Interfaces* **2017**, *4*, 1700738; b) Y. J. Jeong, T. K. An, D.-J. Yun, L. H. Kim, S. Park, Y. Kim, S. Nam, K. H. Lee, S. H. Kim, J. Jang, C. E. Park, *ACS Appl. Mater. Interfaces* **2016**, *8*, 5499.

[12] a) S. Sanctis, R. C. Hoffmann, R. Precht, W. Anwand, J. J. Schneider, *J. Mater. Chem. C* **2016**, *4*, 10935; b) S. Sanctis, N. Koslowski, R. Hoffmann, C. Guhl, E. Erdem, S. Weber, J. J. Schneider, *ACS Appl. Mater. Interfaces* **2017**, *9*, 21328; c) S. Sanctis, J. Krausmann, C. Guhl, J. J. Schneider, *J. Mater. Chem. C* **2018**, *6*, 464; d) J. J. Schneider, R. C. Hoffmann, J. Engstler, O. Soffke, W. Jaegermann, A. Issanin, A. Klyszcz, *Adv. Mater.* **2008**, *20*, 3383; e) J. J. Schneider, R. C. Hoffmann, J. Engstler, S. Dilfer, A. Klyszcz, E. Erdem, P. Jakes, R. A. Eichel, *J. Mater. Chem.* **2009**, *19*, 1449.

[13] B. C. Smith, *Fundamentals of Fourier Transform Infrared Spectroscopy*, CRC Press, Boca Raton, FL **2011**.

[14] R. C. Hoffmann, J. J. Schneider, *J. Am. Ceram. Soc.* **2011**, *94*, 1878.

[15] a) D. S. Bolotin, N. A. Bokach, M. Y. Demakova, V. Y. Kukushkin, *Chem. Rev.* **2017**, *117*, 13039; b) C. Saravanselvi, N. Somasundaram, S. Vijaikumar, C. Srinivasan, *Photochem. Photobiol. Sci.* **2002**, *1*, 607.

[16] a) C. G. Choi, S.-J. Seo, B.-S. Bae, *Electrochem. Solid-State Lett.* **2008**, *11*, H7; b) S. Seok-Jun, C. Chaun Gi, H. Young Hwan, B. Byeong-Soo, *J. Phys. D: Appl. Phys.* **2009**, *42*, 035106.

[17] a) P. K. Nayak, J. A. Caraveo-Frescas, Z. Wang, M. N. Hedhili, H. N. Alshareef, *Adv. Electron. Mater.* **2015**, *1*, 1500014; b) H.-C. Lin, F. Stehlin, O. Soppera, H.-W. Zan, C.-H. Li, F. Wieder, A. Ponche, D. Berling, B.-H. Yeh, K.-H. Wang, *Sci. Rep.* **2015**, *5*, 10490.

[18] X. Yu, J. Smith, N. Zhou, L. Zeng, P. Guo, Y. Xia, A. Alvarez, S. Aghion, H. Lin, J. Yu, R. P. H. Chang, M. J. Bedzyk, R. Ferragut, T. J. Marks, A. Facchetti, *Proc. Natl. Acad. Sci. USA* **2015**, *112*, 3217.

[19] a) M.-C. Nguyen, M. Jang, D.-H. Lee, H.-J. Bang, M. Lee, J. K. Jeong, H. Yang, R. Choi, *Sci. Rep.* **2016**, *6*, 25079; b) S. Kitabayashi, N. Koga, *J. Phys. Chem. C* **2015**, *119*, 16188.

[20] a) M.-G. Kim, H. S. Kim, Y.-G. Ha, J. He, M. G. Kanatzidis, A. Facchetti, T. J. Marks, *J. Am. Chem. Soc.* **2010**, *132*, 10352; b) K. Okamura, D. Nikolova, N. Mechau, H. Hahn, *Appl. Phys. Lett.* **2009**, *94*, 183503.

[21] R. C. Hoffmann, M. Kaloumenos, S. Heinschke, E. Erdem, P. Jakes, R.-A. Eichel, J. J. Schneider, *J. Mater. Chem. C* **2013**, *1*, 2577.

[22] P. Barquinha, A. Pimentel, A. Marques, L. Pereira, R. Martins, E. Fortunato, *J. Non-Cryst. Solids* **2006**, *352*, 1749.

[23] Y. S. Rim, H. S. Lim, H. J. Kim, *ACS Appl. Mater. Interfaces* **2013**, *5*, 3565.

[24] Y. S. Rim, H. Chen, Y. Liu, S.-H. Bae, H. J. Kim, Y. Yang, *ACS Nano* **2014**, *8*, 9680.

[25] M. Yuki, K. Masumo, M. Kunigita, *IEEE Trans. Electron Devices* **1989**, *36*, 1934.

[26] J. J. Schneider, R. C. Hoffmann, A. Issanin, S. Dilfer, *Mater. Sci. Eng.: B* **2011**, *176*, 965.

6.4 Microwave assisted synthesis and characterization of a zinc oxide/tobacco mosaic virus hybrid material. An active semiconductor in a field-effect transistor device.

Fabrication of necessary functional hybrid materials often require well-defined 1D and 2D biological molecules as structure-directing agents, enabling a "bottom-up" approach for building these complex nanoarchitectures. Among the several biological templates, the tobacco mosaic virus (TMV) has shown great potential to function as a robust biological template for the deposition of a variety of inorganic materials under mild fabrication conditions. It possesses a well-defined tube-like structure, consisting of ≈2130 identical protein units, a length of 300 nm and an outer and inner diameter of 18 nm and 4 nm, respectively. It is also displays a remarkable stability for temperatures of up to about 60 °C in a pH range between 2 and 10.

Within this publication, an optimed, tunable selective microwave-assisted deposition of ZnO nanoparticles is demonstrated using the established zinc complex with methoxyiminoprionato ligands. The addition of the optimal amount of the base (TEAOH) provides mild but sufficient basic conditions to ensure an efficient decomposition of the zinc complex at a low temperature as 60 °C enabling the successful formation of crystalline zinc oxide. In the presence of the base and carefully optimised mild microwave condition (avg. power ~15 Watts, reaction time 30 mins.), the precursor undergoes a controlled decomposition with appearance of a NMR characteristic ^{13}C chemical shift corresponding to the formation of acetonitrile (δ = 117.30 ppm) under post decomposition conditions of the precursor complex. Additional chemical shifts from still coordinated as well as from residual free ligands were also present as expected due to the base-catalyzed decomposition of the precursor complex. These residual free ligands also provide stability to the ZnO nanoparticles against flocculation, which assists a uniform coating of the TMV template. The microwave decomposition of the precursor is in full accordance with a second-order type Beckmann rearrangement reaction as observed for its solution based thermal decomposition pathway. For an optimum number (6 cycles) of ZnO deposition/coatings, the best overall FET performance values were obtained with a field-effect mobility (μ_{sat}) of 6.7×10^{-4} $cm^2/V.s$, V_{th} of +4.7 V and an $I_{on/off}$ of 9.0×10^5 without the need for any post-process thermal annealing. A higher $I_{on/off}$ in comparison to previously reported values could possibly be attributed to a greater degree of ZnO nanoparticle orientation on the TMV template resulting from the use of the molecular precursor complex employed. Such a bio-inorganic nanocomposite semiconductor material accessible using a mild and straightforward microwave processing technique could open up new future avenues within the field of bio-electronics.

BEILSTEIN JOURNAL OF NANOTECHNOLOGY

Microwave assisted synthesis and characterisation of a zinc oxide/tobacco mosaic virus hybrid material. An active hybrid semiconductor in a field-effect transistor device

Shawn Sanctis[1], Rudolf C. Hoffmann[1], Sabine Eiben[2] and Jörg J. Schneider[*1,§]

Full Research Paper

Open Access

Address:
[1]Fachbereich Chemie, Eduard-Zintl-Institut, Fachgebiet Anorganische Chemie, Technische Universität Darmstadt, Alarich-Weiss Straße 12, 64287 Darmstadt, Germany and [2]Institute of Biomaterials and Biomolecular Systems, Dept. of Molecular Biology and Plant Virology, University of Stuttgart, 70550 Stuttgart, Germany

Email:
Jörg J. Schneider[*] - joerg.schneider@ac.chemie.tu-darmstadt.de

[*] Corresponding author
§ Fax: +49 6151 163470; Tel: +49 6151 163225

Keywords:
field-effect transistor; microwave synthesis; molecular precursor; thin film transistor; tobacco mosaic virus; zinc oxide

Beilstein J. Nanotechnol. **2015,** *6*, 785–791.
doi:10.3762/bjnano.6.81

Received: 12 September 2014
Accepted: 16 February 2015
Published: 20 March 2015

This article is part of the Thematic Series "Towards multifunctional inorganic materials: biopolymeric templates" and is dedicated to Prof. Dr. mult. Günther Wilke on the occasion of his 90th birthday.

Guest Editors: C. Steinem and J. Bill

Abstract

Tobacco mosaic virus (TMV) has been employed as a robust functional template for the fabrication of a TMV/zinc oxide field effect transistor (FET). A microwave based approach, under mild conditions was employed to synthesize stable zinc oxide (ZnO) nanoparticles, employing a molecular precursor. Insightful studies of the decomposition of the precursor were done using NMR spectroscopy and material characterization of the hybrid material derived from the decomposition was achieved using dynamic light scattering (DLS), transmission electron microscopy (TEM), grazing incidence X-ray diffractometry (GI-XRD) and atomic force microscopy (AFM). TEM and DLS data confirm the formation of crystalline ZnO nanoparticles tethered on top of the virus template. GI-XRD investigations exhibit an orientated nature of the deposited ZnO film along the c-axis. FET devices fabricated using the zinc oxide mineralized virus template material demonstrates an operational transistor performance which was achieved without any high-temperature post-processing steps. Moreover, a further improvement in FET performance was observed by adjusting an optimal layer thickness of the deposited ZnO on top of the TMV. Such a bio-inorganic nanocomposite semiconductor material accessible using a mild and straightforward microwave processing technique could open up new future avenues within the field of bio-electronics.

Introduction

In recent years, the synthesis and fabrication of bio-inorganic nanostructures have gained tremendous importance for the fabrication of nanoscale devices with defined functional properties [1-3]. Significant interest has been dedicated to the generation of multifunctional devices by employing a unique combination of functional biological molecules and inorganic ma-

terials. The use of biological building blocks at the nanoscale include DNA, peptides, bacteriophages and viruses which exhibit diverse properties for the controlled formation of devices with possible application in areas such as sensors, photonics, energy storage as well as electronic transistors [4-8]. Fabrication of necessary functional hybrid materials often require well-defined 1D and 2D biological molecules as structure-directing agents, enabling a "bottom-up" approach for building these complex nanoarchitectures. Among the several biological templates, the tobacco mosaic virus (TMV) has shown great potential to function as a robust biological template for the deposition of a variety of inorganic materials under mild fabrication conditions. With its well-defined tube-like structure, the tobacco mosaic virus is one the most widely studied plant virus consisting of ≈2130 identical protein units, a length of 300 nm and an outer and inner diameter of 18 nm and 4 nm, respectively. It is also displays a remarkable stability for temperatures of up to about 60 °C in a pH range between 2 and 10. Such a rigid nanostructured template offers an interesting opportunity for the directed assembly of inorganic, metallic and semiconducting materials [9,10].

With the aim to generate defined semiconducting nanostructures in the nanometer range, deposition of ZnO nanoparticles onto the wild type TMV (wt TMV) presents itself to be an ideal choice of material combination.

Zinc oxide (ZnO) is one the most widely studied, non-toxic, n-type semiconducting inorganic oxide with a direct band-gap of ≈3.37 eV. This enables the fabrication of functional zinc oxide based transistors [11,12]. The ability to fabricate zinc oxide based transistors from various precursor solutions, under mild basic conditions, makes it a suitable candidate to be deposited upon the TMV template [13]. We have previously reported on the synthesis of air-stable, Schiff base type, molecular zinc complex diaqua-bis[2-(methoxyimino)propanato]zinc(II) which represents an ideal molecular single source precursors for the fabrication of functional zinc oxide transistors at low-temperatures [14]. Employment of such a class of molecular precursor complexes, with a low decomposition temperature and volatile and well defined byproducts ensures the formation of a resultant zinc oxide material with high purity. Additionally, microwave assisted decomposition of this class of precursors in solution has shown to yield stable colloidal nanoparticle dispersions [15,16]. In order to assist the in situ deposition of nanoparticulate zinc oxide onto the wt TMV template, mild microwave synthesis conditions for the zinc oximate precursor were used by us for the first time.

Herein, we report on the fabrication of a functional hybrid semiconducting material based on a microwave assisted ZnO mineralization of the TMV [17]. The resultant TMV/ZnO nanoscale hybrid material exhibits functional transistor behaviour with a reasonable performance without any post-processing at higher temperature.

Experimental section

All reagents were purchased from Sigma-Aldrich or Carl Roth and used as received unless otherwise stated. The molecular precursor, diaqua-bis[2-(methoxyimino)propanato]zinc(II), referred to as the zinc oximato complex in this work, was synthesized as previously reported [14]. The deposition solution was prepared by mixing solutions of the zinc oximato complex and polyvinylpyrrolidone (PVP) (mol. wt ≈ 10k) in methanol and drop wise addition of a solution of tetraethylammonium hydroxide (TEAOH) in methanol, so that the final concentrations were $[Zn^{2+}]$ = 10 mM, [PVP] = 10 mM, and [TEAOH] = 12.5 mM. The microwave reactions were performed in a Discover (CEM Corporation) microwave oven using commercially available glassware supplied by the manufacturer. A few drops of 0.5 mM aqueous zinc acetate solution were deposited on the FET substrate for 5 min and excess was removed and blow-dried under a stream of argon flow. Thereafter, a drop TMV (0.5 µL, 0.5 mg/mL) was placed onto the FET substrate surface and incubated for 10 min. The excess virus suspension was removed by blow drying the substrate under a mild argon flow. The positively charged zinc cations facilitate the efficient immobilization of the negatively charged TMV particles on to the substrate. The FET substrate with the immobilized TMV was immersed in the microwave reaction vessel containing 10 mL of the reaction solution. Reactions were carried out by heating for 30 min, with a maximum applied power of 50 W (dynamic power mode), with an average power of ≈15 W, throughout the experiment. The prefabricated FET substrates (Fraunhofer IWS, Dresden) were sequentially cleaned in an ultra-sonic bath with acetone, DI-water and isopropanol, respectively for ten minutes each, prior to its immersion in the microwave vessel containing the reaction solution. Substrates for the FET devices (15 × 15 mm^2) consisted of n-doped silicon with a 90 nm layer of SiO_2, on which gold electrodes were attached with an intermediate adhesion layer of indium tin oxide. The electrodes possessed an inter-digital structure with a channel width W of 10 mm and a channel length of 20 µm.

^{13}C nuclear magnetic resonance spectroscopy (NMR) was undertaken using a DRX500 (Bruker) spectrometer. Experiments to study the decomposition of the precursor in the microwave were performed by preparing the reaction solution (with and without the TEAOH) in tetra-deuteromethanol (methanol-d_4). The reactions were performed in the absence of the virus to avoid any influence from the TMV. For the NMR studies the

decomposed precursor solution after microwave processing was filtered through a 0.22 μm PTFE syringe filter and was directly analyzed using NMR. Transmission electron microscopy (TEM) was performed using Tecnai F20 G20 (FEI) electron microscope working at 200 kV, using lacey carbon coated copper grids. Dynamic light scattering (DLS) measurements for the ZnO suspensions were carried out using a Zetasizer Nano (Malvern). Atomic force microscopy was performed with CP-II (Bruker-Veeco) microscope using ultra sharp silicon cantilevers. Optical profilometry measurements were performed using the optical Profilometer-NewView 6200 (Zygo). Grazing incidence XRD (GI-XRD) investigations were performed with a Seifert PTS 3003 diffractometer using a Cu anode and a graphite monochromator with an applied current and voltage of 40 mA and 40 kV, respectively. FET characterizations were measured in the dark, using an HP 4155A semiconductor parameter analyzer (Agilent) in a glove box under constant O_2 and H_2O (<0.5 ppm). Charge carrier mobility in the saturation regime μ_{SAT} and the threshold voltage V_{th} were derived from a linear fitting of the square root of the drain-source current (I_{DS}) as a function of the gate–source voltage (V_{GS}).

Tobacco mosaic virus strain U1 was propagated in Nicotiana tabacum 'Samsun' nn plants for 25 days and purified according to the modified protocol of Gooding and Hebert [18].

Results and Discussions

Synthesis and characterization of the wt TMV/ZnO hybrid material

In order to facilitate the controlled mineralization of zinc oxide onto the TMV template, the microwave conditions for synthesis of the zinc oxide in due consideration of the stability of the TMV template had to be optimized. Use of the molecular precursor diaqua-bis[2-(methoxyimino)propanato]zinc(II) [14,19] (referred to as – the zinc oximato complex – in the following) as a source of zinc oxide was employed, herein. Solutions for the controlled formation and deposition of the ZnO nanoparticles were obtained by using a methanolic solution of zinc complex as a zinc source and polyvinylpyrrolidone (PVP) as a growth inhibiting and stabilizing agent for the zinc oxide nanoparticles. PVP has been reported to have a higher efficiency in suppressing the growth of zinc oxide during its formation, in comparison to other polymeric additives [20]. Additionally, a defined amount of tetraethylammonium hydroxide (TEAOH) was added to the precursor solution to create a mild basic environment which assists the controlled formation of the ZnO nanoparticles.

The addition of the optimal amount of the base TEAOH provides mild but sufficient basic conditions to ensure an efficient decomposition of the zinc complex at a low temperature as 60 °C (±3 °C) enabling the successful formation of crystalline zinc oxide. An increased reaction rate, although, with a rapid formation of zinc oxide resulting in unstable aggregates ranging up to several hundred nanometres in size, was observed in the presence of higher amounts of the base. In order to gain insight into the microwave decomposition process of the molecular precursor, the microwave decomposition process was studied in the absence and presence of the base TEAOH using ^{13}C NMR spectroscopy. Without the addition of the base, the precursor complex did not undergo any decomposition after the completion of the microwave reaction under typical reaction conditions. However, in the presence of the base, the precursor does undergo decomposition with appearance of a characteristic ^{13}C chemical shift corresponding to the formation of acetonitrile (δ = 117.30 ppm) under post decomposition conditions of the precursor complex. Additional chemical shifts from still coordinated as well as from residual free ligands were also present as expected due to the base-catalyzed decomposition of the precursor complex (see Supporting Information File 1, Figure S2). The products observed in the microwave initiated decomposition of the oximato complex is in full accordance with a second-order type Beckmann rearrangement reaction as observed for its solution based thermal decomposition pathway [13]. Besides the characteristic signals of the decomposition products, chemical shifts from the undecomposed precursor are still observed after the completion of the microwave reaction. Attempts to completely decompose the precursor were not pursued since long reaction time lead to the formation of undesirable precipitates of zinc oxide aggregates, in a very similar way as addition of excess base TEAOH does. Thus it can be concluded that the microwave decomposition reaction has to be fine tuned in order to obtain pure precipitates of the desired nanoscale ZnO product. A comprehensive reaction and decomposition pathway of the precursor can thus be proposed on the basis of the observed decomposition products from the described NMR experiments (Figure 1).

Systematic experiments have shown that a maximum microwave power of 50 W, temperature of 60 °C (±2 °C) and a synthesis time of 30 min display the optimum conditions leading to the formation of nanocrystalline ZnO. Dynamic light scattering measurements indicate the formation of stable ≈5 nm particles, after a synthesis period of 30 min (see Supporting Information File 1, Figure S1). The indicated particle size is in good agreement with HRTEM investigations of the as-synthesized particles formed from the precursor solution, which yield stable zinc oxide nanoparticles (Figure 2a). TEM also indicates the successful formation of ZnO nanocrystals in solution after the completion of the microwave irradiation process. Grazing incidence X-ray diffractometry (GI-XRD) analysis was employed to gain a deeper insight into the crystallinity of the as deposited

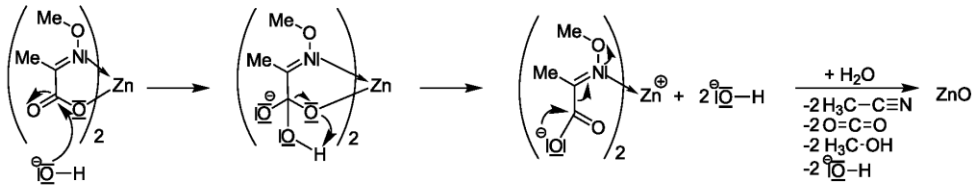

Figure 1: Schematic representation of the microwave decomposition pathway of the zinc oximato precursor in the presence of TEAOH as a base based on NMR spectroscopy. Note that the water ligands are omitted in the starting compound.

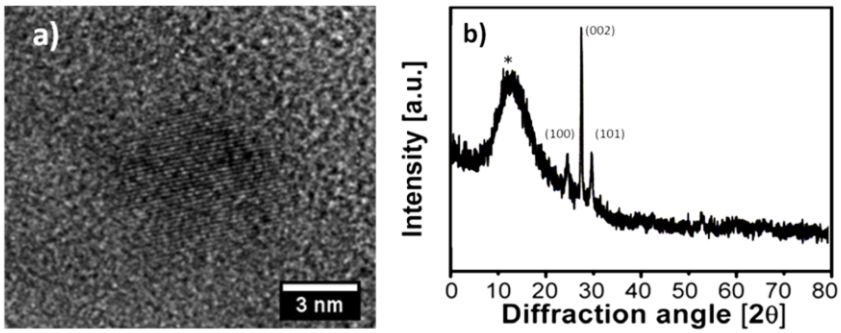

Figure 2: a) HRTEM image of the ZnO nanoparticle obtained from solution and b) GI-XRD spectra of the ZnO thin film after 6 deposition cycles (* = peak intensity arising from the Si/SiO_2 substrate).

ZnO thin film. The ZnO films display a polycrystalline nature of the ZnO being essential for the formation of an active semiconducting layer. Reflection peaks corresponding to the (100), (002) and (101) planes are characteristic of the zincite structure (Figure 2b). A greater intensity in the direction of the c-axis (i.e., perpendicular to the (002) plane) was observed. ZnO nanoparticles undergo an oriented attachment during thin film formation in the presence of PVP which hints at texturing of the ZnO nanoparticles within the deposited ZnO film [21,22].

In order to perform an in situ microwave-based mineralization of the TMV, it is essential to ensure that the virus particle adheres to the substrate during the microwave irradiation. Intense microwave irradiations are known to have a strong tendency to denature proteins and cause potentials damage to its structural integrity [23]. Additionally, prolonged high-power microwave irradiation could lead to unexpected heating of the substrate onto which the TMV are immobilized. The substrates with the docked virus were thus immersed in a control methanolic solution containing the predetermined amounts of the TEAOH and PVP in the absence of the zinc precursor. These substrates were then subjected to the desired microwave irradiation time of 30 min. This ensures that the virus particles do not detach from the substrate. AFM investigations for a control experiment reveal an intact TMV template on the Si/SiO_2 substrate, even after 30 min of mild microwave irradiation showing no visible deformation of its rod-like structure and its original dimensions and morphology (Figure 3a). Irradiation of the reference solution containing the virus-coated substrate with higher microwave power led to uncontrolled, rapid increase of the solution temperature and boiling of the solvent methanol (bp ≈ 65 °C). This led to a detachment of the viruses as no visible virus structures afterwards could be detected on the substrate surface by AFM analysis after this procedure. Once the reliable microwave conditions of the virus attachment and the retention of its structural integrity were confirmed, the virus-coated substrates were immersed in the reaction solution which then leads to the mineralization of the zinc oxide nanoparticles onto the virus template. Such successful mineralization of the zinc oxide onto the TMV template is obtained under low power microwave assisted decomposition of the precursor solution (Figure 3b). Hence, reliable docking of the TMV onto the silicon/silicondioxide (Si/SiO_2) and simultaneous formation of zinc oxide nanoparticles could be achieved. AFM analysis for the bare TMV layer as well as the ZnO mineralized TMV layer after one deposition cycle reveal an average layer thick-

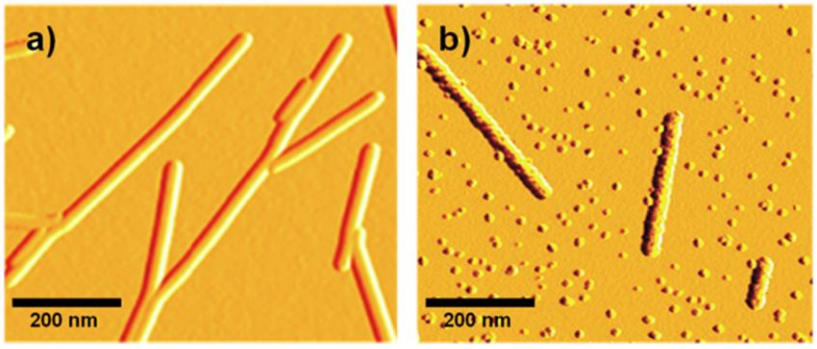

Figure 3: AFM micrographs of (a) the bare wt TMV template immobilized on a Si/SiO_2 substrate as well as (b) the wt TMV template after 1 cycle of ZnO mineralization.

ness of 15.5 nm and 25.8 nm respectively (see Supporting Information File 1, Figure S3).

In order to ensure an optimum thickness and to promote a good transistor performance ZnO layers with increasing number of deposition cycles were analyzed. The increasing thickness of the ZnO films after various cycles was measured using optical profilometry (Figure 4).

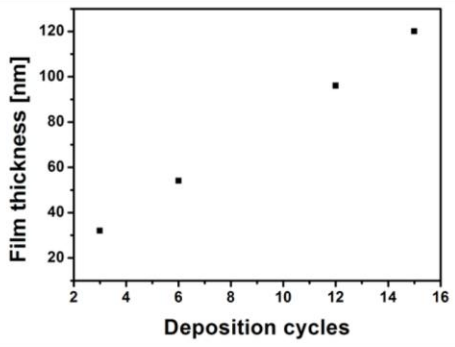

Figure 4: Overall thickness of the wt TMV/ZnO hybrid material as a function of the number of deposition cycles as determined by optical profilometry. ZnO was deposited onto the wt TMV template with an increasing number of deposition cycles from the precursor solution.

The thickness and uniformity of the deposited semiconductor layer bear a crucial importance for FET device performance [12]. Variation in the layer thickness severely affects the transistor performance. For example, a thicker layer increases the resistance across the active material, while thinner layers could possibly lead to non-uniform layer deposition [24]. Therefore the layer thickness should be optimized according to these parameters.

Field effect transistor (FET) properties

In order to assess its FET properties, the wt TMV/ZnO hybrid material template was realised in a bottom gate, bottom contact FET geometry, by employing pre-fabricated FET substrates with external gold electrodes. All fabricated devices exhibit functional transistor properties without any post-processing treatment. As a reference we had measured the electrical characteristics of microwave processed bare nanoscale ZnO without TMV, obtained again from the molecular zinc oximato precursor complex under similar conditions. These results showed only noisy and almost indiscernible signals (measurements not shown). This fact substantiates the point that the FET properties are indeed intrinsic for the microwave processed wt TMV/ZnO hybrid material. Similar results have been reported for thermally processed bare nanoscale ZnO material using the zinc oximato complex as precursor [13].

The transistor behaviour of the wt TMV/ZnO hybrid material was then optimized based on the crucial characteristic FET values, current on/off ratio ($I_{on/off}$), threshold voltage (V_{th}) and charge carrier mobility (μ) which are considered to be essential parameters for the FET performance. Based on these performance parameters, the electrical characteristics of the devices display a stark contrast due to the difference in the number of ZnO deposition cycles which led to the formation of thicker layers. FET characteristics of the ZnO films with increased layer thickness are displayed below (Figure 5 and Table 1).

Fewer deposition cycles (3 cycles) for the ZnO exhibited very weak transfer characteristics with significantly low On and well as Off currents, high V_{th} and poor mobility values. On the other hand, increased number of deposition cycles (12 cycles) of the ZnO led to a slight increase in the mobility values. Also, a positive increase in the On currents accompanied by a drastic

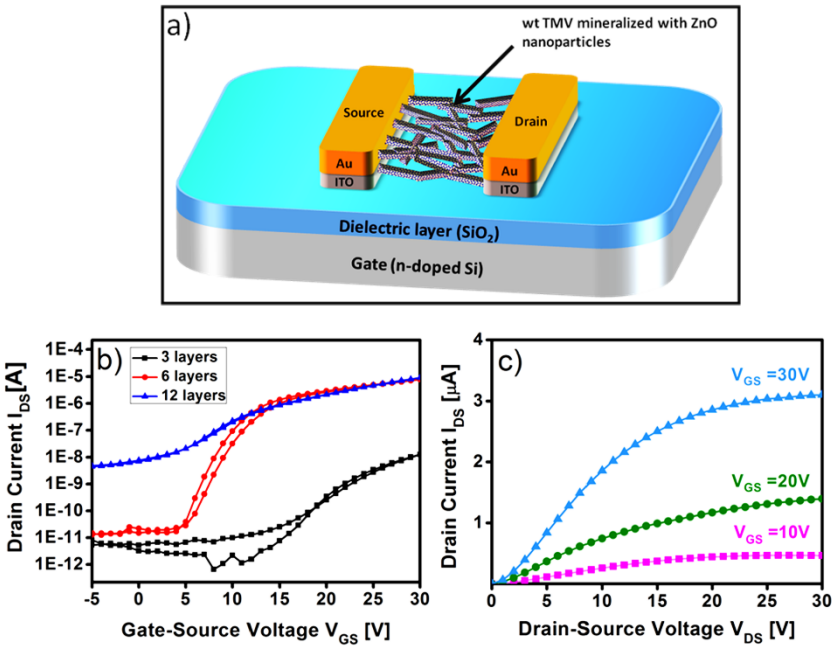

Figure 5: Schematic representation of the wt TMV/ZnO based FET device (a). Performance of the FET device fabricated by increasing the number of ZnO deposition cycles on the wt TMV template; (b) Transfer characteristics for constant drain–source voltage at 30 V; (c) output characteristics of TMV/ZnO hybrid after 6 deposition cycles, obtained at drain–source voltage of 30 V, for gate–source voltage varied from 0–30 V in 10 V steps.

Table 1: Characteristic values for field-effect mobility μ, threshold voltage (V_{th}), and on/off current ratio ($I_{on/off}$) of wt TMV/ZnO hybrid material based transistor devices.

ZnO deposition cycles	μ (mobility in cm^2/Vs)	V_{th} (V)	$I_{on/off}$
3	8.0×10^{-6}	17.79	10.2×10^2
6	6.7×10^{-4}	4.76	9.0×10^5
12	8.4×10^{-4}	6.80	2.1×10^3
15	1.6×10^{-3}	12.02	1.0×10^2

increase in the Off currents led to a deteriorated $I_{on/off}$ ratio. Moreover, an undesirable higher V_{th} value was observed. Further increase in the number of deposition cycles (15 cycles) deteriorated the overall transistor performance giving no significant semiconducting properties. For an optimum number (6 cycles) of ZnO deposition, the best overall FET performance values were obtained with a field-effect mobility (μ) of 6.7×10^{-4} cm^2/Vs, V_{th} of +4.7 V and an $I_{on/off}$ of 9.0×10^5. A higher $I_{on/off}$ in comparison to previously reported values could possibly be attributed to a greater degree of ZnO nanoparticle orientation on the wt TMV template resulting from the use of the molecular precursor complex employed [25].

Conclusion

The ability of the virus template to maintain its structural integrity under mild microwave radiations, while facilitating the deposition of zinc oxide nanoparticles has been implemented for virus-based templating of inorganic nanomaterials, towards functional devices with diverse applications. We have successfully employed a molecular precursor to synthesize zinc oxide nanoparticles, for an in situ deposition on to a virus template. A facile, microwave-assisted approach for generating a TMV/ZnO hybrid bio-inorganic material has been implemented. We confirmed the clean in situ decomposition of the molecular precursor under mild conditions as well as the desired zinc oxide phase formation by resonance, diffractometry and microscopic methods. Moreover, the as-synthesized hybrid material has been successfully employed in a FET device. The best FET performance has been achieved by systematically controlling the thickness of the deposited zinc oxide films. The fabricated FET shows a reasonable performance for the as-prepared device, without any post processing of the bio-inorganic hybrid nanomaterial. Such an approach towards generation of a bio-inorganic material encourages the use of nanoscale virus templates to obtain hybrid materials with functional properties that can be implemented into future device applications.

Supporting Information

Supporting Information File 1
Additional figures.
[http://www.beilstein-journals.org/bjnano/content/supplementary/2190-4286-6-81-S1.pdf]

Acknowledgements

This work has been supported within the DFG SPP 1596, and the Cooperative Research Lab Alliance between Merck KGaA, Darmstadt, and Technische Universität Darmstadt (Merck Lab). We thank Dr. J. Engstler (TEM) and Dr. J. Brötz (GI-XRD) at Technische Universität Darmstadt for material characterizations. TEM studies at ERC, Jülich, Germany, are supported through the ERC-TUD1 contract collaboration. SS would like to acknowledge discussions with Dr. M. Nowotny concerning the NMR studies.

References

1. Sanchez, C.; Julián, B.; Belleville, P.; Popall, M. *J. Mater. Chem.* **2005,** *15*, 3559–3592. doi:10.1039/B509097K
2. Wen, J.; Wilkes, G. L. *Chem. Mater.* **1996,** *8*, 1667–1681. doi:10.1021/cm9601143
3. Niemeyer, C. M. *Angew. Chem.* **2001,** *113*, 4254–4287. doi:10.1002/1521-3757(20011119)113:22<4254::AID-ANGE4254>3.0.CO;2-D
4. Mirkin, C. A.; Letsinger, R. L.; Mucic, R. C.; Storhoff, J. J. *Nature* **1996,** *382*, 607–609. doi:10.1038/382607a0
5. Hoffmann, R. C.; Atanasova, P.; Dilfer, S.; Bill, J.; Schneider, J. J. *Phys. Status Solidi A* **2011,** *208*, 1983–1988. doi:10.1002/pssa.201127064
6. Chen, C.-L.; Rosi, N. L. *Angew. Chem., Int. Ed.* **2010,** *49*, 1924–1942. doi:10.1002/anie.200903572
7. Gazit, E. *Chem. Soc. Rev.* **2007,** *36*, 1263–1269. doi:10.1039/B605536M
8. Scolaro, L. M.; Castriciano, M. A.; Romeo, A.; Micali, N.; Angelini, N.; Lo Passo, C.; Felici, F. *J. Am. Chem. Soc.* **2006,** *128*, 7446–7447. doi:10.1021/ja061726j
9. Shenton, W.; Douglas, T.; Young, M.; Stubbs, G.; Mann, S. *Adv. Mater.* **1999,** *11*, 253–256. doi:10.1002/(Sici)1521-4095(199903)11:3<253::Aid-Adma253>3.0.Co;2-7
10. Balci, S.; Hahn, K.; Kopold, P.; Kadri, A.; Wege, C.; Kern, K.; Bittner, A. M. *Nanotechnology* **2012,** *23*, 045603. doi:10.1088/0957-4484/23/4/045603
11. Sun, B.; Sirringhaus, H. *Nano Lett.* **2005,** *5*, 2408–2413. doi:10.1021/nl051586w
12. Hoffman, R. L.; Norris, B. J.; Wager, J. F. *Appl. Phys. Lett.* **2003,** *82*, 733–735. doi:10.1063/1.1542677
13. Atanasova, P.; Rothenstein, D.; Schneider, J. J.; Hoffmann, R. C.; Dilfer, S.; Eiben, S.; Wege, C.; Jeske, H.; Bill, J. *Adv. Mater.* **2011,** *23*, 4918–4922. doi:10.1002/adma.201102900
14. Schneider, J. J.; Hoffmann, R. C.; Engstler, J.; Dilfer, S.; Klyszcz, A.; Erdem, E.; Jakes, P.; Eichel, R. A. *J. Mater. Chem.* **2009,** *19*, 1449–1457. doi:10.1039/B816376F
15. Schneider, J. J.; Hoffmann, R. C.; Engstler, J.; Klyszcz, A.; Erdem, E.; Jakes, P.; Eichel, R.-A.; Pitta-Bauermann, L.; Bill, J. *Chem. Mater.* **2010,** *22*, 2203–2212. doi:10.1021/cm902300q
16. Sanctis, S.; Hoffmann, R. C.; Schneider, J. J. *RSC Adv.* **2013,** *3*, 20071–20076. doi:10.1039/C3RA44222E
17. Lipowsky, P.; Hoffmann, R. C.; Welzel, U.; Bill, J.; Aldinger, F. *Adv. Funct. Mater.* **2007,** *17*, 2151–2159. doi:10.1002/adfm.200600399
18. Gooding, G. V.; Hebert, T. T. *Phytopathology* **1967,** 1285.
19. Schneider, J. J.; Hoffmann, R. C.; Engstler, J.; Soffke, O.; Jaegermann, W.; Issanin, A.; Klyszcz, A. *Adv. Mater.* **2008,** *20*, 3383–3387. doi:10.1002/adma.200800819
20. Guo, L.; Yang, S.; Yang, C.; Yu, P.; Wang, J.; Ge, W.; Wong, G. K. L. *Chem. Mater.* **2000,** *12*, 2268–2274. doi:10.1021/cm9907817
21. Niwa, D.; Fujie, T.; Lang, T.; Goda, N.; Takeoka, S. *J. Biomater. Appl.* **2012,** *27*, 131–141. doi:10.1177/0885328210394470
22. Lipowsky, P.; Jia, S.; Hoffmann, R. C.; Jin-Phillipp, N. Y.; Bill, J.; Rühle, M. *Z. Metallkd.* **2006,** *97*, 607–613. doi:10.3139/146.101278
23. Bohr, H.; Bohr, J. *Phys. Rev. E* **2000,** *61*, 4310–4314. doi:10.1103/PhysRevE.61.4310
24. Zhang, L.; Zhang, H.; Bai, Y.; Ma, J. W.; Cao, J.; Jiang, X.; Zhang, Z. L. *Solid State Commun.* **2008,** *146*, 387–390. doi:10.1016/j.ssc.2008.03.036
25. Meulenkamp, E. A. *J. Phys. Chem. B* **1999,** *103*, 7831–7838. doi:10.1021/jp9914673

License and Terms

6.5 Understanding the temperature-dependent evolution of solution processed metal oxide transistor characteristics based on molecular precursor derived amorphous indium zinc oxide.

Low-temperature solution processing of amorphous oxide semiconductors has been an area of significant research with a potential to fabricate them onto plastic substrates, eventually enabling the possibility of flexible electronics. Among the most popular routes, combustion processing of metal salts and alkoxide based precursors has been shown as a promising approach in this direction. Although these processes offer remarkable TFT performances, they still require careful adjustment of the precursor solutions by incorporation of additives or processing under inert atmosphere conditions, respectively. The employment of complex precursor mixtures as in the case of combustion processing can also be disadvantageous with respect to the choice of solvents and lead to problems with substrate wetting and void formation in the final ceramic from excessive gaseous by-products. Due to these drawbacks the employment of combustible, air-stable precursors without the use of additional additives paves the way for an improved low-temperature solution-processing technique.

In this publication, we employ specifically designed multimetallic zinc and indium coordination compounds, $[Zn_4O(dmm\text{-}NO)_6]$ and $In_3O_3(dmm\text{-}NO_2)_3\cdot$(toluene) with nitro- and nitroso-functionalized dimethylmalonato ligands for the synthesis of semiconducting indium zinc oxide (IZO) thin films with very good to high performance in TFT applications even at low processing temperatures, starting at 250 up to 450°C. These precursors exhibit excellent stablity under ambient conditions in the solid state as well as in non-toxic iso-propanol solutions. The precursor mixture with an In : Zn = 6 : 4 ratio, exhibited a strongly exothermic decomposition in an oxygen atmosphere. The main significant and most obvious decomposition step occurred at ~150°C, whereby the majority of the mass loss of the mixture was already observed, wherein the tracable by-products via TG coupled IR spectroscopy included volatile, dimethyl carbonate, methanol, carbon monoxide and carbon dioxide. Furthermore, positron anhillation spectroscopy of the investigated IZO processed between 250°C and 450°C, reveal the the film at 250°C have a shorter diffussion length L (2±1)nm in comparison with films annealed a 300°C with an L (25±3)nm, clearly indicating a significant reduction in defect concentration at higher temperatures with improved diffusion lengths. IZO TFTs Devices annealed only at 300 °C already demonstrate a robust FET performance with (μ_{sat}) of 2.1 cm^2/V.s, V_{th} of +11.5 V and an $I_{on/off}$ of 3.3×10^7 greater than that of the conventional amorphous hydrogenated silicon and

also displays its potential to use integrated with plastic compatible temperatures ≤ 300ºC, towards flexible electronics.

Journal of Materials Chemistry C

PAPER

View Article Online
View Journal | View Issue

Cite this: J. Mater. Chem. C, 2016, 4, 10935

Understanding the temperature-dependent evolution of solution processed metal oxide transistor characteristics based on molecular precursor derived amorphous indium zinc oxide†

Shawn Sanctis,[a] Rudolf C. Hoffmann,[a] Ruben Precht,[b] Wolfgang Anwand[c] and Jörg J. Schneider*[a]

Received 8th September 2016,
Accepted 26th October 2016

DOI: 10.1039/c6tc03915d

www.rsc.org/MaterialsC

Amorphous indium zinc oxide (IZO) thin films are accessible by solution-deposition of mixtures of molecular single-source precursors with dimethyl 2-hydroxyimino- and 2-nitromalonato ligands (dmm-NOH and Hdmm-NO_2, respectively). Thermal combustion of the precursor molecules $In_3O_3(dmm\text{-}NO_2)_3$·(toluene) and $[Zn_4O(dmm\text{-}NO)_6]$ leads to a highly exothermic decomposition reaction yielding amorphous indium zinc oxide (IZO) even at a temperature of 150 °C. The main aim of the present investigation is to correlate the electronic performance in such solution processed field-effect transistors (FET) with the presence of surface groups and bulk defects depending on the processing temperatures of the resulting IZO films (250 to 400 °C). In depth electronic characterization using X-Ray- and Photoelectron Emission Spectroscopy (XPS and UPS) reveals major electronic changes during thin film formation in the temperature range between 275 and 300 °C. These findings are confirmed by Positron Annihilation Spectroscopy (PAS) which allows the monitoring of defects in a picometer range in the resulting functional IZO thin films. Resulting transistor mobilities (μ) of the semiconducting IZO films are in the range of those of amorphous silicon even at a processing temperature of 250 °C and increase up to 6 and 9.5 cm^2 $(V\ s)^{-1}$ at 350 and 400 °C with on/off ratios of 105 up to 107, respectively.

1. Introduction

Transparent, amorphous metal-oxide thin film transistors (MO-TFTs) have been of great interest in recent years, due to their vast applicability in the field of next-generation displays.[1–3] The shift from classical silicon technology with its established techniques for integration and miniaturization has also opened up a view for a wider use of the metal oxide materials utilising their inherent advantages. Solution processing offers an economically viable route for the coating of large areas in comparison with conventional counterparts realized primarily *via* vacuum deposition techniques.[4–6] The electronic performance of solution processed semiconductors in MO-TFT devices is already competitive, however further progress in this field requires the manufacturing of films with a well-defined microstructure and phase constitution. This in turn calls for an in depth understanding of their properties. More practical challenges are to decrease the processing temperature for such oxide thin film materials further in order to ensure their compatibility with a wider variety of substrates and other components of the MO-TFT device. Typically an annealing step is applied in order to convert a suitable precursor compound into a functional oxide. This calcination step is often delicate since it includes the transition from a defined molecular state of matter in the molecular precursor into an amorphous ceramic material in the functional oxide. This involves a number of steps such as the removal of adherent surface molecules, *e.g.* ambient gases, moisture, residual solvents and most importantly a well defined route of decomposition of the precursor molecule. Finally introducing or eliminating point defects in the final oxide material by this process might be highly important to tune the electronic performance in the finally obtained thin film oxidic TFT material.[5,6] So far, several types of precursors have been investigated for the effective reduction of the processing temperature in TFT manufacturing. Among them, combustion processing of metal salts[7,8] and alkoxide based precursors[9–11] has been shown as a promising approach in this direction.

[a] Fachbereich Chemie, Eduard-Zintl-Institut, Fachgebiet Anorganische Chemie, Technische Universität Darmstadt, Alarich-Weiss-Straße 12, 64287, Darmstadt, Germany. E-mail: joerg.schneider@ac.chemie.tu-darmstadt.de
[b] Fachgebiet Oberflächenforschung, Technische Universität Darmstadt, Jovanka-Bontschits-Straße 2, 64287, Darmstadt, Germany
[c] Institut für Ionenstrahlphysik und Materialforschung, Helmholtz-Zentrum Dresden-Rossendorf, Bautzner Landstraße 400, 01328 Dresden, Germany

† Electronic supplementary information (ESI) available: Additional IR, TG/IR and AFM data. See DOI: 10.1039/c6tc03915d

Although these processes offer remarkable TFT performances, they still require careful adjustment of the precursor solutions by incorporation of additives or processing under inert atmosphere conditions, respectively. The employment of complex precursor mixtures as in the case of combustion processing can also be disadvantageous with respect to the choice of solvents and lead to problems with wetting on the substrate surface.[12] Therefore spray-coating was suggested as an alternative to spin-coating or printing techniques.[13] Due to these drawbacks the search for other unique approaches which avoid *e.g.* the usage of additional additives or the need for dedicated reaction conditions is promising. Clearly, the goal could be to build on the current knowledge *e.g.* the advantage of the established combustion process for metal salts and to extend that by using dedicated, easy to manipulate precursor molecules and also most easily to apply solution based coating processes for the deposition of high performance semiconducting metal oxide materials. Such developments could also lead to further insight into mechanisms which generate high electrical performance in amorphous metal oxide TFT materials.

Selectively tailored, air stable single-source precursors offer an attractive route for obtaining functional metal oxide semiconductors at low decomposition temperatures.[14,15] The optimized construction of the ligand framework around the metal cation allows the adjustment of the detailed chemical and physical properties of the precursor molecule. Thus, a well determined decomposition pathway of metal oxide precursors in defined and controllable steps could be achieved. Furthermore homogeneous metal oxide layers after drying and thermal processing could be obtained.[16,17]

In this work we extended our single source precursor approach to the synthesis of semiconducting indium zinc oxide (IZO) thin films with very good to high performance in TFT applications even at low processing temperatures, starting at 250 up to 450 °C. Our approach employs specifically designed multimetallic zinc and indium coordination compounds with nitro- and nitroso-functionalized dimethylmalonato ligands. To the best of our knowledge, this class of precursors has not been investigated to fabricate multinary amorphous metal oxides before. They are stable under ambient conditions in the solid state as well as in solution. Their transformation proceeds without additional additives under moderate thermal conditions in a well defined decomposition process and without contamination from stabilizing ligand molecules. Finally they allow an attractive ceramisation yield giving an amorphous IZO material exhibiting very good to excellent semiconducting properties even at as low as 250 °C. Employing photoelectron as well as positron annihilation spectroscopy allows us to gain insights into the electronic and morphological situation of amorphous semiconductor films derived from novel zinc and indium coordination compounds with nitro- and nitroso-functionalized dimethylmalonato ligands as single source precursor molecules.

2. Results and discussion

2.1. Precursor synthesis

In a recent investigation we reported the reaction of functionalised dimethyl malonates, dimethyl 2-hydroxyimino- and 2-nitromalonate

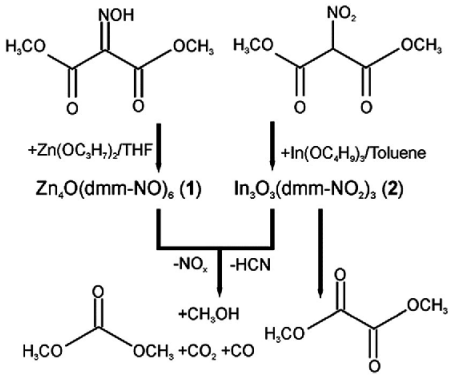

Scheme 1 Schematic representation of the synthesis of precursor molecules (**1**) and (**2**) and their decomposition showing the traceable product formation observed by thermal decomposition of (**1**) and (**2**) as analyzed by TG/MS and TG/IR coupled analysis.

(dmm-NOH and Hdmm-NO_2, respectively) with various zinc(II) compounds yielding the complexes $[Zn_4O(dmm\text{-}NO)_6]$ (**1**) and $[Zn_3(OH)_4(dmm\text{-}NO_2)_2]$ (**2**)[16] The corresponding reaction of indium butoxide with dmm-NOH, however, resulted only in a sparingly soluble product in low yield. In a second series of reactions under inert conditions, the addition of Hdmm-NO_2, however, leads to a coordination compound with a nominal composition $[In_3O_3(dmm\text{-}NO_2)_3]$ (**2**) (Scheme 1). The compound precipitated directly from toluene solution, whereas the reaction in tetrahydrofuran or methyl *tert*-butyl ether required the addition of pentane for precipitation and isolation of the product. According to the IR spectrum (Fig. S1, ESI†) no hydroxo groups are present in compound (**2**), which is in contrast to the zinc complex $[Zn_3(OH)_4(dmm\text{-}NO_2)_2]$, which we have investigated intensively in earlier work.[16]

Recently, we were able to isolate and characterize $Al(dem\text{-}NO_2)_3$ (**3**) with the homologous diethyl 2-nitromalonate (Hdem-NO_2) ligand (C_2H_5 instead of CH_3 in the dmm ligand).[18] (**3**) exhibits an octahedral coordination around aluminum (Fig. 1).

From a coordination chemistry point of view indium complexes with comparable oxygen containing Lewis bases like O_2 or OH frequently adopt more complex structures containing bridging μ-O or μ-OH units than aluminum complexes such as (**3**).

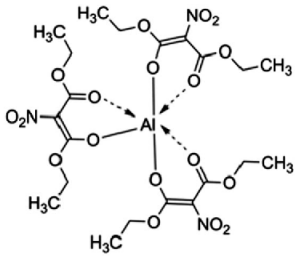

Fig. 1 Molecular structure of the octahedral Al (nitro-malonato) complex (**3**).[18]

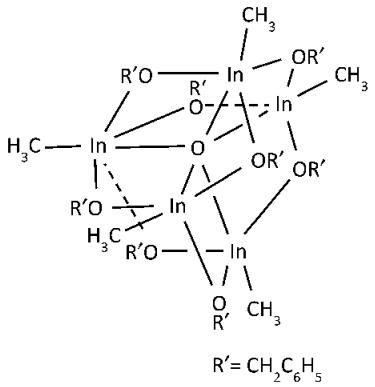

Fig. 2 Polynuclear molecular structure of $[(CH_3In)_5(O)(OCH_2C_6H_5)_8]$ (**4**).[19]

Indium oxo-alkoxides $[In_nO_m(OR)]_o$ (**4**) are a prototype polycyclic example proving this structural nuclearity difference between Al and In (Fig. 2).[19,20]

Similar metal–oxygen cage structures are found in heterometallic indium/tin complexes.[21] Furthermore $[In_2O_2]$ or $[In_3O_3]$ ring moieties are observed in such oligomeric cage structures with μ_2-OH bridging units.[22,23] The multivalency of indium with In(I) and In(III) compared to Al (solely III) metal centers allows for such mixed metal (I, III) oxidation states in the oxo/alkoxy indium clusters as in (**4**) able to realize a wider structural diversity than aluminum.

The thermal decay of (**2**) proceeds in a multistep route (Fig. S2, ESI†). The gaseous reaction products formed were analysed by means of IR spectroscopy (Fig. S3, ESI†), which showed that a plethora of products were formed during conversion to the oxide phase. In contrast to the decomposition of the before-mentioned zinc complexes (**1**) and (**2**), dimethyloxalate (at ~1150 and 1200 cm^{-1}, C–O–C valence vibrations[24]) was detected in addition to dimethylcarbonate (at ~1765 cm^{-1} as well as 1445 cm^{-1} and 1277 cm^{-1}) and methanol (at ~1033 cm^{-1} as well as in the region between 3600 and 3750 cm^{-1}) besides smaller molecules such as carbon dioxide or carbon monoxide (Fig. S2, ESI†). Surprisingly, though, mixtures of (**1**) and (**2**) proved very advantageous for the synthesis of ternary indium tin oxide (IZO). Thermal analysis showed that in contrast to complexes (**1**) and (**2**) alone (Fig. S2, ESI†) a combination of these precursors underwent a very rapid and sharp thermal decomposition in a single step. The results of the TG and DSC measurements are shown in Fig. 3. The precursor mixture with an In to Sn ratio In : Zn = 6 : 4 exhibited a strongly exothermic decomposition in an oxygen atmosphere. The main significant and most obvious decomposition step occurred at ~150 °C, whereby the majority of the mass loss of the 6 : 4 mixture of (**1**) and (**2**) was already observed. This major decomposition was followed only by a very minor and gradual further mass loss at higher temperatures. This unique observation is quite unexpected and points to a synergistic effect of both compounds during their thermal decomposition into the binary mixed metal oxides.

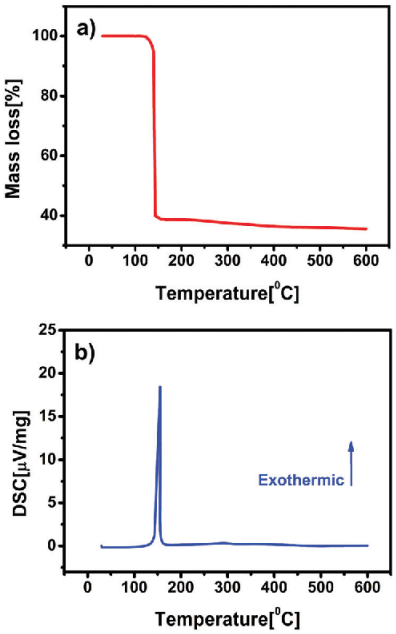

Fig. 3 (a) Thermogravimetric analysis (TGA) and (b) differential scanning calorimetry (DSC) analysis of 6 : 4 mixtures of the precursors (**1**) and (**2**) in oxygen.

Additionally, these functionalized malonato precursor molecules afford reasonable solubility as well as smooth and homogenous film coverage using iso-propanol as a solvent. Using such a low boiling point and a relatively non-toxic solvent in contrast to the most often used 2-methoxyethanol as a solvent has proven to be advantageous with regard to the final device performance.[25,26] Thin films were produced by spin-coating precursor solutions of (**1**) and (**2**) on quartz slides and consequently annealed at temperatures ranging from 250 °C to 400 °C. AFM investigations revealed that the IZO films fabricated at different calcination temperatures all gave smooth and uniform ceramic films (Fig. S4, ESI†). The obtained films from the spin coated precursor mixtures which were calcined at 300 °C and exhibited a reduced roughness (RMS = 0.1 nm) when compared to the 250 °C thin film. This fact hints towards an expected densification of the final ceramic due to Ostwald ripening with increased annealing temperatures.

Grazing-incidence XRD measurements (Fig. 4) showed that the resulting metal oxide films were amorphous in all cases when employing different annealing temperatures. No indications of crystalline phases such as zincite (ZnO) or bixbyite (In_2O_3) were thus observed. This was further confirmed by HRTEM investigations (Fig. 5). Therefore, the simultaneous decomposition of the precursors (**1**) and (**2**) inhibits the formation of interdispersed nanocrystalline phases, thus resulting in a completely amorphous IZO material at different length scales and annealing conditions.

Formation of individual nanocrystalline indium oxide within the amorphous IZO matrix has shown to deteriorate

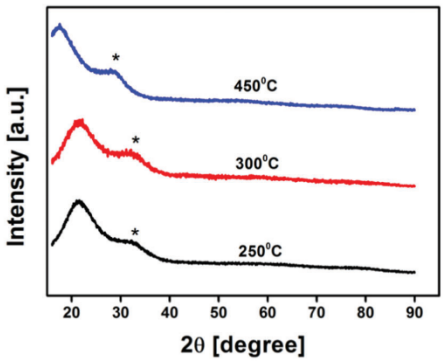

Fig. 4 GI-XRD diffractograms of IZO thin films annealed at 250 °C, 300 °C and 450 °C. The broad peak indicated by (*) arises from the quartz substrate.

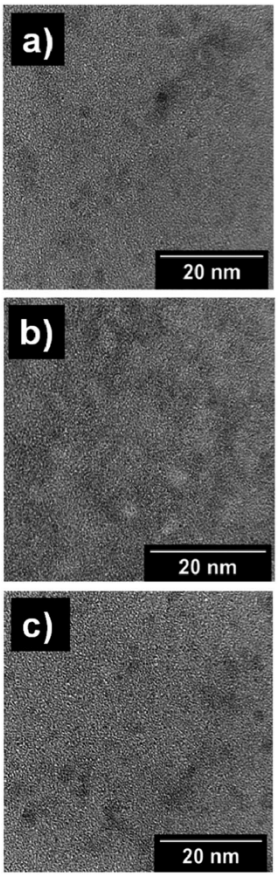

Fig. 5 HRTEM images of IZO thin films obtained from mixtures of (**1**) and (**2**) annealed at 250 °C, 300 °C and 450 °C. For all three calcination temperatures the obtained IZO material is amorphous.

the TFT performance of IZO.[14,27] The combination of the molecular precursors (**1**) and (**2**) employed herein does not only have the advantage that they decompose in a very narrow temperature window, but even at the same temperature point in time. In this way our approach is comparable to the combustion synthesis procedure which, however, typically starts with mixtures of several different precursor components with different chemical behavior as a significant methodological difference. Our approach has the ultimate advantage of employing no additional compounds which in fact need no further fine tuning of the experimental conditions of semiconductor film deposition.[8]

2.2. Thin film transistor studies

A series of FET devices with a bottom gate/bottom contact set-up were manufactured on prefabricated substrates (support/gate: highly n-doped silicon, dielectric is silicon dioxide and inter-digital gold electrodes as contacts). The films were obtained by spin-coating and annealing on a hotplate at temperatures from 250 to 450 °C in air. The transfer and output characteristics of the various FET devices are displayed below (Fig. 6). The FET characteristics of the devices annealed at an even higher temperature of 450 °C have been separately displayed to keep in line with the above mentioned temperature regime (Fig. S6, ESI†). The key performance parameters of these devices, namely the saturation mobility (μ_{sat}), threshold voltage (V_{th}) and the current on–off ratio, are listed in Table 1. A total of eight devices were measured for each of the investigated annealing temperatures and the statistics for the key parameters are displayed (Fig. S5, ESI†). Active semiconductor performance was observed for all of the investigated temperatures.

Devices annealed at 300 °C and higher demonstrate a robust FET performance with charge carrier mobilities greater than that of the conventional amorphous hydrogenated silicon which is typically ≤ 1 cm^2 (V s)$^{-1}$.[28] It is interesting to observe that devices annealed at 250 °C and 275 °C show modest transfer characteristics, although they exhibit a relatively higher degree of hysteresis and a weak current saturation, in comparison with devices annealed at higher temperatures (see Fig. 6a). Furthermore, the output characteristics at these temperatures show a weak dependence on the gate voltage modulation which is undesired in terms of its applicability (Fig. 6b and c). Devices annealed at 300 °C and above show a higher mobility of >1 cm^2 (V s)$^{-1}$ and also a high on–off ratio of $>10^7$.

2.3. XPS and UPS investigations

XPS investigations were performed for IZO films annealed at different temperatures, in order to monitor the evolution of IZO metal oxide formation from the molecular precursor thin films (Fig. 7). The deconvoluted O1s XPS spectra are of particular interest to understand the origin of bulk defects and surface adsorbates.[9,29] For the curve fitting the superposition of two components centered at around 530 and 532 eV was taken into account. These signals reflect contributions from oxidic oxygen ($\sim$530 eV) as well as surface hydroxylation ($\sim$532 eV). The latter is commonly observed on most metal oxide surfaces as an ubiquitous surface layer when samples are prepared under

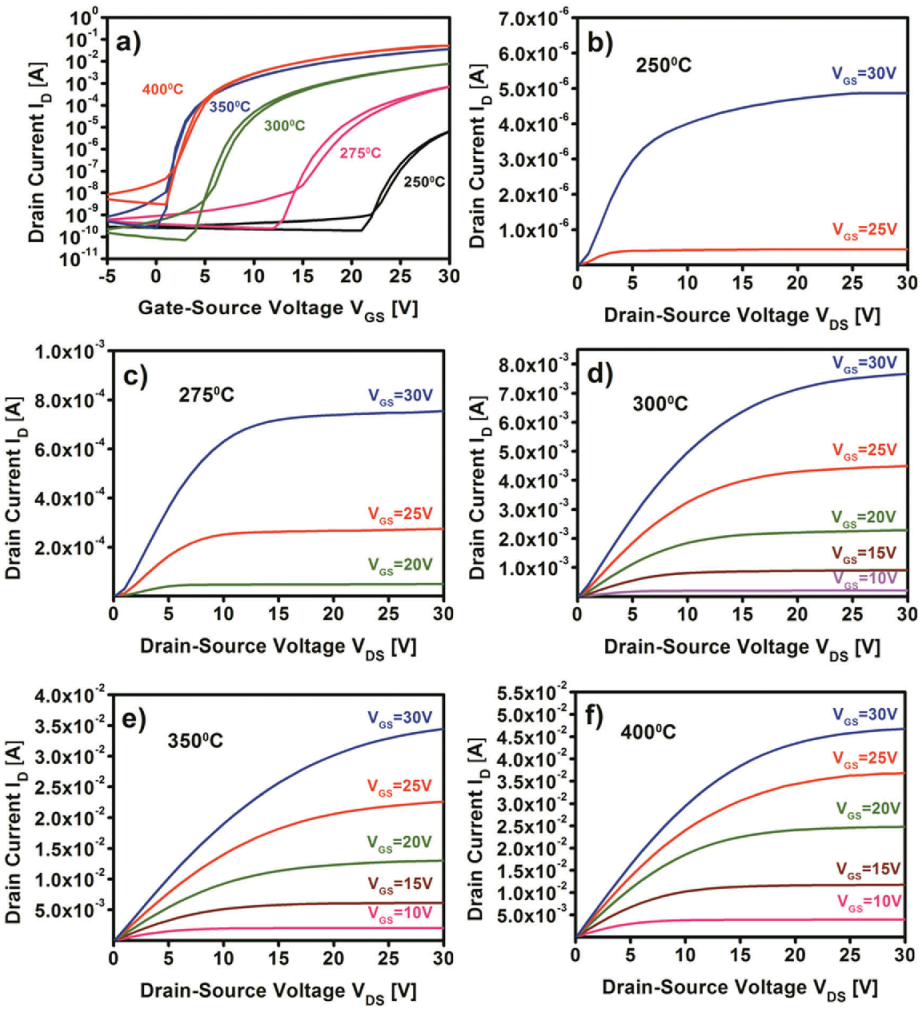

Fig. 6 TFT performance characterization of the IZO films annealed at various temperatures between 250 and 400 °C. (a) Transfer characteristics of devices annealed at 250 up to 400 °C. Output characteristics (b), (c), (d), (e) and (f) of the devices annealed at 250 °C, 275 °C, 300 °C, 350 °C and 400 °C respectively.

ambient conditions without strict exclusion of humidity and oxygen *etc.*[29,30] Consideration of further contributions possibly originating from the interplay of point defects *e.g.* coming from oxygen atoms in the vicinity of oxygen vacancies or interstitial zinc atoms did not lead to a significant change of the observed fitting results.[9,31]

The M–OH peak possesses a larger contribution with respect to the M–O signal at annealing temperatures of 250 and 275 °C. Above a processing temperature of 300 °C, the M–O peak becomes the dominant peak feature with a substantial reduction of the contributions from M–OH species. At even higher temperatures of 350 and 400 °C, there is a further decrease in the intensity of the M–OH peak.

The M–O to M–OH ratio of the binding energies of the studied IZO films subjected to the respective annealing temperatures gives a clear overview of the evolution of the M–O bond with respect to the M–OH contributions. This change in the relative intensity of the two contributions has been correlated with the electronic performance.[9] Thereby surface hydroxylation and the presence of both zinc and oxygen vacancies act simultaneously to change the magnitude of the work function.[31]

UPS (Fig. 8, Table 2) was performed in order to monitor the trend in the electronic situation in the IZO semiconducting thin films. The UPS spectra of the samples annealed up to 300 °C display a work function of ~4 eV, which is in good agreement with values reported for such multinary amorphous semiconducting oxides.[32,33] The valence band maxima (VBM) decrease gradually with an increase in the annealing temperature, with VBM values ranging from 3.6 eV to 3.1 eV for samples

Table 1 TFT performance parameters of IZO based devices annealed at incremental temperatures between 250 and 400 °C (for statistics of key parameters see Fig. S5, ESI)

Annealing temperature [°C]	Mobility μ_{sat} [cm^2 (V s)$^{-1}$]	Threshold voltage V_{th} [V]	Current on/off ratio
250	0.01 ± 0.01	25.5 ± 1.12	1.2(±2.75) × 10^5
275	0.56 ± 0.05	16.6 ± 1.53	7.5(±1.84) × 10^6
300	2.11 ± 0.16	11.5 ± 2.01	3.3(±2.47) × 10^7
350	6.01 ± 0.15	4.7 ± 0.11	7.5(±1.29) × 10^7
400	9.4 ± 0.46	4.1 ± 0.39	5.1(±7.98) × 10^7
450	11.6 ± 0.30	3.5 ± 0.28	8.1 (±4.78) × 10^5

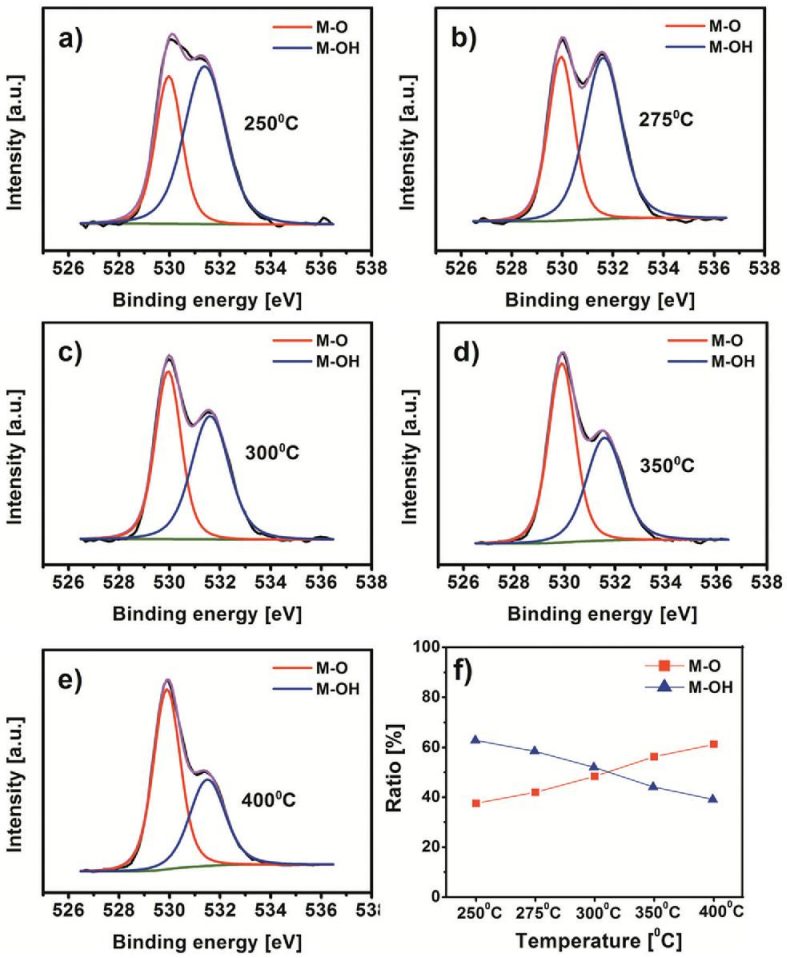

Fig. 7 Deconvoluted O1s XPS spectra (a), (b), (c), (d), and (e) of the IZO films annealed at 250 °C, 275 °C, 300 °C, 350 °C and 400 °C respectively. Ratio of oxygen contributions (f), from co-ordinated metal–oxygen bonds (M–O) and metal hydroxide species (M–OH) of the IZO films with the corresponding annealing temperatures. (The lines connecting the symbols are only a guide for the eye and do not have any physical significance.)

processed at 250 °C up to 400 °C, respectively. VBM features arise mainly from the completely filled 2p oxygen orbitals of the metal oxide. Bearing this in mind, along with the evolution of O 1s spectra from the XPS analysis, larger magnitude of the M–O contribution with incremental annealing temperatures will lead to the lowering of the VBM resulting in its shift to lower binding energies.[28,33,34]

These results correspond nicely with the observed TFT performance, where a relatively high performance of the device is observed for processing temperatures of 300 °C and higher.

More interestingly, there is only a slight reduction of ~0.1 eV, (VBM = 3.1 eV) for samples annealed at ≥350 °C, in comparison with the sample annealed at 300 °C. An increase of point defects such as oxygen vacancies could be proposed as the most likely cause of this effect. It could lead to an increased intrinsic charge carrier concentration, provided no further effects should be considered.[32] These findings can also be correlated with the observed TFT performance of the IZO films. An increased on-current (I_{on}) and a slight reduction in the off-current (I_{off}) were observed for TFT devices processed at 350 and 400 °C, respectively. The employment of ternary oxides in contrast to binary ones has been shown to counter this phenomenon. The addition of strong oxygen binding metal ions ("oxygen getter"), like gallium, functions to control O vacancies and hence can be a valuable experimental parameter to tune the charge carrier concentration and the transport properties in such IZO films.[7,35]

2.4. Positron annihilation spectroscopy

Positron annihilation spectroscopy (PAS) on IZO films obtained at various processing temperatures (250 °C, 300 °C and 450 °C) was carried out in order to characterize and identify any types of defects on a nanometer or even atomic scale. The so-called parameter *S* (defined as the ratio of the counts in the central part of the annihilation peak (between 510.06 and 511.94 keV) to the total number of counts in the whole peak (498–524 keV)) was obtained from the 511 keV annihilation line, which reflects the fraction of positrons annihilating with electrons of low momentum (valance electrons) and is therefore a measure for positron annihilation in any open volume in the IZO layers. Fig. 9 shows the *S* parameter *versus* the positron energy of IZO samples after thermal treatment of the films at 250 °C, 300 °C and 450 °C, respectively.

In all cases the *S* parameter proceeds *via* a minimum between 1.5 and 4 keV. The curves, however, differ significantly in the observed features around the minima. The remarkable step in *S* of the sample annealed at 250 °C indicates that IZO in this sample is divided into two layers, a layer with a high concentration of open volume defects at the surface of the film followed by a second layer with a lower defect concentration. The lower *S* parameter of the IZO layers in the samples annealed at 300 and 450 °C is attributed to a reduction of the defect concentration due to the thermal annealing of small open volume defects, which become mobile already at relatively low annealing temperatures. However, open volume defects still remain in these higher annealed samples. This was proven by the calculation of the positron diffusion lengths in the IZO layers using the software package "VEPFit".[36] The fits resulted in a diffusion length of $L_+ = (2 \pm 1)$ nm for the sample annealed at 250 °C and in $L_+ = (25 \pm 3)$ nm for the samples annealed at

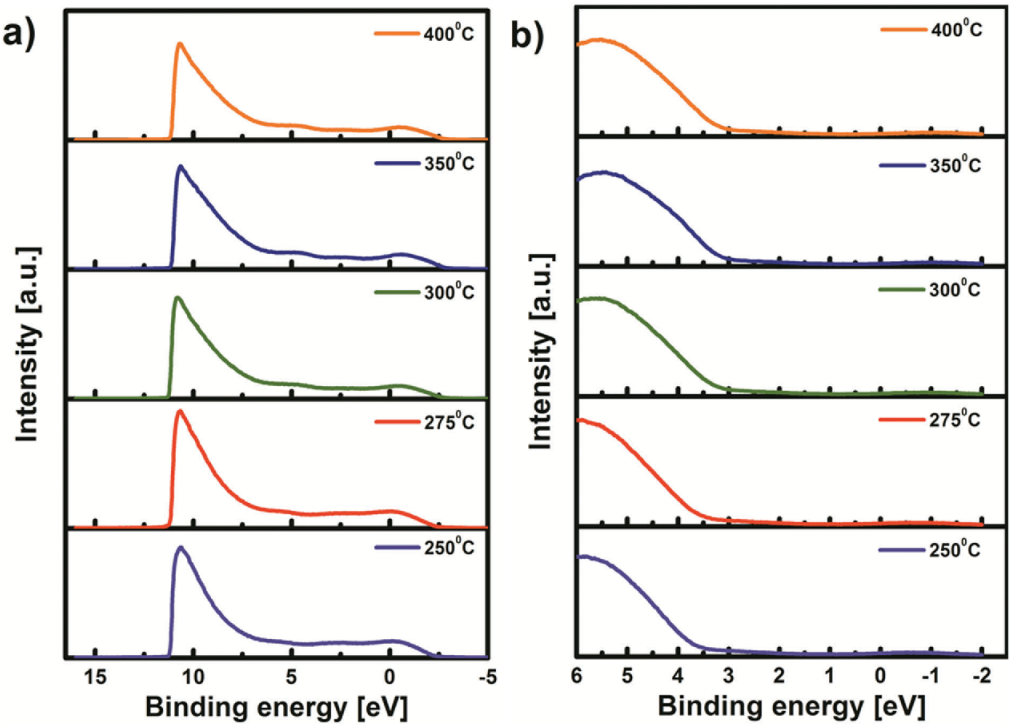

Fig. 8 UPS spectra of IZO thin films annealed at different temperatures: (a) work function determination and (b) VBM edge detection of films annealed at 250 °C, 275 °C, 300 °C, 350 °C and 400 °C.

Table 2 Trends in the binding energies of the extrapolated work function and the corresponding valence band maxima edge of the IZO films at various annealing temperatures

Annealing temperatures [°C]	Work function [eV]	Valence band edge maxima [eV]
250	4.0	3.6
275	4.0	3.5
300	4.0	3.2
350	4.1	3.1
400	4.1	3.1

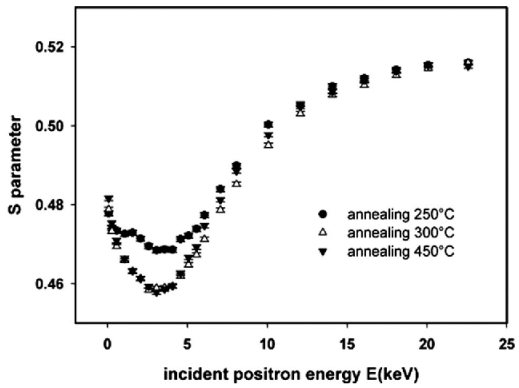

Fig. 9 *S* parameter *versus* incident positron energy *E* of IZO layers annealed at different temperatures.

higher temperatures. A very short diffusion length of 2 nm at 250 °C indicates a high defect concentration.

A short positron diffusion length of 25 nm in the IZO layers after annealing at 300 °C and 450 °C is however shorter than the diffusion lengths measured even for crystalline metal oxides (80–100 nm) and is caused presumably by the amorphous structure of the layers.[37] This finding is in full accord with the observations from the GI-XRD and HRTEM studies.

In order to get information about the size of the open volume and thus possible porosity in the IZO layers, it is useful to prove the annihilation spectra regarding *ortho*-positronium formation inside the layers. The $3\gamma 2\gamma$ ratios for the IZO samples were calculated[38] with a limit of 511 ± 4.25 keV for V and in the range from 350 keV until 500 keV for P. These calculated ratios were compared with the $3\gamma 2\gamma$ ratio obtained for well-annealed iron, where *ortho*-positronium formation can be excluded. All calculated ratios prove that no positronium formation appeared in the IZO layers. For this reason, a porosity with pores or voids of $d > 0.2$ nm could be ruled out inside the IZO. The remaining open volume defects are considered to be even smaller after annealing.

3. Conclusions

Indium and zinc complexes of 1,3-diketones which are functionalised in the 2-position present suitable precursor molecules for the fabrication of indium zinc oxide (IZO) thin films by the solution deposition route. Amorphous oxide semiconductor IZO can be formed by the combination of (**1**) and (**2**) through a highly exothermic combustion process even at a temperature slightly above 150 °C. Only minor amounts of organic residues were present thereafter and could be fully removed by further moderate annealing. Fully operating field-effect transistors (FETs) with these IZO films as semiconducting materials could be fabricated at processing temperatures between 250 and 400 °C. Hereby, annealing at higher temperatures generally leads to a better performance with respect to charge carrier mobility, threshold voltage as well as the $I_{on/off}$ ratio. The microscopic cause of this increased performance was investigated by a number of microscopic and spectroscopic techniques. XRD, HRTEM as well XPS were not able to reveal any significant microscopic differences between the samples obtained under different thermal annealing steps. However, and in contrast, UPS and PAS methods are able to identify on a microscopic scale material features which underwent a clear and significant change. These findings can be interpreted in the way that a change in the charge carrier concentrations is caused by an increase in the magnitude of point defects *e.g.* such as oxygen vacancies. This effect seems to have the most prominent impact on the emergence of the electronic performance of the studied IZO films at different temperatures.

4. Experimental

4.1. Precursor synthesis

Synthesis of (dimethyl 2-hydroxyiminomalonato) zinc [Zn_4O(dmm-$NO)_6$] (**1**): the complex was synthesized according to a procedure published earlier.[16] Synthesis of (dimethyl 2-nitromalonato)indium [In_3O_3(dmm-$NO_2)_3$]·toluene (**2**): indium butoxide (2.0 g, 6.0 mmol) was dissolved in 60 mL toluene in a Schlenk tube. A solution of Hdmm-NO_2 (3.2 g, 18 mmol) in toluene (10 mL) was added using a syringe. The mixture turned yellow and the product started to precipitate after 5 to 10 minutes. After 120 min the product was collected by filtration, dried *in vacuo* and obtained in the form of a white powder (0.87 g, 42.8). Elemental analysis (CHN): found C 26.64, N 4.18, H 2.73%. Anal. calcd for $C_{22}H_{26}In_3N_3O_{21}$ C 26.09, N 4.15, H 2.59%. ^{1}H NMR (500 MHz, [D6]dimethyl sulfoxide, 25 °C): δ = 3.58 (-CH_3) ppm. $^{13}C\{^1H\}$ NMR (500 MHz, [D6]dimethyl sulfoxide, 25 °C): δ = 49.91 (-CH_3); 108.14 (-C-NO_2); 162.67 (-COO) ppm. IR (ATR): ν_S(-NO_2) (vs), ν(C=C) 1681 cm^{-1} (m), ν(C=O) 1714 cm^{-1} (vs). The complete IR spectrum (Fig. S1, ESI†) and the results from thermogravimetry coupled with IR spectroscopy (TG/IR) can be found in the ESI† (Fig. S2 and S3).

4.2. FET characterization

FET substrates were obtained from Fraunhofer IMPS, Dresden. The substrates (15 × 15 mm^2) consist of highly n-doped silicon with a 90 nm silicon-oxide dielectric layer. The source-drain electrodes, with a channel length L = 20 μm and a channel width W = 10 mm, were fabricated with 40 nm of gold (interdigital structure) with a 10 nm intermediate adhesion layer of indium tin oxide (ITO). Quartz substrates (15 × 15 mm^2) were

used for the deposition of the precursor films for grazing incidence X-ray diffraction (GI-XRD) investigations. All the substrates were sequentially cleaned with analytically pure acetone, water and isopropanol for ten minutes. The cleaned substrates were exposed to two minutes of oxygen plasma prior to spin coating, to improve the adhesion of the spin-coating solutions.

For the preparation of the spin-coating solutions, stock solutions of the indium and the zinc precursor were produced by dissolving 1 weight% of the individual precursors in isopropanol. After complete dissolution, a clear yellowish solution was obtained in both cases. The solutions were then filtered through a 0.22 μm PTFE syringe filter. The filtered individual precursor solutions were mixed employing an indium to zinc molar ratio of 6 : 4, which was directly used for spin-coating and fabrication of thin films. The spin coating procedure was carried out under ambient conditions. Thin-films were produced with a spin-speed of 2000 rpm for 20 seconds.

4.3. Material characterization techniques

Transmission electron microscopy (TEM) was carried out using Tecnai F20 (FEI), with an operating voltage of 200 kV. Samples for the TEM investigations were prepared by depositing diluted precursor solutions onto SiO_2 coated copper grids and annealed at desired temperatures. Atomic force microscopy (AFM) measurements were carried out with CP-II (Bruker-Veeco), with silicon cantilevers. Grazing incidence XRD (GI-XRD) measurements were performed using a Seifert PTS 3003 diffractometer using Cu-Kα irradiation and an X-ray mirror on the primary side with a graphite monochromator. Thermogravimetric analysis of the indium and zinc precursors was carried out in oxygen at a heating rate of 100 °C min^{-1} in aluminum crucibles using TG209F1-Iris (Netzsch). DSC coupled TGA measurements were performed in oxygen at a heating rate of 10 °C min^{-1} using a NETZSCH STA 449C thermal analyzer, employing aluminium oxide crucibles.

XPS measurements were carried out in an integrated ultra-high vacuum (UHV) system with a base pressure of 1×10^{-9} mbar, equipped with a PHI 5000 VersaProbe photoelectron spectrometer. XPS measurements were performed using a monochromatized Al-Kα X-ray source. The hemispherical photoelectron analyser was operated with a constant analyser energy of 10 eV (pass energy) to obtain the core spectra with an energy resolution of about 0.6 eV. The spectrometer was calibrated to the Fermi edge and the core level lines of sputtered copper foils. Valence band measurements were measured with ultraviolet photoelectron spectroscopy (UPS) using excitation energy of He I (21.2 eV) and a negative bias of 6 V. The work function was determined by the secondary electron cut-off. The obtained spectra were fitted with Voigt functions and a Shirley background.

Positron annihilation spectroscopy (PAS): samples were measured at the AIDA (apparatus for *in situ* defect analysis) installation at the Helmhotz-Zentrum Dreseden Rossendorf (HZDR). AIDA is a high vacuum system (a base pressure of 7×10^{-9} mbar) that combines several experimental techniques, *i.e.*, ion irradiation, metal evaporation, temperature treatment, sheet resistance and PAS measurements, targeting on defect tailoring and defect analysis. It is located at an end-station of Slow-Positron System of Rossendorf (SPONSOR) that provides a tungsten moderated and magnetically guided variable energy positron beam extracted from a ^{22}Na source. The energy of incident positrons is in general varied in the range of 0.03–36 keV. The coincident Doppler broadening (cDB) of the annihilation line at fixed energy is performed by two High-Purity Germanium (HPGe) detectors with an energy resolution of 780 ± 20 eV at 511 keV, whereas the standard single HPGe detector Doppler broadening (sDB) with an energy resolution of (1.09 ± 0.01) keV is usually utilized for the energy scans.[39,40]

Acknowledgements

SS, RCH and JJS acknowledge financial support through the DFG SPP 1569 programs. TEM investigations were performed at ERC Jülich under contract ERC-TUD1. We acknowledge the assistance of Dr J. Engstler (TUDa) for performing TEM and Drs P. Atanasova and M. Widenmeyer (University of Stuttgart) for performing TGA/DSC measurements and Dr. J. Broetz (TUDa) for GIXRD measurements.

References

1 B. Szyszka, W. Dewald, S. K. Gurram, A. Pflug, C. Schulz, M. Siemers, V. Sittinger and S. Ulrich, *Curr. Appl. Phys.*, 2012, **12**, S2.
2 J. F. Wager, B. Yeh, R. L. Hoffman and D. A. Keszler, *Curr. Opin. Solid State Mater. Sci.*, 2014, **18**, 53.
3 X. G. Yu, T. J. Marks and A. Facchetti, *Nat. Mater.*, 2016, **15**, 383.
4 S. J. Kim, S. Yoon and H. J. Kim, *Jpn. J. Appl. Phys.*, 2014, **53**, 02BA02.
5 R. M. Pasquarelli, D. S. Ginley and R. O'Hayre, *Chem. Soc. Rev.*, 2011, **40**, 5406.
6 S. R. Thomas, P. Pattanasattayavong and T. D. Anthopoulos, *Chem. Soc. Rev.*, 2013, **42**, 6910.
7 J. W. Hennek, J. Smith, A. M. Yan, M. G. Kim, W. Zhao, V. P. Dravid, A. Facchetti and T. J. Marks, *J. Am. Chem. Soc.*, 2013, **135**, 10729.
8 M. G. Kim, M. G. Kanatzidis, A. Facchetti and T. J. Marks, *Nat. Mater.*, 2011, **10**, 382.
9 K. K. Banger, Y. Yamashita, K. Mori, R. L. Peterson, T. Leedham, J. Rickard and H. Sirringhaus, *Nat. Mater.*, 2011, **10**, 45.
10 R. C. Hoffmann, S. Differ, A. Issanin and J. J. Schneider, *Phys. Status Solidi A*, 2011, **208**, 1708.
11 M. Tsaroucha, Y. Aksu, E. Irran and M. Driess, *Chem. Mater.*, 2011, **23**, 2428.
12 B. H. Wang, L. Zeng, W. Huang, F. S. Melkonyan, W. C. Sheets, L. F. Chi, M. J. Bedzyk, T. J. Marks and A. Facchetti, *J. Am. Chem. Soc.*, 2016, **138**, 7067.
13 B. H. Wang, X. G. Yu, P. J. Guo, W. Huang, L. Zeng, N. J. Zhou, L. F. Chi, M. J. Bedzyk, R. P. H. Chang, T. J. Marks and A. Facchetti, *Adv. Electron. Mater.*, 2016, **2**, 1500427.
14 R. C. Hoffmann, M. Kaloumenos, S. Heinschke, E. Erdem, P. Jakes, R. A. Eichel and J. J. Schneider, *J. Mater. Chem. C*, 2013, **1**, 2577.

15 S. Sanctis, R. C. Hoffmann and J. J. Schneider, *RSC Adv.*, 2013, **3**, 20071.
16 R. C. Hoffmann and J. J. Schneider, *Eur. J. Inorg. Chem.*, 2014, 2241.
17 R. C. Hoffmann, M. Kaloumenos, D. Spiehl, E. Erdem, S. Repp, S. Weber and J. J. Schneider, *Phys. Chem. Chem. Phys.*, 2015, **17**, 31801.
18 N. Koslowski, MSc thesis, TU Darmstadt, 2016.
19 N. N. Chamazi, M. M. Heravi and B. Neumüller, *Z. Anorg. Allg. Chem.*, 2006, **632**, 2043.
20 S. Suh and D. M. Hoffman, *J. Am. Chem. Soc.*, 2000, **122**, 9396.
21 M. Veith, D. Summa and V. Huch, *Z. Anorg. Allg. Chem.*, 2012, **638**, 1482.
22 W. Uhl, I. Hahn, M. Koch and M. Layh, *Inorg. Chim. Acta*, 1996, **249**, 33.
23 A. Walz, M. Niemeyer and J. Weidlein, *Z. Anorg. Allg. Chem.*, 1999, **625**, 547.
24 A. P. Kilimov, M. A. Svechnikova, V. I. Shevchenko, V. V. Smirnov, F. V. Kvasnyuk-Mudryi and S. B. Zotov, *Chem. Heterocycl. Compd.*, 1967, **3**, 467.
25 R. Branquinho, D. Salgueiro, A. Santa, A. Kiazadeh, P. Barquinha, L. Pereira, R. Martins and E. Fortunato, *Semicond. Sci. Technol.*, 2015, **30**, 024007.
26 P. K. Nayak, M. N. Hedhili, D. Cha and H. N. Alshareef, *ACS Appl. Mater. Interfaces*, 2013, **5**, 3587.
27 E. Fortunato, A. Pimentel, A. Gonçalves, A. Marques and R. Martins, *Thin Solid Films*, 2006, **502**, 104.
28 T. Kamiya and H. Hosono, *NPG Asia Mater.*, 2010, **2**, 15.
29 N. Abedi and G. Heimel, *Phys. Status Solidi B*, 2015, **252**, 755.
30 L. L. Kelly, D. A. Racke, P. Schulz, H. Li, P. Winget, H. Kim, P. Ndione, A. K. Sigdel, J. L. Bredas, J. J. Berry, S. Graham and O. L. A. Monti, *J. Phys.: Condens. Matter*, 2016, **28**, 094007.
31 H. Li, L. K. Schirra, J. Shim, H. Cheun, B. Kippelen, O. L. A. Monti and J. L. Bredas, *Chem. Mater.*, 2012, **24**, 3044.
32 D. Kang, H. Lim, C. Kim, I. Song, J. Park, Y. Park and J. Chung, *Appl. Phys. Lett.*, 2007, **90**, 192101.
33 K. Nomura, T. Kamiya, H. Yanagi, E. Ikenaga, K. Yang, K. Kobayashi, M. Hirano and H. Hosono, *Appl. Phys. Lett.*, 2008, **92**, 202117.
34 J. Socratous, K. K. Banger, Y. Vaynzof, A. Sadhanala, A. D. Brown, A. Sepe, U. Steiner and H. Sirringhaus, *Adv. Funct. Mater.*, 2015, **25**, 1873.
35 S. Jeong, Y.-G. Ha, J. Moon, A. Facchetti and T. J. Marks, *Adv. Mater.*, 2010, **22**, 1346.
36 A. V. Fedorov, A. van Veen and H. Schut, *Mater. Sci. Forum*, 2001, **363**, 646.
37 I. Makkonen, E. Korhonen, V. Prozheeva and F. Tuomisto, *J. Phys.: Condens. Matter*, 2016, **28**, 224002.
38 X. Yu, J. Smith, N. J. Zhou, L. Zeng, P. J. Guo, Y. Xia, A. Alvarez, S. Aghion, H. Lin, J. S. Yu, R. P. H. Chang, M. J. Bedzyk, R. Ferragut, T. J. Marks and A. Facchetti, *Proc. Natl. Acad. Sci. U. S. A.*, 2015, **112**, 3217.
39 W. Anwand, G. Brauer, M. Butterling, H. R. Kissener and A. Wagner, *Defect Diffus. Forum*, 2012, **331**, 25.
40 M. O. Liedke, W. Anwand, R. Bali, S. Cornelius, M. Butterling, T. T. Trinh, A. Wagner, S. Salamon, D. Walecki, A. Smekhova, H. Wende and K. Potzger, *J. Appl. Phys.*, 2015, **117**, 163908.

6.6 Aqueous solution processing of combustible precursor compounds into amorphous indium gallium zinc oxide (IGZO) semiconductors for thin film transistor applications.

Combustion processing has been at the forefront of low-temperature solution processing of oxide semiconductors. Such an approach allows complete conversion of the precursor at lower temperatures by providing specific amounts of “oxidizer” (e.g. metal nitrates) and a “fuel” (e.g. urea or acetylacetone). However, the need for controlled addition of such sensitive reactive agents often hinder the fabrication process in terms of reproducible performance due to low stability and uncontrolled reactivity of of the chemical species in the solution over ageing with time. Additionally a systematic understanding of the precursor decomposition is rather scare and emphasize on the need of have well-defined precursor compounds with the fuel and oxidizer components available with the precursor ligand/ ion to eliminate the need of any additives prior to the direct solution processing of the precursor films to obtain a high quality oxide semiconductor as low processing temperatures.

In this publicatiuon we demonstrate the synthesis and characterization of well-defined urea nitrate coordination compounds of indium(III), gallium(III) and zinc(II) and their use as single source precursors to access the formation of amorphous IGZO thin films. For the trivalent In and Ga metal atoms were homoleptically coordinated by six urea molecules, whereas for Zn the coordination sphere consisted of four urea and two water molecules completing the octahedral coordination sphere around the zinc center . In all cases, the metal-urea complex is well balanced by the appropriate number of nitrate anions, providing for further stability of the precursors. DSC analysis confirms the exothermic decomposition of all three precursors with a significantly sharp exothermic peak between 100 °C and 200 °C followed by a less intense exothermic peak between 250 °C as a result of the combustion arising from the urea-nitrate (fuel-oxidiser) combination. TG-MS investigations identified the gases during the combustion process which could be assigned to ammonia (m/z^+ 17), water (m/z^+ 18), carbon monoxide or nitrogen (m/z^+ 28), nitric oxide (m/z^+ 30), isocyanic acid (m/z^+ 43) and nitrogen dioxide (m/z^+ 46). The signal corresponding to (m/z^+ 44) can be correlated with the evolution of carbon dioxide or nitrous oxide. The clean decomposition was also verfied via XPS for films annealed between 300 and 350ºC with no significant detection of residual hydrocarbon or nitrogen species in final IGZO film. Interestingly, TFTs processed even at 200ºC show active TFT perfortmance and TFTs annealed at 300°C and 350°C exhibit a good device performance with charge-carrier mobilities μ_{sat} of 1.7 cm^2/V·s and 3.1 cm^2/(V·s), respectively as well as current

on-off ratios of $>10^7$ in both cases. Such precursors are highly suitable for use in aqueous (non-toxic) solution processing of IGZO semiconductors.

ACES Asian Chemical Editorial Society

DOI: 10.1002/asia.201801371

CHEMISTRY AN ASIAN JOURNAL Full Paper

Thin Film Transistors

Aqueous Solution Processing of Combustible Precursor Compounds into Amorphous Indium Gallium Zinc Oxide (IGZO) Semiconductors for Thin Film Transistor Applications

Shawn Sanctis,[a] Rudolf C. Hoffmann,[a] Nico Koslowski,[a] Sabine Foro[++],[c] Michael Bruns[+],[b] and Jörg J. Schneider*[a]

Abstract: Combustion synthesis of semiconducting amorphous indium gallium zinc oxide IGZO (In:Ga:Zn, 7:1:1.5) thin films was carried out using urea nitrate precursor compounds of indium(III), gallium(III) and zinc(II). This approach provides further understanding towards the oxide formation process under a moderate temperature regime by employment of well-defined coordination compounds. All precursor compounds were fully characterized by spectroscopic techniques as well as by single crystal structure analysis. Their intrinsic thermal decomposition was studied by a combination of differential scanning calorimetry (DSC) and thermogravimetry coupled with mass spectrometry and infrared spectroscopy (TG-MS/IR). For all precursors a multistep decomposition involving a complex redox-reaction pathway under in situ formation of nitrogen containing molecular species was observed. Controlled thermal conversion of a mixture of the indium, gallium and zinc urea nitrate complexes into ternary amorphous IGZO films could thus be achieved. Thin film transistors (TFTs) were fabricated from a defined compositional mixture of the molecular precursors. The TFT devices exhibited decent charge carrier mobilities of 0.4 and 3.1 $cm^2/(Vs)$ after annealing of the deposited films at temperatures as low as 250 and 350 °C, respectively. This approach represents a significant step further towards a low temperature solution processing of semiconducting thin films.

Introduction

Amorphous oxide semiconductors (AOS) are among the most rapidly developing classes of materials used for electronic and optoelectronic applications.[1] The intrinsic properties of these wide band gap semiconductors like their almost complete optical transparency in the visible region and their high field effect mobilities recommend them for use in the field of next generation display technology.[2]

Currently the key players are multinary metal oxides, namely indium zinc oxide (IZO), indium gallium zinc oxide (IGZO) or zinc tin oxide (ZTO) which are mainly deposited by means of vacuum-based techniques.[3] Although the solution processing of AOS is possible and comes with the promise of several advantages such as low costs, large area and roll-to-roll deposition[4] as well as direct photo-patterning,[5] these methods did not win sufficient recognition for technological application so far due to the still unresolved inherent problems concerned with their use. Although molecular precursor compounds which start to decompose conveniently at low temperatures of ≈200 °C, unfortunately still contain traces of organic residues from the ligand sphere around the metal center, which remain up to significant higher temperatures in the thin oxide films that is close to 400–500 °C. Typically these carbonic residues severely corrupts the electronic performance.[6] The complete removal of the organic remains thus requires the sufficient supply of atmospheric oxygen and longer annealing times or elevated processing temperatures.[7] Several strategies exist to cope with this drawback. One approach uses the systematic introduction of reactive ligand groups, such as nitro or nitroso functionalities, into the ligand framework of the precursor. This facilitates the start of the decomposition via thermal decay.[8] Another attempt utilizes a so-called "combustion processing" which allows complete conversion of the precursor at lower temperatures by providing specific amounts of "oxidizer" (e.g. metal nitrates) and a "fuel" (e.g. urea or acetylacetone).[9] This

[a] S. Sanctis, Dr. R. C. Hoffmann, N. Koslowski, Prof. J. J. Schneider
Department of Chemistry, Eduard-Zintl Institut für Anorganische und Physikalische Chemie
Technische Universität Darmstadt
Alarich-Weiss-Straße 12, 64287 Darmstadt (Germany)
E-mail: joerg.schneider@ac.chemie.tu-darmstadt.de

[b] Dr. M. Bruns[+]
Institute for Applied Materials-Karlsruhe Nano Micro Facility
Karlsruhe Institute of Technology (KIT)
Hermann-von-Helmholtz-Platz 1, D-76344, Eggenstein-Leopoldshafen (Germany)

[c] S. Foro[++]
Department of Material Science
Technische Universität Darmstadt
Alarich-Weiss-Straße 8, 64287 Darmstadt (Germany)

[++] X-ray crystal structure determination.

[+] XPS investigation.

Supporting information and the ORCID identification number(s) for the author(s) of this article can be found under: https://doi.org/10.1002/asia.201801371.

two-component concept has demonstrated remarkable results, when transferred to the synthesis of AOS.[3a–c] Nevertheless, further insight into the decomposition process occurring during the combustion synthesis leading to metal oxides is needed. The aim of the current work is to introduce a new approach for studying the interplay between the metal nitrate and the urea ligands. This is achieved by introducing the concept of defined molecular precursors. Recent investigations of aqueous solutions of metal nitrate employing urea as an additive has shown the need for appropriate ageing of the solution over several days. The so far described ageing process ensures the in situ complexation of the urea to the metal cation, to obtain the desired combustion effect. Nevertheless this process calls for a controlled solution processing and is vulnerable to problems in processing[10] Herein we have chosen a single source precursor approach in which we combine the urea ligands (the fuel) and the nitrate ions (the oxidizer) in one specific compound. This enables us to elucidate their role in the formation of the desired metal oxides more precisely in a controlled manner.[11] During the thermal decomposition and the subsequent comproportionation, reaction between the nitrogen containing constituents (i.e. nitrate anion and urea) occurs. Hereby, a complex mixture of compounds with nitrogen in various oxidation states can be expected.[12]

In the current work we demonstrate the synthesis and characterization of well-defined urea nitrate coordination compounds of indium(III) (**1**), gallium(III) (**2**) and zinc(II) (**3**) and their use as single source precursors to access the formation of amorphous IGZO thin films. The molecular structures of compounds (**1**)–(**3**) were determined by single crystal X-ray diffraction. A detailed analysis of the thermal conversion of the molecular precursors (1)–(3) to yield the metal oxides was carried out using TG and DSC techniques as well as hyphenated techniques for identifying gaseous by-products by IR and MS.

IGZO based thin films were obtained by spin-coating of the molecular precursors using water as an eco-friendly solvent resulting in the formation of amorphous, smooth homogeneous semiconducting oxide thin films at temperatures between 200 °C to 350 °C which exhibit an excellent TFT transistor behaviour. X-ray photoelectron spectroscopy elucidated the improvement in TFT performance is based largely on the improved metal oxide formation as well as passivation of defects within the local oxygen environment of the metal oxide microstructure.

Results and Discussion

Synthesis and thermal analysis

The precursor complexes $[M(urea)_6][NO_3]_3$ with M = In (**1**) and Ga (**2**) as well as $[Zn(urea)_4(H_2O)_2][NO_3]_2$ (**3**) were synthesized by reaction of the metal nitrate hydrates with stoichiometric amounts of urea in ethanol for (**1**) and (**2**) and n-butanol (**3**) as solvent as described in Figure 1. Subsequent recrystallization can be performed from methanol, by a modified procedure.[13] Compounds (**1**) and (**2**) were isotypic and crystallize in the space group C2/C, whereas crystals of (3) exhibited the space

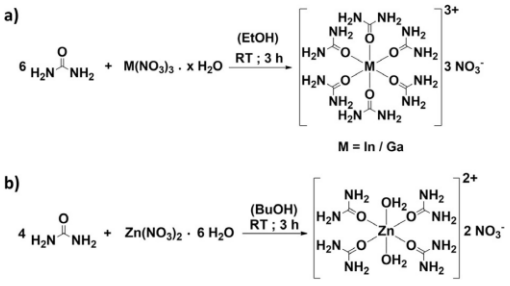

Figure 1. Schematic representation for the synthesis of the metal urea complexes of indium (**1**), gallium (**2**) and zinc (**3**) respectively.

group $P2_1/n$ (Figure 2). Hereby, mononuclear complexes with octahedral coordination of the central metal atoms were observed in all cases. The neutral urea molecule serves as monodentate ligand and coordinates to the central metal atom by its oxygen atom. For (**1**) and (**2**) the trivalent In and Ga metal

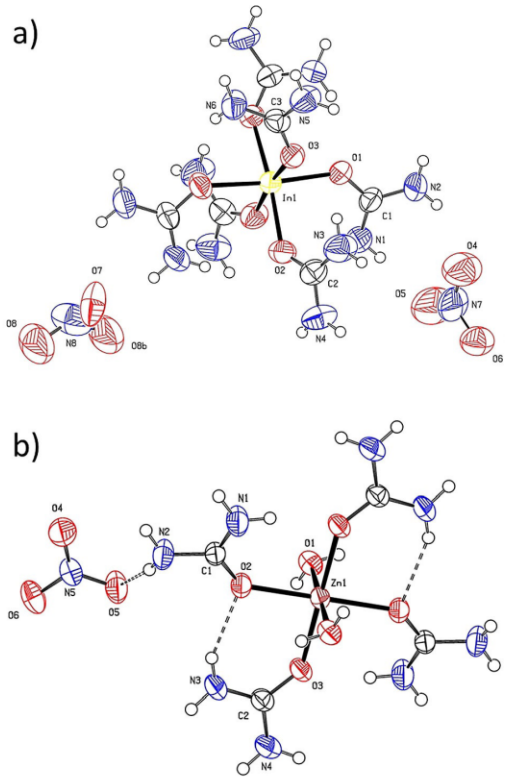

Figure 2. ORTEP plot of the metal urea complexes of a) $[In(urea)_6][NO_3]_3$ (**1**) and b) $[Zn(urea)_4(H_2O)_2][NO_3]_2$ (**3**) drawn at a 50% probability level. (Both crystallographically independent nitrate anions in (**1**) exhibited structural disorder, which in each case was described using two split position. For clarity only one orientation is thus shown. The third nitrate anion is related to the former by crystal symmetry and therefore not shown either.

atoms were homoleptically coordinated by six urea molecules, whereas for (**3**) the coordination sphere consisted of four urea and two water molecules completing the octahedral coordination sphere around the zinc center in (**3**). Weak hydrogen bonds between the urea ligand and the nitrate anions were observed for (**3**), which probably prevents rotational disorder of the nitrate anion in the case. Further details of the complete analytical data of (**1**) can be found in Tables S1 and S2.[37] Such hexakis(urea) compounds with trivalent metal ions are for example, known for chromium,[14] or manganese.[15] Although, the molecular structure of the divalent zinc compound (**3**) has been previously reported,[37] a straight forward procedure to isolate the final product was not established so far.[16] This warrants a report herein. Although homoleptic urea complexes of the composition $M(urea)_6^{n+}$ as observed for (**1**) and (**2**) are quite common[16,17] and under non aqueous reaction conditions a homoleptic zinc coordination $[Zn(urea)_6][NO_3]_2$ was reported,[18] a general composition $M(urea)_4(H_2O)_2^{n+}$ as found for (**3**) is much less common so far.[19] For the Ga compound (**2**) the obtained crystal structure shows a similar co-ordination of the urea ligand to the metal centre as observed for (**1**) (Figure S1). However, the crystal structure refinement was poor and thus unsuitable for a detailed refinement. The connectivity of the atoms for (**2**) could however be established unequivocally.

The influence of the counter anion for such metal urea complexes also plays a crucial role in the nature of their thermal decomposition, whereby the urea complexes with a nitrate anion undergo an enhanced thermal conversion to the ceramic oxide at much lower temperatures due the "fuel/oxidizer" reaction between the urea and the nitrogen containing species (NO_2, HONO) compared to their chloride counterparts. The need of elevated temperatures for urea complexes of metal chlorides is largely due to an endothermic reaction leading to the formation of stable intermediates which undergo further decomposition only at elevated temperatures (>600^{0}C) accompanied by the elimination of hydrochloric acid.[11–12] Figure 3 shows TG mass loss (a) and the corresponding DSC studies (b-d) of the urea-nitrate complexes (**1**), (**2**) and (**3**) in oxygen. Although, complexes (**1**), (**2**) and (**3**) possess identical urea/nitrate ratios of 6:3 for (**1**), (**2**) and 4:2 for (**3**), they exhibit very different mass loss curves (Figure 3a, Figure S2). All three precursors depict a prominent starting decomposition step at about 175 °C with a slight initial mass loss for (**3**) which corresponds to the loss of the two co-ordinated water molecules. Initial mass loss at lower temperatures (<100 °C) resulting from the release of the coordinated water molecules in form of vapor is well known for zinc acetates[20] and zinc acetylacetonates[21] and is in good agreement with our observations.

DSC analysis (Figure 3b–d) confirms the exothermic decomposition of all three precursors with a significantly sharp exothermic peak between 100 °C and 200 °C followed by a less intense exothermic peak between 250 °C. Minor signals of endothermic events in the case of complexes (**1**) and (**3**) can be associated with removal of residual carbonaceous species. The thermal decomposition of (**1**)–(**3**) was carried out in oxygen to get an insight in the decomposition by-products of the precursors. The decomposition behavior of the indium and zinc precursors proceeded as a two-step decomposition where significant mass loss occurs in the first step itself. The residual mass of all the precursors are in good agreement with the expected ceramic yield from the decomposition of the precursors in oxygen ((**1**): $CY_{calc.}$ 21.3%, $CY_{meas.}$ 21.8%; (**2**): $CY_{calc.}$ 15.2%, $CY_{meas.}$ 15.3%, (**3**): $CY_{calc.}$ 17.5% and $CY_{meas.}$ 18.4%. The differential scanning calorimetry analysis of these precursors also indicate a sharp exothermic decomposition which can be associated with the expected redox reactions between the co-ordinated urea and the nitrate anion.[22]

Thermal analysis of the evolved gaseous by-products from the combustion-based decomposition were analyzed by means of TG-MS-FTIR (Figures 4 and 5).

The majority of the observed gases were largely identical where the resultant gases during the combustion process could be assigned to ammonia (m/z^+ 17), water (m/z^+ 18), carbon monoxide or nitrogen (m/z^+ 28), nitric oxide (m/z^+ 30), isocyanic acid (m/z^+ 43) and nitrogen dioxide (m/z^+ 46). The

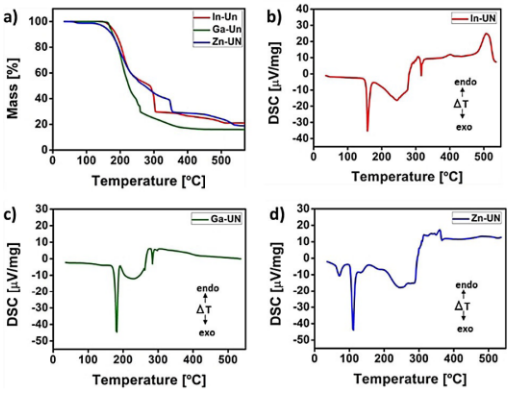

Figure 3. (a) TG mass loss and (b–d) corresponding DSC studies of the urea-nitrate complexes (**1**), (**2**) and (**3**) in oxygen.

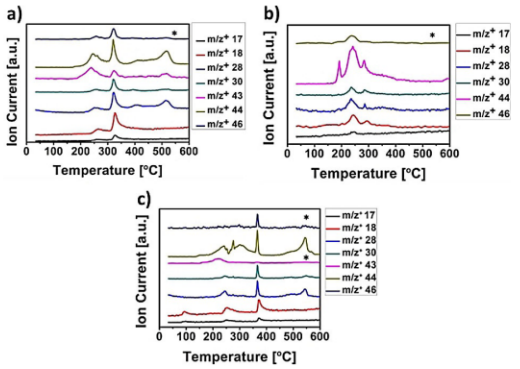

Figure 4. MS intensities of a) Indium precursor b) Gallium precursor and c) Zinc precursor for $m/z+$ peaks corresponding to the TG curves in Figure 3 respectively. (trace marked with * is enhanced by a factor of 10 for clarity).

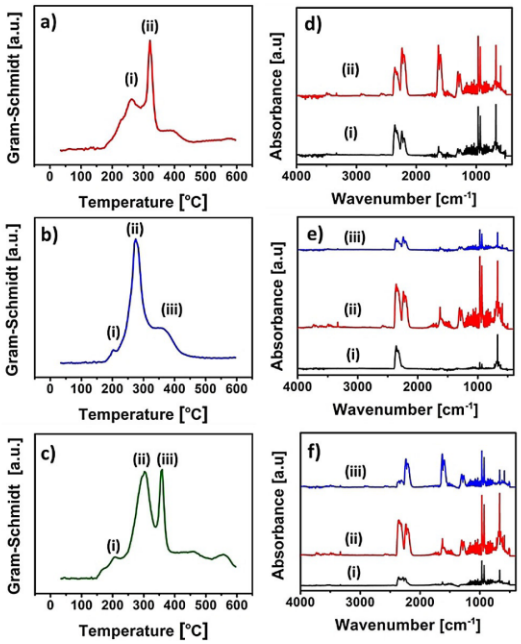

Figure 5. Gram-Schmidt intensities (a–c) of the indium, gallium and the zinc urea-nitrate precursors (**1**)–(**3**) and the corresponding IR signal intesities (d–f) according to the Gram-Schmidt the precursors, respectively.

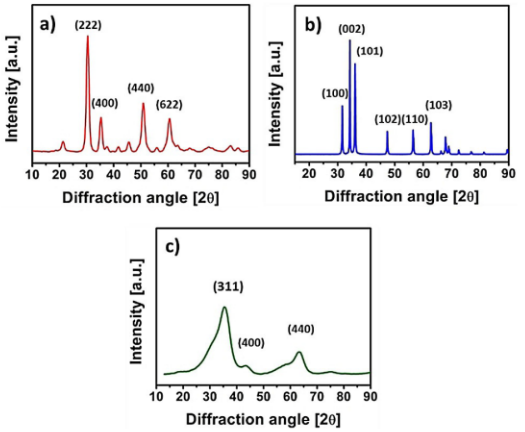

Figure 6. XRD analysis of the metal oxides powders obtained from the thermal combustion of aqueous urea nitrate precursors (**1**)–(**3**) and final calcination at 350 °C for 2 hours, respectively.

signal corresponding to (m/z^+ 44) can be correlated with the evolution of carbon dioxide or nitrous oxide. The IR signals corresponding to the different signal intensities of the Gram-Schmidt signal were recorded to identify the various gases being released as a result of the precursor combustion. For all the three precursors, a clear evolution of ammonia (NH_3 = 968 cm^{-1}) isocyanic acid (HNCO = 2283 and cm^{-1}), carbon-dioxide (CO_2 = 2332 and 2362 cm^{-1}), nitric acid (HNO_3 = 1713 and 1325 cm^{-1}) and nitrous oxide (N_2O = 2241 cm^{-1}) were detected at various decomposition stages ranging between 200 °C and 350 °C. This is in good agreement with observed thermal decomposition products of urea complexes with metal nitrates.[23]

The deduction of a detailed mechanism for the thermal decay of (**1**)–(**3**) remains difficult though. Clearly consecutive processes occur in all cases, but the determinable gaseous reaction products from MS or FTIR do not vary significantly to securely trace down a detailed decomposition pathway.

In order to elucidate the nature of the resultant ceramic oxide after decomposition of precursors (**1**)–(**3**) they were dissolved each in water, subsequently spin-coated on quartz substrates and calcined followed by isolation the calcined AOS material. In addition, thin films of the individual precursors calcined each at 350 °C allow the formation of the individual oxides of indium, zinc and gallium displaying a crystalline nature corresponding to the bixbyite (for In_2O_3) and wurtzite (ZnO) structures as shown in Figure 6. Interestingly, gallium oxide exhibits a weak crystalline phase with broad reflexes which corresponds to the "δ-Ga_2O_3" phase.[24] Annealing precursor (**2**) at even higher temperature of 800°C revealed a clear formation of phase pure monoclinic β-Ga_2O_3 with no detection of any other mixed secondary phase Figure S3. It is known that gallium oxide displays a broad phase distribution depending on the type of precursor used and the thermal calcination history under which this material is obtained. This allows to form different crystalline phases or even mixtures therefrom. In-depth neutron diffraction studies have previously indicated that the "δ-Ga_2O_3" is actually a mixture of hexagonal ε-Ga_2O_3 and β-Ga_2O_3.[25]

AOS thin film characterization

For multinary oxide semiconductor films, it is essential to have the final ceramic film in the amorphous state to avoid any charge transport barriers arising from grain boundaries from the polycrystalline nanoparticles dispersed within the amorphous matrix. In order to gain an insight into the fabricated IGZO film, precursor solution was generated by mixing the individual precursors for (**1**), (**2**) and (**3**) and spin coated on Si/SiO_2 substrates. The aqueous IGZO precursor solutions were spin-coated to generate well-coated thin-films and annealed between 200 °C and 350 °C for 2 hours, respectively. Three iterations of the film-coating procedure were repeated in order to obtain the desired film thickness of the IGZO films for which their transistor performance was assessed later. Attempts to directly spin coat aqueous IGZO solutions from pure metal nitrates analogous to the urea nitrate precursor compounds resulted in inhomogeneous film coatings with poor adhesion to the SiO_2 dielectric and could not be analyzed for further investigations. Similar inconsistencies have been previously reported, which were circumvented by the formation of electrochemically generated aqueous metal-hydroxo nanoclusters.[26] The homogeneity of the coated films from the urea nitrate precursors on a Si/SiO_2 substrate as well as their microstructure was investigated via high-resolution transmission electron mi-

croscopy (HR-TEM) and atomic force microscopy (AFM). The TEM investigations (Figure 7a,b) revealed that films annealed at both temperatures are amorphous in nature with the absence of any partial film crystallinity amorphous matrix.[27]

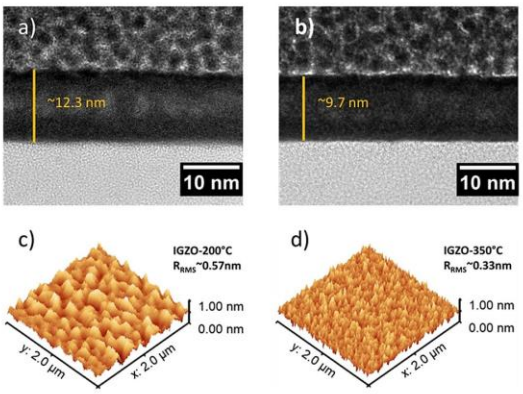

Figure 7. Cross-sectional HR-TEM images with measured film thickness and AFM micrographs and root-mean-square roughness (R_{RMS}) for the IGZO films annealed at (a, c) 200 °C and (b, d) 350 °C respectively.

This serves as a good indication that film annealing at elevated temperatures actively promotes film densification, thereby improving its contact/adhesion with the underlying dielectric layer (SiO_2), which plays a crucial role in eliminating void formation which are usually a consequence of residual organic elimination, and evolution of gaseous by-products.[28] The resultant densification of the film is known to improve the electrical performance of TFT devices by having a good adhesion and as well as passification of interfacial defects.[29]

AFM of the films annealed between 200 °C and 350 °C were analyzed to understand the morphology of the calcined IGZO films (Figure 7c,d). Films annealed at the lower temperature display a more textured surface indicating a relatively rougher film in comparison with films calcined at 350 °C which show a smoother morphology. This is well corroborated with the results obtained from the HR-TEM investigations.

Thin film transistor performance

In order to study the influence of the IGZO thin films, a series of TFT were produced in a bottom gate bottom contact (BGBC) configuration. Device structures with a reasonably large source-drain electrode geometry with a width (W) to length (L) ratio (W/L = 500) were utilized to in order to avoid any overestimation of device mobility. It must be noted that all devices were fabricated with a standard SiO_2. Higher device performances can be typically achieved using high-k dielectrics oxides.[30] Thin films of IGZO were generated in the source drain area of the TFT by spin-coating of an aqueous precursor solution containing (**1**), (**2**), and (**3**) followed by drying and combustion synthesis and finally annealing between 200 °C and 350 °C for two hours. The essential performance metrics of the transistors, such as the saturation mobility (μ_{sat}), threshold voltage (V_{th}) and the current on-off ratio were measured and are shown below Figure 8.

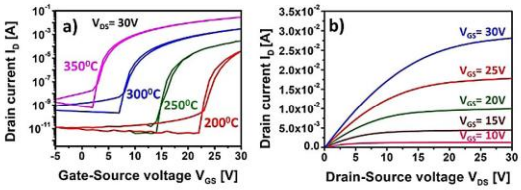

Figure 8. TFT performance characterization based on IGZO thin films annealed at various temperatures. a) Comparative transfer characteristics of IGZO TFTs annealed between 200 °C and 350 °C. b) Output characteristics of the device annealed at 350 °C.

Active transistor performance was observed at all the investigated temperatures and the corresponding transistor performance parameters have been summarized in Table 1.

Table 1. TFT performance parameters of IGZO based devices annealed at incremental temperatures between 200 and 350 °C.

Annealing Temp.	Mobility(μ) $cm^2/[Vs]$	V_{th} [V]	$I_{on/off}$
200 °C	0.09	23	2.3×10^5
250 °C	0.4	17.4	6.4×10^6
300 °C	1.7	8.6	4.1×10^7
350 °C	3.1	4.3	8.4×10^7

TFTs annealed at 300 °C and 350 °C exhibit a good device performance with charge-carrier mobilities μ_{sat} of 1.7 $cm^2/(V\cdot s)$ and 3.1 $cm^2/(V\cdot s)$, respectively as well as current on-off ratios of $>10^7$ in both cases. It is motivating to observe that devices annealed at temperatures at 200 °C and 250 °C still show active semiconductor behavior although the performance in not on par with the that of the devices annealed at higher temperatures, with relatively higher (Vth) and lower on current in the transfer characteristics, accompanied by lower gate- voltage modulation, with a lower potential for device applications. However, devices annealed at higher temperatures show a good mobility >1 $cm^2/(V\cdot s)$. Interestingly, similar trends in increased mobility and negative shifts of the threshold voltages at much higher annealing temperatures, were previously reported for solution processed IGZO films from nitrate salts. The observed improvement in TFT performance was attributed to the formation of oxygen vacancy related point defects at elevated temperatures which enhances the generation of addition electron charge carriers. This in turn facilitates the improvement device mobility as well as threshold voltage.[31]

X-ray photoelectron spectroscopy analysis for the IGZO thin films were carried out in order to probe into the change in the nature of the chemical species involved. The oxygen O1s spectra serves a good indicator of the enhanced formation of the ceramic oxide, thereby facilitating a good understanding of the microstructure -property relation of the metal oxide. The

deconvoluted oxygen O1s spectra of the IGZO films annealed at different temperatures are shown in Figure 9. Curve fitting of the oxygen peak was carried out using contributions with positions centered at ≈530.2 eV, ≈531.8 eV and ≈532.8 eV which are indicative of the different oxygen environments. Quantitative contributions from the different oxygen environments with respect to their atomic percentages can be found in Table S3.

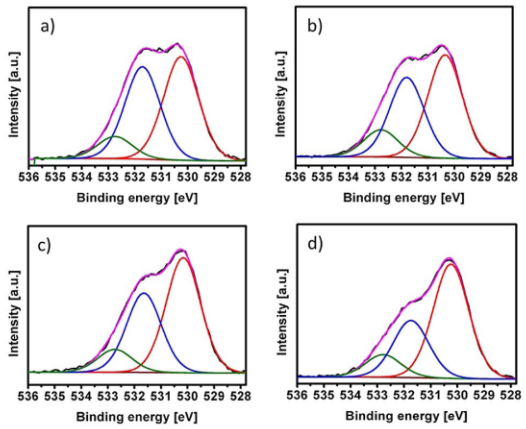

Figure 9. Deconvoluted O1s XPS spectra (a–d) of the IGZO films annealed at 200 °C, 250 °C, 300 °C, 350 °C respectively.

The peak position centered ≈530.2 eV indicates metal-oxygen bonds (M-O) within the IGZO bulk representing a complete coordination environment by O^{2-} ions. The peak at ≈531.8 eV can be attributed to oxide O^{2-} associated with hydroxide species which are coordinated to the metal atoms (M-OH) as well as possible contributions from surface adsorbates.[32] The third contribution to the O1s peak is positioned at an even higher binding energy of ≈532.8 eV and might well originate from oxygen species from the underlying SiO_2 dielectric layer which is known to create an intermixed phase close to the boundary where Si^{4+} diffuses in the Si/IGZO interface.[29] This corroborates well with the ultra-thin films (< 20 nm) as well as its dense morphology (see Figure 7).[29–31,33] Although, such contributions are also known to be due to oxygenated carbon species arising from a topmost contamination layer (e.g. carbonyl, carbonate as well as C-OH groups),[3a,c,32,34] it seems rather less likely for the investigated samples. The shoulder at higher binding energies in the O1s peak was almost similar across all samples with no significant decrease at higher annealing temperatures. Such a thermal treatment should affect surface contaminations due to the ease of their thermal removal. Subsequently, it did not affect the qualitative contributions from the other binding energies (see Suppl. Table S3). A comparative increase in the ratio of the M–O bonds and the simultaneous decrease in the M-OH bonds is clearly observed, which further confirms a thermally assisted densification with a possible interdiffusion of Si^{4+} into the IGZO phase. The charge carrier transport in such amorphous oxide semiconductors is directed through the improved orbital overlap of large vacant s-orbitals at the conduction band minimum, which originates from the co-ordinated M–O bonds in such ionic oxides.[35] This is in good agreement with increase in TFT performance, especially in terms of improved charge carrier mobility of the devices annealed at higher temperatures which generates an improved M-O-M network, accompanied by better percolation pathways for charge carriers in relatively dense films with reduced porosity.[28b,29] Recent investigations consisting UV irradiation of metal nitrate precursors have been explored to produce high performance amorphous semiconducting oxides from a solution process.[36] Such an approach could be attempted in the future, since the urea complexes of metal nitrates are also compounds with the inherent possibility of initiating the combustion reaction via UV processing.

Conclusions

Eco-friendly water-soluble metal urea complexes of indium, gallium and zinc precursors of composition $In/Ga(urea)_6(NO_3)_2$ and $Zn(urea)_4(H_2O)_2(NO_3)_2$ were successfully employed in the generation of active semiconductor IGZO thin films via a solution-processing route. The precursors undergo a desirable exothermic decomposition (combustion) when annealed at relatively low temperatures between 200 and 350 °C, with volatile gaseous by-products affording the formation of clean ceramic oxides which enable the formation of amorphous IGZO thin films. Integration of such solution-processed thin-films enables the formation of active semiconductor materials. At an optimum temperature of 350 °C, TFT performance with the device mobility (μ_{sat}) of 3.1 cm^2/Vs and a current on/off ratio of 10^7 was achieved. The formation of the thin-film oxides from the urea nitrate complexes was investigated with respect to their microstructure-property relationship and the change in the oxygen environment at different annealing temperatures by XPS. HR-TEM and AFM investigations show a visible dependency of the film density and surface morphology, wherein dense and smooth films could be manufactured at reasonable calcination temperatures. This was further confirmed by an improved degree of ceramisation exhibiting a reduced presence of hydroxide species at elevated calcination temperatures. This observation is well corroborated with the observed TFT performance in the IGZO films derived from the urea nitrate complexes.

Experimental Section

Precursor synthesis and analysis

Hexakis(urea)indium(III) nitrate (**1**): Indium nitrate hydrate (3 g, 10 mmol) was dissolved in 100 mL of anhydrous ethanol. An excess of urea (5.40 g, 90 mmol) was added thereafter into the solution. The solution was stirred for 3 hours and the formation of a visible white precipitated product is observed. The product was washed in ethanol to ensure the removal of any by-products and then dried in vacuo (7.45 g, 84%). The compound is soluble in water and moderately soluble in methanol. Crystals suitable for X-

ray crystal structure determination were obtained by creating a saturated solution in methanol and layering with diethylether for several days at room temperature. Anal. calcd (%) for $C_6H_{24}InN_{15}O_{15}$ (661.17 g mol^{-1}) C 10.90 H 3.66 N 31.78; found C 10.64 H 3.76 N 31.57. ^{1}H NMR ([D$_6$] dimethyl sulfoxide, 25 °C) δ = 5.49 ppm (br, -NH$_2$). ^{13}C{^{1}H} NMR ([D$_6$] dimethyl sulfoxide, 25 °C): 159.67 (C=O). IR (crystals) $\tilde{\nu}$ = 3431 (s, $\nu_{NH,out\ of\ phase}$), 3343 (s, $\nu_{NH,in\ phase}$), 3232 (s, $\nu_{NH,ip}$), 1630 (s, ν_{CO}), 1557 (s, δ_{NH}), 1504 (s, δ_{NH}), 1329 (s, ν_{CN}), 1155 (m, ρ_{NH}), 1027 (m, ρ_{NH}), 827 (w, ω_{NH}), 765 (w, ω_{NH}), 611 (m, δ_{CN}), 537 (m, δ_{CN}), 433 cm^{-1} (m, τ_{NH}). The detailed crystallographic data for (**1**) is provided in the Supplementary Information.

Hexakis(urea)gallium(III) nitrate (**2**): The compound was synthesized analogously to the preparation of (**1**), (5.56 g, 67%). The product can be recrystallized in a similar fashion like the indium complex. Anal. calcd (%) for $C_6H_{24}GaN_{15}O_{15}$ (616.07 g mol^{-1}) C 11.70 H 3.93 N 34.10; found C 11.51 H 3.92 N 34.07. ^{1}H NMR ([D$_4$] methanol, 25 °C) δ = 4.90 (br, -NH$_2$). ^{13}C{^{1}H} NMR ([D$_4$] methanol, 25 °C): 162.30 (C=O). IR (crystals) $\tilde{\nu}$ = 3435 (s, $\nu_{NH,out\ of\ phase}$), 3342 (s, $\nu_{NH,\ in\ phase}$), 3235 (s, $\nu_{NH,in\ phase}$), 1630 (s, ν_{CO}), 1560 (s, δ_{NH}), 1505 (s, δ_{NH}), 1332 (s, ν_{CN}), 1152 (m, ρ_{NH}), 1032 (m, ρ_{NH}), 829 (w, ω_{NH}), 762 (w, ω_{NH}), 618 (m, δ_{CN}), 537 (m, δ_{CN}), 433 cm^{-1} (m, τ_{NH}).

Diaqua-tetrakis(urea)zinc(II) nitrate (**3**): Zinc nitrate hexahydrate (5.95 g, 20 mmol) was dissolved in n-butanol. Urea (4.80 g, 80 mmol) was added thereafter into the solution. The solution was stirred for 1 hour and the formation of a visible white precipitated product is observed. The product was washed with butanol to ensure the removal of any by-products and then dried in vacuo (5.90 g, 79%). Crystals for a single crystal structure analysis were obtained by creating a saturated solution in ethanol and layering it with diethyl ether for several days at room temperature. Anal. calcd (%) for $C_4H_{20}N_{10}O_{12}Zn$ (465.64 g mol^{-1}) C 10.32 H 4.33 N 30.08; found C 10.56 H 4.32 N 30.37. ^{1}H NMR ([D$_6$] dimethyl sulfoxide, 25 °C) δ = 5.46 (br, -NH$_2$), 3.47 ppm (br, H$_2$O) ^{13}C{^{1}H} NMR ([D$_6$] dimethyl sulfoxide, 25 °C): 159.62 (C=O). IR (crystals) $\tilde{\nu}$ = 3447 (s, $\nu_{NH,out\ of\ phase}$), 3345 (s, $\nu_{NH,in\ phase}$), 3215 (s, $\nu_{NH,in\ phase}$), 1626 (s, ν_{CO}), 1579 (s, δ_{NH}), 1476 (s, δ_{NH}), 1351 (s, ν_{CN}), 1294 (s, ν_{CN}), 1150 (m, ρ_{NH}), 1015 (m, ρ_{NH}), 819 (w, ω_{NH}), 7778 (w, ω_{NH}), 622 (m, δ_{CN}), 591 (m, δ_{CN}), 522 (m, δ_{CN}), 430 cm^{-1} (m, τ_{NH}).

Thin film transistor fabrication

FET substrates were obtained from Fraunhofer IMPS, Dresden. The substrates (15×15 mm^2) consist of a highly n-doped silicon with a 90 nm silicon-oxide dielectric layer. The source-drain electrodes, with a deliberately large channel length L = 20 μm and a channel width W = 10 mm (W/L = 500), were fabricated with 40 nm of gold (interdigital structure) with a 10 nm intermediate adhesion layer of indium tin oxide (ITO) with a device structure in a bottom gate bottom contact device geometry (BGBC). All substrates were sequentially cleaned, with acetone, water and 2-propanol for ten minutes, respectively. The cleaned substrates were exposed for 10 minutes to UV treatment (Nanobio analytics, UVC-1014, 8watts, peak λ = 256 nm 90%, 184 nm 10%) prior to spin coating, to improve the adhesion of the spin-coating solutions.

For the preparation of the spin coating solutions, stock solutions of the indium(III), gallium(III) and zinc (II) precursor were formed by dissolving five weight % of the respective precursors each in deionised water. After complete dissolution, a clear solution is obtained which is then filtered through a 0.45 μm hydrophylic syringe filter and mixed in the desired ratio (In:Ga:Zn, 7:1:1.5) ratios for spin coating of IGZO thin films. The spin coating was carried out under ambient conditions with a spinning speed of 4000 rpm for 10 seconds. The spin-coated precursor films were subjected to thermal annealing in ambient atmosphere at desired temperatures for 10 minutes. Repeated iterations of the aforementioned procedure were carried out until desired film thickness was achieved. Finally, the films were annealed for two hours under the respective temperature to generate the functional semiconducting oxide thin films.

Material and device characterization

X-ray diffraction data were collected using a STOE STADI IV 4-circle single crystal diffractometer at ambient temperature. The graphical images of the molecules were generated with using the PLATON software. Transmission electron microscopy (TEM) was carried out using Tecnai F20 (FEI), with an operating voltage of 200 kV. Atomic force microscopy (AFM) was conducted on a MFP-3D™ (Asylum Research) system equipped with silicon cantilevers. (AFM) measurements were carried out with CP-II (Bruker-Veeco), with silicon cantilevers. Thermogravimetric analysis (TGA) measurements were performed using a TG209F1-Iris (Netzsch) thermal analyzer, employing aluminum crucibles. XRD was performed on a Rigaku Miniflex 600@40 kV 15 mA diffractometer using $Cu_{K\alpha1}$ radiation (λ = 1.541 Å). XPS measurements were performed using a K-Alpha XPS instrument (Thermo Fisher Scientific, East Grinstead, UK) monochromated $Al_{K\alpha}$ X-ray source (30–400 μm spot size). All spectra were referenced to that of hydrocarbon C1s peak at 285.0 eV. TFT characteristics for 8 devices for all temperature ranges measured and were determined with an HP 4155A Semiconductor Parameter Analyzer (Agilent) in a glove box under exclusion of air and moisture in the dark. The fabricated devices were mechanically isolated prior to measurement. Charge carrier mobility ($\mu_{sat.}$) and threshold voltage Vth were derived from a linear fitting of the square root of the source-drain current ($\sqrt{I_{ds}}$) as a function of gate-source voltage V_{GS}.

Acknowledgements

S.S., R.H. and J.J.S. acknowledge financial support through the DFG SPP 1569 program. TEM investigations were performed at ERC Jülich under contract ERC-TUD1. We gratefully acknowledge J. Engstler and S. Heinschke (both at TUDa) for performing TEM and XRD analysis.

Conflict of interest

The authors declare no conflict of interest.

Keywords: indium · gallium · metal oxides · molecular precursors · thin film transistors · zinc · urea-nitrate compounds

[1] a) T. Kamiya, H. Hosono, *NPG Asia Mater.* **2010**, *2*, 15; b) E. Fortunato, P. Barquinha, R. Martins, *Adv. Mater.* **2012**, *24*, 2945.
[2] J. F. Wager, B. Yeh, R. L. Hoffman, D. A. Keszler, *Curr. Opin. Solid State Mater. Sci.* **2014**, *18*, 53.
[3] a) M.-G. Kim, M. G. Kanatzidis, A. Facchetti, T. J. Marks, *Nat. Mater.* **2011**, *10*, 382; b) J. W. Hennek, M.-G. Kim, M. G. Kanatzidis, A. Facchetti, T. J. Marks, *J. Am. Chem. Soc.* **2012**, *134*, 9593; c) J. W. Hennek, J. Smith, A. Yan, M.-G. Kim, W. Zhao, V. P. Dravid, A. Facchetti, T. J. Marks, *J. Am. Chem. Soc.* **2013**, *135*, 10729; d) K. Banger, Y. Yamashita, K. Mori, R. Peterson, T. Leedham, J. Rickard, H. Sirringhaus, *Nat. Mater.* **2011**, *10*, 45; e) X. Yu, N. Zhou, J. Smith, H. Lin, K. Stallings, J. Yu, T. J. Marks, A. Fac-

chetti, *ACS Appl. Mater. Interfaces* **2013**, *5*, 7983; f) G. Liu, A. Liu, F. Shan, Y. Meng, B. Shin, E. Fortunato, R. Martins, *Appl. Phys. Lett.* **2014**, *105*, 113509; g) S. Jeong, Y. Jeong, J. Moon, *J. Phys. Chem. C* **2008**, *112*, 11082.
[4] J. S. Chang, A. F. Facchetti, R. Reuss, *IEEE J. Emerging Selected Top. Circ. Syst.* **2017**, *7*, 7.
[5] S. Sanctis, R. C. Hoffmann, M. Bruns, J. J. Schneider, *Adv. Mater. Interfaces* **2018**, 1800324.
[6] S. Sanctis, R. C. Hoffmann, R. Precht, W. Anwand, J. J. Schneider, *J. Mater. Chem. C* **2016**, *4*, 10935.
[7] W. H. Jeong, D. L. Kim, H. J. Kim, *ACS Appl. Mater. Interfaces* **2013**, *5*, 9051.
[8] a) Y. Chen, B. H. Wang, W. Huang, X. A. Zhang, G. Wang, M. J. Leonardi, Y. Huang, Z. Y. Lu, T. J. Marks, A. Facchetti, *Chem. Mater.* **2018**, *30*, 3323; b) R. C. Hoffmann, J. J. Schneider, *Eur. J. Inorg. Chem.* **2014**, 2241.
[9] a) S. T. Aruna, A. S. Mukasyan, *Curr. Opin. Solid State Mater. Sci.* **2008**, *12*, 44; b) A. Varma, A. S. Mukasyan, A. S. Rogachev, K. V. Manukyan, *Chem. Rev.* **2016**, *116*, 14493.
[10] R. Branquinho, D. Salgueiro, L. Santos, P. Barquinha, L. Pereira, R. Martins, E. Fortunato, *ACS Appl. Mater. Interfaces* **2014**, *6*, 19592.
[11] Y. Qiu, L. Gao, *J. Am. Ceram. Soc.* **2004**, *87*, 352.
[12] M. S. Lupin, G. E. Peters, *Thermochim. Acta* **1984**, *73*, 79.
[13] D. G. Tuck, E. J. Woodhouse, P. Carty, *J. Chem. Soc. A* **1966**, DOI: https://doi.org/10.1039/J196600010771077.
[14] a) B. N. Figgis, E. S. Kucharski, J. M. Patrick, A. H. White, *Aust. J. Chem.* **1984**, *37*, 265; b) D. Moon, S. Tanaka, T. Akitsu, J. H. Choi, *Acta Crystallogr. Sect. E* **2015**, *71*, 1336.
[15] H. Aghabozorg, G. J. Palenik, R. C. Stoufer, J. Summers, *Inorg. Chem.* **1982**, *21*, 3903.
[16] T. J. Prior, R. L. Kift, *J. Chem. Crystallogr.* **2009**, *39*, 558.
[17] A. Krawczuk, K. Stadnicka, *Acta Crystallogr. Sect. C* **2007**, *63*, m448.
[18] S. Smeets, M. Lutz, *Acta Crystallogr. Sect. C* **2011**, *67*, m50.
[19] M. Koman, E. Jona, D. Nagy, *Z. Kristallogr.* **1995**, *210*, 873.
[20] a) C.-C. Lin, Y.-Y. Li, *Mater. Chem. Phys.* **2009**, *113*, 334; b) H. M. Ismail, *J. Anal. Appl. Pyrolysis* **1991**, *21*, 315.
[21] T. Arii, A. Kishi, *J. Therm. Anal. Calorim.* **2006**, *83*, 253.
[22] a) V. D. Zhuravlev, V. G. Bamburov, A. R. Beketov, L. A. Perelyaeva, I. V. Baklanova, O. V. Sivtsova, V. G. Vasil'ev, E. V. Vladimirova, V. G. Shevchenko, I. G. Grigorov, *Ceram. Int.* **2013**, *39*, 1379; b) J. Baneshi, M. Haghighi, N. Jodeiri, M. Abdollahifar, H. Ajamein, *Ceram. Int.* **2014**, *40*, 14177.
[23] S. Désilets, P. Brousseau, D. Chamberland, S. Singh, H. Feng, R. Turcotte, K. Armstrong, J. Anderson, *Thermochim. Acta* **2011**, *521*, 59.
[24] Y. Zhao, R. L. Frost, W. N. Martens, *J. Phys. Chem. C* **2007**, *111*, 16290.
[25] H. Y. Playford, A. C. Hannon, E. R. Barney, R. I. Walton, *Chem. Eur. J.* **2013**, *19*, 2803.
[26] A. Nadarajah, M. Z. Wu, K. Archila, M. G. Kast, A. M. Smith, T. H. Chiang, D. A. Keszler, J. F. Wager, S. W. Boettcher, *Chem. Mater.* **2015**, *27*, 5587.
[27] G. H. Kim, B. D. Ahn, H. S. Shin, W. H. Jeong, H. J. Kim, H. J. Kim, *Appl. Phys. Lett.* **2009**, *94*, 233501.
[28] a) B. Cui, L. Zeng, D. Keane, M. J. Bedzyk, D. B. Buchholz, R. P. H. Chang, X. Yu, J. Smith, T. J. Marks, Y. Xia, A. F. Facchetti, J. E. Medvedeva, M. Grayson, *J. Phys. Chem. C* **2016**, *120*, 7467; b) X. Yu, J. Smith, N. Zhou, L. Zeng, P. Guo, Y. Xia, A. Alvarez, S. Aghion, H. Lin, J. Yu, R. P. H. Chang, M. J. Bedzyk, R. Ferragut, T. J. Marks, A. Facchetti, *Proc. Natl. Acad. Sci. USA* **2015**, *112*, 3217.
[29] R. Y. Seung, K. H. Jae, *Phys. Status Solidi A* **2014**, *211*, 2195.
[30] Y.-H. Kim, J.-S. Heo, T.-H. Kim, S. Park, M.-H. Yoon, J. Kim, M. S. Oh, G.-R. Yi, Y.-Y. Noh, S. K. Park, *Nature* **2012**, *489*, 128.
[31] S. Hwang, J. H. Lee, C. H. Woo, J. Y. Lee, H. K. Cho, *Thin Solid Films* **2011**, *519*, 5146.
[32] P. K. Nayak, J. A. Caraveo-Frescas, Z. Wang, M. N. Hedhili, Q. X. Wang, H. N. Alshareef, *Sci. Rep.* **2014**, *4*, 4672.
[33] a) T. S. Kang, K. S. Yoon, G. H. Baek, W. B. Ko, S. M. Yang, B. M. Yeon, J. P. Hong, *Adv. Electron. Mater.* **2017**, *3*, 1600452; b) J. Espinós, J. Morales, A. Barranco, A. Caballero, J. Holgado, A. González-Elipe, *J. Phys. Chem. B* **2002**, *106*, 6921; c) J. W. Na, Y. S. Rim, H. J. Kim, J. H. Lee, S. Hong, H. J. Kim, *ACS Appl. Mater. Interfaces* **2017**, *9*, 29849.
[34] a) R. C. Hoffmann, S. Sanctis, J. J. Schneider, *Inorg. Chem.* **2017**, *56*, 7550; b) N. Zydziak, C. Hübner, M. Bruns, A. P. Vogt, C. Barner-Kowollik, *Polym. Chem.* **2013**, *4*, 1525; c) N. Zydziak, C. M. Preuss, V. Winkler, M. Bruns, C. Hübner, C. Barner-Kowollik, *Macromol. Rapid Commun.* **2013**, *34*, 672.
[35] a) S. Jeong, Y.-G. Ha, J. Moon, A. Facchetti, T. J. Marks, *Adv. Mater.* **2010**, *22*, 1346; b) H. Hideo, *SID Symp. Dig. Tech. Pap.* **2007**, *38*, 1830.
[36] R. A. John, N. A. Chien, S. Shukla, N. Tiwari, C. Shi, N. G. Ing, N. Mathews, *Chem. Mater.* **2016**, *28*, 8305.
[37] CCDC 1863798 (**1**) and 704906 (**3**) contain the supplementary crystallographic data for this paper. These data can be obtained free of charge from The Cambridge Crystallographic Data Centre.

Manuscript received: September 12, 2018
Revised manuscript received: October 7, 2018
Version of record online: November 13, 2018

6.7 Stacked indium oxide/zinc oxide heterostructures as semiconductors in thin film transistor devices: a case study using atomic layer deposition.

Atomic layer deposition (ALD) based deposition of oxide semiconductors have gained increasing momentum in the past decade due to the fact that the gas-phase technique ALD relies on a sequential, self-limiting surface reaction mechanism that enables it to offer precise thickness, reproducibility and compositional control of the fabricated layers. Furthermore, ALD enables the growth of high quality films with high uniformity and conformity which makes it a promising candidate for the fabrication of ultra-thin semiconductor layers (< 10nm) with a high degree of conformity over 2D and even 3D surfaces enhancing its potential for devices architectures involved in next-generation semiconductor technology. However, use of ALD has largely been restriced to the deposition of high-k dielectrics (AlO_x and HfO_x) and individual metal oxides such as ZnO with additional layer of a dopant high-k dielectric. Generation of multinary amorphous oxides is rather difficult due the sequential nature of the deposition of individual metal oxide layers and is possible only via sophiticated set-ups enabling co-injection of precursors to fabricate IGZO among other multinary oxide semiconductors.

In this publication, we demonstrate for the very first time, the use of an ALD-based heterostructure design using individualy semiconductors such as ZnO and In_2O_3 to fabricate high performance oxide TFTs based on ultra-thin (<10nm), multilayered heterostructure comprising polycrystalline In_2O_3/ZnO, using conventional ALD precursors and H_2O as an oxidant, for the generation of high performance heterostructure semiconductors. Generation of an optimised heterostructure based on sequential deposition of the aforementioned individual oxides, processed at a reasonably low temperature regime (250–300°C) deliver high performance TFTs. The influence of the overall stack thichness as well as the sequence of the deposited layers reveal a significant influence on the final TFT performance. Reversing positions of the interlayers, starting with deposition of the zinc oxide layer first, followed by indium oxide layer deposition (→ ZnO/In_2O_3, four stack arrangement) yielded only poor TFT performance with an average field-effect mobility ($\mu_{sat.}$) of 1.07 cm^2 /V·.s, *V*th of 10 V, $I_{on/off}$ ratio of 5.2 × 10^6 and a sub-threshold swing (SS) of 1.85 V dec^{-1}. However, when the deposition of the indium oxide layer is first, followed by the zinc oxide layer (→ In_2O_3/ZnO, four stack arrangement) a comparatively high device performance with an average field-effect mobility ($\mu_{sat.}$) of 6.5 cm^2 /V.s, V_{th} of 8.9 V, $I_{on/off}$ ratio of 5 × 10^7 and a substantially reduced subthreshold swing (SS) of 0.7 V dec^{-1} is observed. These effects arise from interplay of intrinsic

vacancy defects of the individual layers, which are based on their position with respect to the dielectric interface, within a heterostructure architecture.

Volume 6 | Number 3 | 21 January 2018 | Pages 403–670

Journal of Materials Chemistry C

Materials for optical, magnetic and electronic devices

rsc.li/materials-c

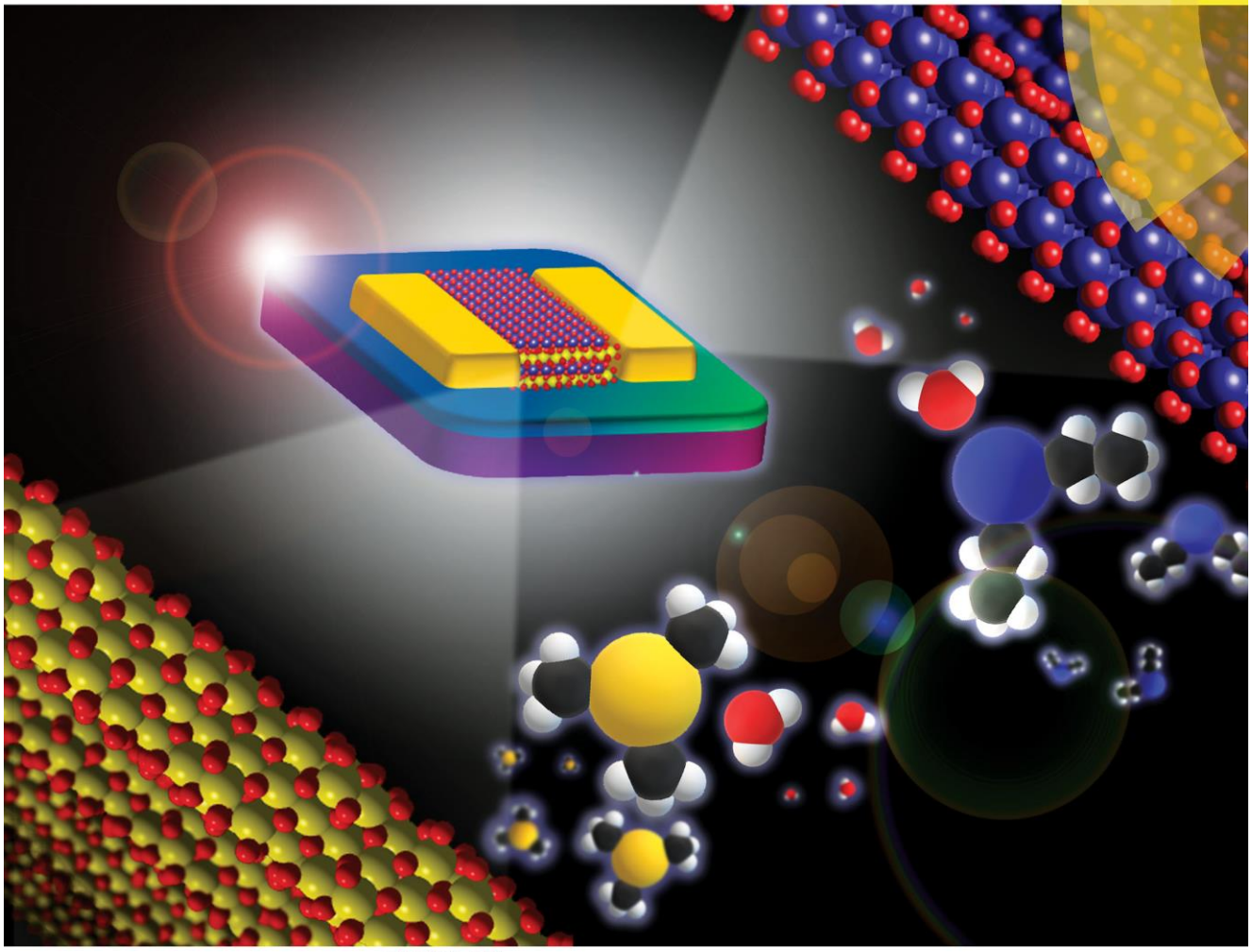

ISSN 2050-7526

ROYAL SOCIETY OF CHEMISTRY

PAPER

Jörg J. Schneider *et al.*

Stacked indium oxide/zinc oxide heterostructures as semiconductors in thin film transistor devices: a case study using atomic layer deposition

Journal of Materials Chemistry C

PAPER

View Article Online
View Journal | View Issue

Cite this: J. Mater. Chem. C, 2018, 6, 464

Stacked indium oxide/zinc oxide heterostructures as semiconductors in thin film transistor devices: a case study using atomic layer deposition†

Shawn Sanctis, ‡[a] Jan Krausmann,‡[a] Conrad Guhl[b] and Jörg J. Schneider *[a]

Received 16th August 2017,
Accepted 4th November 2017

DOI: 10.1039/c7tc03724d

rsc.li/materials-c

Multi-layer heterostructure oxide semiconductors employing a layer-by-layer deposition of alternating indium oxide and zinc oxide thin films generated *via* atomic layer deposition (ALD) are investigated for their feasibility into high performance thin film transistors (TFT). The successful deposition of uniform film thickness across the alternating indium oxide and zinc oxide deposition at 200 °C is achieved using trimethyl indium (TMI), diethyl zinc (DEZ) and water as oxidizing agent. The as-prepared polycrystalline material shows a conductive behaviour which upon additional mild annealing between 250–300 °C demonstrates a high TFT device performance. In addition, insights into the dependency of the defect passivation gradient within the multilayer upon thermal annealing of the oxide stack are presented. Studies towards an optimised film thickness result in a high device performance in enhancement mode with a saturation field-effect mobility (μ_{sat}) of 6.5 $cm^2\ V^{-1}\ s^{-1}$ and an on/off ratio ($I_{on/off}$) of 4.6×10^7 using a deliberately large width to length channel ratio (W/L = 500). The TFT performance turned out to be dependent on the position of the individual oxide layers within the stack and the number of heterostructure stacks. These findings on the influence of semiconductor stack formation allow for a better understanding on the formation of the active semiconductor channel and serve towards the applicability of ALD based heterostructure metal oxide semiconductors in next generation electronics.

1. Introduction

Transparent thin film transistors based on semiconducting metal oxides have become the focal point of next generation display technology since their emergence as superior counterparts to the traditional silicon based transistor technology. Multinary amorphous oxides have been intensively investigated for their superior TFT performance since its inception.[1,2] A variety of ternary and quaternary metal oxides, namely indium zinc oxide (IZO), zinc tin oxide (ZTO) and indium gallium zinc oxide (IGZO) among others, have evolved as promising candidates for integration into commercially relevant next-generation display technology.[3,4] Deposition of such multinary metal oxide combinations have conventionally been realised *via* radio-frequency (RF)/direct-current (DC) sputtering as well as solution-processing especially over the last years, representing an economically feasible approach towards large area fabrication techniques.[5–9] However, ALD based deposition of oxide semiconductors have gained increasing momentum in the past decade. This is largely due to the fact that the gas-phase technique ALD relies on a sequential, self-limiting surface reaction mechanism that enables it to offer precise thickness, reproducibility and compositional control of the fabricated layers.[10–12] Furthermore, ALD enables the growth of high quality films with high uniformity and conformity which makes it a promising candidate for the fabrication of heterostructure based TFTs. However, ALD based deposition of metal oxides has largely been employed for the fabrication of high-k dielectrics (*e.g.* Al_2O_3, HfO_2), since it ensures a facile conformal coating over desired substrates.[13,14] While employing ALD based oxide dielectrics in combination with solution processed organic dielectrics it was demonstrated that device performance could be significantly enhanced in organic TFTs as well.[15–17] Research in metal oxide semiconductors, research has largely focused on ZnO based devices due to their high mobility, scalability and low temperature processing. Especially, the investigation of polycrystalline ZnO based TFTs prepared *via* atomic layer deposition (ALD) has become a fast growing area of research which is related to the feasible tuning of electronic properties.[18,19] Efforts towards the fabrication of ALD based ZnO TFTs combined with other metal oxides were mainly dedicated to enhance the

[a] Fachbereich Chemie, Eduard-Zintl-Institut, Fachgebiet Anorganische Chemie, Technische Universität Darmstadt, Alarich-Weiss-Straße 12, Darmstadt, 64287, Germany. E-mail: joerg.schneider@ac.chemie.tu-darmstadt.de
[b] Fachgebiet Oberflächenforschung, Technische Universität Darmstadt, Jovanka-Bontschits-Straße 2, Darmstadt, 64287, Germany

† Electronic supplementary information (ESI) available: Additional AFM, UV-vis and XPS data. See DOI: 10.1039/c7tc03724d

‡ Authors with equal contribution.

stability of ZnO TFTs under bias stress. To this end, cations like Al or Hf have been utilised, aiming to control the density of defects like oxygen vacancies, resulting in high performance AlZnO (AZO) or ZnHfO TFTs.[20–22] Moreover, high performance ALD based multinary amorphous InGaZnO (IGZO), employing sophisticated precursor co-injection systems, as well as amorphous IZO, obtained by using a more chemically sophisticated indium precursor in combination with diethyl zinc (DEZ), have shown promising potential in terms of amorphous semiconductor oxide deposition.[23,24] However, in recent times, multilayered heterostructure semiconductors, such as ZnO in combination with various dielectric oxides have allowed access to high performance transistors, wherein the engineered insulating oxide layer facilitated the controlled passivation of defects as well as an oriented growth direction of the ZnO component.[20,25,26] Interestingly, ALD deposited multilayer heterostructures based on individual binary semiconductor/semiconductor structures towards TFT applications are rather scarce, where pulsed laser deposition (PLD) based ZnO/SnO_2 stacks consisting of amorphous layers has been reported.[27]

Herein, we show a straightforward approach towards fabrication of a multilayered heterostructure comprising polycrystalline In_2O_3/ZnO, using conventional ALD precursors and H_2O as an oxidant, for the generation of high performance heterostructure semiconductors. Within the intended scope of the current work, we have investigated the deposition of such heterostructures, the change in device performance based on a variation of the position and number of In_2O_3/ZnO heterostructure interfaces as well as the influence of a reasonable post-deposition annealing process. Improved performance in such ALD based polycrystalline heterostructure semiconductor layered stacks would certainly promote interest towards their potential integration into advanced display technology as an alternative to the multinary amorphous oxide semiconductors.

2. Results and discussion

2.1. ALD based thin film deposition

To obtain the desired In_2O_3/ZnO stacks supercycles comprising of individual In_2O_3 and ZnO layers with a fixed In_2O_3 ratio of 0.6 in fraction to the total ALD cycles were deposited.[31] In general, a supercycle or complete stack constitutes the sequential deposition of these different metal oxide layers where the cycle ratio is derived from the number of ALD cycles for the individual oxides. Consequently, a supercycle with a In_2O_3 ratio of 0.6 in fraction can be composed of six cycles of In_2O_3 and four cycles of ZnO or multiples of those. The general procedure of the aforementioned supercycle deposition and its utilisation to generate stacked heterostructures of In_2O_3/ZnO interfaces is shown below [Scheme 1]. Since 200 °C reflects the lower limit of the temperature window for deposition of In_2O_3 from TMI and favourably coincides with the temperature window for ZnO deposition from DEZ, this temperature was chosen for the deposition of the In_2O_3/ZnO heterostructure stacks.

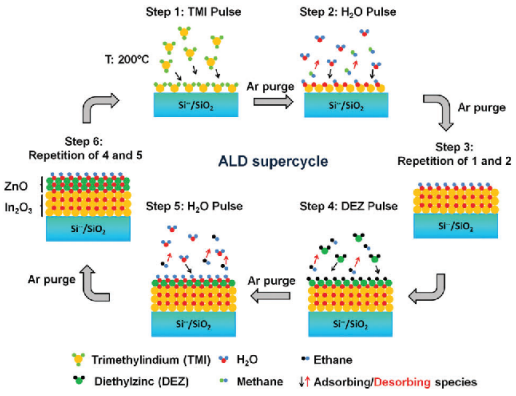

Scheme 1 Schematic representation of a single supercycle performed at 200 °C for the deposition of a In_2O_3/ZnO heterostructure stack from the precursors TMI and DEZ. Steps (1) and (2) depict the indium precursor (TMI) deposition and partial reaction, followed by removal of volatile by-products with an Ar purge and final conversion to the indium oxide with a H_2O pulse. Steps (4) and (5) depict the deposition of the zinc precursor (DEZ) on the indium oxide layer, with analogous reaction steps as for the indium precursor TMI. Steps (3) and (6) indicate multiple iterations of the individual precursor cycles to achieve the desired deposition thicknesses.

The first half of the supercycle (Step 1 and 2) comprises the exposure of the substrate to a TMI pulse (1 s) accompanied with an extended precursor exposure (1.5 s) and the subsequent oxidization with water. In the first step, TMI molecules react with surface OH-groups according to the following equation:[32]

$$(OH)_x^* + In(CH_3)_3\ (g) \rightarrow (-O-)_xIn(CH_3)_{3-x} + xCH_4\ (g)$$

where the surface species are denoted by an asterisk (*). After purging the reactor with carrier gas (Ar), water is introduced into the chamber as an oxidizing agent. As examined in earlier reports, an extremely large Langmuir exposure ($\sim$2 Torr s^{-1}) is required for the surface reaction to convert In–CH_3* molecules into InOH* groups.[33] To provide sufficient conditions for this conversion, an extended water pulse time of 0.1 s was used, followed by Ar purging (20 s). After repeated utilization of the described sequence of TMI and water pulses (Step 3), surface In–OH groups are further subjected to ZnO deposition (Step 4 and 5) to finally obtain the desired In_2O_3/ZnO interfaces. The sequence of ZnO deposition includes the pulsing of DEZ (0.015 s) in the first step, adopting an additional extended exposure of the precursor (1.5 s) with a subsequent Ar purge (15 s), assuming the following reaction of surfacial In–OH*-groups with DEZ:

$$In\text{–}OH^* + Zn(C_2H_5)_2 \rightarrow In\text{–}O\text{–}Zn\text{–}C_2H_5^* + C_2H_6$$

The latter exposure was used to provide sufficient adsorption time and to overcome adsorption delay of the precursor which is known to cause reduced deposition rates when mixed metal oxides are deposited *via* an ALD route.[34] In order to oxidize the resulting Zn–C_2H_5* bound surface species, converting them into Zn–OH* species and providing new adsorption sites for the

successive deposition step, a water pulse (0.015 s) was applied (Step 5), accompanied by Ar purge (15 s). A full supercycle to obtain the desired heterostructures is completed *via* reiteration of the latter sequence (Step 6). The described supercycle was repeated to vary the number of In_2O_3/ZnO interfaces or in more general terms to adjust the thickness of the thin films. Regarding ALD of mixed metal oxides in a supercycle fashion as described, the growth rate of the thin films per ALD cycle can be estimated from the deposition rates of the individual binary oxides according to the rule of mixture:[33]

$$G(In_2O_3/ZnO\ stack) = R(In_2O_3) \times G(In_2O_3) + [1 - R(In_2O_3)] \times G(ZnO)$$

where G denotes the growth rate per cycle for the corresponding metal oxide and R describes the fraction of In_2O_3 cycles in the supercycle.

In order to estimate the deposition rate for the current In_2O_3/ZnO heterostructures, the growth rates of the individual oxides were determined. These could be assigned to 0.4 Å cycle $^{-1}$ and ~1.45 Å cycle $^{-1}$ for In_2O_3 and for ZnO, respectively. Based on these results, the expected growth rate derived from the rule of mixture for the heterostructures was ~0.82 Å cycle $^{-1}$ when an In_2O_3 cycle ratio of 0.6 was used. Compared to this estimation, the actual deposition rate of the stacked heterostructures is significantly lower, exhibiting a value of ~0.54 Å cycle $^{-1}$. The observed trend of a deteriorated growth rate was also reported for amorphous IZO thin films that were generated *via* utilization of TMI, DEZ and water as the metal precursors and oxidizing agent, respectively wherein the lowered growth rate was ascribed to a retarded adsorption of DEZ during ALD growth of the amorphous ternary metal oxide.[33] Similar observations have been made for ALD based zinc tin oxide (ZTO) thin films where it was reported that a change in surface chemistry due to a ligand conversion led to a reduction of –OH groups, consequently reducing the reaction sites for subsequent ZnO deposition.[34]

Cross-sectional transmission electron microscopy (TEM) micrographs obtained by focused ion beam (FIB) preparation of the ultra-thin stacks display a defined deposition of four In_2O_3/ZnO stacks, with In_2O_3 as the first deposited layer on the Si/SiO_2 substrate followed by ZnO deposition. The TEM investigations indeed reflect the growth of an ultrathin layer (~9 nm), comprising a layer-by-layer architecture (Fig. 1a) with distinct individual layers of In_2O_3 (darker contrast) and ZnO (lighter contrast). These layers exhibit a microcrystalline nature of the deposited oxides (Fig. 1b). In order to verify the gradient of the Zn^{2+} and In^{3+} cationic species, Auger electron spectroscopy (AES) was performed on the as-prepared sample. The Auger depth profile exhibits multiple peak profiles indicating the expected distribution of the respective oxides along the vertical gradient of the film showing alternating peaks and troughs related to the atomic concentration assignable to the varying film deposition according to the deposition protocol of the supercycles (Fig. 1c). The variation of chemical composition for both the In^{3+} and Zn^{2+} across the stacks corroborate well

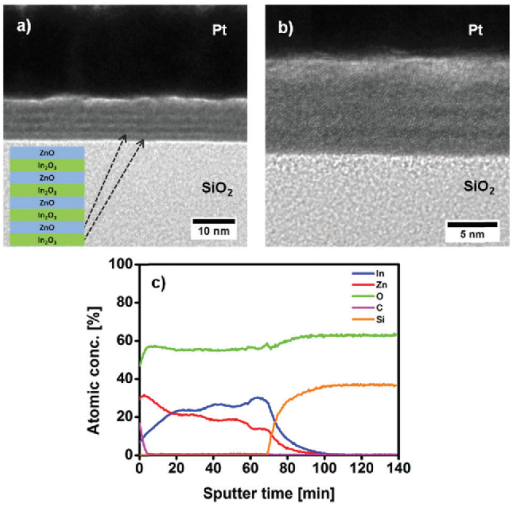

Fig. 1 Cross-sectional TEM micrographs obtained *via* FIB sample preparation of (a) as-deposited, (b) high-resolution image and (c) characteristic auger electron spectroscopy (AES) based depth profile of as-deposited four In_2O_3/ZnO heterostructure stacks.

with the findings from the TEM investigation of the In_2O_3/ZnO heterostructure. Additionally, no significant carbon contamination from undecomposed precursors was observed within the film, showing only carbon related signals arising from surface species, but not from intrinsic contamination of the deposited layers. This clearly indicates a successful conversion of the precursor by solely using H_2O as an oxidant. Presence of minor amounts of adsorbed surface moieties on the thin film can be expected, since the devices were not encapsulated.[7] In order to gain further insight into the evolution of the film quality of the resultant stacked layer, atomic force microscopy (AFM) was performed for the individually deposited In_2O_3 and ZnO films and for the In_2O_3/ZnO stacks with all three films possessing the same thickness (~9 nm) and post calcination at 300 °C (Fig. S1, ESI†). The individually deposited In_2O_3 films (R_{RMS} ~ 0.34 nm) showed a higher degree of roughness in comparison with that of the individually deposited ZnO films (R_{RMS} ~ 0.22 nm). The In_2O_3/ZnO stack layers (R_{RMS} ~ 0.28 nm) exhibit an intermediate degree of roughness compared to their individual oxide counterparts. These observations display that In_2O_3 films obtained from TMI contribute significantly to the overall roughness of the stack and are slightly rougher than the ZnO films obtained using DEZ. Although film roughness might be an important issue to improve the TFT device performance, based on the current investigations it appears that in such ultrathin heterostructure stack films (<10 nm), film roughness does not seem to affect the overall TFT performance. Instead, an even larger effect might arise from the fact that increasing the local charge carrier concentration closer to the dielectric interface, by deposition of a relatively rough In_2O_3 film first, at the dielectric SiO_x interface, instead of a smoother ZnO film.

The deposition of a smoother ZnO film as the first layer followed by an In_2O_3 film just by switching the sequence of the deposited layers within the stack indeed decreased the overall TFT performance drastically (see Section 2.2 – thin film transistor performance). In order to assess the optical transparency, individual In_2O_3, ZnO films as well as the (In_2O_3/ZnO) stacked layer films were investigated (Fig. S2, ESI†). All three films display desirable optical properties, with good optical transparency (> 80%) in the visible region.

To investigate possible changes in the chemical bonding of the of the In_2O_3 and ZnO layers within a stack in its as-prepared state and after post-deposition annealing, X-ray photoelectron spectroscopy (XPS) was performed for the as-prepared stack as well as for those which were post annealed at 250 °C and at 300 °C respectively (Fig. S3 and Table S1, ESI†). Based on the peak position obtained from the core spectra, the $In3d_{5/2}$ and the $In3d_{3/2}$ for all three samples are observed at 444.4 eV and 452 eV respectively, with no significant peak shifts. The observations are in good agreement with typical values reported for In_2O_3, indicating that the indium oxide did not undergo any significant chemical changes due to this post annealing within the investigated temperature regime. However, interestingly significant shifts towards higher binding energies for the Zn peaks are observed when comparing the as-prepared sample with the post annealed sample. Herein, for the as-prepared and annealed sample, the $Zn2p_{3/2}$ and $Zn2p_{1/2}$ values shifted from 1021.3 eV to 1021.8 eV and 1044.4 eV to 1044.9 eV respectively. Similar shifts towards higher binding energies were observed in recent literature for ultrathin bilayer In_2O_3/ZnO films, where the peak shifts with increased processing temperature were attributed to an improved passivation of oxygen vacancy related defects as well as the potential interplay between the oxygen related species at the bilayer In_2O_3/ZnO interface, arising from the formation of individual oxides during the post-deposition annealing.[35] The correlation of the chemical composition of the thin films, with respect to the nature and concentration of oxygen related species across the depth of the stacks were thus further studied *via* angle resolved XPS (ARXPS). The core oxygen O1s spectra are deconvoluted into two primary peaks at ~530 eV and ~532 eV. The former is attributed to the co-ordinated metal–oxygen bonds, while the latter is observed due to the residual hydroxide species present within the film, due the conditions employed for film growth.[36] Deconvoluted O1s spectra of the as-prepared film as well as the 300 °C annealed films across different sample tilt angles (STA) however reveal distinct changes in the ratio of oxygen related species of the observed O1s spectrum (Fig. 2 and Table 1).

A lower STA reveals contributions mainly from the surface and a gradual increase in STA accounts for contributions from the surface along with the increasing contributions closer to the dielectric interface (semiconductor/SiO_x). The ARXPS analysis hints towards the higher concentration of residual hydroxyl groups at the interface, which also correlates with the conductive behaviour observed in thicker films and the need for post-deposition annealing temperatures.[36,37]

One possible reason for this observation can be allocated to the fact that if the films are stronger oxidized on the surface,

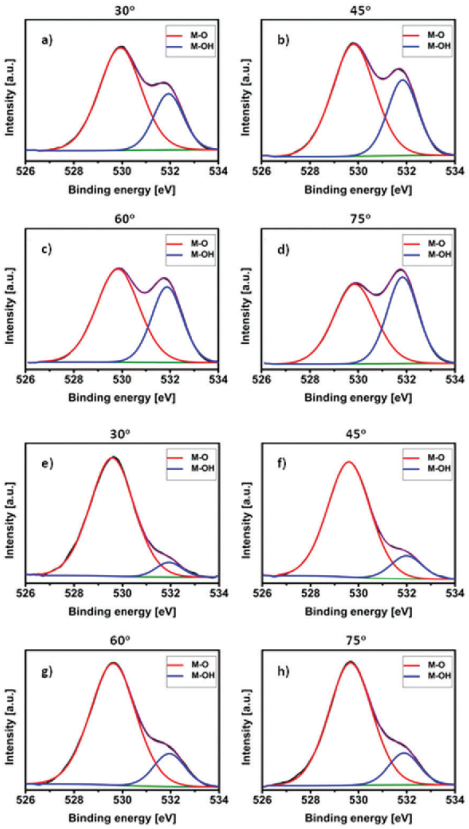

Fig. 2 Angle resolved O1s spectra of (a–d) as-deposited In_2O_3/ZnO heterostructures (four stacks) and (e–h) In_2O_3/ZnO heterostructures annealed at 300 °C for 2 hours for different sample tilt angles (STA). An increasing STA (30° → 75°) reflects oxygen contributions arising from the region close to the surface (30°), graduating towards the interface at 75°.

the density of the formed oxide at the surface may serve as a strong oxygen diffusion barrier which however, could be overcome with an additional thermal annealing step.[36] This idea is well supported by the fact that a high pressure annealing of sputter based IGZO in different environments, while maintaining a low thermal budget, has indeed shown a remarkable improvement in performance as well a substantial reduction in processing temperature.[38,39]

2.2. Thin film transistor performance

In order to understand the influence of each of the individual oxides on the overall TFT performance, devices with bottom gate/bottom contact (BGBC) set-up were fabricated to evaluate the performance of the active layers. A sufficiently large source–drain electrode geometry with a channel width (W) to length (L) ratio (W/L = 500) was deliberately chosen to avoid any overestimation of field-effect mobility for the measured TFTs. Choice of electrode dimensions with extremely small W/L ratio

Table 1 Atomic % ratio of co-ordinated metal to oxygen bonds (M–O) and hydroxide species (M–OH) of the O1s spectra based on ARXPS of heterostructure [In_2O_3] films together with the corresponding processing conditions. An increasing STA from 30° to 75° reflects oxygen contributions mainly arising from the surface and graduating towards the interface

Sample In_2O_3/ZnO	STA 30°		STA 45°		STA 60°		STA 75°	
	M–O (at%)	M–OH (at%)	M–O (at%)	M–OH (at%)	M–O (at%)	M–OH (at%)	M–O (at%)	M–OH (at%)
As-prepared	72.6	27.4	67.7	32.3	63.2	36.8	55.7	44.3
Annealed at 300 °C	93.2	6.8	87.1	12.9	84.8	15.2	84.5	15.5

could easily lead to an overestimation of the effective TFT mobility of up to 400%.[40,41] TFTs based on indium oxide as well as zinc oxide (both ~9 nm) were fabricated, resembling similar thickness conditions as that of the optimised heterostructure layer with four stacks.

After post-annealing (300 °C for 2 hours), the indium oxide based TFTs exhibited a conductive behaviour, with a $I_{on/off}$ ratio ~1, while the zinc oxide based TFT exhibited a clear semiconducting behaviour with an average saturation field effect mobility ($\mu_{sat.}$) of 0.48 cm^2 (V^{-1} s^{-1}), *V*th of 12.7 V, $I_{on/off}$ ratio of 3×10^6 and a subthreshold swing (SS) of 1.61 V dec^{-1} (Fig. 3). This serves as a good indication that in comparison with zinc oxide, indium oxide generated, possesses a higher defect concentration, wherein further thermal annealing (300 °C), did not passivate the defects sufficiently to exhibit a semiconductive behaviour when integrated into a TFT device.[42] This is also in agreement with the XPS results discussed earlier, where the peak shifts (Zn2p, In3d) were observed only for ZnO and not for In_2O_3 within the stack.

Additionally, based on the metal oxide employed and its observed semiconducting properties, deposition (either sputtering or solution processing) of semiconducting layers with a higher charge carrier concentration at the dielectric interface, followed by subsequent deposition of layers with reduced charge carrier concentration has shown substantial improvement in the overall transistor performance.[43,44] Our preliminary examination of reversing positions of the interlayers, starting with deposition of the zinc oxide layer first, followed by indium oxide layer deposition (→ ZnO/In_2O_3, four stack arrangement) yielded only poor TFT performance with an average field-effect mobility ($\mu_{sat.}$) of 1.07 cm^2 V^{-1} s^{-1}, *V*th of 10 V, $I_{on/off}$ ratio of 5.2×10^6 and a sub-threshold swing (SS) of 1.85 V dec^{-1}. However, when the deposition of the indium oxide layer is first, followed by the zinc oxide layer (→ In_2O_3/ZnO, four stack arrangement) a comparatively high device performance with an average field-effect mobility ($\mu_{sat.}$) of 6.5 cm^2 V^{-1} s^{-1}, *V*th of 8.9 V, $I_{on/off}$ ratio of 5×10^7 and a substantially reduced subthreshold swing (SS) of 0.7 V dec^{-1} is observed (Fig. 3). This observation is in good agreement with reported observations based on synergistic effects of device performance arising from interplay of intrinsic vacancy defects of the individual layers, which are based on their position with respect to the dielectric interface, within a heterostructure architecture.[45–47]

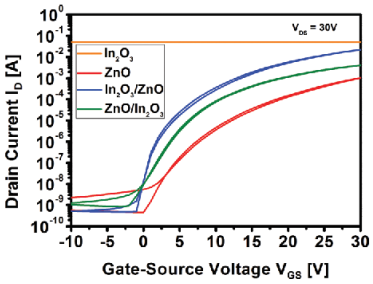

Fig. 3 Individual transfer characteristics of TFTs based on individual In_2O_3, ZnO layers, [(In_2O_3/ZnO), four stacks] and on [(ZnO/In_2O_3), four stacks] each sample annealed at 300 °C for 2 hours.

Based on the TFT performance of the individual oxides, preliminary experiments were then performed to determine the critical number of deposition cycles for In_2O_3 and the subsequently needed cycles for ZnO in order to understand the required stack architecture for which active semiconductor behaviour in a relatively low temperature regime at 300 °C could be observed. Once this was achieved, device optimisation was performed in order to assess the number of In_2O_3/ZnO stacks needed, followed by a subsequent impact of post deposition annealing temperature on TFT performance. Active film thickness was increased by performing multiple deposition iterations of a single supercycle *via* ALD, followed by post processing of all the TFTs at 300 °C. Film thicknesses for three, four, five and six stacks were 7 nm, 9 nm, 11 nm and 13 nm respectively, as determined *via* ellipsometry. The measured transfer and output characteristics for an increasing number of stacks and its corresponding evaluation of the critical device performance parameters are shown (Fig. 4 and Table 2).

From the evaluation of the transfer characteristics, a systematic increase in film conductivity is observed, as one increases the number of deposited stacks. A primary effect observed for an increasing thickness of the semiconducting layer is a gradual increase of the off-current and a negative shift of the threshold voltage *V*th. The need for a compromise between the device mobility and other performance parameters such as *V*th, $I_{on/off}$ ratio and subthreshold swing is a well reported observation with inorganic oxide based TFTs.

Several recent strategies to control the local carrier concentration gradient across the film-thickness by manipulating the oxygen environment during sputter based thin film deposition or by modulating the cation species within metal oxide systems (ranging from binary to quaternary oxides) have demonstrated their efficacy in substantially improving device performance.[43,44,46–48] The latter approach is also in accordance with the results demonstrated within the current work, whereby increasing the overall

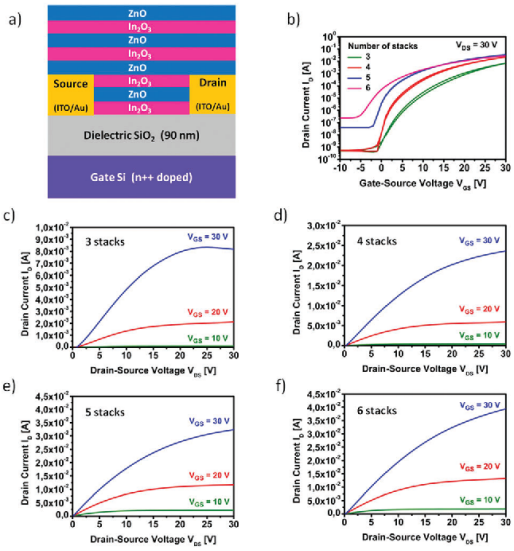

Fig. 4 (a) Schematic representation of the TFTs (not to scale) fabricated employing ALD based In_2O_3/ZnO heterostructure stacks as an active semiconducting layer. (b) Collective transfer characteristics of three, four, five and six stacks and (c–f) output characteristics of devices with three, four, five and six In_2O_3/ZnO heterostructure stacks, respectively.

Table 2 Evaluated TFT performance parameters for devices with three, four, five and six In_2O_3/ZnO heterostructure stacks, respectively

Number of stacks	Mobility $\mu_{sat.}$ [cm^2 (V^{-1} s^{-1})]	Threshold voltage *V*th [V]	Current on/off ratio $I_{on/off}$	Subthreshold slope SS [V dec^{-1}]
3	2.3	14.8	8×10^6	1.3
4	6.5	8.9	5×10^7	0.7
5	7.1	5	1×10^6	1.1
6	4.6	3.3	1×10^5	1.9

charge carrier concentration at the interface (by In_2O_3 deposition as the first layer of the stack) appears to be a straight-forward fabrication route using ALD.

The TFT characteristics of the thinnest sample (three stacks) indicate this thickness to be the threshold limit of critical thickness of the active layer herein, where sufficient charge carriers are not present within the sub-optimal stack thickness with a visibly lower on-current (I_{on}) in the saturation regime (Fig. 4b and c). For the optimal stack (four stacks), the best trade-off between mobility, threshold voltage, current on/off ratio and sub-threshold swing is achieved, with modest $\mu_{sat.}$ and *V*th values accompanied by improved subthreshold swing and high $I_{on/off}$. Hence, we consider the four stacks as an optimum stack within the current work. Moreover, the mobility and *V*th does improve with increased film thickness (four and five stacks), but the subthreshold swing and $I_{on/off}$ are compromised, which is undesired. Additionally, for an increasing film thickness, an increase in off-current and a negative shift in the *V*th has been attributed to deep-donor like states arising from oxygen vacancy related defects, thereby increasing the overall trap density.[26,49,50] A similar correlation of TFT performance parameters with increasing thickness has been reported for sputter-based IZO films, wherein deterioration of $\mu_{sat.}$, $I_{on/off}$ and SS are observed for incremental film thickness beyond the optimal range.[51] The observed changes of these performance parameters with increasing film thickness were attributed mainly to charge scattering processes arising from the bulk portion in the thicker films. This begins to add up significantly to the existing interfacial trap states as the film thickness is increased beyond the optimum range. This could account for the notably decreased $\mu_{sat.}$, $I_{on/off}$ (higher I_{off}) and increased SS (six stacks) in the current investigation, which is indeed reflected in the stack thickness based evolution of the transfer characteristics (Fig. 4b).

Since the active layer with four stacks displayed the best overall TFT characteristics, compromising a mobility of 6.5 cm^2 V^{-1} s^{-1}, a threshold voltage of 8.9 V and a reasonably high $I_{on/off}$ ratio of 4.6×10^7, we investigated the influence of annealing temperature on the TFT characteristics of this device configuration in order to further study the role of oxygen vacancy passivation by thermal annealing on the TFT characteristics. For that reason the TFT performance of devices annealed for two hours at 250 °C and 300 °C in air is compared (Fig. 5 and Table 3). Comparing the TFT output characteristics, films post annealed at 300 °C exhibit a reduced saturation drain current and an improved gate modulation, indicating a more efficient reduction of free charge carriers *via* defect passivation at higher annealing temperature compared to the as-prepared ones. In comparison with a TFT device annealed at 250 °C, the ones annealed at 300 °C also show an improvement in mobility, accompanied by an increased $I_{on/off}$ of about a decade and a substantial reduction in SS from 1.9 V dec^{-1} to 0.7 V dec^{-1}. Further improvement of device performance by annealing at higher temperatures (350 °C) was not observed.

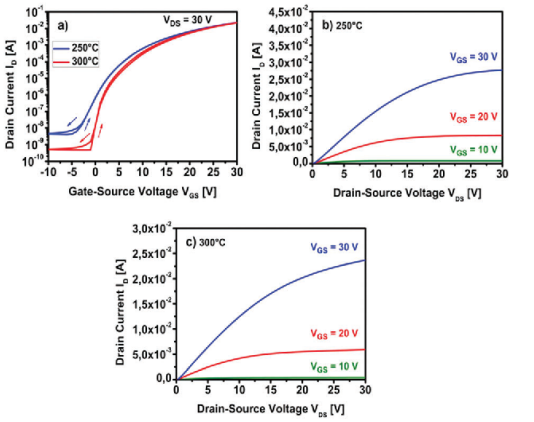

Fig. 5 (a) Transfer characteristics, (b) and (c) output characteristics for the TFT devices annealed to 250 °C and 300 °C, respectively.

Table 3 Summary of the TFT parameters electron mobility, threshold voltage and $I_{on/off}$ ratio for devices annealed at 250 °C and 300 °C

Annealing temperature [°C]	Mobility $\mu_{sat.}$ [$cm^2 V^{-1} s^{-1}$]	Threshold voltage Vth [V]	Current on/off ratio $I_{on/off}$	Subthreshold slope SS [V dec^{-1}]
250	4.8	7.6	4×10^6	1.9
300	6.5	8.9	5×10^7	0.7

Additionally, average performance parameters of the mentioned devices annealed at 250 °C (four stacks) are similar to those of devices based on six stacks, obtained at an annealing temperature of 300 °C, with respect to the obtained mobility and SS values. These observations clearly exhibit that, apart from achieving an optimum stack In_2O_3/ZnO thickness, thermal annealing plays an equally important role in improving device performance, whereby the synergistic effect of heterostructure architecture alone may not be sufficient to render a high TFT performance.

3. Conclusion

To conclude, an ALD based In_2O_3/ZnO heterostructure design yielding high performance TFTs has been successfully demonstrated using trimethyl indium and diethyl zinc as molecular precursors. Employment of a layer by layer deposition of individual semiconducting oxides provides a potential alternative pathway to conventional amorphous semiconductors which are otherwise rather difficult to fabricate *via* ALD based deposition systems. TFT devices fabricated solely on indium and zinc oxide thin layer films were not found to be feasible towards generation of high performance device characteristics. However, generation of an optimised heterostructure based on sequential deposition of the aforementioned individual oxides, processed at a reasonably low temperature regime (250–300 °C) deliver high performance TFTs. Devices based on such a fabrication process demonstrated an average saturation field-effect mobility ($\mu_{sat.}$) of 6.5 cm^2 V^{-1} s^{-1} and a high current on/off ratio of 4.6×10^7 and a low subthreshold swing (SS) of 0.7 V dec^{-1} respectively, at a reasonable processing temperature of 300 °C. Such ALD based semiconductor heterostructure architecture presents itself as a facile strategy towards a cost-effective fabrication technique with potential applications in the field of large-area oxide electronics.

4. Experimental section

4.1. ALD process

The heterostructure thin film depositions of (In_2O_3/ZnO) stacks were performed in a Savannah S 100 system (Cambridge Ultratech) at a base pressure of 0.8 Torr. The precursors used for the depositions were trimethyl indium 98+% (99.9% In, Strem Chemicals), diethyl zinc (min. 95%, Strem Chemicals) and water (HPLC grade, Sigma-Aldrich). All thin films were deposited *via* ALD supercycles with a cycle ratio of In of 0.6 in fraction. To obtain the desired film-thickness, the numbers of supercycle iterations were varied accordingly. All precursors were maintained at room temperature. Argon (99.9999%, Alpha Gaz™) was used as a carrier gas, for the depositions and maintained at a constant flow rate of 20 sccm. For the deposition of the thin-films a custom-configured precursor exposure recipe was developed. In particular, for the In_2O_3 deposition, the sequential deposition cycle is as follows: TMI pulse of 1 s, precursor exposure of 1.5 s, argon purge for 10 s, H_2O pulse of 0.1 s and a final argon purge for 20 s. For the ZnO deposition, the sequence is as follows: DEZ-pulse of 0.015 s, precursor exposure of 1.5 s, argon purge for 15 s, H_2O pulse of 0.015 s and a final argon purge for 15 s. It must be noted that the exposure time is the additional time, provided for sufficient adhesion of the precursor molecules to the substrate to undergo partial reaction after being introduced in the ALD chamber.

4.2 Material characterization

Transmission electron microscopy (TEM) was carried out using a Tecnai G2 F20 (FEI), with an operating voltage of 200 kV.[28] Samples for the TEM investigations were prepared by thin-film deposition on Si/SiO_2 substrates (10×10 mm^2) and annealed at the desired temperatures. Samples for focussed ion beam (FIB) were prepared using a gallium focussed ion beam (Helios-400, FEI) and coated with a platinum layer.[29] Film thicknesses were obtained *via* ellipsometry (Accurion EP^3 System) at a wavelength of 632.8 nm. Atomic force microscopy (AFM) measurements were carried out with MFP-3D™ (Asylum Research), using silicon cantilevers. UV-vis measurements were carried out on clean quartz substrates (Thermo Scientific-Evolution 600). XPS measurements were carried out in an integrated ultra-high vacuum (UHV) system with a base pressure 1×10^{-9} mbar, equipped with a PHI 5000 VersaProbe photoelectron spectrometer.[30] Auger spectroscopy was performed on a PHI 680 (Physical Electronics) scanning Auger nanoprobe operated under ultra-high vacuum (3×10^{-10} mbar) at an acceleration voltage of 10 keV and a current of 20 nA. Sputtering was carried out under ultra high vacuum (5×10^{-9} Torr) with an argon ion gun operated at 250 eV and 500 nA.

4.3 Thin film transistor characterization

TFT substrates with pre-fabricated source–drain electrodes in a bottom-gate-bottom-contact (BGBC) device geometry were obtained from the Fraunhofer IMPS, Dresden. The substrates consist of highly n-doped silicon with a 90 nm silicon-oxide dielectric layer. The source–drain electrodes, with a channel length L = 20 μm and a channel width W = 10 mm (W/L = 500), comprise 40 nm of gold (interdigital structure) with a 10 nm intermediate adhesion layer of indium tin oxide (ITO). Devices were isolated *via* a controlled mechanical scribing process post fabrication. The FET substrates, Quartz slides (1.5×1.5 cm^2) and bare Si/SiO_2 substrates were all cleaned sequentially *via* ultrasonication in acetone, DI-water and iso-propanol (all HPLC grade) for 10 minutes each. TFT characteristics were determined with an HP 4155A Semiconductor Parameter Analyzer (Agilent) in a glove box under exclusion of air and moisture in

the dark. Charge carrier mobility ($\mu_{sat.}$) and threshold voltage Vth were derived from a linear fitting of the square root of the source–drain current ($\sqrt{I_{ds}}$) as a function of gate-source voltage V_{GS}.

Conflicts of interest

There are no conflicts to declare.

Acknowledgements

S. S. and J. K. contributed equally towards this work. S. S. and J. J. S. acknowledge financial support through the DFG SPP 1569 program. TEM investigations were performed at ERC Jülich under contract ERC-TUD1. Auger measurements were carried out at Karlsruhe Nano Micro Facility (KNMF proposal number 2016-015-010549) at Karlsruhe Institute of Technology (KIT). We thank Tobias Weingärtner (KIT) for Auger measurements and Dr Jörg Engstler (TUDa) for TEM studies.

References

1 K. Nomura, H. Ohta, A. Takagi, T. Kamiya, M. Hirano and H. Hosono, *Nature*, 2004, **432**, 488–492.
2 H. Yabuta, M. Sano, K. Abe, T. Aiba, T. Den, H. Kumomi, K. Nomura, T. Kamiya and H. Hosono, *Appl. Phys. Lett.*, 2006, **89**, 112123.
3 T. Kamiya and H. Hosono, *NPG Asia Mater.*, 2010, **2**, 15–22.
4 E. Fortunato, P. Barquinha and R. Martins, *Adv. Mater.*, 2012, **24**, 2945–2986.
5 J. K. Jeong, J. H. Jeong, H. W. Yang, J.-S. Park, Y.-G. Mo and H. D. Kim, *Appl. Phys. Lett.*, 2007, **91**, 113505.
6 W. Lim, S. Kim, Y.-L. Wang, J. W. Lee, D. P. Norton, S. J. Pearton, F. Ren and I. I. Kravchenko, *J. Electrochem. Soc.*, 2008, **155**, H383–H385.
7 K. K. Banger, Y. Yamashita, K. Mori, R. L. Peterson, T. Leedham, J. Rickard and H. Sirringhaus, *Nat. Mater.*, 2011, **10**, 45–50.
8 R. M. Pasquarelli, D. S. Ginley and R. O'Hayre, *Chem. Soc. Rev.*, 2011, **40**, 5406–5441.
9 J. S. Park, H. Kim and I.-D. Kim, *J. Electroceram.*, 2014, **32**, 117–140.
10 M. Ritala, K. Kukli, A. Rahtu, P. I. Räisänen, M. Leskelä, T. Sajavaara and J. Keinonen, *Science*, 2000, **288**, 319.
11 H. Kim and P. C. McIntyre, *J. Korean Phys. Soc.*, 2006, **48**, 5–17.
12 L. Niinistö, M. Nieminen, J. Päiväsaari, J. Niinistö, M. Putkonen and M. Nieminen, *Phys. Status Solidi A*, 2004, **201**, 1443–1452.
13 S. Gieraltowska, L. Wachnicki, B. S. Witkowski, M. Godlewski and E. Guziewicz, *Thin Solid Films*, 2012, **520**, 4694–4697.
14 M. Leskelä and M. Ritala, *Thin Solid Films*, 2002, **409**, 138–146.
15 X. F. She, J. Wang, Q. Xue and W. Xu, *RSC Adv.*, 2016, **6**, 114593–114598.
16 W. Xu and S.-W. Rhee, *J. Mater. Chem.*, 2011, **21**, 998–1004.
17 W. Xu, F. Wang and S.-W. Rhee, *J. Mater. Chem.*, 2012, **22**, 1482–1488.
18 L. Grzegorz, G. Marek, G. Elzbieta, S. Pavlo, C. Vladyslav and V. Dmytro, *Semicond. Sci. Technol.*, 2012, **27**, 074006.
19 K. Semyung, B. Seokhwan, L. Seungjun, J. Sunyeol, J. Wooho, K. Hyungchul, G. Su Cheol, C. Ho Jung, P. Hyung-ho and J. Hyeongtag, *Semicond. Sci. Technol.*, 2009, **24**, 035015.
20 P. K. Nayak, Z. Wang, D. H. Anjum, M. N. Hedhili and H. N. Alshareef, *Appl. Phys. Lett.*, 2015, **106**, 103505.
21 Y. J. Chung, W. J. Choi, S. G. Kang, C. W. Lee, J.-O. Lee, K.-J. Kong and Y. K. Lee, *J. Mater. Chem. C*, 2014, **2**, 9274–9282.
22 C. H. Ahn, M. G. Yun, S. Y. Lee and H. K. Cho, *IEEE Trans. Electron Devices*, 2014, **61**, 73–78.
23 A. Illiberi, B. Cobb, A. Sharma, T. Grehl, H. Brongersma, F. Roozeboom, G. Gelinck and P. Poodt, *ACS Appl. Mater. Interfaces*, 2015, **7**, 3671–3675.
24 J. Sheng, H.-J. Lee, S. Oh and J.-S. Park, *ACS Appl. Mater. Interfaces*, 2016, **8**, 33821–33828.
25 C. H. Ahn, K. Senthil, H. K. Cho and S. Y. Lee, *Sci. Rep.*, 2013, **3**, 2737.
26 P. K. Nayak, Z. Wang and H. N. Alshareef, *Adv. Mater.*, 2016, **28**, 7736–7744.
27 S.-J. Lee, C.-S. Hwang, J.-E. Pi, J.-H. Yang, C.-W. Byun, H. Chu, K. I. Cho and S. Cho, *ETRI J.*, 2015, **37**, 1135–1142.
28 M. Luysberg, M. Heggen and K. Tillmann, *J. Large-Scale Res. Facil.*, 2016, **2**, 77.
29 D. Meertens, M. Kruth and K. Tillmann, *J. Large-Scale Res. Facil.*, 2016, **2**, 60.
30 S. Sanctis, R. C. Hoffmann, R. Precht, W. Anwand and J. J. Schneider, *J. Mater. Chem. C*, 2016, **4**, 10935–10944.
31 D.-J. Lee, J.-Y. Kwon, J. I. Lee and K.-B. Kim, *J. Phys. Chem. C*, 2011, **115**, 15384–15389.
32 A. U. Mane, A. J. Allen, R. K. Kanjolia and J. W. Elam, *J. Phys. Chem. C*, 2016, **120**, 9874–9883.
33 D. J. Lee, J. Y. Kwon, J. Kim, K.-J. Kim, Y.-H. Cho, S.-Y. Cho, S.-H. Kim, J. Xu and K.-B. Kim, *J. Phys. Chem. C*, 2014, **118**, 408–415.
34 J. T. Tanskanen, C. Hägglund and S. F. Bent, *Chem. Mater.*, 2014, **26**, 2795–2802.
35 K. Tetzner, I. Isakov, A. Regoutz, D. J. Payne and T. D. Anthopoulos, *J. Mater. Chem. C*, 2017, **5**, 59–64.
36 T. Kamiya and H. Hosono, *ECS Trans.*, 2013, **54**, 103–113.
37 H. J. Kim, S. Y. Park, H. Y. Jung, B. G. Son, C.-K. Lee, C.-K. Lee, J. H. Jeong, Y.-G. Mo, K. S. Son, M. K. Ryu, S. Lee and J. K. Jeong, *J. Phys. D: Appl. Phys.*, 2013, **46**, 055104.
38 W.-G. Kim, Y. J. Tak, B. Du Ahn, T. S. Jung, K.-B. Chung and H. J. Kim, *Sci. Rep.*, 2016, **6**, 23039.
39 H. S. Shin, Y. S. Rim, Y.-G. Mo, C. G. Choi and H. J. Kim, *Phys. Status Solidi A*, 2011, **208**, 2231–2234.
40 K. Okamura, D. Nikolova, N. Mechau and H. Hahn, *Appl. Phys. Lett.*, 2009, **94**, 183503.
41 M. G. Kim, H. S. Kim, Y.-G. Ha, J. He, M. G. Kanatzidis, A. Facchetti and T. J. Marks, *J. Am. Chem. Soc.*, 2010, **132**, 10352–10364.
42 J. Sheng, D.-w. Choi, S.-H. Lee, J. Park and J.-S. Park, *J. Mater. Chem. C*, 2016, **4**, 7571–7576.
43 Y. S. Rim, H. Chen, X. Kou, H.-S. Duan, H. Zhou, M. Cai, H. J. Kim and Y. Yang, *Adv. Mater.*, 2014, **26**, 4273–4278.

44 S. Yoon, S. J. Kim, Y. J. Tak and H. J. Kim, *Sci. Rep.*, 2017, **7**, 43216.
45 G. X. Liu, A. Liu, F. K. Shan, Y. Meng, B. C. Shin, E. Fortunato and R. Martins, *Appl. Phys. Lett.*, 2014, **105**, 113509.
46 M. Nag, A. Chasin, M. Rockele, S. Steudel, K. Myny, A. Bhoolokam, A. Tripathi, B. van der Putten, A. Kumar, J.-L. van der Steen, J. Genoe, F. Li, J. Maas, E. van Veenendaal, G. Gelinck and P. Heremans, *J. Soc. Inf. Disp.*, 2013, **21**, 129–136.
47 X. Yu, N. Zhou, J. Smith, H. Lin, K. Stallings, J. Yu, T. J. Marks and A. Facchetti, *ACS Appl. Mater. Interfaces*, 2013, **5**, 7983–7988.
48 Y. H. Lin, H. Faber, J. G. Labram, E. Stratakis, L. Sygellou, E. Kymakis, N. A. Hastas, R. Li, K. Zhao, A. Amassian, N. D. Treat, M. McLachlan and T. D. Anthopoulos, *Adv. Sci.*, 2015, **2**, 1500058.
49 G. Wakimura, Y. Yamauchi, T. Matsuoka and Y. Kamakura, *J. Adv. Simulat. Sci. Eng.*, 2014, **2**, 201–210.
50 E. N. Cho, J. H. Kang and I. Yun, *Microelectron. Reliab.*, 2011, **51**, 1792–1795.
51 P. Barquinha, A. Pimentel, A. Marques, L. Pereira, R. Martins and E. Fortunato, *J. Non-Cryst. Solids*, 2006, **352**, 1749–1752.

7 Summary and conclusion

The investigations performed within this dissertation provide several strategies for the development and fabrication of multinary metal oxide semiconductors via the solution processing of molecular precursor compounds and atomic layer deposition The work presented in **Section 6.1** began with the direct microwave synthesis of colloidal indium zinc oxide nanoparticles (IZO NP) using the molecular oximato precursor compounds of indium and zinc. The synthesized IZO nanoparticles could be rapidly synthesized within a few minutes of microwave irradiation of the precursor solution with a monomodal size distribution of the formed nanoparticles. The size of the nanoparticles was carefully optimized by controlling the precursor concentration, choice of solvent and the microwave irradiation power. The synthesized stable colloidal suspension was directly spin-coated without any further stabilizers for the formation of IZO thin film semiconductors and resulted in the generation of homogeneous smooth IZO films upon further thermal annealing which delivered a reproducible high TFT performance. The investigations provided in **Section 6.2** provides a novel strategy for the formation of indium-free, amorphous zinc tin oxide (ZTO) semiconductors via the use a novel air-stable Sn(II) oximato precursor compound and the previously mentioned Zn-oximato compound The Sn(II) oximato precursor enables a lower precursor decomposition temperature in comparison with the routinely used $SnCl_2$ which need a higher decomposition temperature and consist of anion (Cl^-) impurities which act as electronic traps which deteriorate the TFT performance of the semiconductor. Additionally, EPR measurements indicated that the SnO_2 consists of a higher defect concentration in comparison with the ZnO, derived from these precursors and clarifies the need for higher Sn precursor ration in the ZTO precursor solution mixture (Sn:Zn, 7:3), which is different in comparison with traditional precursor ratio (Sn:Zn, 3:7) employed for the generation of ZTO thin films from the routinely used metal chloride salts. **Section 6.3** presents a novel strategy for the direct photopatterning of solution processed IZO and ZTO semiconductors via DUV irradiation which is enabled due to the intrinsic ability of the oximato precursors to absorb UV wavelengths significantly which was verified via UV-vis spectroscopy. Optimized and selective UV exposure to the IZO and ZTO precursor films led to the partial decomposition of the oximato ligand via the decomposition of the methoxy side groups as well as the N-O bond cleavage of the ligand backbone. This in turn leads to the partial decomposition and cross-linking of the exposed area of the precursor films and the unexposed areas could be easily washed away in the parent solvent, leaving behind the desired patterned

film. Further thermal annealing at moderate temperatures ensured the complete conversion into the amorphous oxide semiconductors which exhibited a high TFT performance for the IZO and ZTO semiconductors in comparison with exiting literature. Additionally, photopatterning of the ZTO semiconductor was successfully demonstrated for the very first time.

In **Section 6.4**, We have successfully employed a molecular precursor (zinc oximato) to synthesize zinc oxide nanoparticles, for an in-situ deposition on to a virus template. A facile, microwave-assisted approach for generating a TMV/ZnO hybrid bio-inorganic material was demonstrated. The clean in situ microwave-based decomposition of the molecular precursor under mild basic conditions as well as the desired zinc oxide phase formation was confirmed by NMR, XRD and AFM characterization methods. Moreover, the as-synthesized hybrid material has been successfully employed in a FET device. The best FET performance was achieved by systematically controlling the thickness of the deposited zinc oxide films via desired number of mineralization cycles. The fabricated FET shows a reasonable performance for the as-prepared device, without any post processing of the bio-inorganic hybrid nanomaterial which promotes the use of nanoscale virus templates to obtain hybrid materials with functional properties that can be implemented into future device applications.

In **Section 6.5,** indium and zinc complexes of 1,3-diketones (malonato complexes) which are functionalised in the 2-position present suitable precursor molecules for the fabrication of indium zinc oxide (IZO) thin films by the solution deposition route. Amorphous oxide semiconductor IZO were formed through a highly exothermic combustion process of the precursor mixture, even at a temperature slightly above 150°C enabling a low-temperature fabrication of IZO thin film semiconductors. Only minor amounts of organic residues were present thereafter and could be fully removed by further moderate annealing. Fully operating field-effect transistors (FETs) with these IZO films as semiconducting materials could be fabricated at processing temperatures between 250 and 400°C. Hereby, annealing at higher temperatures generally led to a better performance with respect to charge carrier mobility, threshold voltage as well as the $I_{on/off}$ ratio. PAS methods are able to identify on a microscopic scale material features which underwent a clear and significant changes wherein IZO processed between 250°C and 450°C, reveal the the film at 250°C have a shorter diffussion length L (2±1)nm in comparison with films annealed a 300°C with an L (25±3)nm, clearly indicating a significant reduction in defect concentration at higher temperatures with improved diffusion lengths which clearly demonstrated the reduction in the open pore volume and defects within the film with increasing temperature.

Within **Section 6.6,** eco-friendly water-soluble metal urea complexes of indium, gallium and zinc precursors of composition In/Ga(urea)$_6$(NO$_3$)$_2$ and Zn(urea)$_4$(H$_2$O)$_2$(NO$_3$)$_2$ were successfully employed in the generation of active semiconductor IGZO thin films via a solution-processing route. The precursors undergo a desirable exothermic decomposition (combustion) when annealed at relatively low temperatures between 200 and 350°C, with volatile gaseous by-products affording the formation of clean ceramic oxides which enable the formation of amorphous IGZO thin films. Integration of such solution-processed thin-films enabled the formation of active semiconductor materials. At an optimum temperature of 350 °C, TFT performance with the device mobility of 3.1 cm^2/V.s and a current on/off ratio of 10^7 was achieved. The formation of the thin-film oxides from the urea nitrate complexes was investigated with respect to their microstructure-property relationship and the change in the oxygen environment at different annealing temperatures by XPS. HR-TEM and AFM investigations. These results demonstrated a visible dependency of the film density and surface morphology, wherein dense and smooth films could be manufactured at reasonable annealing temperatures. This was further confirmed by an improved degree of ceramisation exhibiting a reduced presence of hydroxide species at elevated annealing temperatures which was well corroborated with the observed TFT performance in the IGZO films derived from the urea nitrate complexes.

In the final **Section 6.7** an ALD based In$_2$O$_3$/ZnO heterostructure design yielding high performance TFTs was successfully demonstrated using trimethyl indium and diethyl zinc as molecular precursors. Employment of a layer by layer deposition of individual semiconducting oxides enabled a potential alternative pathway to conventional amorphous semiconductors which are otherwise rather difficult to fabricate via ALD based deposition systems. TFT devices fabricated solely on indium and zinc oxide thin layer films were not found to be feasible towards generation of high performance device characteristics. However, generation of an optimised heterostructure based on sequential deposition of the aforementioned individual oxides, processed at a reasonably low temperature regime (250–300°C) deliver high performance TFTs by the likely formation of 2D electron gas transport at the heterostructure interface. Devices based on such a fabrication process demonstrated an average saturation field-effect mobility of 6.5 cm^2/V.s and a high current on/off ratio of 4.6 x 10^7 and a low subthreshold swing (SS) of 0.7 V/dec. respectively, at a reasonable processing temperature of 300°C. Such ALD based semiconductor heterostructure architecture provides a facile strategy towards a cost-effective

semiconductor architecture fabrication technique with potential applications in the field of large-area oxide electronics.

To summarize, several strategies to overcome existing hurdles in the formation of multinary metal oxide semiconductors mainly via the use of molecular precursor compounds as well as an ALD based approach were demonstrated within this thesis The precursor chemistry, material analysis as well as the electronic performance of the oxide semiconductor thin films displayed several unique strategies for the microwave-based synthesis and mineralization of IZO NPs, ZTO and ZnO/TMV hybrid semiconductors, direct photopatterning of amorphous IZO and ZTO TFTs, combustible IZO and IGZO precursors for the low temperature fabrication of oxide TFTs via the malonato complexes of indium and zinc as well as the water soluble urea-nitrate precursor compounds of indium, gallium and zinc respectively. Lastly, an ALD based, novel In_2O_3/ZnO heterostructure design demonstrating high performance TFTs using trimethyl indium and diethyl zinc as molecular precursors. All of the above mentioned works certainly pave the way and display great potential towards the improvement in precursor formulations, material deposition and processing strategies towards numerous applications based on multinary metal oxide semiconductors.

8 Appendix

This section of the dissertation contains all the necessary reproductoion rights and permission for the figures obtained from third-party publications as well as the first author publications presented herein.

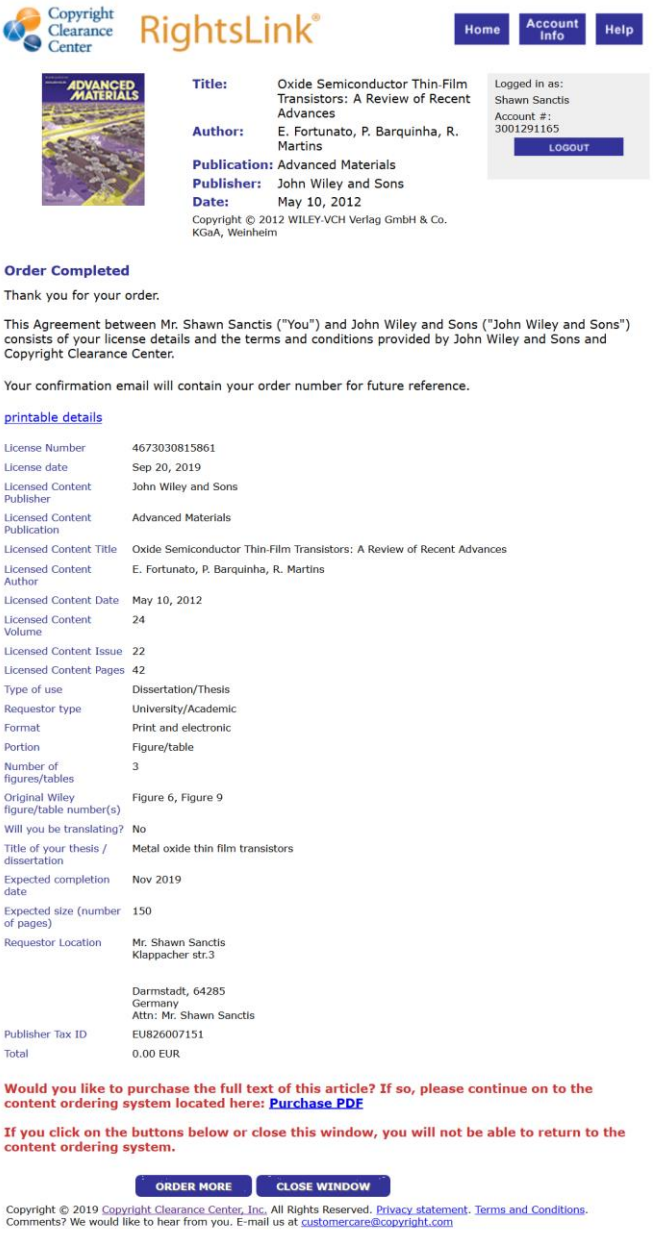

Copyright Clearance Center RightsLink®

Home | Account Info | Help

Title: Oxide Semiconductor Thin-Film Transistors: A Review of Recent Advances
Author: E. Fortunato, P. Barquinha, R. Martins
Publication: Advanced Materials
Publisher: John Wiley and Sons
Date: May 10, 2012
Copyright © 2012 WILEY-VCH Verlag GmbH & Co. KGaA, Weinheim

Logged in as:
Shawn Sanctis
Account #:
3001291165
LOGOUT

Order Completed

Thank you for your order.

This Agreement between Mr. Shawn Sanctis ("You") and John Wiley and Sons ("John Wiley and Sons") consists of your license details and the terms and conditions provided by John Wiley and Sons and Copyright Clearance Center.

Your confirmation email will contain your order number for future reference.

printable details

License Number	4673030815861
License date	Sep 20, 2019
Licensed Content Publisher	John Wiley and Sons
Licensed Content Publication	Advanced Materials
Licensed Content Title	Oxide Semiconductor Thin-Film Transistors: A Review of Recent Advances
Licensed Content Author	E. Fortunato, P. Barquinha, R. Martins
Licensed Content Date	May 10, 2012
Licensed Content Volume	24
Licensed Content Issue	22
Licensed Content Pages	42
Type of use	Dissertation/Thesis
Requestor type	University/Academic
Format	Print and electronic
Portion	Figure/table
Number of figures/tables	3
Original Wiley figure/table number(s)	Figure 6, Figure 9
Will you be translating?	No
Title of your thesis / dissertation	Metal oxide thin film transistors
Expected completion date	Nov 2019
Expected size (number of pages)	150
Requestor Location	Mr. Shawn Sanctis Klappacher str.3 Darmstadt, 64285 Germany Attn: Mr. Shawn Sanctis
Publisher Tax ID	EU826007151
Total	0.00 EUR

Would you like to purchase the full text of this article? If so, please continue on to the content ordering system located here: Purchase PDF

If you click on the buttons below or close this window, you will not be able to return to the content ordering system.

ORDER MORE | CLOSE WINDOW

Figure 4 Electrical characterization of a typical TFT (a) output curves (I_D against V_D) in linear scales and (b) transfer curve (I_D against V_G) in a logarithmic y-scale. Adapted with permission.[2] Copyright 2012, WILEY-VCH Verlag GmbH & Co. KGaA.

Copyright Clearance Center RightsLink®

Home | Account Info | Help

SPRINGER NATURE

Title: Material characteristics and applications of transparent amorphous oxide semiconductors
Author: Toshio Kamiya et al
Publication: NPG Asia Materials
Publisher: Springer Nature
Date: Jan 21, 2010
Copyright © 2010, Springer Nature

Logged in as:
Shawn Sanctis
Account #:
3001291165
LOGOUT

Order Completed

Thank you for your order.

This Agreement between Mr. Shawn Sanctis ("You") and Springer Nature ("Springer Nature") consists of your license details and the terms and conditions provided by Springer Nature and Copyright Clearance Center.

Your confirmation email will contain your order number for future reference.

printable details

License Number	4673031493340
License date	Sep 20, 2019
Licensed Content Publisher	Springer Nature
Licensed Content Publication	NPG Asia Materials
Licensed Content Title	Material characteristics and applications of transparent amorphous oxide semiconductors
Licensed Content Author	Toshio Kamiya et al
Licensed Content Date	Jan 21, 2010
Type of Use	Thesis/Dissertation
Requestor type	academic/university or research institute
Format	print and electronic
Portion	figures/tables/illustrations
Number of figures/tables /illustrations	1
High-res required	no
Will you be translating?	no
Circulation/distribution	500 - 999
Author of this Springer Nature content	no
Title	Metal oxide thin film transistors
Institution name	n/a
Expected presentation date	Nov 2019
Portions	Figure 4
Requestor Location	Mr. Shawn Sanctis Klappacher str.3 Darmstadt, 64285 Germany Attn: Mr. Shawn Sanctis
Total	0.00 EUR

ORDER MORE | CLOSE WINDOW

Copyright © 2019 Copyright Clearance Center, Inc. All Rights Reserved. Privacy statement. Terms and Conditions.
Comments? We would like to hear from you. E-mail us at customercare@copyright.com

Figure 5 A visual timeline of significant achievements related to developments in field of transistor materials and technology. Adapted with permission.[2] Copyright 2012, WILEY -VCH Verlag GmbH & Co. KGaA.

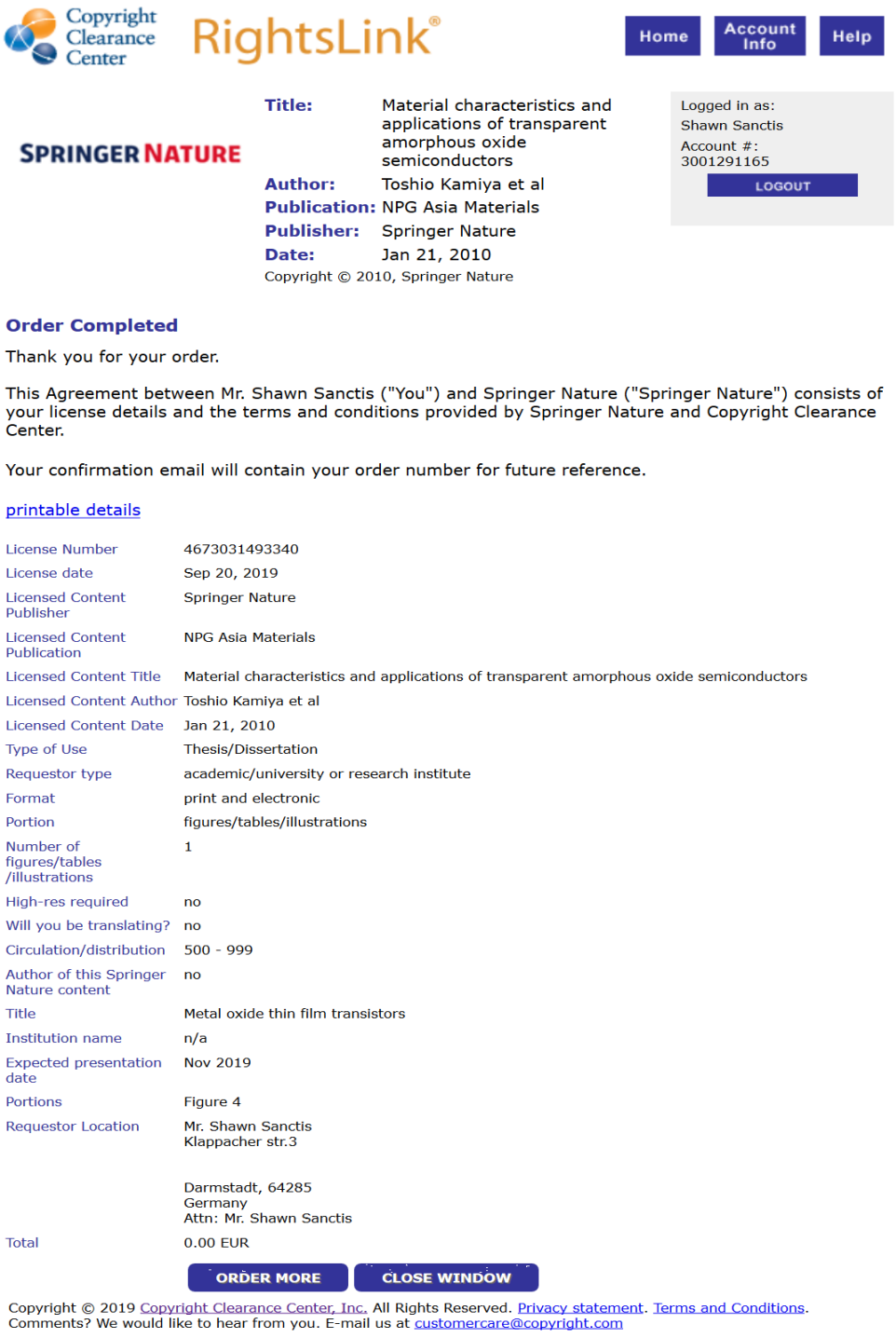

Copyright Clearance Center RightsLink®

Home | Account Info | Help

SPRINGER NATURE

Title: Material characteristics and applications of transparent amorphous oxide semiconductors
Author: Toshio Kamiya et al
Publication: NPG Asia Materials
Publisher: Springer Nature
Date: Jan 21, 2010
Copyright © 2010, Springer Nature

Logged in as:
Shawn Sanctis
Account #:
3001291165
LOGOUT

Order Completed

Thank you for your order.

This Agreement between Mr. Shawn Sanctis ("You") and Springer Nature ("Springer Nature") consists of your license details and the terms and conditions provided by Springer Nature and Copyright Clearance Center.

Your confirmation email will contain your order number for future reference.

printable details

License Number	4673031493340
License date	Sep 20, 2019
Licensed Content Publisher	Springer Nature
Licensed Content Publication	NPG Asia Materials
Licensed Content Title	Material characteristics and applications of transparent amorphous oxide semiconductors
Licensed Content Author	Toshio Kamiya et al
Licensed Content Date	Jan 21, 2010
Type of Use	Thesis/Dissertation
Requestor type	academic/university or research institute
Format	print and electronic
Portion	figures/tables/illustrations
Number of figures/tables /illustrations	1
High-res required	no
Will you be translating?	no
Circulation/distribution	500 - 999
Author of this Springer Nature content	no
Title	Metal oxide thin film transistors
Institution name	n/a
Expected presentation date	Nov 2019
Portions	Figure 4
Requestor Location	Mr. Shawn Sanctis Klappacher str.3 Darmstadt, 64285 Germany Attn: Mr. Shawn Sanctis
Total	0.00 EUR

ORDER MORE | CLOSE WINDOW

Copyright © 2019 Copyright Clearance Center, Inc. All Rights Reserved. Privacy statement. Terms and Conditions.
Comments? We would like to hear from you. E-mail us at customercare@copyright.com

Figure 6 Schematic representation of covalent and ionic oxide semiconductors. Adapted with permission.[40] Copyright 2006, Elsevier.

Figure 7 Schematic electronic structures of silicon and ionic oxide semiconductors. (a–c) Bandgap formation mechanisms in (a) covalent and (b,c) ionic semiconductors. (d–g) Electronic structures of defects in (d,f) silicon and (e,g) metal oxides. Solid and hollow circles are used to represent the occupied and unoccupied states, respectively. Adapted with permission.[40] Copyright 2006, Elsevier.

Figure 9 Schematic representation of the general steps involved in the solution processing of metal oxide thin films. Adapted with permission.[80] Copyright 2011, Royal society of Chemistry

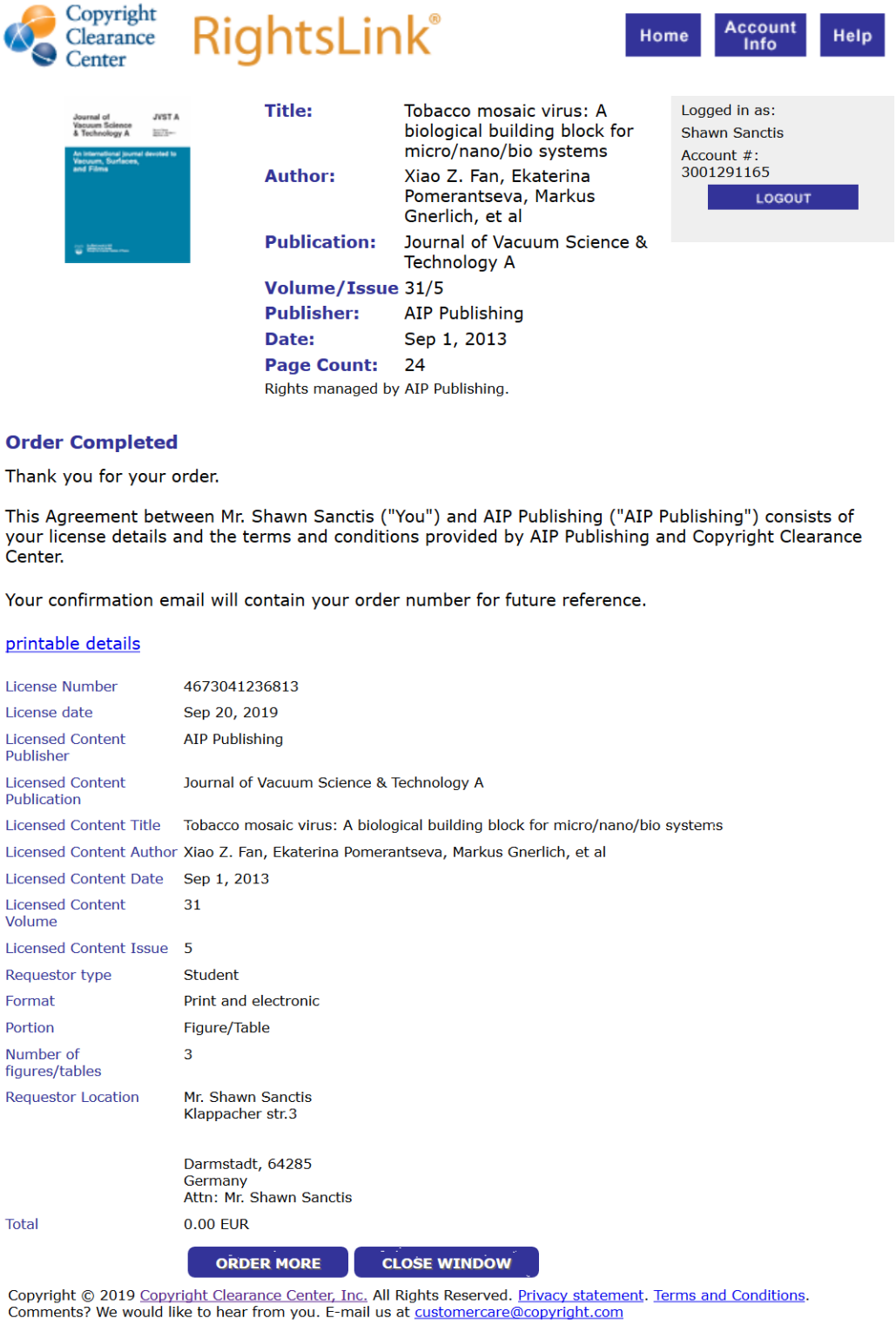

Copyright Clearance Center RightsLink®

Home | Account Info | Help

Logged in as:
Shawn Sanctis
Account #: 3001291165
LOGOUT

Title: Tobacco mosaic virus: A biological building block for micro/nano/bio systems
Author: Xiao Z. Fan, Ekaterina Pomerantseva, Markus Gnerlich, et al
Publication: Journal of Vacuum Science & Technology A
Volume/Issue 31/5
Publisher: AIP Publishing
Date: Sep 1, 2013
Page Count: 24
Rights managed by AIP Publishing.

Order Completed

Thank you for your order.

This Agreement between Mr. Shawn Sanctis ("You") and AIP Publishing ("AIP Publishing") consists of your license details and the terms and conditions provided by AIP Publishing and Copyright Clearance Center.

Your confirmation email will contain your order number for future reference.

printable details

License Number	4673041236813
License date	Sep 20, 2019
Licensed Content Publisher	AIP Publishing
Licensed Content Publication	Journal of Vacuum Science & Technology A
Licensed Content Title	Tobacco mosaic virus: A biological building block for micro/nano/bio systems
Licensed Content Author	Xiao Z. Fan, Ekaterina Pomerantseva, Markus Gnerlich, et al
Licensed Content Date	Sep 1, 2013
Licensed Content Volume	31
Licensed Content Issue	5
Requestor type	Student
Format	Print and electronic
Portion	Figure/Table
Number of figures/tables	3
Requestor Location	Mr. Shawn Sanctis Klappacher str.3 Darmstadt, 64285 Germany Attn: Mr. Shawn Sanctis
Total	0.00 EUR

ORDER MORE | CLOSE WINDOW

Figure 18 Molecular model of the a) horizontal cross section and b) vertical section the rod-like wild-type (wt) TMV. Adapted with permission.[218] Copyright 2013, AIP publishing.

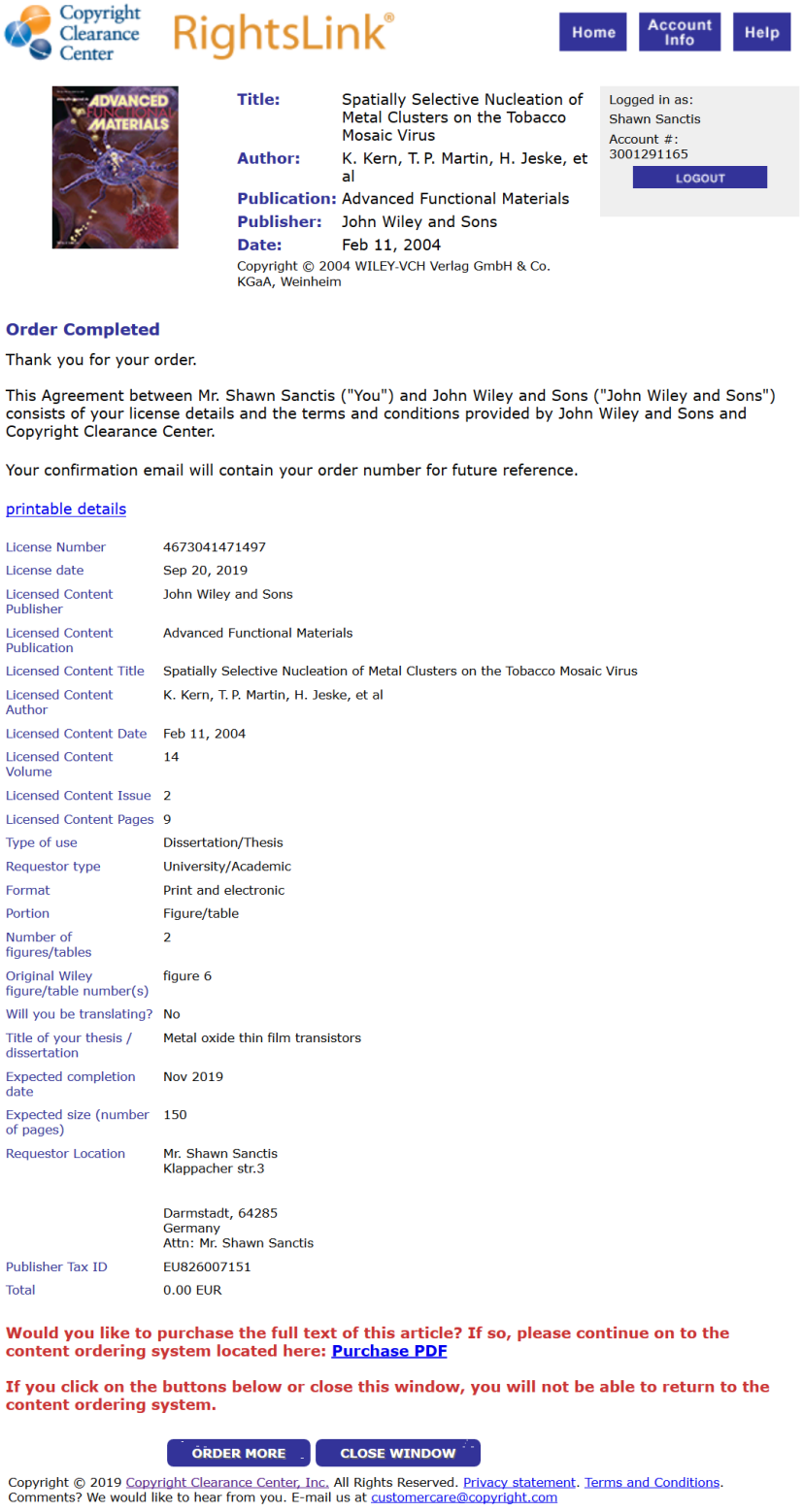

Copyright Clearance Center RightsLink®

Home | Account Info | Help

Logged in as:
Shawn Sanctis
Account #:
3001291165
LOGOUT

Title: Spatially Selective Nucleation of Metal Clusters on the Tobacco Mosaic Virus
Author: K. Kern, T. P. Martin, H. Jeske, et al
Publication: Advanced Functional Materials
Publisher: John Wiley and Sons
Date: Feb 11, 2004
Copyright © 2004 WILEY-VCH Verlag GmbH & Co. KGaA, Weinheim

Order Completed

Thank you for your order.

This Agreement between Mr. Shawn Sanctis ("You") and John Wiley and Sons ("John Wiley and Sons") consists of your license details and the terms and conditions provided by John Wiley and Sons and Copyright Clearance Center.

Your confirmation email will contain your order number for future reference.

printable details

License Number	4673041471497
License date	Sep 20, 2019
Licensed Content Publisher	John Wiley and Sons
Licensed Content Publication	Advanced Functional Materials
Licensed Content Title	Spatially Selective Nucleation of Metal Clusters on the Tobacco Mosaic Virus
Licensed Content Author	K. Kern, T. P. Martin, H. Jeske, et al
Licensed Content Date	Feb 11, 2004
Licensed Content Volume	14
Licensed Content Issue	2
Licensed Content Pages	9
Type of use	Dissertation/Thesis
Requestor type	University/Academic
Format	Print and electronic
Portion	Figure/table
Number of figures/tables	2
Original Wiley figure/table number(s)	figure 6
Will you be translating?	No
Title of your thesis / dissertation	Metal oxide thin film transistors
Expected completion date	Nov 2019
Expected size (number of pages)	150
Requestor Location	Mr. Shawn Sanctis Klappacher str.3 Darmstadt, 64285 Germany Attn: Mr. Shawn Sanctis
Publisher Tax ID	EU826007151
Total	0.00 EUR

Would you like to purchase the full text of this article? If so, please continue on to the content ordering system located here: Purchase PDF

If you click on the buttons below or close this window, you will not be able to return to the content ordering system.

ORDER MORE | CLOSE WINDOW

Figure 19 Pt(II) pretreated TMVs metallized with (b) nickel and (c) cobalt by electroless deposition. Adapted with permission. [243] Copyright 2004, WILEY-VCH Verlag GmbH & Co. KGaA.

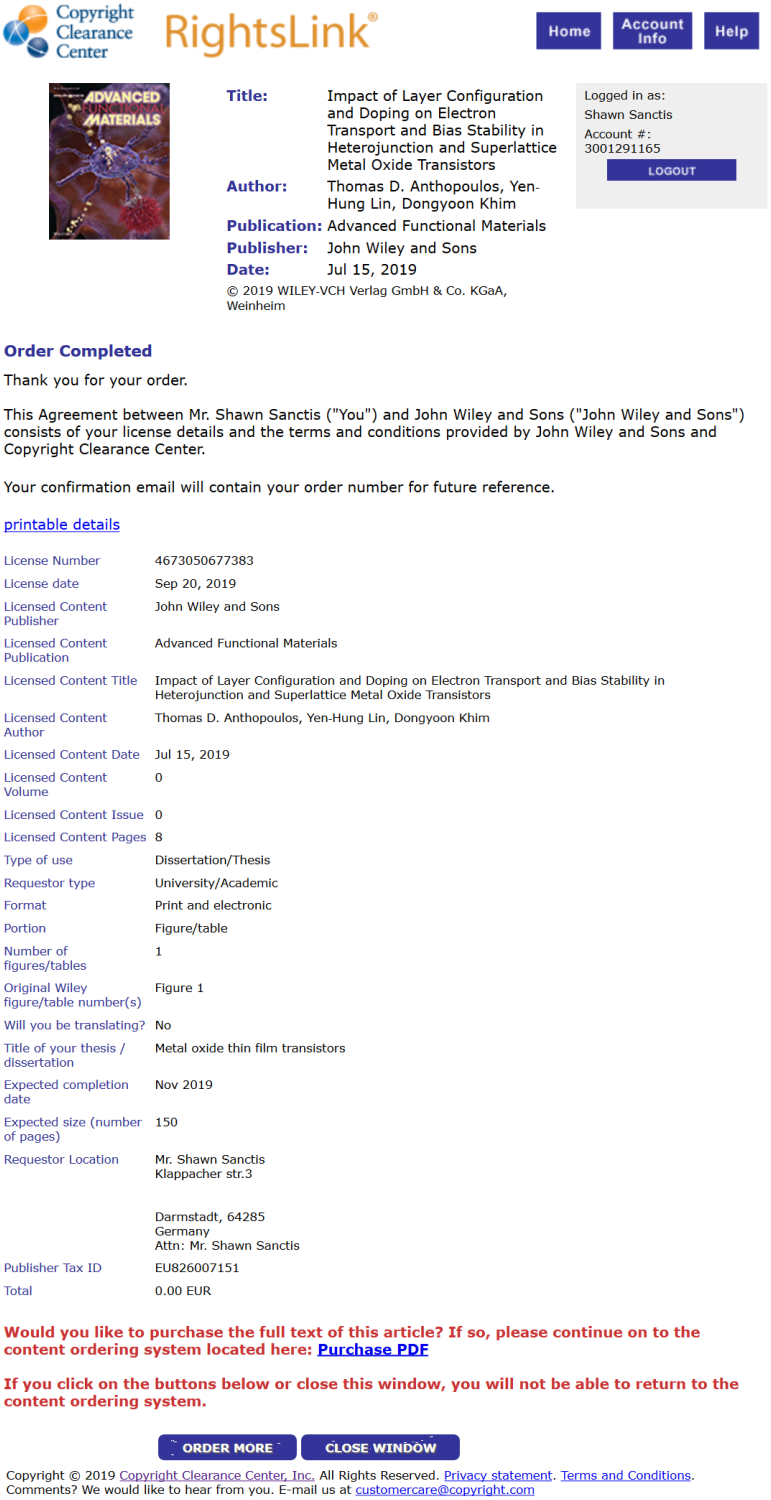

Copyright Clearance Center RightsLink®

Home | Account Info | Help

Title: Impact of Layer Configuration and Doping on Electron Transport and Bias Stability in Heterojunction and Superlattice Metal Oxide Transistors

Author: Thomas D. Anthopoulos, Yen-Hung Lin, Dongyoon Khim

Publication: Advanced Functional Materials

Publisher: John Wiley and Sons

Date: Jul 15, 2019

© 2019 WILEY-VCH Verlag GmbH & Co. KGaA, Weinheim

Logged in as:
Shawn Sanctis
Account #:
3001291165
LOGOUT

Order Completed

Thank you for your order.

This Agreement between Mr. Shawn Sanctis ("You") and John Wiley and Sons ("John Wiley and Sons") consists of your license details and the terms and conditions provided by John Wiley and Sons and Copyright Clearance Center.

Your confirmation email will contain your order number for future reference.

printable details

License Number	4673050677383
License date	Sep 20, 2019
Licensed Content Publisher	John Wiley and Sons
Licensed Content Publication	Advanced Functional Materials
Licensed Content Title	Impact of Layer Configuration and Doping on Electron Transport and Bias Stability in Heterojunction and Superlattice Metal Oxide Transistors
Licensed Content Author	Thomas D. Anthopoulos, Yen-Hung Lin, Dongyoon Khim
Licensed Content Date	Jul 15, 2019
Licensed Content Volume	0
Licensed Content Issue	0
Licensed Content Pages	8
Type of use	Dissertation/Thesis
Requestor type	University/Academic
Format	Print and electronic
Portion	Figure/table
Number of figures/tables	1
Original Wiley figure/table number(s)	Figure 1
Will you be translating?	No
Title of your thesis / dissertation	Metal oxide thin film transistors
Expected completion date	Nov 2019
Expected size (number of pages)	150
Requestor Location	Mr. Shawn Sanctis Klappacher str.3 Darmstadt, 64285 Germany Attn: Mr. Shawn Sanctis
Publisher Tax ID	EU826007151
Total	0.00 EUR

Would you like to purchase the full text of this article? If so, please continue on to the content ordering system located here: Purchase PDF

If you click on the buttons below or close this window, you will not be able to return to the content ordering system.

ORDER MORE | CLOSE WINDOW

Figure 23 Distribution of charge carrier density (NCV) measured from the C–V data as a function of heterojunction depth where an increase charge carrier concentration is observed. d) Energy band diagram and accumulation of charge carriers (electrons) of the In_2O_3/ZnO heterointerface. Adapted with permission.[296] Copyright 2019, WILEY-VCH Verlag GmbH & Co. KGaA

Microwave synthesis and field effect transistor performance of stable colloidal indium-zinc-oxide nanoparticles

S. Sanctis, R.C. Hoffmann and J. J. Schneider, *RSC Adv.*, 2013, **3,** 20071

DOI: 10.1039/C3RA44222E

Section 6.1 Microwave synthesis and field effect transistor performance of stable colloidal indium zinc oxide nanoparticles.

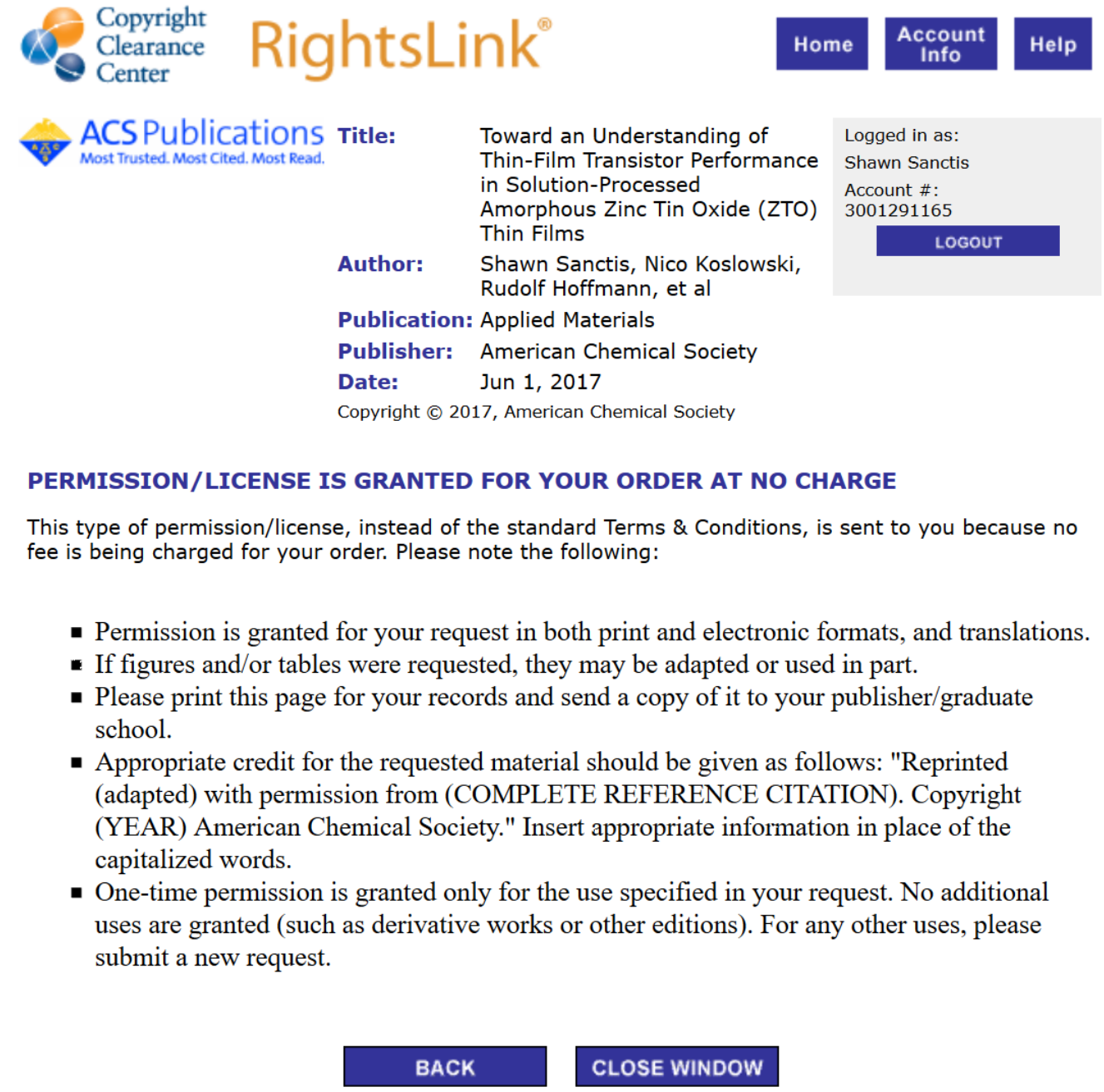

Copyright Clearance Center RightsLink®

Home | Account Info | Help

ACS Publications
Most Trusted. Most Cited. Most Read.

Title: Toward an Understanding of Thin-Film Transistor Performance in Solution-Processed Amorphous Zinc Tin Oxide (ZTO) Thin Films

Author: Shawn Sanctis, Nico Koslowski, Rudolf Hoffmann, et al

Publication: Applied Materials

Publisher: American Chemical Society

Date: Jun 1, 2017

Copyright © 2017, American Chemical Society

Logged in as:
Shawn Sanctis
Account #:
3001291165
LOGOUT

PERMISSION/LICENSE IS GRANTED FOR YOUR ORDER AT NO CHARGE

This type of permission/license, instead of the standard Terms & Conditions, is sent to you because no fee is being charged for your order. Please note the following:

- Permission is granted for your request in both print and electronic formats, and translations.
- If figures and/or tables were requested, they may be adapted or used in part.
- Please print this page for your records and send a copy of it to your publisher/graduate school.
- Appropriate credit for the requested material should be given as follows: "Reprinted (adapted) with permission from (COMPLETE REFERENCE CITATION). Copyright (YEAR) American Chemical Society." Insert appropriate information in place of the capitalized words.
- One-time permission is granted only for the use specified in your request. No additional uses are granted (such as derivative works or other editions). For any other uses, please submit a new request.

BACK | CLOSE WINDOW

Copyright © 2019 Copyright Clearance Center, Inc. All Rights Reserved. Privacy statement. Terms and Conditions.
Comments? We would like to hear from you. E-mail us at customercare@copyright.com

Copyright Clearance Center RightsLink®

Home | Account Info | Help

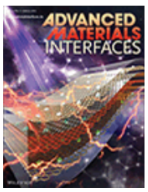

Title: Direct Photopatterning of Solution–Processed Amorphous Indium Zinc Oxide and Zinc Tin Oxide Semiconductors—A Chimie Douce Molecular Precursor Approach to Thin Film Electronic Oxides

Author: Shawn Sanctis, Rudolf C. Hoffmann, Michael Bruns, et al

Publication: Advanced Materials Interfaces

Publisher: John Wiley and Sons

Date: Jun 27, 2018

Logged in as:
Shawn Sanctis
Account #:
3001291165
LOGOUT

Order Completed

Thank you for your order.

This Agreement between Mr. Shawn Sanctis ("You") and John Wiley and Sons ("John Wiley and Sons") consists of your license details and the terms and conditions provided by John Wiley and Sons and Copyright Clearance Center.

Your confirmation email will contain your order number for future reference.

printable details

License Number	4673010711149
License date	Sep 20, 2019
Licensed Content Publisher	John Wiley and Sons
Licensed Content Publication	Advanced Materials Interfaces
Licensed Content Title	Direct Photopatterning of Solution–Processed Amorphous Indium Zinc Oxide and Zinc Tin Oxide Semiconductors—A Chimie Douce Molecular Precursor Approach to Thin Film Electronic Oxides
Licensed Content Author	Shawn Sanctis, Rudolf C. Hoffmann, Michael Bruns, et al
Licensed Content Date	Jun 27, 2018
Licensed Content Volume	5
Licensed Content Issue	15
Licensed Content Pages	8
Type of use	Dissertation/Thesis
Requestor type	Author of this Wiley article
Format	Print and electronic
Portion	Full article
Will you be translating?	No
Title of your thesis / dissertation	Metal oxide thin film transistors
Expected completion date	Nov 2019
Expected size (number of pages)	150
Requestor Location	Mr. Shawn Sanctis Klappacher str.3 Darmstadt, 64285 Germany Attn: Mr. Shawn Sanctis
Publisher Tax ID	EU826007151
Total	0.00 EUR

Would you like to purchase the full text of this article? If so, please continue on to the content ordering system located here: Purchase PDF

If you click on the buttons below or close this window, you will not be able to return to the content ordering system.

ORDER MORE | CLOSE WINDOW

Setion 6.3 Toward Direct photopatterning of solution processed amorphous indium zinc oxide and zinc tin oxide semiconductors- A chimie douce molecular precursor approach to thin film electronic oxides.

Figure 20 AFM micrographs of a) the bare wt. TMV template immobilized on a Si/SiO_2 substrate as well as b) the wt TMV template after 1 cycle of ZnO mineralization performed in this work. c) Schematic representation of the TMV/ZnO hybrid semiconductor employed in a TFT device. Adapted with permission under creative commons. Copyright Beilstein Institut.

Section 6.4 Microwave assisted synthesis and characterization of a zinc oxide/tobacco mosaic virus hybrid material. An active semiconductor in a field-effect transistor device.

Understanding the temperature-dependent evolution of solution processed metal oxide transistor characteristics based on molecular precursor derived amorphous indium zinc oxide

S. Sanctis, R.C. Hoffmann, R. Precht, W. Anwand and J. J. Schneider, *J. Mater. Chem. C*, 2016, **4**, 10935

DOI: 10.1039/C6TC03915D

Section 6.5 Understanding the temperature-dependent evolution of solution processed metal oxide transistor characteristics based on molecular precursor derived amorphous indium zinc oxide.

Copyright Clearance Center RightsLink®

Home | Account Info | Help

Title: Aqueous Solution Processing of Combustible Precursor Compounds into Amorphous Indium Gallium Zinc Oxide (IGZO) Semiconductors for Thin Film Transistor Applications

Author: Jörg J. Schneider, Michael Bruns, Sabine Foro, et al

Publication: Chemistry - An Asian Journal

Publisher: John Wiley and Sons

Date: Nov 13, 2018

Logged in as:
Shawn Sanctis
Account #:
3001291165
LOGOUT

Order Completed

Thank you for your order.

This Agreement between Mr. Shawn Sanctis ("You") and John Wiley and Sons ("John Wiley and Sons") consists of your license details and the terms and conditions provided by John Wiley and Sons and Copyright Clearance Center.

Your confirmation email will contain your order number for future reference.

printable details

License Number	4672990002780
License date	Sep 20, 2019
Licensed Content Publisher	John Wiley and Sons
Licensed Content Publication	Chemistry - An Asian Journal
Licensed Content Title	Aqueous Solution Processing of Combustible Precursor Compounds into Amorphous Indium Gallium Zinc Oxide (IGZO) Semiconductors for Thin Film Transistor Applications
Licensed Content Author	Jörg J. Schneider, Michael Bruns, Sabine Foro, et al
Licensed Content Date	Nov 13, 2018
Licensed Content Volume	13
Licensed Content Issue	24
Licensed Content Pages	8
Type of use	Dissertation/Thesis
Requestor type	Author of this Wiley article
Format	Print and electronic
Portion	Full article
Will you be translating?	No
Title of your thesis / dissertation	Metal oxide thin film transistors
Expected completion date	Nov 2019
Expected size (number of pages)	150
Requestor Location	Mr. Shawn Sanctis Klappacher str.3 Darmstadt, 64285 Germany Attn: Mr. Shawn Sanctis
Publisher Tax ID	EU826007151
Total	0.00 EUR

Would you like to purchase the full text of this article? If so, please continue on to the content ordering system located here: Purchase PDF

If you click on the buttons below or close this window, you will not be able to return to the content ordering system.

ORDER MORE | CLOSE WINDOW

Section 6.6 Aqueous solution processing of combustible precursor compounds into amorphous indium gallium zinc oxide (IGZO) semiconductors for thin film transistor applications.

Stacked indium oxide/zinc oxide heterostructures as semiconductors in thin film transistor devices: a case study using atomic layer deposition

S. Sanctis, J. Krausmann, C. Guhl and J. J. Schneider, *J. Mater. Chem. C*, 2018, **6**, 464

DOI: 10.1039/C7TC03724D

9 References

1. K. Nomura, H. Ohta, A. Takagi, T. Kamiya, M. Hirano and H. Hosono, *Nature*, 2004, **432**, 488-492.
2. E. Fortunato, P. Barquinha and R. Martins, *Adv. Mater.*, 2012, **24**, 2945-2986.
3. H. Kumomi, T. Kamiya and H. Hosono, *ECS Transactions*, 2015, **67**, 3-8.
4. R. A. Street, *Adv. Mater.*, 2009, **21**, 2007-2022.
5. P. Semenza, *Information Display*, 2012, **28**, 18-21.
6. J. F. Wager, *Information Display*, 2016, **32**, 16-21.
7. J. F. Wager, *Information Display*, 2014, **30**, 26-29.
8. K. L. Cunningham, *Information Display*, 2015, **31**, 28-33.
9. R. M. Soneira, *Information Display*, 2014, **30**, 12-15.
10. H. Ohshima, *IEEE (A-SSCC)*2014, 1-4.
11. Y. Kuo, *Poly-crystalline Silicon Thin Film Transistors*, 2004.
12. D. S. Ginley and C. Bright, *MRS Bull.*, 2000, **25**, 15-18.
13. T. Minami, *Semicond. Sci. Technol.*, 2005, **20**, S35.
14. K. Nomura, A. Takagi, T. Kamiya, H. Ohta, M. Hirano and H. Hosono, *Jpn. J. Appl. Phys.*, 2006, **45**, 4303.
15. T. Kamiya and H. Hosono, *NPG Asia Materials*, 2010, **2**, 15.
16. B. S. Meyerson, F. K. LeGoues, T. N. Nguyen and D. L. Harame, *Appl. Phys. Lett.*, 1987, **50**, 113-115.
17. E. W. Haas and M. S. Schnoller, *IEEE Trans. Electron Devices*, 1976, **23**, 803-805.
18. H. Klasens and H. Koelmans, *Solid-State Electron.*, 1964, **7**, 701-702.
19. G. Boesen and J. E. Jacobs, *Proc. IEEE*, 1968, **56**, 2094-2095.
20. H. Klasens and H. Koelmans, *Solid·State Electron.*, 1964, **7**, 701-702.
21. G. Boesen and J. Jacobs, *Proc. IEEE*, 1968, **56**, 2094-2095.
22. S. Masuda, K. Kitamura, Y. Okumura, S. Miyatake, H. Tabata and T. Kawai, *J. Appl. Phys.*, 2003, **93**, 1624-1630.
23. R. Hoffman, B. J. Norris and J. Wager, *Appl. Phys. Lett.*, 2003, **82**, 733-735.
24. P. Carcia, R. McLean, M. Reilly and G. Nunes Jr, *Appl. Phys. Lett.*, 2003, **82**, 1117-1119.
25. E. Fortunato, A. Pimentel, L. Pereira, A. Gonçalves, G. Lavareda, H. Águas, I. Ferreira, C. N. Carvalho and R. Martins, *J. Non-Cryst. Solids*, 2004, **338-340**, 806-809.
26. R. Presley, C. Munsee, C. Park, D. Hong, J. Wager and D. Keszler, *J. Phys. D: Appl. Phys.*, 2004, **37**, 2810.
27. V. K. Gueorguiev, L. I. Popova, G. D. Beshkov and N. A. Tomajova, *Sensors and Actuators A: Physical*, 1990, **24**, 61-63.

28. T. L. Breen, P. M. Fryer, R. W. Nunes and M. E. Rothwell, *Langmuir*, 2002, **18**, 194-197.
29. Y. Shigesato and D. C. Paine, *Appl. Phys. Lett.*, 1993, **62**, 1268-1270.
30. G. Lavareda, C. N. de Carvalho, E. Fortunato, A. Ramos, E. Alves, O. Conde and A. Amaral, *J. Non-Cryst. Solids*, 2006, **352**, 2311-2314.
31. Y. Vygranenko, K. Wang and A. Nathan, *Appl. Phys. Lett.*, 2007, **91**, 263508.
32. S.-S. Cheng, C.-Y. Yang, C.-W. Ou, Y.-C. Chuang, M. C. Wu and C.-W. Chu, *J. Phys. D: Appl. Phys.*, 2008, **41**, 092006.
33. T. Kamiya and H. Hosono, *Handbook of Visual Display Technology*, 2014, 1-28.
34. H. Hosono, M. Yasukawa and H. Kawazoe, *J. Non-Cryst. Solids*, 1996, **203**, 334-344.
35. K. Nomura, H. Ohta, A. Takagi, T. Kamiya, M. Hirano and H. Hosono, *Nature*, 2004, **432**, 488.
36. H. Hosono, Y. Yamashita, N. Ueda, H. Kawazoe and K. i. Shimidzu, *Appl. Phys. Lett.*, 1996, **68**, 661-663.
37. M. Yasukawa, H. Hosono, N. Ueda and H. Kawazoe, *Jpn. J. Appl. Phys.*, 1995, **34**, L281.
38. M. Orita, H. Ohta, M. Hirano, S. Narushima and H. Hosono, *Philos. Mag. B*, 2001, **81**, 501-515.
39. H. Hosono, N. Kikuchi, N. Ueda, H. Kawazoe and K. i. Shimidzu, *Appl. Phys. Lett.*, 1995, **67**, 2663-2665.
40. H. Hosono, *J. Non-Cryst. Solids*, 2006, **352**, 851-858.
41. T. Kamiya, K. Nomura and H. Hosono, *Sci. Technol. Adv. Mater.*, 2010, **11**, 044305.
42. J. Sun, D. A. Mourey, D. Zhao and T. N. Jackson, *J. Electron. Mater.*, 2008, **37**, 755-759.
43. M. Ofuji, K. Abe, H. Shimizu, N. Kaji, R. Hayashi, M. Sano, H. Kumomi, K. Nomura, T. Kamiya and H. Hosono, *IEEE Electron Device Lett.*, 2007, **28**, 273-275.
44. H. Yin, S. Kim, H. Lim, Y. Min, C. J. Kim, I. Song, J. Park, S.-W. Kim, A. Tikhonovsky and J. Hyun, *IEEE Trans. Electron Devices*, 2008, **55**, 2071-2077.
45. P.-T. Liu, Y.-T. Chou and L.-F. Teng, *Appl. Phys. Lett.*, 2009, **94**, 242101.
46. R. Lujan and R. Street, *IEEE Electron Device Lett.*, 2012, **33**, 688-690.
47. Y.-C. Shen, C.-H. Yang, S.-W. Chen, S.-H. Wu, T.-L. Yang and J.-J. Huang, *Biosensors Bioelectron.*, 2014, **54**, 306-310.
48. J.-C. Lin, B.-R. Huang and Y.-K. Yang, *Sensors Actuators B: Chem.*, 2013, **184**, 27-32.
49. S. Jeon, S. Park, I. Song, J.-H. Hur, J. Park, S. Kim, S. Kim, H. Yin, E. Lee and S. Ahn, 2010.
50. T.-Y. Hsieh, T.-C. Chang, T.-C. Chen, Y.-C. Chen, Y.-T. Chen, P.-Y. Liao, A.-K. Chu, W.-W. Tsai, W.-J. Chiang and J.-Y. Yan, *Appl. Phys. Lett.*, 2012, **101**, 212104.
51. Ü. Özgür, Y. I. Alivov, C. Liu, A. Teke, M. Reshchikov, S. Doğan, V. Avrutin, S.-J. Cho and H. Morkoc, *J. Appl. Phys.*, 2005, **98**, 11.
52. Z. Tang, G. K. Wong, P. Yu, M. Kawasaki, A. Ohtomo, H. Koinuma and Y. Segawa, *Appl. Phys. Lett.*, 1998, **72**, 3270-3272.

53. D. Bagnall, Y. Chen, Z. Zhu, T. Yao, S. Koyama, M. Y. Shen and T. Goto, *Appl. Phys. Lett.*, 1997, **70**, 2230-2232.
54. C. G. Granqvist and A. Hultåker, *Thin Solid Films*, 2002, **411**, 1-5.
55. J. Kim, C. Fuentes-Hernandez, W. Potscavage Jr, X.-H. Zhang and B. Kippelen, *Appl. Phys. Lett.*, 2009, **94**, 142107.
56. L. Yuan, X. Zou, G. Fang, J. Wan, H. Zhou and X. Zhao, *IEEE Electron Device Lett.*, 2011, **32**, 42.
57. C.-Y. Tsay, C.-H. Cheng and Y.-W. Wang, *Ceram. Int.*, 2012, **38**, 1677-1682.
58. T. Kawamura, H. Uchiyama, S. Saito, H. Wakana, T. Mine, M. Hatano, K. Torii and T. Onai,*IEEE International Electron Devices Meeting* 2008.
59. T. Kamiya, K. Nomura and H. Hosono, *J. Disp. Technol.*, 2009, **5**, 468-483.
60. R. Martins, A. Nathan, R. Barros, L. Pereira, P. Barquinha, N. Correia, R. Costa, A. Ahnood, I. Ferreira and E. Fortunato, *Adv. Mater.*, 2011, **23**, 4491-4496.
61. X. Yu, J. Smith, N. Zhou, L. Zeng, P. Guo, Y. Xia, A. Alvarez, S. Aghion, H. Lin and J. Yu, *Proc. Natl. Acad. Sci.*, 2015, **112**, 3217-3222.
62. B.-Y. Oh, M.-C. Jeong, M.-H. Ham and J.-M. Myoung, *Semicond. Sci. Technol.*, 2007, **22**, 608.
63. R. Hayashi, M. Ofuji, N. Kaji, K. Takahashi, K. Abe, H. Yabuta, M. Sano, H. Kumomi, K. Nomura and T. Kamiya, *Soc. Inf. Disp.*, 2007, **15**, 915-921.
64. M. Hata, K. Tanaka, T. Watanabe, M. Noma, A. Tagawa, K. Yoshida, K. Yamamoto, K. Nagata, S. Miyazaki and D. Kitagawa, *Soc. Inf. Disp*, 2018, **26**, 229-236.
65. J. Donelan, *J. Inf. Disp.*, 2018, **34**, 8-27.
66. H. Yabuta, M. Sano, K. Abe, T. Aiba, T. Den, H. Kumomi, K. Nomura, T. Kamiya and H. Hosono, *Appl. Phys. Lett.*, 2006, **89**, 112123.
67. A. Suresh, P. Gollakota, P. Wellenius, A. Dhawan and J. F. Muth, *Thin Solid Films*, 2008, **516**, 1326-1329.
68. A. Illiberi, B. Cobb, A. Sharma, T. Grehl, H. Brongersma, F. Roozeboom, G. Gelinck and P. Poodt, *ACS Appl. Mater. Inter.*, 2015, **7**, 3671-3675.
69. S.-M. Yoon, N.-J. Seong, K. Choi, G.-H. Seo and W.-C. Shin, *ACS Appl. Mater. Inter.*, 2017, **9**, 22676-22684.
70. M. Lorenz, M. R. Rao, T. Venkatesan, E. Fortunato, P. Barquinha, R. Branquinho, D. Salgueiro, R. Martins, E. Carlos and A. Liu, *J. Phys. D: Appl. Phys.*, 2016, **49**, 433001.
71. B. Norris, J. Anderson, J. Wager and D. Keszler, *J. Phys. D: Appl. Phys.*, 2003, **36**, L105.
72. W. J. Lee, W. T. Park, S. Park, S. Sung, Y. Y. Noh and M. H. Yoon, *Adv. Mater.*, 2015, **27**, 5043-5048.
73. B. Wang, X. Yu, P. Guo, W. Huang, L. Zeng, N. Zhou, L. Chi, M. J. Bedzyk, R. P. Chang and T. J. Marks, *Adv. Electron. Mater.*, 2016, **2**, 1500427.

74. C.-H. Choi, L.-Y. Lin, C.-C. Cheng and C.-h. Chang, *ECS ECS J. Solid State Sci. Technol.*, 2015, **4**, P3044-P3051.
75. J. Leppäniemi, O. H. Huttunen, H. Majumdar and A. Alastalo, *Adv. Mater.*, 2015, **27**, 7168-7175.
76. W. J. Scheideler, J. Jang, M. A. U. Karim, R. Kitsomboonloha, A. Zeumault and V. Subramanian, *ACS Appl. Mater. Inter.*, 2015, **7**, 12679-12687.
77. J. J. Schneider, R. C. Hoffmann, J. Engstler, O. Soffke, W. Jaegermann, A. Issanin and A. Klyszcz, *Adv. Mater.*, 2008, **20**, 3383-3387.
78. H.-C. Cheng, C.-F. Chen and C.-C. Lee, *Thin Solid Films*, 2006, **498**, 142-145.
79. D. Redinger and V. Subramanian, *IEEE Trans. Electron Devices*, 2007, **54**, 1301-1307.
80. R. M. Pasquarelli, D. S. Ginley and R. O'Hayre, *Chem. Soc. Rev.*, 2011, **40**, 5406-5441.
81. L. L. Hench and J. K. West, *Chem. Rev.*, 1990, **90**, 33-72.
82. S. Jeong, Y. G. Ha, J. Moon, A. Facchetti and T. J. Marks, *Adv. Mater.*, 2010, **22**, 1346-1350.
83. M.-G. Kim, H. S. Kim, Y.-G. Ha, J. He, M. G. Kanatzidis, A. Facchetti and T. J. Marks, *JACS*, 2010, **132**, 10352-10364.
84. C. G. Choi, S.-J. Seo and B.-S. Bae, *Electrochem. Solid-State Lett.*, 2008, **11**, H7-H9.
85. Y. H. Hwang, J. H. Jeon, K. J. Seo and B. S. Bae, *Electrochem. Solid State Lett.*, 2009, **12**, H336-H339.
86. H. S. Kim, M. G. Kim, Y. Q. Ha, M. G. Kanatzidis, T. J. Marks and A. Facchetti, *JACS*, 2009, **131**, 10826.
87. F. Babonneau, S. Doeuff, A. Leaustic, C. Sanchez, C. Cartier and M. Verdaguer, *Inorg. Chem.*, 1988, **27**, 3166-3172.
88. U. Schubert, *J. Mater. Chem.*, 2005, **15**, 3701-3715.
89. M. Yu, M. Liang, J. Liu, S. Li, B. Xue and H. Zhao, *Appl. Surf. Sci.*, 2016, **363**, 229-239.
90. D. E. Walker, M. Major, M. Baghaie Yazdi, A. Klyszcz, M. Haeming, K. Bonrad, C. Melzer, W. Donner and H. von Seggern, *ACS Appl. Mater. Inter*, 2012, **4**, 6835-6841.
91. H. Chen, Y. S. Rim, C. Jiang and Y. Yang, *Chem. Mater.*, 2015, **27**, 4713-4718.
92. S. Jeong and J. Moon, *J. Mater. Chem.*, 2012, **22**, 1243-1250.
93. Y.-J. Chang, D.-H. Lee, G. Herman and C.-H. Chang, *Electrochem. Solid-State Lett.*, 2007, **10**, H135-H138.
94. D. H. Lee, Y. J. Chang, G. S. Herman and C. H. Chang, *Adv. Mater.*, 2007, **19**, 843-847.
95. W. H. Jeong, J. H. Bae and H. J. Kim, *IEEE Electron Device Lett.*, 2012, **33**, 68-70.
96. E. Bacaksiz, M. Parlak, M. Tomakin, A. Özçelik, M. Karakız and M. Altunbaş, *J. Alloys Compd.*, 2008, **466**, 447-450.
97. L. Prabhumirashi and J. Khoje, *Thermochim. Acta*, 2002, **383**, 109-118.

98. K.-H. Lim, J. Lee, J.-E. Huh, J. Park, J.-H. Lee, S.-E. Lee and Y. S. Kim, *J. Mater. Chem. C*, 2017, **5**, 7768-7776.
99. S. J. Heo, D. H. Yoon, T. S. Jung and H. J. Kim, *J. Info. Disp.*, 2013, **14**, 79-87.
100. J. J. Schneider, R. C. Hoffmann, J. Engstler, O. Soffke, W. Jaegermann, A. Issanin and A. Klyszcz, *Adv. Mater.*, 2008, **20**, 3383-3387.
101. J. J. Schneider, R. C. Hoffmann, J. Engstler, S. Dilfer, A. Klyszcz, E. Erdem, P. Jakes and R. A. Eichel, *J. Mater. Chem.*, 2009, **19**, 1449-1457.
102. K. Banger, Y. Yamashita, K. Mori, R. Peterson, T. Leedham, J. Rickard and H. Sirringhaus, *Nature Mater.*, 2011, **10**, 45.
103. X. Yu, J. Smith, N. Zhou, L. Zeng, P. Guo, Y. Xia, A. Alvarez, S. Aghion, H. Lin, J. Yu, R. P. H. Chang, M. J. Bedzyk, R. Ferragut, T. J. Marks and A. Facchetti, *Proc. Natl. Acad. Sci. U.S.A.*, 2015, **112**, 3217-3222.
104. A. G. Merzhanov, *J. Mater. Chem.*, 2004, **14**, 1779-1786.
105. R. Tukhtaev, V. Boldyrev, A. Gavrilov, S. Larionov, L. Myachina and Z. Savel'Eva, *Inorg. Mater.*, 2002, **38**, 985-991.
106. H. C. Yi and J. Moore, *J. Mater. Sci.*, 1990, **25**, 1159-1168.
107. D. W. Gidley, H.-G. Peng and R. S. Vallery, *Annu. Rev. Mater. Res.*, 2006, **36**, 49-79.
108. K. Sato, D. Shanai, Y. Hotani, T. Ougizawa, K. Ito, K. Hirata and Y. Kobayashi, *Phys. Rev. Lett.*, 2006, **96**, 228302.
109. M. Butterling, https://www.hzdr.de/db/Cms?pOid=35245&pNid=3225, (accessed 31st, August, 2019).
110. B. Wang, L. Zeng, W. Huang, F. S. Melkonyan, W. C. Sheets, L. Chi, M. J. Bedzyk, T. J. Marks and A. Facchetti, *JACS*, 2016, **138**, 7067-7074.
111. S. T. Meyers, J. T. Anderson, C. M. Hung, J. Thompson, J. F. Wager and D. A. Keszler, *JACS*, 2008, **130**, 17603-17609.
112. P. Benard, J. Auffredic and D. Louer, *Thermochim. Acta*, 1994, **232**, 65-76.
113. T. Biswick, W. Jones, A. Pacuła, E. Serwicka and J. Podobinski, *J. Solid State Chem.*, 2007, **180**, 1171-1179.
114. Y.-H. Lin, H. Faber, K. Zhao, Q. Wang, A. Amassian, M. McLachlan and T. D. Anthopoulos, *Adv. Mater.*, 2013, **25**, 4340-4346.
115. J. Livage, M. Henry and C. Sanchez, *Prog. Solid State Chem.*, 1988, **18**, 259-341.
116. Y. S. Rim, H. Chen, T.-B. Song, S.-H. Bae and Y. Yang, *Chem. Mater.*, 2015, **27**, 5808-5812.
117. H.-H. Tseng, P. J. Tobin, S. Kalpat, J. K. Schaeffer, M. E. Ramon, L. R. Fonseca, Z. X. Jiang, R. Hegde, D. H. Triyoso and S. Semavedam, *IEEE Trans. Electron Devices*, 2007, **54**, 3267-3275.
118. A. C. Pierre, *Introduction to sol-gel processing*, Springer Science & Business Media, 2013.

119. J.-P. Jolivet, M. Henry and J. Livage, *Metal oxide chemistry and synthesis: from solution to solid state*, Wiley-Blackwell, 2000.
120. G. R. Patzke, F. Krumeich and R. Nesper, *Angew. Chem. Int. Ed.*, 2002, **41**, 2446-2461.
121. C. Burda, X. Chen, R. Narayanan and M. A. El-Sayed, *Chem. Rev.*, 2005, **105**, 1025-1102.
122. A. Gurav, T. Kodas, T. Pluym and Y. Xiong, *Aerosol Sci. Technol.*, 1993, **19**, 411-452.
123. F. E. Kruis, H. Fissan and A. Peled, *J. Aerosol Sci*, 1998, **29**, 511-535.
124. R. Strobel and S. E. Pratsinis, *J. Mater. Chem.*, 2007, **17**, 4743-4756.
125. B. L. Cushing, V. L. Kolesnichenko and C. J. O'Connor, *Chem. Rev.*, 2004, **104**, 3893-3946.
126. X. Wang and Y. Li, *Chem. Commun.*, 2007, 2901-2910.
127. C. Rao, S. Vivekchand, K. Biswas and A. Govindaraj, *Dalton Trans.*, 2007, 3728-3749.
128. S. G. Kwon and T. Hyeon, *Acc. Chem. Res.*, 2008, **41**, 1696-1709.
129. W. T. Yao and S. H. Yu, *Adv. Funct. Mater.*, 2008, **18**, 3357-3366.
130. D. Wang, T. Xie and Y. Li, *Nano Res.*, 2009, **2**, 30-46.
131. N. Pinna and M. Niederberger, *Angew. Chem. Int. Ed.*, 2008, **47**, 5292-5304.
132. P. H. Mutin and A. Vioux, *Chem. Mater.*, 2009, **21**, 582-596.
133. Y. w. Jun, J. s. Choi and J. Cheon, *Angew. Chem. Int. Ed.*, 2006, **45**, 3414-3439.
134. J. Park, J. Joo, S. G. Kwon, Y. Jang and T. Hyeon, *Angew. Chem. Int. Ed.*, 2007, **46**, 4630-4660.
135. M. Niederberger, *Acc. Chem. Res.*, 2007, **40**, 793-800.
136. M. Rajamathi and R. Seshadri, *Curr. Opin. Solid State Mater. Sci.*, 2002, **6**, 337-345.
137. K. Byrappa and T. Adschiri, *Prog. Cryst. Growth Charact. Mater.*, 2007, **53**, 117-166.
138. K. S. Suslick and G. J. Price, *Annu. Rev. Mater. Sci.*, 1999, **29**, 295-326.
139. A. Gedanken, *Ultrason. Sonochem.*, 2004, **11**, 47-55.
140. A. Huczko, *Appl. Phys. A*, 2000, **70**, 365-376.
141. L. A. Estroff and A. D. Hamilton, *Chem. Mater.*, 2001, **13**, 3227-3235.
142. C. Sanchez, H. Arribart and M. M. G. Guille, *Nature materials*, 2005, **4**, 277.
143. Y. Oaki and H. Imai, *J. Mater. Chem.*, 2007, **17**, 316-321.
144. R. L. Brutchey and D. E. Morse, *Angew. Chem.*, 2006, **118**, 6714-6716.
145. J. Sun and B. Bhushan, *Rsc Advances*, 2012, **2**, 7617-7632.
146. V. K. LaMer and R. H. Dinegar, *JACS*, 1950, **72**, 4847-4854.
147. E. Matijevic, *Chem. Mater.*, 1993, **5**, 412-426.
148. E. Matijevic, *Langmuir*, 1986, **2**, 12-20.
149. C. O. Kappe, *Angew. Chem. Int. Ed.*, 2004, **43**, 6250-6284.
150. C. O. Kappe, D. Dallinger and S. S. Murphree, *Strategies, Instruments, and Protocols (Wiley-VCH, Weinheim, Germany, 2009)*, 2009.
151. B. L. Hayes, *Microwave synthesis: chemistry at the speed of light*, Cem Corporation, 2002.

152. I. Bilecka and M. Niederberger, *Nanoscale*, 2010, **2**, 1358-1374.
153. C. O. Kappe, *CHIMIA International J.Chem.*, 2006, **60**, 308-312.
154. E. Grant and B. J. Halstead, *Chem. Soc. Rev.*, 1998, **27**, 213-224.
155. K. Okamura, N. Mechau, D. Nikolova and H. Hahn, *Appl. Phys. Lett.*, 2008, **93**, 083105.
156. S. Bubel, D. Nikolova, N. Mechau and H. Hahn, *J. Appl. Phys.*, 2009, **105**, 064514.
157. T. V. Richter, F. Stelzl, J. Schulz-Gericke, B. Kerscher, U. Würfel, M. Niggemann and S. Ludwigs, *J. Mater. Chem.*, 2010, **20**, 874-879.
158. H. Faber, M. Burkhardt, A. Jedaa, D. Kälblein, H. Klauk and M. Halik, *Adv. Mater.*, 2009, **21**, 3099-3104.
159. J. r. J. Schneider, R. C. Hoffmann, J. r. Engstler, A. Klyszcz, E. Erdem, P. Jakes, R. d.-A. Eichel, L. Pitta-Bauermann and J. Bill, *Chem. Mater.*, 2010, **22**, 2203-2212.
160. S. Sanctis, R. C. Hoffmann and J. J. Schneider, *RSC Adv.*, 2013, **3**, 20071-20076.
161. Y.-H. Kim, J.-S. Heo, T.-H. Kim, S. Park, M.-H. Yoon, J. Kim, M. S. Oh, G.-R. Yi, Y.-Y. Noh and S. K. Park, *Nature*, 2012, **489**, 128.
162. S. Dasgupta, R. Kruk, N. Mechau and H. Hahn, *ACS nano*, 2011, **5**, 9628-9638.
163. D. Kim, Y. Jeong, K. Song, S.-K. Park, G. Cao and J. Moon, *Langmuir*, 2009, **25**, 11149-11154.
164. S. Dilfer, R. C. Hoffmann and E. Dörsam, *Appl. Surf. Sci.*, 2014, **320**, 634-642.
165. D. Spiehl, M. Häming, H. M. Sauer, K. Bonrad and E. Dörsam, *IEEE Trans. Electron Devices*, 2015, **62**, 2871-2877.
166. D. Kim, D. Lee, S. Yoon, J. Jang and M. Hong, *Current Applied Physics*, 2012, **12**, S48-S51.
167. T. Arai, *J.Soc. Info. Disp.*, 2012, **20**, 156-161.
168. T. Aoi, N. Oka, Y. Sato, R. Hayashi, H. Kumomi and Y. Shigesato, *Thin Solid Films*, 2010, **518**, 3004-3007.
169. S. Tsao, T.-C. Chang, S.-Y. Huang, M.-C. Chen, S. Chen, C. Tsai, Y. Kuo, Y. Chen and W. Wu, *Solid·State Electron.*, 2010, **54**, 1497-1499.
170. Y. S. Rim, H. S. Lim and H. J. Kim, *ACS Appl. Mater. Inter.*, 2013, **5**, 3565-3571.
171. J. Kim, M.-G. Kim, J. Kim, S. Jo, J. Kang, J.-W. Jo, W. Lee, C. Hwang, J. Moon and L. Yang, *Sci. Rep.*, 2015, **5**, 14520.
172. H. Han, J. Bissell, F. Yaghmaie and C. E. Davis, *Langmuir*, 2009, **26**, 515-520.
173. H. Xu, L. Lan, M. Xu, J. Zou, L. Wang, D. Wang and J. Peng, *Appl. Phys. Lett.*, 2011, **99**, 253501.
174. S. H. Ryu, Y. C. Park, M. Mativenga, D. H. Kang and J. Jang, *ECS Solid State Letters*, 2012, **1**, Q17-Q19.
175. K. Seong, K. Kim, S. Y. Park and Y. S. Kim, *Chem. Commun.*, 2013, **49**, 2783-2785.
176. C. Gu and J.-S. Lee, *RSC Adv.*, 2016, **6**, 43147-43151.

177. Y. Choi, G. H. Kim, W. H. Jeong, H. J. Kim, B. D. Chin and J.-W. Yu, *Thin Solid Films*, 2010, **518**, 6249-6252.
178. S. Sung, S. Park, S. Cha, W.-J. Lee, C.-H. Kim and M.-H. Yoon, *RSC Advances*, 2015, **5**, 38125-38129.
179. H.-C. Lin, F. Stehlin, O. Soppera, H.-W. Zan, C.-H. Li, F. Wieder, A. Ponche, D. Berling, B.-H. Yeh and K.-H. Wang, *Sci. Rep.*, 2015, **5**, 10490.
180. Y. J. Jeong, T. K. An, D.-J. Yun, L. H. Kim, S. Park, Y. Kim, S. Nam, K. H. Lee, S. H. Kim and J. Jang, *ACS Appl. Mater. Inter*, 2016, **8**, 5499-5508.
181. H. S. Lim, Y. S. Rim and H. J. Kim, *Scientific reports*, 2014, **4**, 4544.
182. C. C. Yeh, S. Colis, P. Fioux, H. W. Zan, D. Berling and O. Soppera, *Adv. Mater. Inter.*, 2017, **4**, 1700738.
183. J. S. Heo, J.-W. Jo, J. Kang, C.-Y. Jeong, H. Y. Jeong, S. K. Kim, K. Kim, H.-I. Kwon, J. Kim and Y.-H. Kim, *ACS Appl. Mater. Inter.* , 2016, **8**, 10403-10412.
184. R. A. John, N. A. Chien, S. Shukla, N. Tiwari, C. Shi, N. G. Ing and N. Mathews, *Chem. Mater.*, 2016, **28**, 8305-8313.
185. K. Umeda, T. Miyasako, A. Sugiyama, A. Tanaka, M. Suzuki, E. Tokumitsu and T. Shimoda, *J. Appl. Phys.*, 2013, **113**, 184509.
186. J. Leppäniemi, K. Ojanperä, T. Kololuoma, O.-H. Huttunen, J. Dahl, M. Tuominen, P. Laukkanen, H. Majumdar and A. Alastalo, *Appl. Phys. Lett.*, 2014, **105**, 113514.
187. M. Miyakawa, M. Nakata, H. Tsuji and Y. Fujisaki, *Sci. Rep.*, 2018, **8**, 12825.
188. T. Y. Lee, T. M. Roper, E. S. Jonsson, I. Kudyakov, K. Viswanathan, C. Nason, C. Guymon and C. E. Hoyle, *Polymer*, 2003, **44**, 2859-2865.
189. C. Decker, *Prog. Polym. Sci.*, 1996, **21**, 593-650.
190. C. S. Brazel and S. L. Rosen, *Fundamental principles of polymeric materials*, John Wiley & Sons, 2012.
191. I. Aksay, M. Trau, S. Manne, I. Honma, N. Yao, L. Zhou, P. Fenter, P. Eisenberger and S. Gruner, *Science*, 1996, **273**, 892-898.
192. K. K. Wong, T. Douglas, S. Gider, D. D. Awschalom and S. Mann, *Chem. Mater.*, 1998, **10**, 279-285.
193. K. K. Wong and S. Mann, *Adv. Mater.*, 1996, **8**, 928-932.
194. T. Douglas and M. Young, *Nature*, 1998, **393**, 152.
195. M. Pazirandeh, S. Baral and J. Campbell, *Biomimetics*, 1992, **1**, 41-50.
196. W. Shenton, D. Pum, U. B. Sleytr and S. Mann, *Nature*, 1997, **389**, 585.
197. S. A. Davis, S. L. Burkett, N. H. Mendelson and S. Mann, *Nature*, 1997, **385**, 420.
198. D. D. Archibald and S. Mann, *Nature*, 1993, **364**, 430.

199. S. Baral and P. Schoen, *Chem. Mater.*, 1993, **5**, 145-147.
200. E. Braun, Y. Eichen, U. Sivan and G. Ben-Yoseph, *Nature*, 1998, **391**, 775.
201. C. A. Mirkin, R. L. Letsinger, R. C. Mucic and J. J. Storhoff, *Nature*, 1996, **382**, 607.
202. A. P. Alivisatos, K. P. Johnsson, X. Peng, T. E. Wilson, C. J. Loweth, M. P. Bruchez Jr and P. G. Schultz, *Nature*, 1996, **382**, 609.
203. J. L. Coffer, S. R. Bigham, X. Li, R. F. Pinizzotto, Y. G. Rho, R. M. Pirtle and I. L. Pirtle, *Appl. Phys. Lett.*, 1996, **69**, 3851-3853.
204. K. T. Nam, R. Wartena, P. J. Yoo, F. W. Liau, Y. J. Lee, Y.-M. Chiang, P. T. Hammond and A. M. Belcher, *PNAS*, 2008, **105**, 17227-17231.
205. D. Ghosh, Y. Lee, S. Thomas, A. G. Kohli, D. S. Yun, A. M. Belcher and K. A. Kelly, Nat. Nanotechnol., 2012, **7**, 677.
206. D. Oh, X. Dang, H. Yi, M. A. Allen, K. Xu, Y. J. Lee and A. M. Belcher, *Small*, 2012, **8**, 1006-1011.
207. B. Neltner, B. Peddie, A. Xu, W. Doenlen, K. Durand, D. S. Yun, S. Speakman, A. Peterson and A. Belcher, *ACS Nano*, 2010, **4**, 3227-3235.
208. D. Oh, J. Qi, B. Han, G. Zhang, T. J. Carney, J. Ohmura, Y. Zhang, Y. Shao-Horn and A. M. Belcher, *Nano Lett.*, 2014, **14**, 4837-4845.
209. R. J. Tseng, C. Tsai, L. Ma, J. Ouyang, C. S. Ozkan and Y. Yang, *Nat. Nanotechnol.*, 2006, **1**, 72.
210. L. Song, H. Wang, S. Wang, H. Zhang, H. Cong and P. Tien, *J. Mater. Sci*, 2014, **49**, 2693-2704.
211. C. Wang, P. Gu, B. Hu and Q. Zhang, *J. Mater. Chem. C*, 2015, **3**, 10055-10065.
212. C. Tsai, R. J. Tseng, Y. Yang and C. S. Ozkan, *JNO*, 2008, **3**, 133-136.
213. M. Gnerlich, E. Pomerantseva, K. Gregorczyk, D. Ketchum, G. Rubloff and R. Ghodssi, *J. Micromechanics Microengineering*, 2013, **23**, 114014.
214. M. Knez and U. Gösele, *Nature Nanotechnol*, 2006, **1**, 22.
215. J. Alonso, M. Górzny and A. Bittner, *Trends Biotechnol.*, 2013, **31**, 530-538.
216. W. Shenton, T. Douglas, M. Young, G. Stubbs and S. Mann, *Adv. Mater.*, 1999, **11**, 253-256.
217. S. Balci, K. Hahn, P. Kopold, A. Kadri, C. Wege, K. Kern and A. M. Bittner, *Nanotechnology*, 2012, **23**, 045603.
218. X. Z. Fan, E. Pomerantseva, M. Gnerlich, A. Brown, K. Gerasopoulos, M. McCarthy, J. Culver and R. Ghodssi, *J. Vac. Sci. Tech. A*, 2013, **31**, 050815.
219. K. M. Bromley, A. J. Patil, A. W. Perriman, G. Stubbs and S. Mann, *J. Mater. Chem.*, 2008, **18**, 4796-4801.
220. J. Vesenka, S. Manne, R. Giberson, T. Marsh and E. Henderson, *Biophys. J.*, 1993, **65**, 992-997.
221. A. A. Khan, E. K. Fox, M. Ł. Górzny, E. Nikulina, D. F. Brougham, C. Wege and A. M. Bittner, *Langmuir*, 2013, **29**, 2094-2098.
222. K. Zhou, J. Zhang and Q. Wang, *Small*, 2015, **11**, 2505-2509.

223. F. J. Eber, S. Eiben, H. Jeske and C. Wege, *Angew. Chem.*, 2013, **125**, 7344-7348.
224. M. Knez, A. Kadri, C. Wege, U. Gösele, H. Jeske and K. Nielsch, *Nano Lett.*, 2006, **6**, 1172-1177.
225. S. Balci, A. Bittner, M. Schirra, K. Thonke, R. Sauer, K. Hahn, A. Kadri, C. Wege, H. Jeske and K. Kern, *Electrochim. Acta*, 2009, **54**, 5149-5154.
226. E. S. Royston, A. D. Brown, M. T. Harris and J. N. Culver, *J. Colloid Interface Sci.*, 2009, **332**, 402-407.
227. S. Sanctis, R. C. Hoffmann, S. Eiben and J. J. Schneider, *B. J. Nanotechnol.*, 2015, **6**, 785-791.
228. S.-Y. Lee, E. Royston, J. N. Culver and M. T. Harris, *Nanotechnology*, 2005, **16**, S435.
229. H. Yi, S. Nisar, S.-Y. Lee, M. A. Powers, W. E. Bentley, G. F. Payne, R. Ghodssi, G. W. Rubloff, M. T. Harris and J. N. Culver, *Nano Lett.*, 2005, **5**, 1931-1936.
230. A. A. McCormick and K. E. Palmer, *Expert review of vaccines*, 2008, **7**, 33-41.
231. X. Fan, L. Naves, N. Siwak, A. Brown, J. Culver and R. Ghodssi, *Nanotechnology*, 2015, **26**, 205501.
232. A. J. Love, V. Makarov, I. Yaminsky, N. O. Kalinina and M. E. Taliansky, *Virology*, 2014, **449**, 133-139.
233. L. D. Bolisay, J. N. Culver and P. Kofinas, *Biomacromolecules*, 2007, **8**, 3893-3899.
234. M. Wnęk, M. Ł. Górzny, M. Ward, C. Wälti, A. Davies, R. Brydson, S. Evans and P. Stockley, *Nanotechnology*, 2012, **24**, 025605.
235. T. L. Schlick, Z. Ding, E. W. Kovacs and M. B. Francis, *JACS*, 2005, **127**, 3718-3723.
236. R. A. Miller, A. D. Presley and M. B. Francis, *JACS*, 2007, **129**, 3104-3109.
237. B. Lu, G. Stubbs and J. N. Culver, *Virology*, 1996, **225**, 11-20.
238. J. L. Santos, J. A. Bispo, G. F. Landini and C. F. Bonafe, *Biophys. Chem.*, 2004, **111**, 53-61.
239. Z. Niu, M. A. Bruckman, S. Li, L. A. Lee, B. Lee, S. V. Pingali, P. Thiyagarajan and Q. Wang, *Langmuir*, 2007, **23**, 6719-6724.
240. K. Gerasopoulos, M. McCarthy, P. Banerjee, X. Fan, J. Culver and R. Ghodssi, *Nanotechnology*, 2010, **21**, 055304.
241. K. Gerasopoulos, M. McCarthy, E. Royston, J. N. Culver and R. Ghodssi, *J. Micromechanics and Microengineering*, 2008, **18**, 104003.
242. E. Royston, A. Ghosh, P. Kofinas, M. T. Harris and J. N. Culver, *Langmuir*, 2008, **24**, 906-912.
243. M. Knez, M. Sumser, A. M. Bittner, C. Wege, H. Jeske, T. P. Martin and K. Kern, *Adv. Funct. Mater.*, 2004, **14**, 116-124.
244. A. Janotti and C. G. Van de Walle, *Rep. Prog. Phys.*, 2009, **72**, 126501.
245. U. Ozgur, D. Hofstetter and H. Morkoc, *Proc. IEEE*, 2010, **98**, 1255-1268.
246. J. Nishii, F. M. Hossain, S. Takagi, T. Aita, K. Saikusa, Y. Ohmaki, I. Ohkubo, S. Kishimoto, A. Ohtomo and T. Fukumura, *Jpn. J. Appl. Phys.*, 2003, **42**, L347.

247. H.-C. Huang and T.-E. Hsieh, *Nanotechnology*, 2010, **21**, 295707.
248. Y. Ohya, T. Niwa, T. Ban and Y. Takahashi, *Jpn. J. Appl. Phys.*, 2001, **40**, 297.
249. P. Atanasova, D. Rothenstein, J. J. Schneider, R. C. Hoffmann, S. Dilfer, S. Eiben, C. Wege, H. Jeske and J. Bill, *Adv. Mater.*, 2011, **23**, 4918-4922.
250. Y. Vashpanov, J. I. Jung and K. Dal Kwack, *Phys. Status Solidi (a)*, 2011, **208**, 1683-1687.
251. H. Lewerenz, *Phys. Status Solidi i (b)*, 2008, **245**, 1884-1898.
252. D. Skoda, P. Urbánek, J. Sevcik, L. Munster, J. Antos and I. Kuritka, *Mater. Sci. Eng.: B*, 2018, **232**, 22-32.
253. L. Guy Donaruma and W. Z. Heldt, *Organic reactions*, 2004, **11**, 1-156.
254. L. Zhang, H. Zhang, Y. Bai, J. W. Ma, J. Cao, X. Jiang and Z. L. Zhang, *Solid State Commun.*, 2008, **146**, 387-390.
255. S. M. George, *Chem. Rev.*, 2010, **110**, 111-131.
256. T. Suntola, *Mater. Sci. Rep.*, 1989, **4**, 261-312.
257. H. Kim and W.-J. Maeng, *Thin Solid Films*, 2009, **517**, 2563-2580.
258. G. N. Parsons, S. E. Atanasov, E. C. Dandley, C. K. Devine, B. Gong, J. S. Jur, K. Lee, C. J. Oldham, Q. Peng, J. C. Spagnola and P. S. Williams, *Coord. Chem. Rev.*, 2013, **257**, 3323-3331.
259. L. Henn-Lecordier, M. Anderle, E. Robertson and G. W. Rubloff, *J.Vac. Sci. Tech. A:*, 2011, **29**, 051509.
260. V. R. Rai, V. Vandalon and S. Agarwal, *Langmuir*, 2010, **26**, 13732-13735.
261. J. S. Ponraj, G. Attolini and M. Bosi, *Crit. Rev. Solid State Mater. Sci.*, 2013, **38**, 203-233.
262. M. Leskelä and M. Ritala, *Thin Solid Films*, 2002, **409**, 138-146.
263. H. Kim, *J.Vac. Sci. Tech. B:*, 2003, **21**, 2231-2261.
264. H. Kim, P. C. McIntyre and K. C. Saraswat, *Appl. Phys. Lett.*, 2003, **82**, 106-108.
265. S. K. Kim, C. S. Hwang, S.-H. K. Park and S. J. Yun, *Thin Solid Films*, 2005, **478**, 103-108.
266. S. Obuchovsky, I. Deckman, M. Moshonov, T. S. Peretz, G. Ankonina, T. Savenije and G. Frey, *J. Mater. Chem. C*, 2014, **2**, 8903-8910.
267. E. Guziewicz, M. Godlewski, L. Wachnicki, T. Krajewski, G. Luka, S. Gieraltowska, R. Jakiela, A. Stonert, W. Lisowski and M. Krawczyk, *Semicond. Sci. Technol.*, 2012, **27**, 074011.
268. G. Luka, T. Krajewski, L. Wachnicki, B. Witkowski, E. Lusakowska, W. Paszkowicz, E. Guziewicz and M. Godlewski, *Phys. Status Solidi (a)*, 2010, **207**, 1568-1571.
269. N. Huby, G. Tallarida, M. Kutrzeba, S. Ferrari, E. Guziewicz and M. Godlewski, *Microelectron. Eng.*, 2008, **85**, 2442-2444.
270. J.-E. Kim, S.-M. Bae, H.-S. Yang and J.-H. Hwang, *J. Korean Ceram. Soc.*, 2010, **47**, 353-356.
271. Z. Chai, X. Lu and D. He, *Surf. Coat. Technol.*, 2012, **207**, 361-366.

272. D. H. Levy, D. Freeman, S. F. Nelson, P. J. Cowdery-Corvan and L. M. Irving, *Appl. Phys. Lett.*, 2008, **92**, 192101.
273. T. Krajewski, G. Łuka, B. Witkowski, B. Kowalski, K. Kopalko, J. Domagala, M. Guziewicz, M. Godlewski and E. Guziewicz, *Thin Solid Films*, 2010, **518**, 4556-4559.
274. S.-H. K. Park, C.-S. Hwang, H. Y. Jeong, H. Y. Chu and K. I. Cho, *Electrochem. Solid-State Lett.*, 2008, **11**, H10-H14.
275. P. Carcia, R. McLean and M. Reilly, *Appl. Phys. Lett.*, 2006, **88**, 123509.
276. D. Kim, H. Kang, J.-M. Kim and H. Kim, *Appl. Surf. Sci.*, 2011, **257**, 3776-3779.
277. S. Kwon, S. Bang, S. Lee, S. Jeon, W. Jeong, H. Kim, S. C. Gong, H. J. Chang, H.-h. Park and H. Jeon, *Semicond. Sci. Technol.*, 2009, **24**, 035015.
278. S. Lee, S. Bang, J. Park, S. Park, W. Jeong and H. Jeon, *Phys. Status Solidi i (a)*, 2010, **207**, 1845-1849.
279. B.-Y. Oh, Y.-H. Kim, H.-J. Lee, B.-Y. Kim, H.-G. Park, J.-W. Han, G.-S. Heo, T.-W. Kim, K.-Y. Kim and D.-S. Seo, *Semicond. Sci. Technol.*, 2011, **26**, 085007.
280. S. Bang, S. Lee, J. Park, S. Park, W. Jeong and H. Jeon, *J. Phys. D: Appl. Phys.*, 2009, **42**, 235102.
281. T. Tynell and M. Karppinen, *Semicond. Sci. Technol.*, 2014, **29**, 043001.
282. Y.-Y. Lin, C.-C. Hsu, M.-H. Tseng, J.-J. Shyue and F.-Y. Tsai, *ACS Appl. Mater. Inter.*, 2015, **7**, 22610-22617.
283. P. K. Nayak, Z. Wang, D. H. Anjum, M. N. Hedhili and H. N. Alshareef, *Appl. Phys. Lett.*, 2015, **106**, 103505.
284. Y. J. Chung, W. J. Choi, S. G. Kang, C. W. Lee, J.-O. Lee, K.-J. Kong and Y. K. Lee, *J. Mater. Chem. C*, 2014, **2**, 9274-9282.
285. C. H. Ahn, M. G. Yun, S. Y. Lee and H. K. Cho, *IEEE Trans. Electron Devices*, 2014, **61**, 73-78.
286. C. H. Ahn, K. Senthil, H. K. Cho and S. Y. Lee, *Sci. Rep.*, 2013, **3**, 2737.
287. P. K. Nayak, Z. Wang and H. N. Alshareef, *Adv. Mater.*, 2016, **28**, 7736-7744.
288. S. J. Lee, C. S. Hwang, J. E. Pi, J. H. Yang, C. W. Byun, H. Y. Chu, K. I. Cho and S. H. Cho, *ETRI Journal*, 2015, **37**, 1135-1142.
289. P. Barquinha, A. Pimentel, A. Marques, L. Pereira, R. Martins and E. Fortunato, *J. Non-Cryst. Solids*, 2006, **352**, 1749-1752.
290. G. Wakimura, Y. Yamauchi and Y. Kamakura, *Journal of Advanced Simulation in Science and Engineering*, 2015, **2**, 201-210.
291. Y. H. Lin, H. Faber, J. G. Labram, E. Stratakis, L. Sygellou, E. Kymakis, N. A. Hastas, R. Li, K. Zhao and A. Amassian, *Adv. Sci.*, 2015, **2**, 1500058.
292. E. N. Cho, J. H. Kang and I. Yun, *Microelectron. Reliab.*, 2011, **51**, 1792-1795.

293. Y. S. Rim, H. Chen, X. Kou, H. S. Duan, H. Zhou, M. Cai, H. J. Kim and Y. Yang, *Adv. Mater.*, 2014, **26**, 4273-4278.
294. S. Yoon, S. J. Kim, Y. J. Tak and H. J. Kim, *Sci. Rep.*, 2017, **7**, 43216.
295. H. Faber, S. Das, Y.-H. Lin, N. Pliatsikas, K. Zhao, T. Kehagias, G. Dimitrakopulos, A. Amassian, P. A. Patsalas and T. D. Anthopoulos, *Sci. Adv.*, 2017, **3**, e1602640.
296. D. Khim, Y.-H. Lin and T. D. Anthopoulos, *Adv. Funct. Mater.*, **0**, 1902591.
297. T. J. Drummond, W. T. Masselink and H. Morkoc, *Proc. IEEE*, 1986, **74**, 773-822.
298. G. Meneghesso, G. Verzellesi, F. Danesin, F. Rampazzo, F. Zanon, A. Tazzoli, M. Meneghini and E. Zanoni, *IEEE Trans. Device Mater. Reliab.*, 2008, **8**, 332-343.
299. D. Dumka, H. Tserng, M. Kao, E. Beam and P. Saunier, *IEEE Electron Device Lett.*, 2003, **24**, 135-137.
300. R. S. Pal, S. Sharma and S. Dasgupta, *ICEDSS*, 2017.
301. P. Lin and Q. Xia, *J. Appl. Phys.*, 2018, **124**, 152001.
302. P. S. Maydannik, T. O. Kääriäinen, K. Lahtinen, D. C. Cameron, M. Söderlund, P. Soininen, P. Johansson, J. Kuusipalo, L. Moro and X. Zeng, *J Vac. Sci.Technol. A:*, 2014, **32**, 051603.
303. K. Ali, K. H. Choi and N. M. Muhammad, *Chem. Vap. Deposition*, 2014, **20**, 380-387.

10 Curriculum Vitae

Personal information

Name:	Shawn Sanctis
Date of birth:	10/03/1986
Place of birth:	Mumbai, India
Address:	201 Paraclete Apt I.C.Colony, Borivli - West Mumbai – 400103 India

Education

05/2013 - present	Dr.rer.nat Dept. Of Inorganic Chemistry Technische Universität Darmstadt, Germany
09/2009 - 11/2010	Master of Science (Nanotechnology and Nanoelectronic Devices) Dept. of Engineering and Physical Sciences University of Surrey, United Kingdom
08/2005 - 05/2009	Bachelor of Engineering Dept. of Electronics and Telecommunication Engineering University of Mumbai Mumbai, India
06/2003 - 06/2004	Higher Secondary Education Maharashtra State Board of Secondary and Higher Secondary Education Mumbai, India

Shawn Sanctis